

JLU GIESSEN

DOCTORAL THESIS

**A kinetic Fokker-Planck algorithm for
simulating multiscale gas flows**

Author:
Christian Hepp

Supervisor:
Prof. Dr. Klaus Hannemann
Prof. Dr. Christian Heiliger

*A thesis submitted in fulfillment of the requirements
for the degree of Doctor of Physics*

in the

Working Group Spacecraft

FB07 - Mathematik und Informatik, Physik, Geographie
and

Spacecraft Department , Göttingen
German Aerospace Center (DLR)

2022-10-18

Declaration of Authorship

I declare that I have completed this dissertation single-handedly without the unauthorized help of a second party and only with the assistance acknowledged therein. I have appropriately acknowledged and cited all text passages that are derived verbatim from or are based on the content of published work of others, and all information relating to verbal communications. I consent to the use of an anti-plagiarism software to check my thesis. I have abided by the principles of good scientific conduct laid down in the charter of the Justus Liebig University Giessen „Satzung der Justus-Liebig-Universität Gießen zur Sicherung guter wissenschaftlicher Praxis“ in carrying out the investigations described in the dissertation.

Signed:

Date:

“Ludwig Boltzmann, who spent much of his life studying statistical mechanics, died in 1906, by his own hand. Paul Ehrenfest, carrying on the work, died similarly in 1933. Now it is our turn to study statistical mechanics. Perhaps it will be wise to approach the subject cautiously ...”

David L. Goodstein, *States of Matter*

Abstract

Numerical, aerodynamic analysis of spacecraft requires the modeling of rarefied hypersonic flows. Such flow regimes are usually dominated by broad shock waves and strong expansion flows. In such areas of the flow the gas is far from its equilibrium state and therefore conventional modeling approaches such as the Euler or Navier-Stokes equations cannot be used. Instead, non-equilibrium modeling approaches must be applied. While most non-equilibrium flow solvers are computationally expensive, a recently introduced kinetic Fokker-Planck (FP) method shows the potential of describing non-equilibrium flows with satisfactory accuracy and, at the same time, significantly reducing computational costs. However, the application of kinetic FP solvers was so far still limited to simple, single species gases.

The aim of this study is to extend the capabilities of the kinetic FP approach for describing complex gas flows. Particular attention is paid to the modeling of non-equilibrium aerodynamics, as it is relevant for describing spacecraft related gas flows.

Methods for describing polyatomic species as well as gas mixtures within the kinetic FP framework are constructed. All models are intensively validated by comparison to already established numerical methods, as well as in comparison to experimental studies.

Excited energy states are modeled by a stochastic jump process described by a master equation. This approach allows the description of both continuous and discrete energy levels. Gas mixtures are modeled based on the hard-sphere and variable hard-sphere collision potentials. For both cases, FP models are constructed for an arbitrary number of species. The efficiency of the described models is investigated and different strategies are proposed to use kinetic FP methods efficiently.

The expansion of synthetic air from an axially symmetric orifice is numerically reproduced using the developed models and results are compared with experimental measurements. Although the numerical simulations capture several magnitudes of Knudsen numbers, from the continuum flow in the reservoir up to the free-molecular far field, good agreement between simulation and experiment is seen.

Kurzfassung

Die numerische, aerodynamische Analyse von Raumfahrzeugen erfordert die Modellierung verdünnter Hyperschallströmungen. Solche Strömungen werden im Allgemeinen von breiten Stößen und starken Expansionen dominiert. In solchen Bereichen der Strömung ist das Gas weit von seinem Gleichgewichtszustand entfernt, weshalb konventionelle Modellierungsansätze, wie die Euler- oder Navier-Stokes-Gleichungen, nicht verwendet werden können. Stattdessen müssen Nichtgleichgewichtsmodelle zur Strömungsmodellierung herangezogen werden. Während der Rechenaufwand konventioneller Nichtgleichgewichts-Strömungslöser für viele Anwendungsbereiche unhaltbar hoch ist, zeigt ein kürzlich vorgeschlagenes kinetisches Fokker-Planck (FP) Verfahren das Potential, Nichtgleichgewichtsströmungen mit großer Genauigkeit, aber akzeptabler Rechenzeit, modellieren zu können. Trotz großem Interesse an dem Verfahren, ist dieses momentan lediglich zur Modellierung einfacher Gase mit nur einer Spezies einsetzbar.

Diese Arbeit verfolgt das Ziel, das kinetische FP Verfahren zu erweitern, um damit komplexe Gasströmungen simulieren zu können. Besonderes Augenmerk wird auf die Modellierung von Nichtgleichgewichtsströmungen gelegt, wie sie bei der aerodynamischen Beschreibung von Raumfahrzeugen auftreten.

Es werden Modelle entwickelt um mehratomige Gase und Gasgemische mit dem FP Verfahren modellieren zu können. Alle Modelle werden durch Vergleich zu bereits etablierten numerischen Verfahren, sowie im Vergleich zu experimentellen Studien, intensiv validiert.

Angeregte Energiezustände werden durch einen stochastischen Sprungprozess, beschrieben durch eine Mastergleichung, modelliert. Dieser Ansatz erlaubt die Beschreibung von sowohl kontinuierlicher als auch diskreter Energielevel. Gasgemische werden basierend auf dem Hartkugel und dem variablen Hartkugel Kollisionspotentials modelliert. Für beide Fälle werden FP Verfahren für eine beliebige Anzahl von Spezies konstruiert. Die Effizienz der beschriebenen Modelle wird untersucht und es werden verschiedene Strategien vorgeschlagen, um kinetische FP Methoden effizient einzusetzen.

Die Expansion von synthetischer Luft aus einer axial symmetrischen Öffnung wird mit den entwickelten Modelle numerisch nachvollzogen und Ergebnisse werden mit experimentellen Messungen verglichen. Obwohl die numerischen Simulationen mehrere Größenordnungen des Verdünnungsgrades, von der Kontinuumsströmung im Reservoir bis hin zum frei-molekularen Fernfeld, abbilden, ist eine gute Übereinstimmung zwischen Simulation und Experiment zu erkennen.

Acknowledgements

The fact that I was able to complete this work, and hopefully made a small contribution to the numerics of rarefied gas flows, is thanks to many people, to whom I would like to express my gratitude at this point.

First of all, I would like to express my sincere thanks to my recently deceased supervisor Prof. Dr. Klaus Hannemann. While I was still a student, he sparked my interest in numerical space aerothermodynamics through his excellent lecture "Fundamentals of Space Flight" at the JLU Gießen. Afterwards, Klaus gave me the opportunity for several internships and my master thesis in his research group, the Spacecraft Department at the DLR Göttingen, and he provided the financial framework for my PhD position. Klaus has always been very supportive and has given me the opportunity to gain valuable experience at several international conferences. Through the many interesting discussions with Klaus, especially about the connection between classical continuum mechanics and kinetic modeling of gases, I was able to broaden my horizon a lot and realized how important it is to look at a scientific question from different directions. Last but not least, I would like to mention the extraordinary achievement of Klaus to provide this text with valuable comments until shortly before the end, which enabled me to improve my thesis fundamentally.

I would also like to express my special thanks to Prof. Dr. Christian Heiliger and Prof. Dr. Manuel Torrilhon, who agreed to grade this thesis as first and second correctors after the passing away of Prof. Dr. Klaus Hannemann. In this context, I would also like to thank Prof. Dr. Peter J. Klar and Prof. Dr. Chris Volkmar for their willingness to attend my colloquium as first and second examiner.

My very special thanks go to Dr. Martin Grabe for mentoring me since my first days as an intern at DLR and for introducing me to the world of dilute gas flows. It was only through his way that I became interested in the numerics of dilute gases, and it was also only through Martin's initiative that I learned about my later PhD topic, the kinetic Fokker-Planck method. I would especially like to thank Martin for introducing me to the scientific community of dilute gases, for showing me what it means to work scientifically, for the countless discussions on a wide variety of topics, through which I was able to broaden my horizons, and of course for always having my back so that I had time to work on my Phd Thesis. And, of course, Martin's support in the preparation of my publications and my doctoral thesis must not go unmentioned, especially his unspeakable patience when it comes to correcting my grammatical excesses.

Last but not least, I would like to thank Martin for his advices on the formal preparation of my thesis, even after I left DLR. That is certainly not a matter of course!

I would also like to express my sincere thanks to all my colleagues during my time at the Spacecraft Department at DLR Göttingen and DLR Braunschweig. Through the many joint discussions, lunches, coffee breaks and excursions, this is a time that

I will always remember very positively.

At the same time, I would like to thank all the proofreaders of this work for supporting me in eliminating my grammatical and spelling excesses.

And last but not least, I would like to thank my family, especially my parents, who have supported me mentally and financially over the past few years and whose commitment awakened my fascination for the natural sciences in my younger years. Likewise, I would like to thank my girlfriend for always supporting me and showing me again and again that there is also a world outside the doctoral thesis.

List of publications

This thesis is not a cumulative dissertation. Nevertheless, it should be mentioned that the results of Ch. 3, Ch. 4 and Ch. 5 have already been published in the following publications:

- C. Hepp et al. "Master equation approach for modeling diatomic gas flows with a kinetic Fokker-Planck algorithm". In: *Journal of Computational Physics* 418 (2020), p. 109638. DOI: 10.1016/j.jcp.2020.109638
- C. Hepp et al. "A kinetic Fokker-Planck approach to model hard-sphere gas mixtures". In: *Physics of Fluids* 32.2 (2020), p. 027103. DOI: 10.1063/1.5141909
- C. Hepp et al. "A kinetic Fokker-Planck approach for modeling variable hard-sphere gas mixtures". In: *AIP Advances* 10.8 (2020), p. 085219. DOI: 10.1063/5.0017289

In addition, the results from Ch. 3 were presented in the following talks:

- C. Hepp. "Modeling of internal energy relaxation in a kinetic Fokker-Planck solver". DSMC 2019 Conference, Santa Fe. 2019
- C. Hepp. "Modeling of rarefied gas flows with particle methods". Department of Mechanical Engineering, University of New Mexico, Invited by Dr. D. T. Banuti. 2019

Contents

Declaration of Authorship	iii
Abstract	vii
Acknowledgements	xi
List of publications	xiii
1 Introduction	1
1.1 Non-equilibrium aerodynamics in space engineering	2
1.2 Modeling of non-equilibrium gas flows	5
1.3 The Fokker-Planck equation and kinetic Fokker-Planck methods	8
1.4 Objectives of this thesis	10
1.5 Structure of this thesis	11
2 Methods	13
2.1 Kinetic theory of gases	13
2.1.1 Statistical description	13
2.1.2 Kinetic models	14
2.1.3 Polyatomic species and multi species gases	16
2.2 Direct Simulation Monte Carlo Method	20
2.2.1 Numerical and physical approximations	20
2.2.2 Generation of particles	21
2.2.3 Moving of particles	22
2.2.4 Calculation of particle collisions	23
2.2.5 Calculation of averages	27
2.3 Kinetic Fokker-Planck method	29
2.3.1 Fokker-Planck approximation of the Boltzmann equation	29
2.3.2 Kinetic description	31
2.3.3 Models for polyatomic species	35
2.3.4 Models for gas mixtures	37
2.3.5 Applicability of the kinetic Fokker-Planck method	38
3 Modeling of polyatomic species	41
3.1 Master equation ansatz	41
3.2 Stochastic equations of motion	44
3.3 Models for rate coefficients	45
3.3.1 DLT model	45
3.3.2 CLT model	46
3.3.3 DLB model	47
3.4 Discussion of the model	51
3.4.1 Separation of the distribution function	51
3.4.2 Moment relaxation	51

3.5	Solving stochastic equations of motion	53
3.5.1	DLT model	54
3.5.2	CLT model	55
3.5.3	DLB model	56
3.6	Test cases	57
3.6.1	Heat bath	58
3.6.2	Spherical expansion flow	60
3.6.3	Shock wave	62
3.6.4	Flow past a perpendicular flat plate	65
3.7	Efficiency considerations	67
3.7.1	Restrictions on the time step size	68
3.7.2	Computational efficiency	69
3.8	Summary and conclusion	70
4	Modeling of hard sphere gas mixtures	73
4.1	Fokker-Planck model for hard sphere mixtures	73
4.1.1	Linear model	75
4.1.2	Higher order model	76
4.2	Stochastic solution algorithm	77
4.3	Testcases	79
4.3.1	Heat bath	79
4.3.2	Couette flow	82
4.3.3	Supersonic Couette flow	85
4.3.4	One-dimensional mass diffusion	87
4.4	Summary and conclusion	90
5	Modeling of variable hard sphere gas mixtures	93
5.1	Fokker-Planck method for a VHS gas mixture	93
5.2	Test cases	94
5.2.1	Supersonic Couette flow	95
5.2.2	Diffusion flow	96
5.2.3	Flat plate	96
5.3	Summary and conclusion	99
6	Modeling of polyatomic variable hard sphere gas mixtures	101
6.1	Fokker-Planck model	101
6.2	Stochastic equations of motion	103
6.3	Models for rate coefficients	104
6.3.1	DLT model	104
6.3.2	CLT model	105
6.3.3	DLB model	105
6.4	Test cases	106
6.4.1	Adiabatic heat bath	107
6.4.2	Spherical expansion flow	109
6.4.3	One-dimensional flow past a shock wave	110
6.4.4	Flow past a perpendicular flat plate	111
6.5	Summary and conclusion	113

7	Efficiency considerations	115
7.1	Linear system of evolution equations	115
7.2	Validity considerations	117
7.2.1	Relaxation of flow quantities	117
7.2.2	Supersonic Couette flow	120
7.3	Efficiency considerations	120
7.4	Summary and conclusion	123
8	Gas expansion into a vacuum environment	125
8.1	Test case description and experimental setup	125
8.2	Numerical setup	126
8.3	Results	128
8.3.1	Grid convergence study	128
8.3.2	Reservoir size	129
8.3.3	Numerical considerations	131
8.3.4	Comparison with experiments	131
8.3.5	Impact of thermodiffusion	133
8.4	Summary and conclusion	135
9	Conclusion and Outlook	139
9.1	Summary	139
9.2	Conclusion	140
A	DSMC	145
A.1	Particle selection scheme	145
B	Internal energies	147
B.1	Conservation equation	147
B.1.1	Mass conservation	147
B.1.2	Momentum conservation	148
B.1.3	Energy conservation	148
B.2	H-Theorem	149
C	HS mixtures	153
C.1	HS-Boltzmann production terms	153
C.2	Fokker-Planck production terms	155
C.3	Linear system of equations	156
C.4	Time evolution of moments	157
D	VHS mixtures	159
D.1	VHS Boltzmann production terms	159
E	Expansion flows	163
E.1	Temperature anisotropy in free molecular expansion	163
F	Collision parameters	165
	Bibliography	167

List of symbols

Abbreviations

BGK	B hatnagar- G ross K rook
CCL	C ercignani- L ampis
CFL	C ourant- F riedrichs- L ewy
CLT	continuous energy structure, macroscopic L andau- T eller
DLB	discrete energy structure, microscopic L arsen- B orgnakke
DLT	discrete energy structure, macroscopic L andau- T eller
DSMC	direct simulation M onte- C arlo
DV	discrete velocity
FP	F okker- P lanck
ES-BGK	ellipsoidal statistical B hatnagar- G ross K rook model
HS	h ard sphere
LB	L arsen- B orgnakke
LD	low d iffusion
NTC	n o time counter
PDF	partricle d istribution function
SPARTA	stochastic p arallel rarefied-gas t ime-accurate analyzer
STG-CT	S imulationsanlage T reibstrahlen G öttingen für chemische T riebwerke
VHS	variable h ard sphere

Latin symbols

A	drift coefficient	m/s^2
$\mathbf{A}^{(\alpha)}$	drift coefficient of species α	m/s^2
A	area	m^2
A, B	matrices	$1/\text{s}$
B_n	combined FP-master equation operator for internal energy state n	s^2/m^6
$B_n^{(\alpha)}$	combined FP-master equation operator for internal energy state n of species α	s^2/m^6
$b, b_{\alpha\beta}$	impact parameter α	m
c	thermal velocity	m/s
\mathbf{c}_{\parallel}	parallel component of thermal velocity	m/s
\mathbf{c}_{\perp}	perpendicular component of thermal velocity	m/s
$\mathbf{c}^{(\alpha)}$	thermal velocity of species α (with respect to species velocity)	m/s
$\hat{\mathbf{c}}^{(\alpha)}$	thermal velocity of species α (with respect to mixture velocity)	m/s
$d\mathbf{c}, d\mathbf{c}^{(\alpha)}$	thermal velocity element	m^3/s^3
$\mathbf{c}_r, \mathbf{c}_r^{(\alpha\beta)}$	relative collision velocity	m/s
$\mathbf{c}_{r,\text{ref}}$	reference collision velocity	m/s
$d\mathbf{c}_r$	increment of absolute relative collision velocity	m/s
$c_p, c_p^{(\alpha)}$	heat capacity at constant pressure	J/K

$c_v, c_v^{(\alpha)}$	heat capacity at constant volume	J/K
d_{int}	Number of internal degrees of freedom	-
d_{vib}	Number of vibrational degrees of freedom	-
$d_{\text{ref}}, d_{\text{ref}}^{(\alpha\beta)}$	Reference diameter of HS/VHS molecule.	m
$d^{(\alpha-\beta)}$	Reference diameter for a collision between an α and β particle	m
D_{int}	Damköhler number	-
D	diffusion coefficient	$\text{m/s}^{3/2}$
$D^{(\alpha)}$	diffusion coefficient of species α (unit refers to Eq. (6.1))	$\text{m/s}^{3/2}$
d	diameter	m
d_{coll}	collision diameter	m
E_{int}	average internal energy per molecule	J
$E_{\text{int}}^{(\text{eq})}$	average internal energy per molecule in equilibrium	J
dE	energy increment	J
e	energy per molecule	J
$e_i, e_i^{(\alpha)}$	energy level	J
f	particle distribution function	s^3/m^6
f_r	distribution function of relative particle velocities	s^3/m^6
f_i	particle distribution function for energy state i	s^3/m^6
$f^{(\alpha)}$	particle distribution function of species α	s^3/m^6
$f_i^{(\alpha)}$	particle distribution function of species α in energy state i	s^3/m^6
F_N	scaling factor defining number of computational particles	-
f_{eq}	Maxwell distribution	s^3/m^6
\mathbf{F}	force	N
g	species weight	-
$g_n, g_n^{(\alpha)}$	probability distribution function	-
$H_i, H_i^{(\alpha)}$	quantity, describing energy structure of molecules	J/s
H	entropy function	-
$\mathbf{h}^{(\alpha)}$	reduced heat flux	kg/s/m^2
J_1, J_4, J_6, J_7	collision integrals	-
\mathbf{j}	mass flux density	kg/s/m^2
Kn	Knudsen number	-
Kn_{local}	local Knudsen number	-
$K, K', K^{(\alpha)}$	constant, describing internal energy exchange	$\text{m/s}^{3/2}$
$K_i^{(\alpha)}$	part of multi-species model	m/s^2
$K_i,$	sum of rate coefficients	1/s
k	thermal conductivity	W/K/m
k_B	Boltzmann constant	J/K
L	linear part of drift coefficient	m/s^2
l_{ref}	reference length	m
M	Mach number	-
m	particle mass	kg
$m^{(\alpha)}$	particle mass of species α	kg
$m_r, m_r^{(\alpha\beta)}$	reduced mass	kg
$\dot{m}_{\text{num}}, \dot{m}_{\text{exp}}$	mass flow rate	kg/s
N_p	number of particles	-
N_t	number of time steps	-
N_s	number of species	-
N_{in}	number of incoming particles	-
N_{coll}	number of collisions	-

N_{\max}	maximum number of energy states	-
$\mathbf{N}, \mathbf{N}^{(\alpha)}$	non-linear part of drift coefficient	m/s^2
n	particle density	$1/\text{m}^3$
n_{∞}	inflow particle density	$1/\text{m}^3$
n_i	number density of particles in internal energy state i	$1/\text{m}^3$
$n^{(\alpha)}$	particle density of species α	$1/\text{m}^3$
$n_j^{(\alpha)}$	particle density of species α and energy state j	$1/\text{m}^3$
P	probability	-
$P_1(\tau, i, j),$ $P_2(i, j)$	Probability density functions	-
P_{ij}	probability for an change from state i to state j	-
$P_{\text{inel}}, P_{\text{inel}}^{(\alpha\beta)}$	probability for an inelastic collision	-
P_{coll}	collision probability	-
$P_{\text{rot}}, P_{\text{rot},i}$	Probability for rotational relaxation	-
$P_{\text{vib}}, P_{\text{vib},i}$	Probability for vibrational relaxation	-
$(P_{\text{coll}})_{\max}$	maximum collision probability	-
P_{Ψ}	production term for collision operator Ψ	-
$P_{\Psi}^{(\alpha)}$	production term for collision operator Ψ of species α	-
p_{ij}	pressure tensor	Pa
$p_{ij}^{(\alpha)}$	pressure tensor of species α	Pa
p	pressure	Pa
$p_{\text{vp}}^{(\alpha)}$	vapour pressure	Pa
Pr	Prandtl number	-
\mathbf{q}	translational heat flux	Js/m^4
$\mathbf{q}^{(\alpha)}$	translational heat flux of species α	Js/m^4
\mathbf{q}_{int}	internal heat flux	Js/m^4
\mathbf{q}	heat flux	Js/m^4
$Q, Q^{(\alpha)}$	partition function	-
Q_{nom}	scaling factor (BL model)	-
$Q_{\alpha,\beta}^l$	effective cross sections	m^2
$R_{ij}, R_{ij}^{(\alpha)}$	rate coefficient	$1/\text{s}$
R	scattering kernel	-
\mathbb{R}	random number	-
S_{Boltz}	Boltzmann collision operator	s^2/m^6
$S_{\text{Boltz}}^{(\text{el})}$	elastic part of Boltzmann collision operator	s^2/m^6
$S_{\text{Boltz}}^{(\text{inel})}$	inelastic part of Boltzmann collision operator	s^2/m^6
S_{FP}	FP collision operator	s^2/m^6
$S_{\text{FP}}^{(\alpha)}$	FP collision operator of species α	s^2/m^6
S_v, S_e	part of inelastic Boltzmann collision operator	s^2/m^6
T	(translational) temperature	K
T_{W}	wall temperature	K
T_{int}	internal temperature	K
T_{rot}	rotational temperature	K
T_{vib}	vibrational temperature	K
$T_{\text{ref}}, T_{\text{ref}}^{(\alpha\beta)}$	reference temperature	K
T_{∞}	inflow (translational) temperature	K
$T^{(\alpha)}$	(translational) temperature of species α	K
T_{\parallel}	parallel component of translational temperature α	K

T_{\perp}	perpendicular component of translational temperature α	K
t	time	s
Δt	time step, time interval	s
dt	time increment	s
\mathbf{u}	flow velocity	m/s
$\mathbf{u}^{(\alpha)}$	flow velocity of species α	m/s
$\mathbf{u}_d^{(\alpha)}$	diffusion velocity of species α	m/s
V	volume	m^3
V_c	cell volume	m^3
\mathbf{v}_i	velocity vector	m/s
\mathbf{v}	eigenvector	-
\mathbf{v}	velocity	m/s
\mathbf{v}_0	initial velocity	m/s
$\mathbf{v}^{(\alpha)}$	velocity of species α	m/s
\mathbf{V}	random process of velocity	m/s
$\mathbf{V}^{(\alpha)}$	random process of velocity of species α	m/s
$d\mathbf{v}$	velocity element	m^3/s^3
$VHS[i]$	VHS scaling parameter	-
$dW, dW^{(\alpha)}$	increment of Wiener process	-
X^n	average number of particles at timestep N	-
Y^n	average velocity moment at timestep N	-
\mathbf{x}	position vector	m
\mathbf{x}_0	initial position vector	m
\mathbf{X}	random process of position vector	m
$\mathbf{X}^{(\alpha)}$	random process of position vector for species α	m
$d\mathbf{x}$	volume element	m^3
X	average number of particles	-
Y	average moment	-
Z^{tot}	total collision number	-
Z^{inel}	inelastic collision number	-
$Z_{\text{int}}^{(\alpha\beta)}$	inelastic collision number	-

Greek symbols

α	accommodation coefficient	-
α	scaling factor	-
α_n	normal accommodation coefficient	-
α_t	tangential accommodation coefficient	-
β	correction factor	-
β	inverse temperature	1/J
$\gamma_i, \gamma_i^{(\alpha)}$	model parameter (cubic model)	m
γ	heat capacity ratio	-
Δ	difference	-
ϵ	distance between energy states	J
$\hat{\theta}$	vector of reduced temperatures	J/kg
$\theta, \theta^{(\alpha)}$	reduced temperature	J/kg
$\theta^{(\alpha\beta)}$	average reduced temperature	J/kg
$\Delta\theta^{(\alpha\beta)}$	difference of average reduced temperature	J/kg
$\theta, \theta^{(\alpha)}$	characteristic vibrational temperature	K

κ	heat capacity ratio	-
Λ	stability constant	s/m ²
$\Lambda^{(\alpha)}$	stability constant for species α	s/m ²
λ	mean free path	m
$\lambda^{(\alpha)}$	mean free path of species α	m
λ	eigenvalue	-
μ	(dynamic) viscosity	Pa s
μ_{ref}	reference (dynamic) viscosity	Pa s
$\mu^{(\alpha)}$	mass fraction of α species (in relation to species β)	-
$\nu^{(\alpha\beta)}$	Collision frequency between α and β species	1/s
$\nu_{\text{coll}}, \nu_{\text{coll}}^{(\alpha\beta)}$	Collision frequency	1/s
$\nu_{\text{VHS}}, \nu_{\text{VHS}}^{(\alpha\beta)}$	VHS Collision frequency	1/s
ν	VHS velocity exponent	-
Ω	rotational velocity	m/s
$d\Omega$	rotational velocity increment	m/s
ρ	mass density	kg/m ³
$\rho^{(\alpha)}$	mass density of species α	kg/m ³
Σ	rotational velocity	m/s
$d\Sigma$	rotational velocity increment	m/s
$\Sigma_{\alpha,\beta}^{l,r}$	collision integrals	m ²
σ_{T}	total collision cross section	m ²
σ_{ij}	stress tensor	Pa
σ_{ij}	cross section for inelastic collision	m ²
$\sigma_{ij}^{(\alpha)}$	stress tensor of species α	Pa
$\sigma_{ij}^{(\alpha\beta)}$	reference cross section	m ²
τ	relaxation time	s
τ_{c}	characteristic time	s
τ_{rot}	rotational relaxation time	s
τ_{rot}	vibrational relaxation time	s
$\tau_{\text{int}}, \tau_{\text{int}}^{(\alpha\beta)}$	internal relaxation time	s
$\tau_{\text{int}}^{(\alpha)}$		
τ_{flow}	characteristic time of the flow	s
Φ	reduced time step and cell size	-
Φ	relaxation factor	-
ϕ	angle	-
ϕ	relaxation parameter	-
χ	mole fraction	-
χ	deflection angle	-
Ψ	vibrational velocity	m/s
$d\Psi$	vibrational velocity increment	m/s
$\Psi_{ij}, \Psi_{ij}^{(\alpha)}$	model parameter (cubic model)	1/s
ω	viscosity exponent	-
$\omega^{(\alpha\beta)}$	viscosity exponent for $\alpha - \beta$ particle collision	-
Ξ	velocity scaling parameter	-
ξ	normal random number	-

Pointer

ave	average
Boltz	Boltzmann
back	background
c	cell
coll	collision
cubic	cubic FP model
eq	equilibrium
exp	experiment
FP	Fokker-Planck
flow	flow
in	incoming
inel	inelastic
int	internal
linear	linear FP model
MA	Master
MAX	Maxwell
max	maximum
min	minimum
mix	mixture
n	normal component
n	time step number
nom	normalization
p	particle
ref	reference
rel	relaxation
rot	rotational
s	species
t	tangential component, time
tot	total
tr	translational
out	outgoing
vib	vibrational
	parallel
⊥	perpendicular
0	initial condition / reservoir condition
∞	inflow value
(α)	with respect to species α
($\alpha\beta$)	with respect to species α and species β
*	throat condition

Mathematics

$Q_{\langle ij \rangle}$	deviatoric part of matrix Q_{ij}
Γ	gamma function
$\frac{D}{Dt}$	total derivation
\mathbb{R}	random number
δ_{ij}	Kronecker delta

Chapter 1

Introduction

The impact of satellite utilization on our society has increased dramatically in recent decades. While the first artificial object in space, the Russian Sputnik 1 vehicle, was only able to transmit a simple signal, modern satellites have become essential for a variety of recent technologies and research projects. Many aspects of our modern life, including the daily weather forecast, telecommunication or navigation via smart phones, are directly related to satellites. Furthermore, technologies such as the surveillance of global maritime transport [20] or even monitoring of variations in vegetation activity [148], were enabled through satellites.

In order to operate a satellite, it must be equipped with an attitude control system that is used to control its orientation in space. Such a control system must work precisely and reliably, but it should also be simple and small. Therefore, many satellites rely on conventional cold gas systems [77, 99], since they are technically very easy to handle and can be designed to precisely control a large number of different thrust levels. Cold gas thrusters, however, generate exhaust plumes. Since propellant is exhausted in a vacuum environment, the plume can become significant large and might affect the satellite. For example, propellant might deposit on vehicle surfaces, which can lead to pollution of essential parts of the spacecraft, such as solar panels or scientific experiments. In order to estimate and avoid such phenomena, it is of great importance to correctly model and simulate the aerodynamics of exhaust plumes, generated by cold gas thrusters.

As another example, note that some tasks require a satellite to move in a very low orbit. Examples are the GOCE satellite, which was used to measure the earth's gravitational field, or also the International Space Station. Due to the residual atmosphere in such low orbits, low-flying satellites experience a frictional force, which in the long-term leads to unwanted re-entry into the earth's atmosphere. To counteract this effect, low flying satellites are equipped with engines that can compensate for this frictional force. In order to design the engine system, however, it is necessary to know the exact influence of the residual atmosphere on the spacecraft. For this it is of great importance to correctly model and simulate the aerodynamics of such satellites in a dilute atmosphere.

These two examples illustrate the great importance of aerodynamics in the field of space engineering. Aerodynamic properties of a spacecraft are typically investigated numerically or experimentally. While the latter is essential to perform final validation studies, extreme environmental conditions in space make it very difficult and expensive to experimentally model many relevant scenarios. This is one of the reasons why numerical investigations have become increasingly popular in recent decades. In the spirit of this development, this work contributes to the numerical

modeling of space engineering related gas flows. This entails the development of numerical methods suitable to describe the physics within this specific environment.

The structure of this introduction is as follows. Subchapter 1.1 gives a brief introduction to physical phenomena that are important in the analysis of gas flows related to space engineering. Subchapter 1.2 reviews mathematical models and numerical methods that are applicable to describe such gas flows. Subchapter 1.3 provides a brief historical overview over the Fokker-Planck (FP) equation and introduces the kinetic FP simulation method, which is used throughout this thesis. Finally, Subch. 1.4 and Subch. 1.5 describe the objectives and structure of this thesis.

1.1 Non-equilibrium aerodynamics in space engineering

Aerodynamics in the context of space engineering is strongly affected by non-equilibrium phenomena that are inherent to hypersonic flow velocities as well as strong expansion effects.¹ For the aerodynamic analysis of space systems, it is therefore crucial to properly model such non-equilibrium gas flows. Depending on the physical effects which are involved, different kinds of non-equilibrium can occur.

Thermal non-equilibrium refers to the velocity distribution of the underlying atoms and molecules. In thermal equilibrium, particle velocities are distributed as described by a Maxwell distribution. Accordingly, a non-equilibrium state is characterized by deviations from a Maxwell distribution. Since the velocity distribution is driven to equilibrium by particle collisions, thermal non-equilibrium mainly appears when only few collisions occur on flow-relevant time and length scales. This is the case, when the mean free path of particles is large compared to a characteristic length scale of the flow. Hence, in order to characterize thermal non-equilibrium, the Knudsen number is introduced:

$$Kn = \frac{\lambda}{l_{\text{ref}}}. \quad (1.1)$$

Here λ is the particle mean free path, which characterizes the average distance traveled by a particle between two collisions. The length l_{ref} is case dependent and characterizes relevant dimensions of the flow. Traditional definitions of the Knudsen number employ a constant reference length for the entire flow field, for example the diameter of a reentry capsule or the nozzle throat diameter. More recent approaches

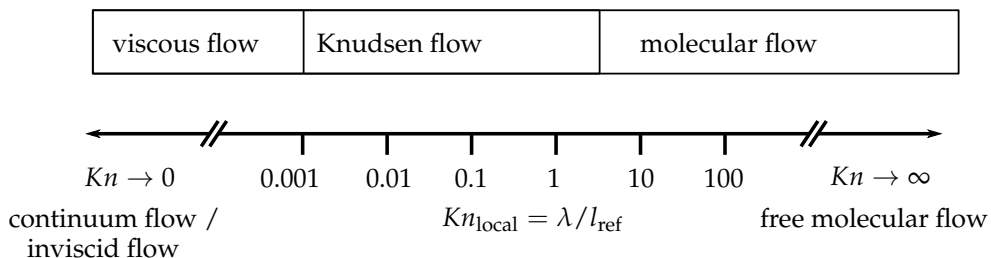


FIGURE 1.1: Different flow regimes, depending on the Knudsen number.

¹ Historically a hypersonic flow is defined by a flow velocity that is at least five times higher than the speed of sound. [5]

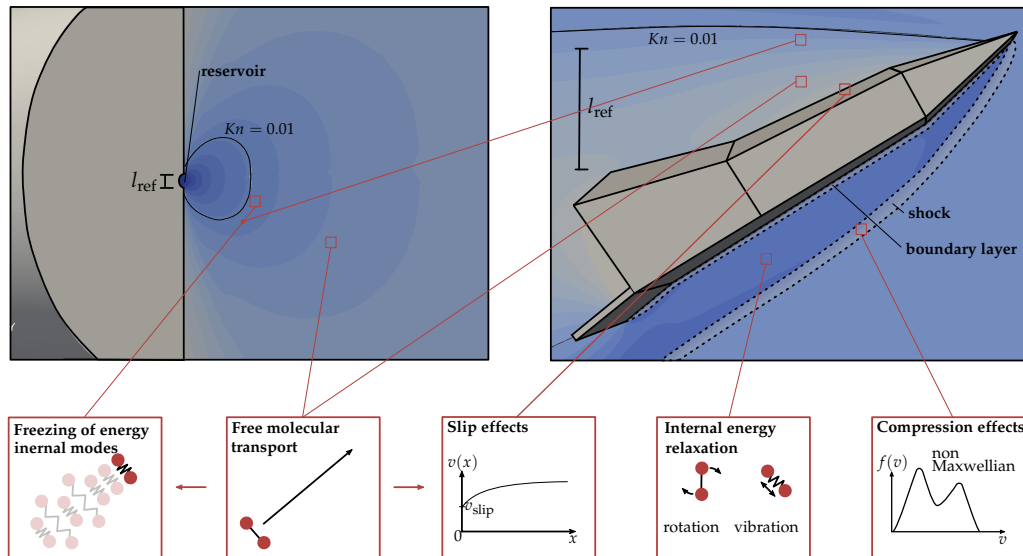


FIGURE 1.2: Various non-equilibrium effects in a slit expansion and a hypersonic re-entry flow. Contours show levels of constant Knudsen numbers. Reference length scales are the diameter of the slit and the diameter of the vehicle. The black lines indicate a Knudsen number of $Kn = 0.01$, that might be used as a limit value to indicate the appearance of the Knudsen regime.

define local length scales, for example the magnitude of local gradients [18]. In general, a high Knudsen number indicates a strong tendency of the flow to develop thermal non-equilibrium. The Knudsen number is also employed for characterizing different flow regimes, which are reviewed in Fig. 1.1.

A continuum flow is defined by vanishing Knudsen numbers. Many particle collisions occur in this regime, which causes the particle velocity distribution to become a local Maxwell distribution. As a result, viscous effects and heat transport are absent in a continuum flow. In addition, interaction between the gas and surfaces can be described as frictionless.

In a viscous flow, the velocity distribution deviates slightly from the equilibrium case. Viscous effects, such as heat conduction or diffusion and friction on surfaces and shear layers must be taken into account.

In a Knudsen flow, the average time and the distance between collisions are no longer negligibly small compared to the time and length scales of the flow. As a result the number of particle collisions in the flow field decreases and the velocity distribution begins to deviate greatly from the equilibrium case. As a typical result, slip effects can be observed, which means, that the flow velocity and temperature are no longer balanced with surfaces.

In the molecular flow regime, free molecular transport arises. The frequency of particle-particle collisions drops considerably and particles are traveling on free-flight trajectories, along distances that are in the same size as the characteristic scale l_{ref} . As a result, flow structures are more and more dominated by particle-wall interactions.

A free molecular flow is defined by an infinite Knudsen number. No particle-particle collisions occur anymore and the flow is fully dominated by particle-wall interactions.

Internal non-equilibrium refers to the distribution of internal particle energies, such

as rotational or vibrational energy states. In an equilibrium state, internal energies are described by a Boltzmann distribution and the temperature of the internal modes coincides with the thermal particle temperature. A non-equilibrium state is characterized by deviations of the energy distribution from a Boltzmann distribution as well as resulting deviations of the internal temperatures from the thermal temperature. Similar to particle velocities, internal energies are driven to equilibrium mainly by inelastic collisions. Hence, internal non-equilibrium occurs, when the characteristic time between inelastic particle collisions becomes large, compared to a characteristic time scale of the flow. To characterize this effect, the Damköhler number is introduced:

$$D_{\text{int}} = \frac{\tau_{\text{flow}}}{\tau_{\text{int}}}. \quad (1.2)$$

Here τ_{int} is the relaxation time of an internal energy mode and τ_{flow} denotes a characteristic time-scale of the flow. A small Damköhler number indicates a tendency of the flow to develop internal non-equilibrium. Since inelastic collisions are less likely than elastic collisions, internal non-equilibrium occurs more frequently than thermal non-equilibrium.

For practical problems, mostly a combination of thermal and internal non-equilibrium effects occur. Figure 1.2 gives some examples in order to highlight the complexity of non-equilibrium flow fields, as they occur in spacecraft related aerothermodynamics.

Gas expansion through a slit into a vacuum environment is a common model problem to investigate strong expansion phenomena, that occur when using chemical thrusters in a space environment. The gas is completely in equilibrium inside the reservoir. However, the strong expansion process leads to a rapidly decreasing density distribution with progressive expansion. As a result, the number of particle collisions decreases and the flow is characterized by the Knudsen and molecular regime. As described above, flow velocity and temperature do not equilibrate with surfaces any more, which leads to slip effects. In addition, a separation of different thermal temperature modes can be observed (see App. E) and internal energy modes become frozen, which means they do not equilibrate with translational modes any more. As the expansion proceeds, the gas is fully dominated by free molecular transport, leading to a strong self similarity of flow structures.

A re-entry flight leads to strong mechanical and thermal loads, in particular on the vehicle windward face. An accurate prediction of such loads can efficiently drive the design of the thermal protection system without leading to unnecessary mass addition to the overall vehicle weight. A common task of aerothermodynamics is therefore to predict these loads. Since re-entry vehicles are traveling at hypersonic speed, a shock wave is generated in front of the spacecraft. A shock wave features an area of thermal non-equilibrium which is generated by strong compression effects. The wave has a width of several mean free paths. Hence, in low Knudsen number flows it is negligibly small. In contrast, in high Knudsen number flows the size of the shock wave increases. As a result the inner area of the shock wave starts dominating the flow, making it necessary to properly model the thermal non-equilibrium region inside the shock wave.

The shock wave causes a rapid increase in the gas temperature, which can lead to excitation of internal energy modes. In particular vibrational energy modes feature a small relaxation time τ_{vib} . Consequently the Damköhler number D_{vib} of this process is small, resulting in internal non-equilibrium behind the shock wave. Such

processes can, for example, have a major impact on the thermal loads acting on the vehicle surface.

Due to the high flow velocity, only a few particles penetrate the wake region in the leeward part of the vehicle. As a consequence, the particle density decreases rapidly in this area, leading to a high local Knudsen number. This results in thermal non-equilibrium effects behind the vehicle, as described above.

1.2 Modeling of non-equilibrium gas flows

The following chapter provides an overview of the most common numerical techniques for modeling non-equilibrium gas flows.

The Boltzmann equation features the most detailed model for describing non-equilibrium gas flows. Originally suggested by Ludwig Boltzmann in 1872 for describing dilute gas flows [104], extensions have been proposed for modeling internal energy modes [29], chemical reactions [23] and dense gases [33, 30]. The Boltzmann equation describes the evolution of a particle distribution function (PDF) in phase space. Once the equation is solved, the PDF can be employed to calculate arbitrary macroscopic quantities. However, the high dimension of the phase space, as well as the complexity of the Boltzmann equation, renders its direct solution to a complex task. For this reason, several numerical methods have been derived that approximate the solution of the Boltzmann equation. Figure 1.3 gives an overview about the most established numerical techniques for solving and approximating the Boltzmann equation, while Fig. 1.4 shows the validity range of these methods, depending on the Knudsen number.

Discrete velocity (DV) methods discretize the velocity space [126, 21, 144]. Although particle velocities are not restricted and the velocity space is therefore infinitely large, this approach is applicable. This is, because the velocity distribution function tends to vanish for high velocities.² Hence, the distribution function can be bounded and a finite number of discrete points is sufficient to represent it in velocity space. In order to calculate the temporal evolution of the PDF, operator splitting techniques

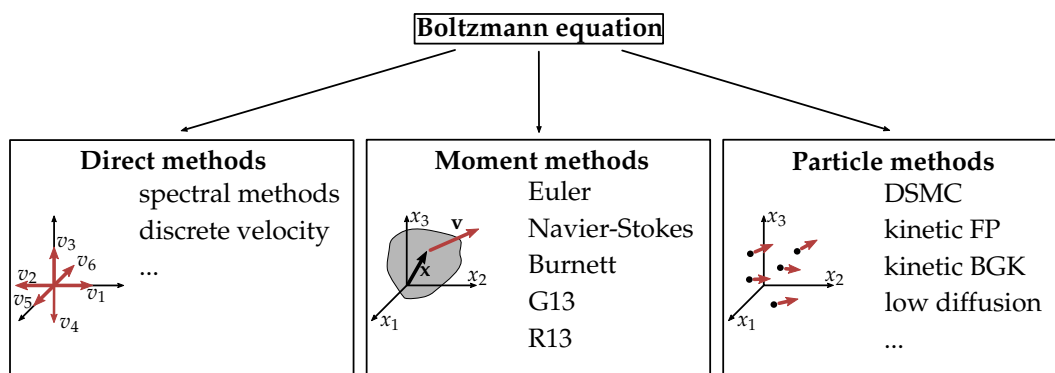


FIGURE 1.3: Various computational methods for describing non-equilibrium gas flows, deduced from the Boltzmann equation.

² This phenomenon can be made clear by the following argumentation: A gas can only store a finite amount of energy. Correspondingly, only finite particle velocities can occur. Therefore, the velocity distribution function must be negligibly small for large particle velocities.

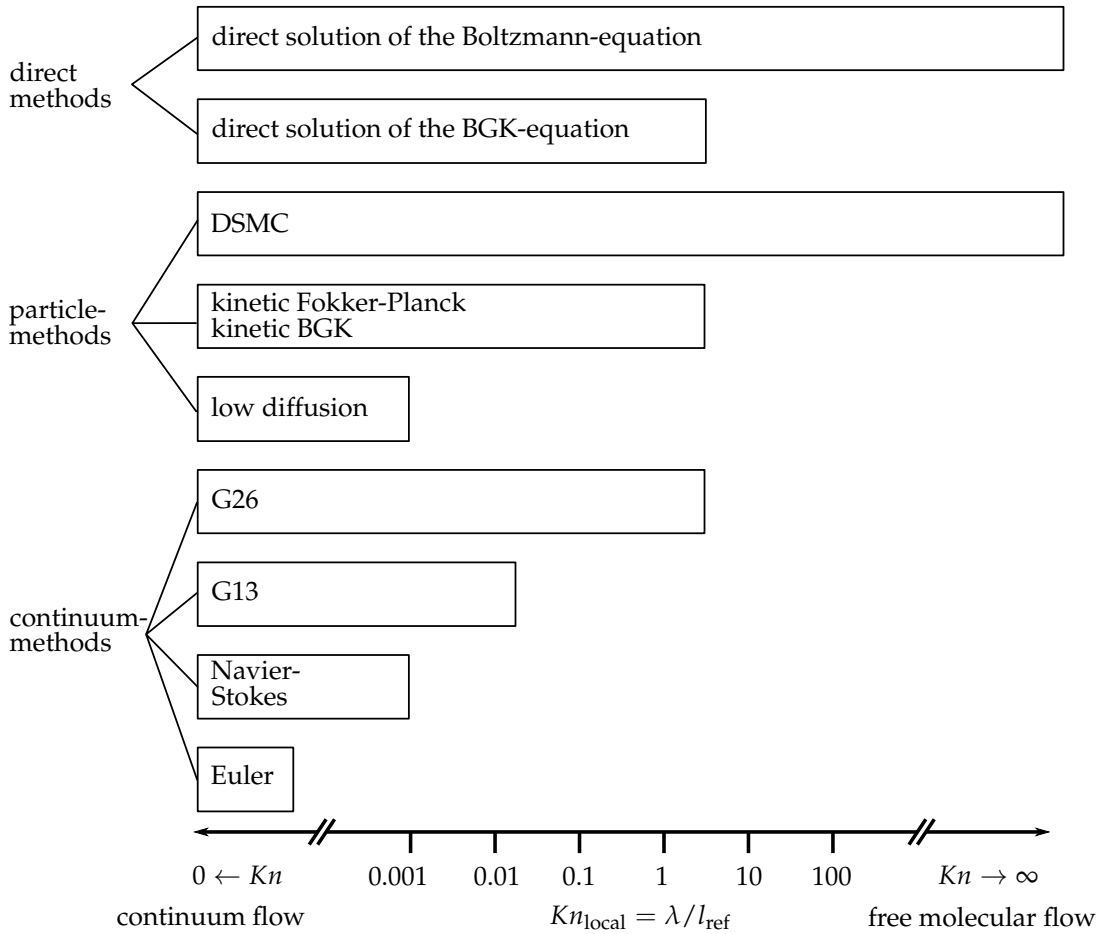


FIGURE 1.4: Applicability of different methods to describe non-equilibrium gas flows. Please note that the specific Knudsen number range only serves as a rough guide. The actual applicability depends heavily on the specific flow problem as well as on the flow quantities that are being investigated. Also, the graphic only shows whether the methods can in principle be used for the corresponding Knudsen number and not whether the applicability makes sense from a computational point of view.

are mostly applied. This leads to a separation of the collision and transport term of the Boltzmann equation, but results in very strict requirements for the temporal and spatial discretization, which must resolve the mean collision time and the mean free path. DV methods require a large amount of memory, because the entire velocity space must be discretized for each spatial grid point. In particular the treatment of hypersonic flows becomes problematic, since high particle velocities can occur, requiring many points to discretize the velocity space.

Spectral methods overcome that problem by using a Fourier transformation of the distribution function in velocity space [115, 37, 36, 146]. This technique leads to an efficient calculation of the collision term, but strict requirements concerning temporal and spatial resolution are still present.

In order to reduce the computational effort of such methods, it is common practice not to solve the Boltzmann equation directly, but to consider one of its approximations [144]. Important examples feature the **B**hatnagar-**G**ross-**K**rook (BGK) model [7] as well as its extensions, the ellipsoidal statistical BGK (ES-BGK) model [79]

and the Shakov model [132]. However, these models are only valid to describe low Knudsen number gases.

In the framework of kinetic gas theory and the Boltzmann equation, macroscopic flow quantities such as density or temperature, are referred to as *moments*. Moment methods describe a gas flow through such macroscopic quantities [136]. Based on the Boltzmann equation, a mathematically non-closed system of evolution equations for moments can be derived. In order to close the system, an approximation of the PDF is assumed, which is applied to calculate non-closed higher order moments.

As a famous example, Chapman and Enskog expanded the velocity distribution function in terms of the Knudsen number [30]. When first and second order terms are included in the expansion, Euler and Navier-Stokes equations are obtained, while higher order terms result in the Burnett and the super-Burnett equation [30, 133]. An alternative approach is offered by Grad [61, 62] who expanded the velocity distribution function based on Hermite polynomials, resulting in Grad's G13 and G26 equations [61, 62] and their extensions, the R13 equations [137, 138].

While moment methods are in general the most efficient approach to model non-equilibrium gas flows, it is worth noting, that they suffer from several shortcomings. In their derivation, the velocity distribution function is expanded around an equilibrium distribution. Lower order methods that are based on the Euler, Navier-Stokes and G13 equations, are therefore only valid for low Knudsen number flows. Higher order methods can extend the range of applicability, but result in very complex boundary conditions for higher order moments.

Particle methods approximate the PDF by a set of computational particles, which can be interpreted, from a physical point of view, as atoms and molecules. Particle trajectories are simulated by a stochastic approach, while macroscopic quantities are calculated by averaging over microscopic particle attributes.

One of the most famous particle method features the **direct simulation Monte-Carlo** (DSMC) algorithm [10]. The DSMC method directly describes the microscopic molecular particle motion. Molecular transport and collision processes are assumed to be decoupled. As a result, particle collisions and particle transport are modeled independently. Collisions are described in a stochastic approach, so that fundamental conservation laws of mass, momentum and energy are fulfilled, while the particle transport is assumed to be free molecular.

DSMC was first proposed in the sixties [8] and has since then become a standard tool for modeling non-equilibrium gas flows. The method has been shown to be consistent with the solution of the Boltzmann equation for the monatomic case [143] and has been intensively validated for the diatomic case [15, 16]. Hence, DSMC can be applied to describe gases at arbitrary non-equilibrium.

However, it is worth noting that the DSMC method suffers from several disadvantages. Since particle trajectories are modeled in a stochastic approach, macroscopic quantities exhibit statistical fluctuations. Therefore, the application of DSMC to flows with a low ratio of flow to thermal velocity, featuring a low signal to noise ratio, can become computational expensive. Since particle collisions and transport processes are treated separately, strict requirements concerning the spatial and temporal resolution must be fulfilled. To obtain meaningful DSMC results, the temporal resolution must be limited by the mean collision time and the spatial resolution by the mean free path [19]. As a result, the computational effort for DSMC increases strongly as the Knudsen number decreases.

Continuum particle methods try to overcome the requirement of resolving molecular scales. Therefore, molecular collision and transport processes are approximated on a macroscopic level. Such methods are typically only valid for small Knudsen number flows. However, the algorithmic similarity with the DSMC method results in a simple coupling of these methods with DSMC. Hence, hybrid continuum-DSMC particle methods can be constructed in order to efficiently and accurately simulate the entire range of Knudsen numbers [26, 57, 121].

A famous example features the kinetic BGK method [25, 41, 119, 123, 121], which applies a stochastic relaxation approach based on the BGK operator, for updating particle velocities. This approach leads to an efficient approximation of inter-molecular collisions for low Knudsen number gases and overcomes the requirement to resolve the mean free path. However, similar to the DSMC method, the BGK method decouples particle collisions and particle transport processes. Since particle transport is assumed as free molecular, the BGK method is subject to the same limitations in terms of temporal resolution as DSMC.

A special approach offers the low diffusion (LD) particle method [24]. In the LD method, particles do not feature a thermal velocity component. Instead, temperature is treated as quantity and assigned to each particle. Hence, the particles do not represent a distribution function, but the particle motion is constructed to reproduce the same flow behavior, as predicted by the Navier-Stokes equations. Simply spoken, the particles move along streamlines without the direct influence of a thermal velocity component. This approach prevents the need for resolving molecular length scales, but tends to numerical instabilities in hypersonic flows [90].

Another promising candidate is the kinetic FP method. Since this method is used throughout this thesis, it will be discussed in detail in the next chapter.

1.3 The Fokker-Planck equation and kinetic Fokker-Planck methods

Here the kinetic FP method is introduced. Since this method is based on the FP equation, first a brief historical overview of this equation is given.

Based on the work of Einstein [32] and Fokker [38] concerning Brownian motion and radiative absorption, Max Planck derived in 1917 an evolution equation for a distribution function for the case that the underlying microscopic particle states undergo only slight temporal and spatial changes [124]. Independently, Kolmogorov derived in 1934 a similar equation, describing the distribution of stochastic processes which are characterized by only small changes in time. The result is today known as FP equation and has since then been applied in a variety of different fields in physics and science. As an example, a search in Elsevier's scopus database [131] results in over 11.000 publications where the keyword *Fokker-Planck equation* is directly mentioned in title or abstract. For instance, the equation has been applied to describe charged particle collisions in plasmas [118], the behavior of non-equilibrium liquids [103] as well as galactic cluster systems [48].

The FP equation has also been used to model rarefied gas flows. Please note that the following models all use the same type of FP equation, but with different model coefficients. Pawula [117] was one of the first authors who applied the FP equation for describing rarefied gas flows. For this purpose he used the FP equation as

an approximation of the linear Boltzmann equation³. However, his model resulted in a wrong prediction of heat fluxes in the Navier-Stokes limit⁴, which restricts the applicability of the model considerably. Several decades later, Bogomolov [13] derived a FP equation as an approximation of the Boltzmann equation for the limit of small Knudsen numbers. This work provided the first mathematical justification for applying the FP equation as approximation for the Boltzmann equation. Heinz [70] was the first author who proposed a stochastic method to model rarefied gases, based on the FP equation. Therefore, he adapted a model which was originally developed by Kirkwood [93] to describe liquids and proposed a stochastic method to describe the change of molecular velocities due to collisions. He proofed that his stochastic method is equivalent to a description of the PDF by a FP equation.

Based on the work of Heinz [70], many kinetic FP methods were introduced in the last decade. These methods describe a gas by a FP equation, but instead of solving the FP equation directly, the methods simulate the underlying particle motion by solving an associated stochastic process. The great advantage of this approach compared to the previously discussed particle methods lies in the strict mathematical relationship between the FP equation on the one hand and the stochastic processes that describe the particle movement on the other. In particular, the equations of motion for particle velocity and position are not a priori decoupled. As a result, if the equations of motion can be solved with sufficient accuracy, the time step does not necessarily have to resolve the mean collision time, as it is for example the case with the BGK method.

Pioneering work concerning kinetic FP was conducted by Jenny et al. [84] who introduced their *linear model*, for describing single species, monatomic gases. Based on that model they derived a simulation method that was successfully applied to several test cases, but predicts wrong heat fluxes in the Navier-Stokes limit. To correct this issue, various authors developed extensions for the linear model. For example, the model of Singh et al. [135] modifies the flow term of the FP equation, while the ellipsoidal (ES) model of Mathiaud et al. [110] modifies the diffusion coefficient in the FP operator. A very promising and successful extension is represented by Gorji's cubic model [55] that modifies the drift coefficient compared to the original linear model. Gorji's cubic model and Mathiaud's ES model have been taken up by various other authors for modeling hypersonic flows [76, 87] and expansion flows [60, 122].

In the last decade, two approaches for using the kinetic FP method were developed. In one approach the kinetic FP method is coupled with the DSMC method [57, 91, 88, 101, 76, 122, 60]. DSMC is used, when kinetic FP becomes invalid due to strong thermal non-equilibrium effects, for instance in shock waves or areas of strong dilution. However, some authors also use the kinetic FP method as a stand alone method, which means they do not couple it with any other non-equilibrium solver. This approach is based on the observation that the FP method seems to be suitable for describing also non-equilibrium flow phenomena, like for example shock waves,

³ It is important to differentiate between the *linear* and the *linearized* Boltzmann equation: The linearized Boltzmann equation can be derived from the normal Boltzmann equation if the collision operator is linearized. The linear Boltzmann equation, on the other hand, is an evolution equation for the PDF that does not directly describe the interactions between the particles, but only with a given background medium.

⁴ In this work, the *Navier-Stokes limit* describes flows with small Knudsen numbers, that can still be described by the Navier-Stokes equations.

with sufficient accuracy [120, 87, 52], even if the FP equation only assumes small spatial and temporal changes of the particles, which suggests that the equation should actually only be applicable for the modeling of small Knudsen number flows. No matter which approach is employed, for the treatment of engineering applications it is required to model complex gas flows. In particular, the description of polyatomic species as well as gas mixtures is of great importance.

Only a few publications address the modeling of polyatomic species in conjunction with the kinetic FP method. Similar to the modeling of translational modes, Gorji et al. [53] assumed the internal molecular energy structure to be a continuous scalar. Hence, the relaxation process of internal energies can in principle be described by a FP equation with associated random processes. A similar approach is used by Mathiaud et al. [111] to extend the ES FP model [110] for the treatment of polyatomic species. In both cases, no discrete internal energy structure is modeled and only little attention is paid to the relaxation of the internal energy distribution function. To the authors' knowledge, so far only one study addresses the modeling of gas mixtures within the kinetic FP method. In analogy to the cubic model, Gorji et al. [51] derived a mixture FP model based on the Maxwell molecule model. Derivations are performed only for a binary mixture and the model is only tested for a very simple Couette flow. Therefore it is not clear, if this model can be applied to more complex gas flows.

1.4 Objectives of this thesis

In order to classify the objectives of this thesis, it is necessary to have a clear understanding about the various development phases that are passed through in the course of the development of a numerical simulation method. Based on work that has been published in recent years, four different development phases can be identified:

In the studies of the first development phase, the theoretical basics for the later simulation method are described. In the case of the kinetic FP method, the work of Einstein[32] and Fokker[38] as well as the work of Kolmogorov[94] should be mentioned, who were the first who described the Fokker-Planck equation. But also other publications, in which the Fokker-Planck equation was further developed as a model for dilute gases, belong to this first development phase [93, 117, 70, 13].

The second development phase is about demonstrating the feasibility of the numerical simulation method. In particular, the aim of phase two studies is to show that, based on the theoretical considerations previously made, a numerical method can be developed. As part of this phase, mainly conceptual questions are answered, e.g. whether the simulation method is stable or whether it delivers the correct solution for small Knudsen number flows. These questions are usually checked using simple numerical test cases. In the case of the kinetic Fokker-Planck method, the work of Gorji should be mentioned [55, 51, 53], who for the first time demonstrated the functionality of the FP method for more complex flows. But also some other publications, in which different FP methods are presented, fall into this development phase [110, 135]

In the third development phase, the numerical development of the method is further

refined. The aim is to use the findings of the second phase to construct a numerical algorithm with which real use cases can be calculated. This includes the precise examination of the validity range of the simulation method, as well as the derivation of efficient numerical solution procedures. For the kinetic FP method studies of the third development phase are for example the work of Küchlin [100], who developed a parallel implementation of the cubic FP method and the work of Jun et al. [89], who examined the applicability range of different FP methods.

Finally, the aim of fourth phase studies is to apply the simulation method to investigate new problems in fluid mechanics. To the best of the author's knowledge, such studies had not yet been carried out for the FP method at the time this thesis was written.

Even if most authors were probably not aware of this classification when preparing their work, most publications can be divided into one of these four phases.

This thesis takes up the latest work in the second development phase for the kinetic FP method and continues this work with the aim of demonstrating the applicability of the FP method for simulating hypersonic rarefied flows. For this purpose the kinetic FP method is expanded to simulate internal energy relaxation and gas mixtures. The reader should note, that both are essential prerequisites for the simulation of many applications in aerothermodynamics.

It is important to note that the work of this thesis falls mainly into the second of the development phases described above. This means that this thesis is primarily about developing the numerical methods and showing the conceptual feasibility of these. Some detailed questions, on the other hand, are left open for later studies. In order to show that the proposed methods can also be used for realistic scenarios, a complex expansion test case is calculated at the end of this thesis. This part of the thesis can be classified in phase four described above. However, the reader should be aware that this part of the thesis is primarily about demonstrating the applicability of the developed method and not about assessing the test case from a flow physics point of view.

1.5 Structure of this thesis

This work is divided into nine chapters, which describe the extension of existing FP methods for the description of internal energies and gas mixtures:

Chapter 2 introduces numerical methods and theoretical concepts that are applied throughout the thesis. In particular, the kinetic theory of gases as well as recent kinetic FP methods are discussed. The DSMC method is introduced, since it is applied to perform reference simulations for many test cases discussed in this thesis.

Chapter 3 presents an approach for extending arbitrary monatomic kinetic FP methods to describe polyatomic species. Gorji's cubic model [55, 53] is used for implementing the proposed scheme. Several test cases are examined to demonstrate the accuracy of the method, paying special attention to the relaxation of internal energy distribution functions.

Chapter 4 extends the ideas of Gorji et al. [51] to construct a FP method for describing hard sphere gas mixtures. The method is designed to reproduce Grad's 13

moment equations on a Navier-Stokes level of accuracy⁵ for gas mixtures with an arbitrary number of constituents. Several test cases, for example a one-dimensional Couette flow, are examined to show the performance of the proposed method in predicting correct shear stress, heat flux and diffusion velocity distributions for a He-Ar mixture.

Chapter 5 extends the FP method described in the previous chapter for modeling variable hard sphere gas mixtures. Test cases of different complexity, for example a one-dimensional Couette flow or a two-dimensional hypersonic flow over a flat plate, are examined in order to demonstrate the capability of the proposed method.

Chapter 6 combines the FP methods described in Ch. 3 and Ch. 5 to construct a FP method describing polyatomic, variable hard sphere gas mixtures.

Chapter 7 discusses the efficiency of the proposed FP methods. In addition, an efficient integration algorithm for the proposed mixture FP method is derived.

Chapter 8 applies the proposed FP methods to a complex test case. The expansion of air from a small slit into a vacuum environment is studied. Numerical results are compared with experimental measurements that were taken in the DLR high-vacuum plume test facility for chemical thrusters (Simulationsanlage für Treibstrahlen Göttingen - chemische Triebwerke / **STG-CT**) at the German Aerospace Center (DLR), Göttingen [59].

Chapter 9 summarizes the results of this work and gives a conclusion about the applicability of the FP method.

⁵ *Navier-Stokes level of accuracy* means that the same transport laws are yield as used in the Navier-Stokes equations.

Chapter 2

Methods

This chapter presents the theoretical concepts and numerical methods that are used throughout this thesis. Subchapter 2.1 gives a brief introduction to the kinetic theory of gases. The DSMC approach, which is used to perform reference simulations for various test cases in this work, is discussed in Subch. 2.2. Finally, Subch. 2.3 gives an overview of recent kinetic Fokker-Planck models.

2.1 Kinetic theory of gases

The kinetic theory of gases provides methods for describing a gas from a molecular point of view. The following subchapters give only a brief overview about concepts, that are necessary for the further understanding of this thesis. For more details, the reader is referred to the literature [78, 141, 136, 97].

For the sake of simplicity, Subch. 2.1.1 and Subch. 2.1.2 discuss theory only for a single, monatomic particle species. The generalization to gases with excited internal energy modes and multiple species is straight forward and described in Subch. 2.1.3.

2.1.1 Statistical description

In kinetic theory, a gas is described from a microscopic point of view, as a composition of atoms and molecules. Since even in a small volume of a gas many particles occur, it is usually not possible to describe each particle directly. Instead, the particles are modeled by a statistical approach. A particle distribution function $f(\mathbf{x}, \mathbf{v}, t)$ is introduced, which describes the number of particles that can be found in a small volume $d\mathbf{x}$ around a position \mathbf{x} , with velocities in a small range $d\mathbf{v}$ around a velocity \mathbf{v} at time t . The PDF¹ is normalized with the total number of particles N_p in the system:

$$N_p = \iiint_V \iiint_{-\infty}^{\infty} f(\mathbf{x}, \mathbf{v}, t) d\mathbf{v} d\mathbf{x} = \int \int f(\mathbf{x}, \mathbf{v}, t) d\mathbf{v} d\mathbf{x}. \quad (2.1)$$

Here V denotes the volume of the system. For simplicity, the three integrals on the left side of Eq. 2.1 are expressed by a single integral and limit values of the integrals are suppressed. Macroscopic quantities can be calculated by taking moments of the PDF. In general, a velocity moment with respect to the PDF f is defined as:

$$\langle \mathbf{g} | f \rangle = \int f(\mathbf{x}, \mathbf{v}, t) \mathbf{g}(\mathbf{v}) d\mathbf{v}. \quad (2.2)$$

Here $\mathbf{g}(\mathbf{v})$ denotes an arbitrary function of microscopic particle velocities \mathbf{v} . The reader should note, that moments (2.2) feature a spatial and temporal dependency,

¹ The particle distribution function should not be confused with the probability density function, which is sometimes also abbreviated as PDF.

that is suppressed for the sake of simplicity. As an example, the number density is given by:

$$n(\mathbf{x}, t) = \langle 1|f \rangle, \quad (2.3)$$

and the mean velocity of the gas can be calculated as:

$$\mathbf{u}(\mathbf{x}, t) = \frac{1}{n(\mathbf{x}, t)} \langle \mathbf{v}|f \rangle. \quad (2.4)$$

It is conventional to decompose the microscopic particle velocity into the mean velocity and a thermal velocity component \mathbf{c} :

$$\mathbf{v} = \mathbf{u} + \mathbf{c}. \quad (2.5)$$

The reader should note, that $d\mathbf{c} = d\mathbf{v}$. Thermal particle velocities are employed to calculate several macroscopic quantities. Important examples feature the thermal temperature:

$$T(\mathbf{x}, t) = \frac{m}{3k_B n(\mathbf{x}, t)} \langle \mathbf{c}^2|f \rangle, \quad (2.6)$$

the pressure tensor:

$$p_{ij}(\mathbf{x}, t) = m \langle c_i c_j|f \rangle, \quad (2.7)$$

and the heat flux density:

$$q_i(\mathbf{x}, t) = \frac{1}{2} m \langle c_i \mathbf{c}^2|f \rangle. \quad (2.8)$$

Here m denotes the particle mass and the indices $i, j \in \{1, 2, 3\}$ refer to components of the thermal velocity vector \mathbf{c} .

The particle mean free path denotes the average distance particles are traveling between two collisions. When assuming a simple hard sphere collision model (see Subch. 2.2.4) and thermal equilibrium conditions, one can find the following expression for the mean free path:

$$\lambda = \frac{1}{\sqrt{2} \pi n d_{\text{ref}}^2}. \quad (2.9)$$

In the equation above, d_{ref} describes the diameter of particles within the hard sphere collision model.

The main goal of the kinetic theory of gases is to determine the PDF for a given problem in order to calculate macroscopic quantities as described above. As shown in the next subchapter, this is in general a difficult task. However, for continuum flows, i.e. for a vanishing Knudsen number, the PDF is driven to local equilibrium. In this case, the gas can be described by a local Maxwell distribution:

$$f_{\text{eq}}(\mathbf{x}, \mathbf{v}, t) = \frac{n(\mathbf{x}, t)}{(2\pi k_B T(\mathbf{x}, t) / m)^{3/2}} \exp\left(-\frac{m}{2k_B T(\mathbf{x}, t)} (\mathbf{v} - \mathbf{u}(\mathbf{x}, t))^2\right). \quad (2.10)$$

2.1.2 Kinetic models

The evolution of a PDF is driven by molecular collisions and transport processes of particles. The Boltzmann equation [104] features the most general approach to

describe such processes for a rarefied gas:

$$\underbrace{\frac{\partial f}{\partial t} + v_k \frac{\partial f}{\partial x_k} + \frac{F_k}{m} \frac{\partial f}{\partial v_k}}_{\frac{Df}{Dt}} = \underbrace{\int d\mathbf{v}_1 \int_0^{2\pi} d\psi \int_0^{\pi/2} d\alpha \sin\alpha g I(\mathbf{c}_r, \alpha, \psi)}_{S_{\text{Boltz}}} (f' f'_1 - f f_1). \quad (2.11)$$

Here $f_1(\mathbf{x}, \mathbf{v}_1, t)$ and $f(\mathbf{x}, \mathbf{v}, t)$ denote pre-collision PDF's, f' and f'_1 denote post-collision PDF's, α and ψ describe the orientation of the post-collision relative particle velocity compared to the pre-collision relative particle velocity, \mathbf{c}_r is the relative particle velocity, I denotes the differential cross section for elastic collisions and \mathbf{F} refers to an external force. The left side of Eq. (2.11) describes free molecular transport of particles, while the collision operator S_{Boltz} models the change of the distribution function due to molecular collisions.

To derive the Boltzmann equation, the following four assumptions are made [97]:

- It is assumed that binary collisions are much more likely than collisions with three or more partners, so that the latter can be ignored.
- It is assumed that during a time interval of the size of the mean collision time, i. e. the average time between collisions, the effect of external forces on particles is negligible compared to the effect of particle-particle collisions.
- It is assumed that the pre- and post-collisional velocities are not correlated. This means, that the pre-collision velocity of one particle does not depend on the pre-collision velocity of the other particle. Similar, the post-collision velocity of one particle does not depend on the post-collision velocity of the other particle. These hypotheses are also known as the *Molecular chaos hypothesis*.
- It is assumed that the PDF does not change significantly over a time interval that is less than the mean collision time or a distance less than the mean free path.

Note, that these assumptions are equivalent to the definition of a rarefied gas. For modeling high-density flows, the collision operator can be expanded to describe also collisions involving more than two particles [33, 30].

The collision operator fulfills several fundamental properties:

$$S_{\text{Boltz}}(f) = 0 \iff f = f_{\text{eq}}, \quad (2.12)$$

$$\int X S_{\text{Boltz}}(f) d\mathbf{v} = 0 \text{ for any } f \text{ when } X \in \{1, \mathbf{v}, \mathbf{v}^2\}. \quad (2.13)$$

Equation (2.12) ensures, that a local equilibrium condition is not changed by collisions any more, while Eq. (2.13) is directly related to the conservation of mass, momentum and energy in elastic particle collisions.

Theoretically, Eq. (2.11) can be used to accurately model gases at arbitrary Knudsen numbers, but as described in Subch. 1.2, the direct solution of the Boltzmann equation is a computational expensive task.

Kinetic models approximate the Boltzmann collision operator by less complex operators, while preserving as many of its properties as possible. For example, the Fokker-Planck operator, discussed in more detail in Subch. 2.3, approximates the effect of particle collisions by a diffusive process in velocity space. A different approach features the BGK-Operator, which postulates a simple relaxation behavior [7]

for the particle distribution function.

Often gas flows are only slightly diluted, which means they feature mainly small Knudsen numbers. In such cases it is not necessary to solve the entire Boltzmann equation. Instead, only the behaviour of the Boltzmann-equation in small Knudsen number flows is of interest. This can be analyzed, for example, by a Chapman-Enskog expansion [30] or Grad's expansion in Hermite polynomials [61, 62], as discussed in Subch.1.2. Please note, that such expansions can be performed for the Boltzmann-equation as well as for any other kinetic model. Of particular importance for these derivations are production terms:

$$P_{\Psi}(X) = m \int S_{\Psi} X d\mathbf{c}, \quad (2.14)$$

where $\Psi \in (\text{Boltz}, \text{FP}, \text{BGK})$ refers to the underlying collision operator. In particular, kinetic models that feature the same lower order production terms $P_{\Psi}(c_i c_j)$ and $P_{\Psi}(c_i c^2)$ lead to the same transport coefficients, like viscosity and thermal conductivity, in the Navier-Stokes limit. Hence, production terms are a powerful indicator for analyzing the behavior of kinetic models in the limit of small Knudsen numbers.

2.1.3 Polyatomic species and multi species gases

The following subchapter generalizes the concepts described above to polyatomic gases and gases with multiple species.

Polyatomic species

In order to describe polyatomic gases, internal energy modes, caused by rotational and vibrational excitation, must be taken into account. Therefore, the dependency of the PDF is extended by an additional parameter i , describing the internal energy state of particles:

$$f(\mathbf{x}, \mathbf{c}, \mathbf{t}) \rightarrow f_i(\mathbf{x}, \mathbf{c}, \mathbf{t}). \quad (2.15)$$

For the sake of simplicity only a single, discrete internal energy mode is assumed. The normalization condition (2.1) changes to:

$$N_p = \sum_i \int \int f_i(\mathbf{x}, \mathbf{v}, t) d\mathbf{v} d\mathbf{x}. \quad (2.16)$$

Moments of a PDF can be calculated similar as in the monatomic case, only additional summation with respect to the internal energy states has to be carried out:

$$\langle \mathbf{g} | f \rangle = \sum_i \int \int f_i(\mathbf{x}, \mathbf{c}, t) \mathbf{g}(\mathbf{c}) d\mathbf{c}. \quad (2.17)$$

Please keep in mind, that $\mathbf{g}(\mathbf{c})$ represents an arbitrary functional relationship of the thermal particle velocities \mathbf{c} . For instance, the average internal energy E_{int} per molecule can be calculated as a moment of microscopic internal energies e_i :

$$E_{\text{int}} = \frac{1}{n} \langle e_i | f \rangle. \quad (2.18)$$

Note, that internal energy and internal temperature T_{int} are related via:

$$E_{\text{int}} = \frac{d_{\text{int}}}{2} k_B T_{\text{int}}. \quad (2.19)$$

Here d_{int} denotes the number of internal degrees of freedom. Another important quantity is the internal heat flux density:

$$(q_{\text{int}})_k(\mathbf{x}, t) = m \langle c_k e_i | f \rangle. \quad (2.20)$$

which describes the heat flux due to the internal particle excitation.

The generalization of the Boltzmann equation is straightforward [29]:

$$\frac{Df_i}{Dt} = \sum_{jkl} \int d\mathbf{v} \int_0^{2\pi} d\psi \int_0^\pi d\alpha \sin\alpha g I_{ij}^{kl}(\mathbf{c}_r, \alpha, \psi) \left(f_k' f_l' - f_i^1 f_j \right), \quad (2.21)$$

where I_{ij}^{kl} denotes the differential cross section for an inelastic collision between particles with internal pre-collision states i and j and resulting post-collision states k and l . Note, that elastic collisions are naturally included in Eq. (2.21) when assuming $k, l = i, j$.

For the case of internal equilibrium, internal energies are distributed as described by a Boltzmann distribution:

$$f_i^{\text{eq}} \sim \exp\left(-\frac{e_i}{k_B T_{\text{int}}}\right). \quad (2.22)$$

Similar to the monatomic case, kinetic models can be constructed to approximate the Boltzmann equation for polyatomic molecules. For example, the BGK approach is widely used in order to describe diatomic species [114].

A Chapman-Enskog analysis can be performed to investigate the behavior of kinetic, polyatomic models in the Navier-Stokes limit. Depending on the physical assumptions that are made, equations of varying complexity can be derived. In conventional approaches, internal energy states are described by a single temperature [29], while recent state-to-state methods try to model internal energy states separately [98]. However, the latter approach results in a large number of equations that have to be solved.

Gas mixtures

In order to describe gas mixtures, separate PDF's $f^{(\alpha)}$ are introduced for each species:

$$f(\mathbf{x}, \mathbf{v}, \mathbf{t}) \rightarrow f^{(\alpha)}(\mathbf{x}, \mathbf{v}^{(\alpha)}, \mathbf{t}). \quad (2.23)$$

In this thesis, superscript indices in brackets refer to particle species. The PDF's are normalized to the total number of particles per species in the system:

$$N_p^{(\alpha)} = \int \int f^{(\alpha)}(\mathbf{x}, \mathbf{v}^{(\alpha)}, t) d\mathbf{v}^{(\alpha)} d\mathbf{x}. \quad (2.24)$$

Moments are defined with respect to a specific particle species:

$$\langle \mathbf{g} | f^{(\alpha)} \rangle = \int f^{(\alpha)}(\mathbf{x}, \mathbf{v}^{(\alpha)}, t) \mathbf{g}(\mathbf{v}^{(\alpha)}) d\mathbf{v}^{(\alpha)}. \quad (2.25)$$

As an example, the species flow velocities are given by:

$$\mathbf{u}^{(\alpha)}(\mathbf{x}, t) = \frac{1}{n^{(\alpha)}} \langle \mathbf{v}^{(\alpha)} | f^{(\alpha)} \rangle, \quad (2.26)$$

where $n^{(\alpha)} = \langle 1 | f^{(\alpha)} \rangle$ denotes the species number density. Thermal particle velocities are defined with respect to the species flow velocities:

$$\mathbf{c}^{(\alpha)} = \mathbf{v}^{(\alpha)} - \mathbf{u}^{(\alpha)}. \quad (2.27)$$

It should be noted, that some authors [63] define thermal velocities based on the velocity of the entire mixture as given by Eq. (2.32):

$$\hat{\mathbf{c}}^{(\alpha)} = \mathbf{v}^{(\alpha)} - \mathbf{u}. \quad (2.28)$$

However, if not explicitly mentioned, this definition is not further used in this thesis. Similar to the single species case, a species specific temperature is defined as:

$$T^{(\alpha)}(\mathbf{x}, t) = \frac{m^{(\alpha)}}{3k_B n^{(\alpha)}} \langle \mathbf{c}^{(\alpha)} \mathbf{c}^{(\alpha)} | f^{(\alpha)} \rangle. \quad (2.29)$$

The species specific pressure tensor is given by:

$$p_{ij}^{(\alpha)}(\mathbf{x}, t) = m^{(\alpha)} \langle c_i^{(\alpha)} c_j^{(\alpha)} | f^{(\alpha)} \rangle, \quad (2.30)$$

and heat fluxes can be calculated as:

$$q_i^{(\alpha)}(\mathbf{x}, t) = \frac{1}{2} m^{(\alpha)} \langle c_i^{(\alpha)} c_j^{(\alpha)} c_j^{(\alpha)} | f^{(\alpha)} \rangle. \quad (2.31)$$

Average quantities for the entire mixture include all species and are given by summation over species specific moments. An important example features the flow velocity:

$$\mathbf{u}(\mathbf{x}, t) = \frac{1}{\rho} \sum_{\alpha=1}^{N_s} \langle \mathbf{u}^{(\alpha)} | f^{(\alpha)} \rangle m^{(\alpha)}, \quad (2.32)$$

where $\rho^{(\alpha)} = m^{(\alpha)} \cdot n^{(\alpha)}$ denotes the species mass density, $\rho = \sum_{\alpha=1}^{N_s} \rho^{(\alpha)}$ the mixture mass density and N_s the number of species in the mixture. To calculate the mixture temperature, additional diffusion velocities must be taken into account:

$$\frac{3}{2} k_B n T(\mathbf{x}, t) = \sum_{\alpha=1}^{N_s} \left(\frac{3}{2} k_B n^{(\alpha)} T^{(\alpha)} + \frac{1}{2} \rho^{(\alpha)} \mathbf{u}_d^{(\alpha)} \mathbf{u}_d^{(\alpha)} \right), \quad (2.33)$$

where diffusion velocities are defined as:

$$\mathbf{u}_d^{(\alpha)} = \mathbf{u}^{(\alpha)} - \mathbf{u}. \quad (2.34)$$

The mean free path in gas mixtures includes contributions for all species. For the hard sphere collision model one can find [10]:

$$\lambda = \sum_{\alpha=1}^{N_s} \frac{n^{(\alpha)}}{n} \lambda^{(\alpha)}, \quad (2.35)$$

where:

$$\lambda^{(\alpha)} \equiv \left[\sum_{\beta=1}^{N_s} \pi \left(d^{(\alpha-\beta)} \right)^2 n^{(\beta)} \sqrt{1 + \frac{m^{(\beta)}}{m^{(\alpha)}}} \right]^{-1}. \quad (2.36)$$

denotes the mean free path of an individual species α . It should be noted that λ is only an average over the mean free paths of all species in the gas mixture. Depending on the mass and collision properties of specific species, different species can adopt very different mean free paths $\lambda^{(\alpha)}$. For example, if a specific species α has a much smaller mass than other species in the gas mixture, this one will usually develop a much smaller mean free path $\lambda^{(\alpha)}$ than the other species in the gas mixture. This fact must be considered when interpreting the Eq. (2.35).

The generalization of the Boltzmann equation for multi species is straight forward [63]:

$$\frac{Df^{(\alpha)}}{Dt} = \sum_{\beta=1}^{N_s} \int d\mathbf{v}^{(\alpha)} \int_0^{2\pi} d\psi \int_0^{\pi} d\alpha \sin\alpha g I^{(\alpha\beta)}(\mathbf{c}_r, \alpha, \psi) \left(f'^{(\alpha)} f_i'^{(\beta)} - f_i^{(\alpha)} f_j^{(\beta)} \right). \quad (2.37)$$

Here $I^{(\alpha\beta)}$ denotes the differential cross section for an elastic collision between an α and β particles.

Gas mixtures with polyatomic species

The concepts described above can be combined for describing gases featuring multiple species and internal energy states. In this case, separate distribution functions are introduced for each combination of particle species and internal energy states:

$$f(\mathbf{x}, \mathbf{v}, \mathbf{t}) \rightarrow f_i^{(\alpha)}(\mathbf{x}, \mathbf{v}^{(\alpha)}, \mathbf{t}). \quad (2.38)$$

Moments of the distribution function can be taken for evaluating macroscopic quantities. The procedure is very similar as described for gas mixtures above and simply includes an additional sum over internal energy states. These concepts are not explicitly repeated.

2.2 Direct Simulation Monte Carlo Method

The **Direct Simulation Monte Carlo (DSMC)** method simulates a gas by directly modeling the microscopic motion of atoms and molecules [10]. Each particle is described by its position, velocity and internal energy state. Intermolecular collisions and collisions between particles and simulation boundaries lead to new velocities and internal energy states and are model in a stochastic approach. Macroscopic quantities are calculated by averaging over microscopic particles attributes.

DSMC is proven to be consistent with the solution of the Boltzmann equation for the monatomic case [143], but can also be used to model complex physical phenomena such as internal energy relaxation [15, 16] or chemical reactions [42]. Hence in recent decades, DSMC has become a standard tool for modeling non-equilibrium gas flows from a molecular point of view.

The structure of this subchapter is as follows. Subchapter 2.2.1 summarizes numerical and physical approximations, that are utilized in the DSMC method. Subchapter 2.2.2 to Subch. 2.2.5 discuss different parts of the DSMC algorithm in more detail.

For the sake of simplicity, the DSMC method is only discussed for a single particle species. However, it is straight forward to derive the method for multi-species flows.

2.2.1 Numerical and physical approximations

As described in the last subchapter, the large number of particles that are present even in a small volume of a gas, renders the direct simulation of each particle to a computationally impossible task. For this reason, the DSMC algorithm processes only a representative number of simulator particles, each representing many physical particles. This simplification is justified, since one is in general not interested in the motion of individual particles but only in macroscopic quantities such as density or temperature. The ratio between the number of real to simulated particles defines the scaling factor F_N .

To efficiently calculate the motion of particles, transport and molecular collision processes are treated separately. This simplification is justified, if the mean free path of particles is large, compared to the range of inter-molecular forces.

Hence, as schematically shown in Fig. 2.1, a DSMC simulation alternately updates particle positions and velocities. The domain is discretized into grid cells and collisions are modeled randomly between particles that are located in the same cell, while particle transport is calculated as free molecular.

Due to the separation of collision and particle transport processes and the assumption of free molecular particle transport, the spatial and temporal resolution for the

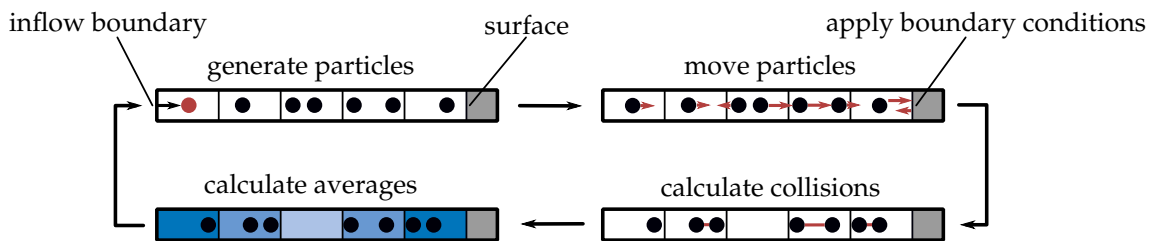


FIGURE 2.1: Typical DSMC simulation loop for a simple 1-D case.

numerical scheme must be limited by the particle mean free path and the mean collision time. The latter is by definition the average time between successive collisions of a particle. Otherwise, numerical errors due to non-physical diffusion and collision processes become dominant [19].

The following subchapters describe the different parts of the DSMC algorithm in more detail.

2.2.2 Generation of particles

Particles are generated at simulation boundaries according to macroscopic inflow conditions. An example features the *stream boundary condition*, which initializes a stream of particles with a certain density, temperature and velocity [10, 105, 140]. Since this boundary condition is used by default in many DSMC codes and also in this thesis, it is discussed in more detail below.

Generation of particles is done in a two-step process. First, the number of particles to be generated is calculated. Afterwards, positions, velocities and internal energy states are assigned to particles.

To keep things simple, a stationary gas is assumed in the following. Then, the average number of particles passing an area A , in a time interval Δt is given by:

$$\langle N_{\text{in}} \rangle = n_{\infty} A \sqrt{\frac{k_{\text{B}} T_{\infty}}{2\pi m}} \Delta t. \quad (2.39)$$

Here n_{∞} and T_{∞} denote the inflow number density and temperature. Please note that the above equation only applies to a stationary gas, which means, the assumption is made that the inflow gas does not have a average flow velocity. In such a case, the inflow condition described here only models the particles that enter the simulation area due to diffusion effects. If the gas is not stationary, the equation is supplemented by further terms that describe the influence of the average flow velocity on the number of arriving particles. In general, evaluating Eq. (2.39) yields a non-integer value. In order to generate a number of particles N_{in} that on average yields Eq. (2.39), proper rounding must be performed. Simple random rounding $N_{\text{in}} = \lfloor \langle N_{\text{inflow}} \rangle + \mathbb{R} \rfloor$ with a random number $\mathbb{R} \in [0, 1]$ leads to incorrect inflow conditions [140]. Instead, the number of inflow particles should be sampled from a Poisson distribution with mean value $\langle N_{\text{in}} \rangle$.

After the number of incoming particles is determined, they are assigned to positions, velocities and internal energy states. Therefore, the velocity components tangential to the inflow direction are sampled from a Maxwell distribution with temperature T_{∞} , while the component perpendicular to the inflow direction is sampled from a biased Maxwell distribution. In case of polyatomic species, internal energy states are sampled from a Boltzmann distribution with temperature T_{∞} . Particle positions are randomly distributed along the inflow surface. In order to create a continuous flux of incoming particles, the positions are additionally shifted into the domain by a random fraction of the time step Δt :

$$\mathbf{x}_0 \rightarrow \mathbf{x}_0 + \mathbf{v}_0 \mathbb{R} \Delta t, \quad \mathbb{R} \in [0, 1]. \quad (2.40)$$

Please note that the inflow condition described above creates a constant flux of incoming particles under the assumption that the particles are in an equilibrium state. Although DSMC is mainly used to simulate non-equilibrium flows, the equilibrium assumption for the incoming particles is justified in most practical cases. Otherwise it is also possible to construct inflow conditions for particles that are not initially

in equilibrium, for example based on a Chapman-Enskog distribution [43]. Also it possible to construct boundary conditions that do not result in a constant flux of incoming particles, but in a constant pressure at the inflow boundary [106]. Since such inflow conditions are not used in this thesis, they will not be considered further.

2.2.3 Moving of particles

Particles are moved based on the free flight assumption. Hence, new particle positions are calculated by a simple linear displacement:

$$\mathbf{x}(t + \Delta t) = \mathbf{x}(t) + \mathbf{v}(t) \Delta t. \quad (2.41)$$

Here Δt denotes the time step size and $\mathbf{v}(t)$ the particle velocity at time t . When external forces are acting on the particle, for example gravity or electrical forces, Eq. (2.41) has to be extended by additional terms, describing the resulting acceleration of the particle.

Due to the high computing effort, the assignment of particles to new grid cells is a crucial part of the algorithm. If an unstructured grid geometry is employed, particles are alternately moved between cells. Algorithms to track the particle path are for example described by Haselbacher et al. [68]. When a Cartesian grid geometry is employed [40], the assignment to new grid cells can be directly calculated. This approach is very efficient, but the interaction of particles with simulation boundaries must be tested separately.

Interaction with boundaries

When a particle hits a simulation boundary, the particle path is adjusted accordingly. For an outflow boundary condition, the particle is simply removed from the simulation.

Interaction with solid boundaries is modelled by scattering kernels [6]. A scattering kernel $R(\mathbf{v} \rightarrow \mathbf{v}')$ describes the probability for a particle that hits the surface with a velocity \mathbf{v} to leave the surface with a velocity \mathbf{v}' . The concept of scattering kernels is adopted from the kinetic theory of gases, where scattering kernels are employed to calculate the PDF of remitted particles.

Mathematically, kernels should satisfy the principle of detailed balance, which restricts the number of possible scattering kernels strongly [6]. In a DSMC simulation, algorithms are constructed to statistically reproduce specific scattering kernel. Figure 2.2 shows the effect of common scattering kernels, that are used in DSMC simulations.

Specular reflection changes the direction of the particle's velocity component normal to the wall, while the velocity component tangential to the wall stays unaffected. As a result, neither momentum nor energy is transferred to the surface. Hence, specular reflection corresponds to a frictionless, adiabatic wall in classical continuum mechanics.

In the case of a diffusive reflection, the particle loses every information about its incoming state. The new particle speed is sampled from a Maxwell distribution corresponding to a wall temperature T_w , while the direction of the new velocity is sampled by a cosine distribution. Internal energy states are sampled from a Boltzmann distribution. Since the post-collision state is not related to the incoming particle state, momentum and energy is transferred to the surface. For flows with small Knudsen

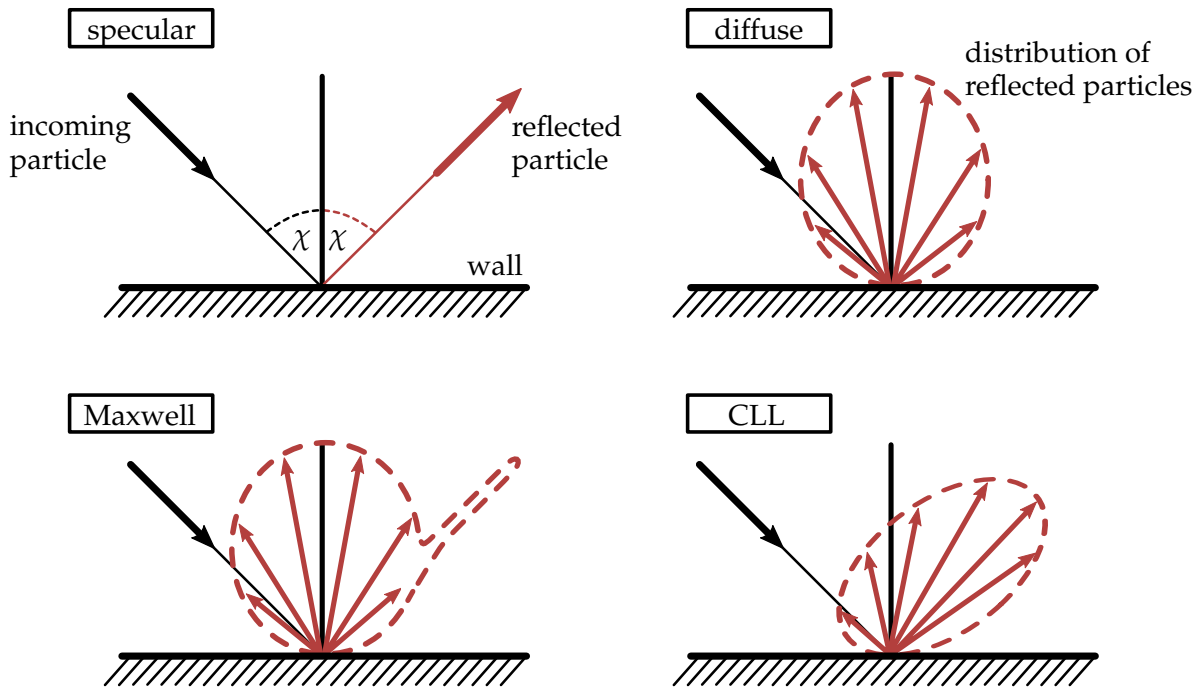


FIGURE 2.2: Effect of different scattering kernels on a scattered particle. The peak in the distribution of reflected particles for the Maxwell kernel is infinitely small and has been drawn broadened for clarity only.

numbers, the diffusive scattering kernel corresponds to an isothermal, viscous wall in continuum mechanics.

The Maxwell model combines the specular and the diffusive reflection model. An accommodation coefficient $\alpha \in [0, 1]$ is introduced, describing the equilibration between gas and surface. When a particle hits the surface, it performs a diffusive reflection with probability α or a specular reflection with probability $1 - \alpha$. For supersonic gas flows, the Maxwell model is widely applied. Because of its simplicity, the model is also employed in this thesis.

In order to better reproduce experimental data from molecular beam measurements, the Cercignani-Lampis (CCL) model [28, 107] introduces a separate tangential $\alpha_t \in [-1, 1]$ and perpendicular $\alpha_n \in [0, 1]$ accommodation coefficient, describing equilibration of tangential and perpendicular velocity components with a surface separately. Specular and diffusive reflection are included as limit cases in the CLL model. The CCL model has been generalized for diatomic molecules by Gorji et al. [54].

In addition to the common boundary conditions described above, boundary conditions for various other situations can also be constructed. For example, different approaches have been developed to model viscose, adiabatic walls [4, 113].

2.2.4 Calculation of particle collisions

DSMC collisions are modeled in a two-step process. Initially, collision partners are selected. Afterwards, collisions between selected particle pairs are carried out, which lead to new particle velocities and internal energy states.

Selection of collision partners

Collision partners should be selected, such that a proper mean collision rate is captured [10]:

$$\nu_{\text{coll}} = \langle \sigma_{\text{T}} c_{\text{r}} | f_{\text{r}} \rangle. \quad (2.42)$$

Here f_{r} denotes the distribution of relative particle velocities, c_{r} refers to the absolute value of the relative particle velocity and σ_{T} denotes the total collision cross section. The total cross section depends on the molecular collision model, which will be discussed later in this subchapter.

To reproduce Eq. (2.42) for a DSMC cell with volume V_{c} and N_{p} particles, one could simply select all $\frac{1}{2}N_{\text{p}} \cdot (N_{\text{p}} - 1)$ possible particle pairs and apply a collision probability of $P'_{\text{coll}} = \sigma_{\text{T}} c_{\text{r}} \Delta t / V_{\text{c}} \cdot F_{\text{N}}$. However, such a particle selection would be rather inefficient, since the probability P'_{coll} is very small, leading to many non-colliding particle pairs that have to be considered. To overcome that problem, different selection schemes were developed. Common approaches are the *time counter* [9], the *no time counter* (NTC) [10] and the *major frequency* scheme [81, 82]. Since the NTC scheme is used in this work, it is described in more detail below.

The NTC algorithm scales the probability P'_{coll} by its maximum value:

$$P_{\text{coll}} \equiv \frac{P'_{\text{coll}}}{(P'_{\text{coll}})_{\text{max}}} = \frac{\sigma_{\text{T}} c_{\text{r}}}{(\sigma_{\text{T}} c_{\text{r}})_{\text{max}}}. \quad (2.43)$$

The maximum value $(\sigma_{\text{T}} c_{\text{r}})_{\text{max}}$ is saved separately for each grid cell and is continuously updated during a simulation. Consequently, the number of collisions that has to be tested scales to:

$$N_{\text{coll}} = \underbrace{\left\lfloor \frac{1}{2} N_{\text{p}} (N_{\text{p}} - 1) F_{\text{N}} \frac{(\sigma_{\text{T}} c_{\text{r}})_{\text{max}}}{V_{\text{c}}} \Delta t + \mathbb{R} \right\rfloor}_{z_{\text{max}}}. \quad (2.44)$$

The floor function $\lfloor \cdot \rfloor$ and the random number $\mathbb{R} \in [0, 1]$ are required to reach a statistical exact collision count. Figure 2.3 summarizes the collision procedure for the NTC algorithm.

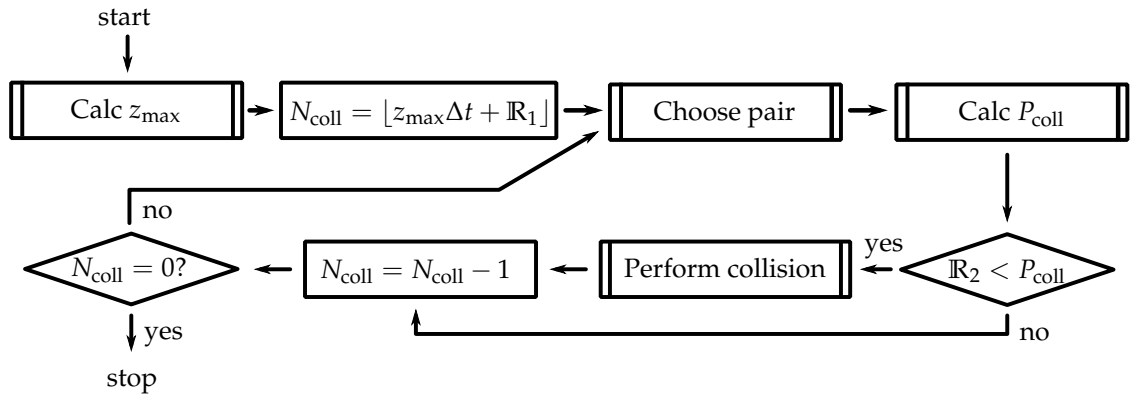


FIGURE 2.3: NTC scheme to select colliding particle pairs. $\mathbb{R}_1, \mathbb{R}_2 \in [0, 1]$ refer to uniformly distributed random numbers. z_{max} is defined in Eq. (2.44)

Early DSMC implementations simply selected collision partners out of all particles in the same grid cell. In order to avoid non-physical selections, the size of a grid cell has to be limited by the particle mean free path in this case. To relax this limitation, various techniques have been developed for selecting collision partners based on their position within a grid cell.

A common technique introduces an additional layer of sub-cells and selects collision pairs from particles that are located in the same sub-cell [10, 102]. This approach is common for modern DSMC codes, but requires additional computing time for sorting particles into the sub-cell structure. Problems also arise when too few particles are located in a single sub-cell.

Gallis et al. [40] proposed an alternative approach that selects collision partners featuring a close trajectory. Therefore, possible collision partners are searched for in a sphere with a radius that is proportional to the time step size and the speed of the particle. While this approach reduces the limitation on the cell size, the simulation becomes more sensitive regarding the time step size.

DSMC collision models

Once collision pairs are selected, particle velocities and internal energy states are adjusted based on collision models. DSMC collision models are usually derived from the physics of molecular collision processes: Such models are designed to reproduce the basic conservation laws of mass and momentum, but due to the complexity of molecular collision processes, they cannot fully describe such processes in detail. Instead, each model contains some free parameters that are selected in order to adapt the behavior of a collision model as well as possible. Usually the model parameters are chosen in such a way that the models reflect correct transport coefficients in the limit of small Knudsen numbers, as this is a necessary prerequisite for most practical applications of DSMC. Whether the models are also suitable for modeling non-equilibrium flows is then examined by comparing numerical simulations with experimental measurements.

A simple example features the **hard sphere (HS)** model, that describes particles as hard spheres. As illustrated in Fig. 2.4, the interaction potential is fully described by a collision diameter $d_{\text{coll}} = d_{\text{ref}}$, given by the diameter d_{ref} of the colliding particles. The total collision cross section is a constant:

$$\sigma_T = \pi d_{\text{coll}}^2, \quad (2.45)$$

and the scattering angle χ is isotropic in the center of mass reference system. For a single species gas, the HS model yields the following expression for viscosity in the Navier-Stokes limit:

$$\mu = \mu_{\text{ref}} \left(\frac{T}{T_{\text{ref}}} \right)^{0.5}. \quad (2.46)$$

The model parameters μ_{ref} and T_{ref} are uniquely depended on the reference diameter d_{ref} :

$$d_{\text{ref}}^2 = \frac{5}{16\sqrt{\pi}} \frac{\sqrt{m_r k_B T_{\text{ref}}}}{\mu_{\text{ref}}}. \quad (2.47)$$

In order to apply the HS model in DSMC simulations, suitable values for collision diameters must be found. In general, collision diameters are adjusted, so that the collision model reproduces correct transport coefficients in the Navier-Stokes limit.

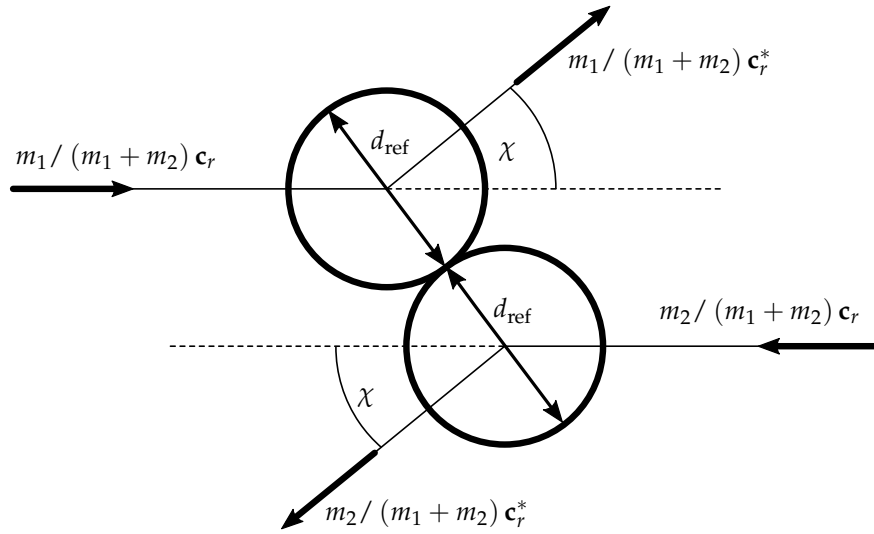


FIGURE 2.4: Collision process in the center of mass reference system for a simple hard sphere model.

Therefore, Eq. (2.46) is fitted to experimentally measured viscosity data and Eq. (2.47) is used to evaluate species specific collision diameters.

For better reproducing experimentally measured transport coefficients, Bird [11] designed the variable hard sphere (VHS) model. As in the HS model, the scattering angle χ is isotropic in the center of mass reference, but in contrast to the HS model, the collisions diameters depend on the relative collision velocity:

$$d_{\text{coll}} = d_{\text{ref}} \left(\frac{c_{r,\text{ref}}}{c_r} \right)^{\omega - \frac{1}{2}}. \quad (2.48)$$

The reference velocity $c_{r,\text{ref}}$ and the viscosity exponent ω feature additional model parameters. Note, that the HS model is a limiting case of the VHS model, when setting $\omega = 1/2$. For a single species gas, the VHS model yields the following expression for viscosity:

$$\mu = \mu_{\text{ref}} \left(\frac{T}{T_{\text{ref}}} \right)^{\omega}. \quad (2.49)$$

The reference diameter d_{ref} uniquely depends on the the model parameters μ_{ref} , T_{ref} and ω :

$$d_{\text{ref}}^2 = \frac{15}{2\sqrt{\pi}} \frac{\sqrt{m_r k_B T_{\text{ref}}}}{(5 - 2\omega)(7 - 2\omega) \mu_{\text{ref}}}. \quad (2.50)$$

As for the HS model, Eq. (2.49) and Eq. (2.50) are applied for calculating species specific collision diameters based on measured viscosity data.²

Because of its simplicity and accuracy, the VHS model is widely used in the DSMC community. However, more complex collision models can be constructed in order to reproduce experimentally measured transport coefficients even better. Examples are

² In principle, the diffusion coefficient or the coefficient of thermal conductivity could also be used to determine the parameters of the HS and VHS collision models. However, it has become established to adapt these collision models to the law of viscosity and then to examine, based on the comparison with the experiment, whether the model also reproduces the correct diffusion coefficient and the correct thermal conductivity.

the variable soft sphere (VSS) model [96, 95] or the generalized hard sphere (GHS) model [69].

When describing polyatomic species, inelastic collision processes must be taken into account. Therefore, rotational and vibrational energy states are adapted during the collision procedure. In recent decades, a variety of models with different complexity were developed to describe inelastic collision within the DSMC algorithm. While traditional DSMC models [14, 108] were constructed to reproduce a specific relaxation of internal temperatures, recent state-to-state models attempt to directly describe transition processes of internal energy states [16, 1, 2, 47]. However, all models have in common that they maintain the elastic collision procedures described above for updating particle velocities. In the following, the models that are used in this work are described in more detail.

In a first step, particles pairs that were already been selected for an elastic collision are tested for an inelastic collision. Therefore, the particle selection scheme described by Zhang et al. [147] is applied. The scheme is preferable since it can be easily applied for modeling gases with multiple species. It is described in more detail in Appendix A.

For the case that a particle pair is selected for an inelastic collision, internal energy is redistributed between the colliding particles. Therefore, the Larsen-Borgnakke (LB) model [14] is applied, which was first introduced for describing continuous internal energy states [14] and was later extended for modeling discrete energy levels [17, 6]. The model redistributes the total collision energy according to an equilibrium distribution function. Even if this assumption means that the LB model does not reproduce the exact microscopic processes in detail, this leads to a Boltzmann distribution of the internal energies in the equilibrium state. This is a desirable property when modeling the relaxation of internal energies within a DSMC simulation. Therefore, as long as it is not necessary to simulate the detailed internal energy structure of a molecule, the LB model is a good and simple way to describe internal energies within DSMC.

Finally, elastic collision procedures as described above are performed in order to calculate new particle velocities. The particle velocities are scaled to conserve the total collision energy.

The schemes described above are adjusted to achieve a relaxation of internal energies, as described by the Landau-Teller law:

$$\frac{dE_{\text{int}}}{dt} = \frac{1}{\tau_{\text{int}}} (E_{\text{int}}^{\text{eq}} - E_{\text{int}}). \quad (2.51)$$

Here E_{int} denotes the average internal energy, $E_{\text{int}}^{\text{eq}}$ the corresponding equilibrium energy, $\tau_{\text{int}} = Z_{\text{int}}/\nu_{\text{coll}}$ the internal relaxation time with the mean collision frequency ν_{coll} and a relaxation number Z_{int} .

2.2.5 Calculation of averages

Macroscopic quantities, such as density, temperature, heat fluxes or skin friction, are calculated by averaging over microscopic particle attributes. Since collision cells should resolve the mean free path, macroscopic quantities do not change much over the spread of a cell. Accordingly, averaging is usually carried out separately for

each cell. In this way it can be ensured that all essential flow structures are resolved. However, it is also possible to define separate cells for averaging. Such then comprise several collision cells. As a result, an averaging cell contains more particles than a collision cell, which means that the macroscopic quantities are calculated with less noise [12].

In general, macroscopic velocity moments can be approximated as follows:

$$\frac{1}{n} \langle Q|f \rangle \approx \frac{1}{N_p} \sum_{i=1}^{N_p} Q_i. \quad (2.52)$$

Here N_p means the number of particles located in the cell, f denotes the PDF the particles are representing and Q denotes an arbitrary microscopic quantity, for example the particle energy. With reference to the concepts described in Subch. 2.1, Eq. (2.52) can be applied to calculate arbitrary macroscopic quantities.

Since microscopic particle attributes follow a random process, the right side of Eq. (2.52) exhibit statistical fluctuations. In general, the relative standard deviation of such fluctuations is proportional to $1/\sqrt{N_p}$. In order to reduce the statistical noise, various techniques can be applied.

The scaling factor F_N can be decreased, resulting in a larger number of simulation particles N_p . However, increasing the number of particles also increases the computational effort.

In stationary simulations additional time averaging can be applied. In early DSMC implementations, the right side of Eq. (2.52) was simply averaged over time. However, this approach, known as *sample averaged measurement*, can lead to additional bias errors in non-equilibrium gas flows. To avoid such problems, a *cumulative average measurement* technique is recommended [139]:

$$\frac{1}{n} \langle Q|f \rangle \approx \frac{\sum_{j=1}^{N_t} \sum_{i=1}^{N_p(t)} Q_i}{\sum_{j=1}^{N_t} N_p(t)} \quad (2.53)$$

Here N_t denotes the number of time averages which are taken. The relative standard deviation of macroscopic averages decreases to $1/\sqrt{N_p N_t}$ for this case.

In the case of a non-stationary flow, time averaging can not be performed. Instead, the results of many statistically independent simulations may be averaged.

2.3 Kinetic Fokker-Planck method

The kinetic Fokker-Planck method is a recently proposed particle simulation method that can be used to model gas flows upto moderate Knudsen numbers [84, 55, 110, 135].

The method is based on the Fokker-Planck equation which serves as a model for the Boltzmann equation in the case of moderate Knudsen numbers. The Fokker-Planck equation is not solved directly, instead the underlying particles are modeled by solving associated stochastic processes. No collisions are calculated in the FP method, so that larger cell and time step sizes compared to a DSMC calculation can be used. Therefore, the FP method holds the potential to be more efficient than DSMC, where the Knudsen number is small.

The structure of this subchapter is as follows. Subchapter 2.3.1 presents recently developed models for the model parameters of the FP equation, describing monatomic, single species gases. Subchapter 2.3.2 discusses the kinetic description of these FP models. Stochastic processes that are employed to simulate particles are introduced and their solutions are discussed. Subchapter 2.3.3 and Subch. 2.3.4 present recent methods for describing diatomic molecules and gases with multiple species within the kinetic FP framework. Finally Subch. 2.3.5 discuss the applicability range of the kinetic FP method.

2.3.1 Fokker-Planck approximation of the Boltzmann equation

Within the kinetic Fokker-Planck method the Boltzmann equation is approximated by the Fokker-Planck equation in velocity space:

$$\frac{\partial f}{\partial t} + v_i \frac{\partial f}{\partial x_i} + \frac{F_i}{m} \frac{\partial f}{\partial v_i} = \underbrace{-\frac{\partial}{\partial v_i} A_i f + \frac{\partial^2}{\partial v_k \partial v_k} \frac{D^2}{2} f}_{S_{FP}(f)}. \quad (2.54)$$

Here S_{FP} denotes the Fokker-Planck operator and the drift coefficient \mathbf{A} and the diffusion coefficient D are open model parameters. The justification for this approximation is provided, for example, by the work of Bogomolov [13], who derives the FP operator in the Navier-Stokes limit from the Boltzmann collision operator. Drift and diffusion coefficient may be calculated directly from this derivation. However, Bogomolov's derivation leads to complex formulas that may not be suitable for defining a computational particle method. For this reason, in most approaches these coefficients are used as open model parameters for adjusting the properties of the FP method. Usually, a similar approach is applied as described in Subch. 2.2.4 for DSMC collision models: the model parameters are chosen in such a way that the FP method reflects correct Navier-Stokes transport coefficients in the limit of small Knudsen numbers, as this is a necessary prerequisite for most practical applications of kinetic FP. Whether the method is also suitable for modeling non-equilibrium flows is then examined by comparing numerical simulations with experimental measurements.

The following subchapters describe two models for these model parameters in more detail.

Linear model

The *linear model* [84] employs a drift coefficient that depends linearly on the thermal particle velocities:

$$\mathbf{A} = -\frac{\mathbf{c}}{\tau}. \quad (2.55)$$

The relaxation time τ represents a model parameter and is set so that the model reproduces a given viscosity μ in the Navier-Stokes limit:

$$\tau = \frac{2\mu}{p}. \quad (2.56)$$

Here p denotes the pressure. Hence, the viscosity is an input parameter for the model. The diffusion coefficient is set so that the model conserves energy:

$$D = \sqrt{\frac{2k_{\text{B}}T}{\tau m}}. \quad (2.57)$$

The linear model yields the Euler and the Navier-Stokes equations with viscosity μ in the Navier-Stokes limit, but produces a wrong thermal conductivity. In particular, the Prandtl number becomes $Pr_{\text{linear}} = 3/2$ for the linear model, while an analysis of the Boltzmann equation yields a Prandtl number of $Pr_{\text{Boltz}} = 2/3$ for monatomic species [84]. Therefore, the model cannot be applied to cases where heat fluxes become relevant. Note, that the Prandtl number $Pr = c_p\mu/k$ is calculated based on the viscosity, the specific heat c_p and the thermal conductivity k .

Cubic model

To correct the wrong prediction of heat fluxes of the linear model, Gorji et al. [55] proposed the *cubic model*. Here, the diffusion coefficient (2.57) of the linear model is adopted, while the drift coefficient (2.55) is extended by second and third order terms in thermal particle velocities:

$$A_i = -\frac{1}{\tau}c_i + \psi_{ij}c_j + \gamma_i \left(c_jc_j - \frac{3k_{\text{B}}T}{m} \right) + \Lambda \left(c_ic_jc_j - \frac{2q_i}{\rho} \right). \quad (2.58)$$

Here $\Lambda = -|\det(\sigma_{ij})|/(\tau \langle c_ic_i|f \rangle^4 \cdot \rho^3)$ presents a scalar value which is introduced to ensure stability of the model, σ_{ij} the stress tensor and q_i means the i -th component of the heat flux vector. The relaxation time $\tau = 2\mu/p$ is chosen identical as in the linear model, while the matrix ψ_{ij} is assumed to be symmetric. The nine model parameters ψ_{ij} and γ_i are chosen, so that the model yields a correct viscosity and thermal conductivity in the Navier-Stokes limit. As described in Subch. 2.1.2, this is achieved when the FP operator reproduces lower order Boltzmann production terms:

$$P_{\text{FP}}(X) = P_{\text{Boltz}}(X), \quad (2.59)$$

$$X \in (c_ic_j, \mathbf{c}c_i).$$

Hence, in order to construct the FP model, Boltzmann production terms must be evaluated. In general, Boltzmann production terms depend on both the molecular interaction potential as well as the PDF. However, for the Maxwell molecule model, Boltzmann production terms become independent of the PDF and the right-hand

side of Eq. (2.59) can be evaluated [136]:

$$P_{\text{Boltz}}(c_i c_j) = -\frac{p}{\mu} \sigma_{ij}, \quad (2.60)$$

$$P_{\text{Boltz}}(\mathbf{c}c_i) = -\frac{2}{3} \frac{p}{\mu} q_i. \quad (2.61)$$

Combining Eq. (2.59) with Eq. (2.60) and Eq. (2.61) yields a system of nine linear equations, that is solved in order to calculate the model parameters γ_i and ψ_{ij} . In recent years, the cubic model was successfully applied to supersonic flows [91], nozzle flows [57, 100] as well as expansion flows [60, 88].

2.3.2 Kinetic description

As mentioned above, the FP equation is not solved directly. Instead, the underlying particles are simulated. This kinetic particle algorithm is described in more detail below.

For the case that f obeys the FP equation, the motion of individual particles is characterized by a set of stochastic processes [84]:

$$d\mathbf{X} = \mathbf{V}dt, \quad (2.62)$$

$$d\mathbf{V} = \mathbf{A}dt + Dd\mathbf{W} + \mathbf{F}. \quad (2.63)$$

Note, that \mathbf{X} and \mathbf{V} denote particle velocity and position and $d\mathbf{W}$ refers to a Wiener process with zero expectation and $\langle dW_i dW_j \rangle = \delta_{ij}$. The kinetic FP method uses this relationship in order to construct a particle simulation algorithm. Therefore, particles are simulated according to the stochastic processes (2.62) and (2.63).

Figure 2.5 illustrates the relationship between the FP equation and the kinetic FP method in more detail. The distribution of particles that are simulated in the kinetic FP method converges to the distribution function $f(\mathbf{x}, \mathbf{v}, t)$ that obeys the Fokker-Planck equation in the limit of an infinite number of particles [84, 55]. Hence, the kinetic FP method solves the FP equation on a kinetic level.

Stochastic equation of motions

To construct a particle algorithm, the system (2.62) and (2.63) must be solved. Due to the complexity of drift and diffusion coefficient, it is in general not possible to find

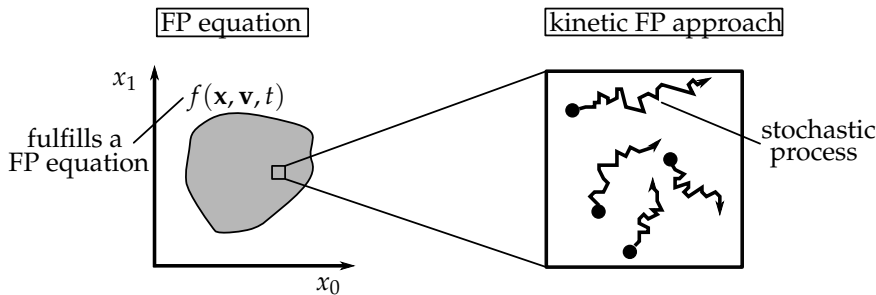


FIGURE 2.5: Relationship between the FP equation and the kinetic FP method. The kinetic FP method solves the FP equation on a microscopic level.

an exact solution. Instead, approximation methods must be found. These are usually constructed, so that, under the assumption of an homogeneous system in space, the time evolution of velocity and position moments up to a specific order, for example shear stresses or heat fluxes, are correctly reproduced. For example, Gorji et al. [55] constructed a kinetic algorithm for the cubic model that exactly reproduce first and second conditional and joint conditional moments of velocity and position. This allows to increase the time step size compared to a scheme which does not exactly reproduce such moments. However, due to its complexity, this approach is not used in this thesis.

Instead, the scheme described in reference [56] is applied. It correctly predicts conditional velocity moments up to second order, leading to the conservation of energy and momentum independently of the time step size, while updating particle positions similar as in the DSMC method. The solution of the scheme reads:

$$V_i^{n+1} = \frac{1}{\alpha} \left(C_i^n \exp\left(-\frac{\Delta t}{\tau}\right) + \left(1 - \exp\left(-\frac{\Delta t}{\tau}\right)\right) \tau N_i^n + \sqrt{\frac{k_B T}{m} \left(1 - \exp\left(-2\frac{\Delta t}{\tau}\right)\right)} \xi_i \right) + u_i + F_i \Delta t, \quad (2.64)$$

$$X_i^{n+1} = X_i^n + V_i^n \Delta t + \frac{F_i}{2} \Delta t^2. \quad (2.65)$$

The index n refers to different time steps, Δt denotes the time step size, $\mathbf{C} = \mathbf{V} - \mathbf{u}$ denotes the thermal part of the particle velocity \mathbf{V} , ξ_i are independent standard normal deviates and the parameter N_i^n is defined as:

$$N_i^n = \psi_{ij} C_j^n + \gamma_i \left(C_j^n C_j^n - \frac{3k_B T}{m} \right) + \Lambda_i \left(C_i^n C_j^n C_j^n - \frac{2q_i}{\rho} \right). \quad (2.66)$$

The parameter α is set such that energy in case of a vanishing external force F_i is conserved. Note, that the quantities τ , T , \mathbf{u} , \mathbf{q} and ρ are assumed to be constant during a time step.

Particle algorithm

Equation (2.64) and Eq. (2.65) are used to calculate the particle motion within a kinetic FP simulation. Figure 2.6 shows the general procedure for such a simulation. While generation of particles and calculation of averages can be performed as in the DSMC algorithm, updating of particle velocities and positions requires more

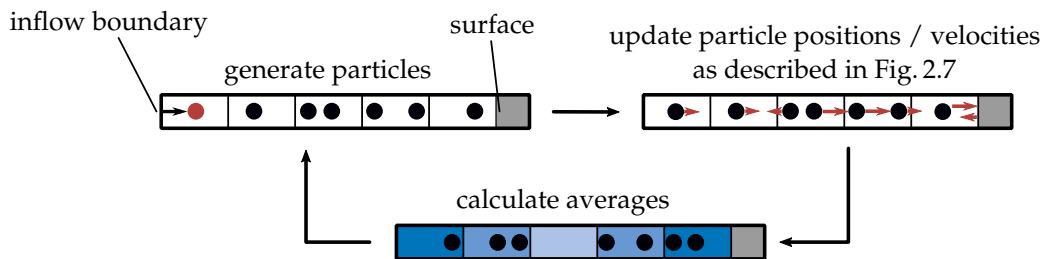


FIGURE 2.6: Typical kinetic FP simulation loop for a simple 1-D case.

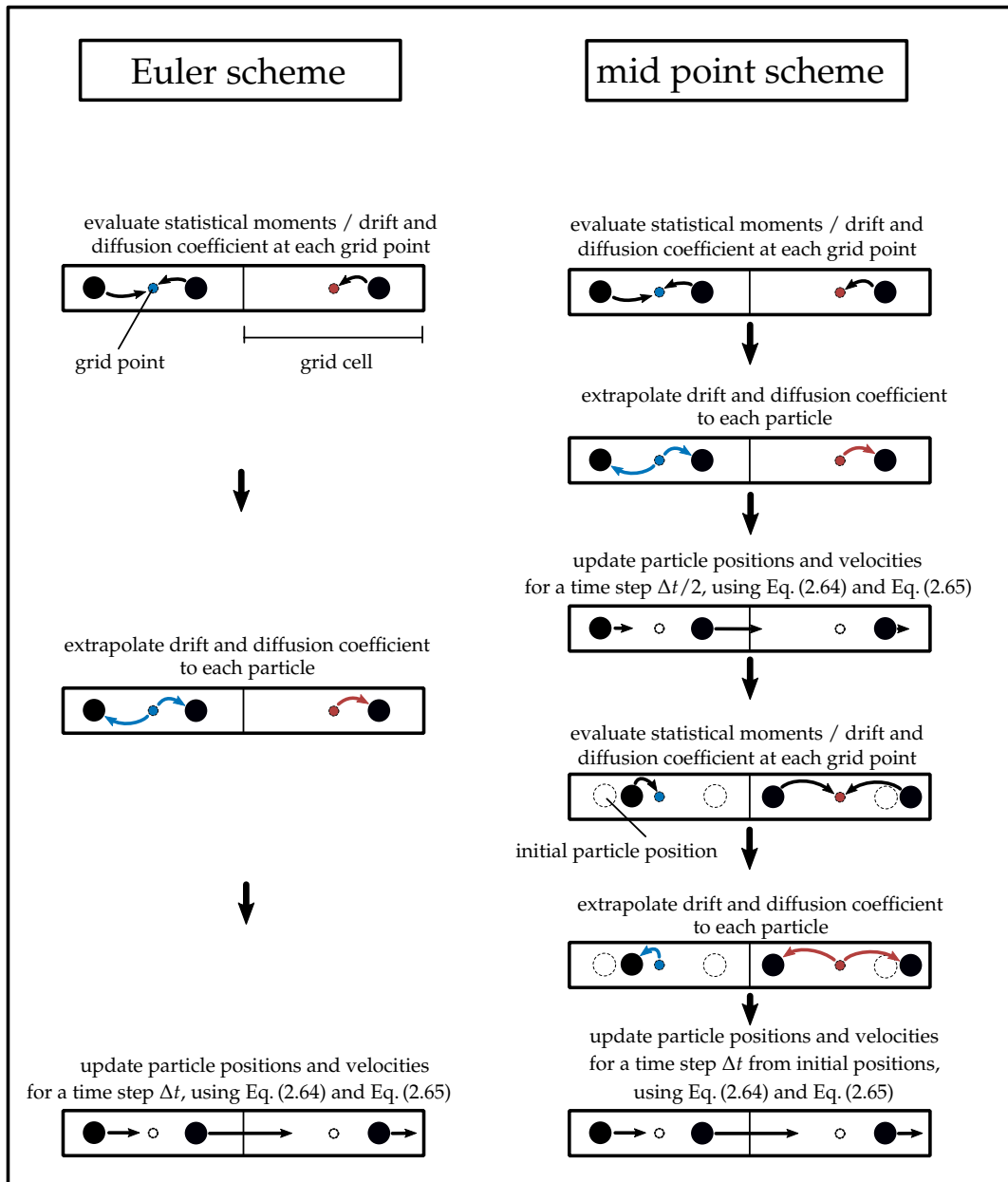


FIGURE 2.7: Calculation of particle positions and velocities in a kinetic FP simulation. Left: Euler scheme. Right: Mid point scheme.

detailed considerations.

In contrast to the DSMC method it is not assumed that the particle velocity will remain constant over a time step. Instead, the particle velocity changes over a time step due to collisions with other particles that may take place. Equation (2.64) describes the final particle speed as is to be expected at the end of the time step under the assumption, that macroscopic quantities τ , T , \mathbf{u} , \mathbf{q} and ρ are constant over the time step. However, these macroscopic quantities may also change over a time step. In order to do justice to this fact, different integration schemes can be constructed, as exemplary shown in Fig. 2.7.

In a simple *Euler scheme*, the final particle velocities and positions are calculated

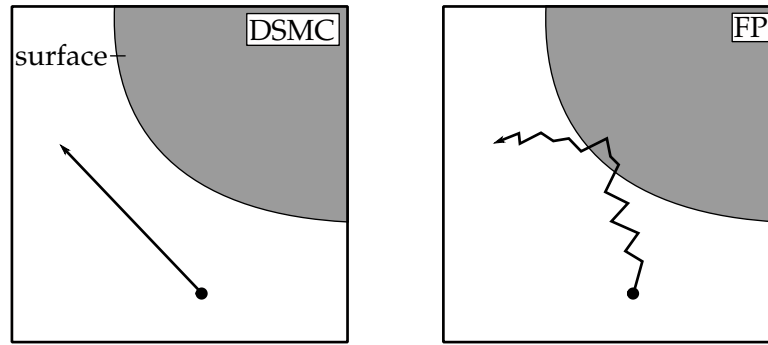


FIGURE 2.8: Particle evolution over a time step Δt . Left: In traditional DSMC particles are shifted on linear trajectories. To detect for surface collisions it is sufficient to check, if the straight line between initial and final particle position crosses the surface. Right: In kinetic FP, trajectories represent a diffusive process. Surface collisions might occur, even when the line between end and initial position does not cross a surface.

only based on the initial state of each particle: Velocity moments, such as temperature and heat flux, are evaluated at each time step for each grid cell by averaging over the particle ensemble. Based on that, the model parameters γ_i and ψ_{ij} are calculated for each grid cell by solving the linear system of equations, discussed in Subch. 2.3.1. Thereafter, the velocity moments and model parameters are extrapolated to the particle positions and new particle positions and velocities, based on Eq. (2.64) and Eq. (2.65) are calculated.

A higher order integration scheme features the *mid point scheme*. In this scheme the particles are first evolved for half a time step, based on the initial particle state. Subsequently, velocities moments and model parameters are recalculated based on the the new particle positions. These velocities moments and model parameters are then used to calculate a new spatial displacements for each particle. Finally, these values are then applied to evolve the particles for a full time step, based on the initial conditions. Compared to the Euler scheme, the mid point scheme allows to use larger time step sizes. However, for the sake of simplicity, this work adopts the Euler scheme.

In order to extrapolate model parameters and velocity moments to the particle positions, higher order extrapolation may be used to increase the accuracy of the method and to allow the use larger cell sizes. However, for the sake of simplicity, this work assumes that moments are constant over a grid cell.

Special care has to be taken about the boundary conditions. As shown in Fig. 2.8, particle paths represent not a straight line but a diffusive random walk. Therefore, particles might hit a surface, even if the straight line between initial and end point of the particle trajectory is located outside of the surface. Hence, it is a complex task to estimate interaction of particles with surfaces. To overcome this problem, different techniques were developed.

Önskog et al. [149] derived a method based on an estimate of the first point in time when particle driven by a stochastic diffusion process hits a boundary. However, to the author's knowledge, this scheme was so far only applied to a simple, zero dimensional heat bath test case.

Fei et al. [35] proposed a method in which the particle motion is divided into a stochastic and a deterministic part. The interaction with boundaries is determined separately for each part. A similar method was also suggested in reference [34].

A different method is suggested by Jiang et al. [87], who define cells that are closer than a specified distance to surfaces as *near boundary zone*. The path of particles within this zone is subdivided into small parts and the movement along each part is approximated as linear displacement. As a result, the interaction of particles with boundaries can be easily tested separately for each linear path.

Küchlin [100] simply ignored the diffusive nature of the random process and calculated surface interaction similar as in the DSMC algorithm, assuming a linear displacement. The author argued, that errors introduced by this linear approximation are negligible small when using local time steps, since the temporal discretization is usually very small in the vicinity of surfaces. Due to the same reasoning, no specific method for modeling the particle-wall interaction is used in this thesis either.

Evaluation of statistical moments

Averaging velocity moments is a crucial task for updating particle positions and velocities via Eq.(2.64) and Eq.(2.65). In general, a velocity moment can be approximated by averaging over the particle ensemble in the cell, as described in Subch.2.2.5. However, for a finite number of particles, averaging can lead to additional bias errors [86]. In order to reduce these errors, an under-relaxation technique can be applied for stationary problems [84]. For this purpose, an average number of particles X^n per cell at time step n is continuously calculated by:

$$X^{n+1} \equiv \Phi X^n + (1 - \Phi) N_p^n. \quad (2.67)$$

Here N_p^n denotes the number of particles in the cell at time step n and $\Phi \in (0,1)$ is a relaxation parameter. Similar, time averaged moments Y^n are continuously calculated for each time step:

$$Y^{n+1} \equiv \Phi Y^n + (1 - \Phi) \sum_{i=1}^{N_p^n} Q_i. \quad (2.68)$$

Here Q_i refers to a microscopic particle quantity. Finally, statistical moments at time step n can be approximated by:

$$\frac{1}{\rho/m} \langle Q^n | f^n \rangle \approx \frac{Y^n}{X^n}. \quad (2.69)$$

Using $\Phi = 1 - \frac{1}{N_t}$ leads to similar statistical noise, than regular time averaging over N_t time steps, as described by Eq.(2.53). Time averaged moments as defined by Eq.(2.69) always develop slower than the instantaneously averaged moments as given by Eq.(2.52). Therefore, the use of time averaged moments in unsteady problems is not recommended. However, for steady gas flows, this technique can dramatically reduce the number of required particles per cell [85].

2.3.3 Models for polyatomic species

As a major topic of this thesis, a new method for modeling polyatomic species within the kinetic FP framework is constructed. Therefore, this subchapter summarizes recently proposed models for describing polyatomic gases related to the kinetic FP method.

Cubic FP model

Gorji et al. [53] proposed a method for describing diatomic species within the cubic FP model. For this purpose, rotational and vibrational „velocities “ Ω and Ψ are introduced. It should be noted that these velocities have no physical meaning and are only defined in order to handle internal energy modes mathematically equivalent to translational modes. Similar to translational modes, internal energies can be calculated from rotational and vibrational velocities:

$$e_{\text{rot}} = \frac{1}{2}m\Omega\Omega, \quad (2.70)$$

$$e_{\text{vib}} = \frac{1}{2}m\Psi\Psi. \quad (2.71)$$

As for the translational velocities, it is assumed that the distribution of internal velocities obeys the Fokker-Planck equation. Hence, the microscopic motion of internal velocities can be described by a stochastic process:

$$d\Omega = -\frac{1}{2\tau_{\text{rot}}}\Omega dt + \sqrt{\frac{k_B}{\tau_{\text{rot}}}}T dW, \quad (2.72)$$

$$d\Psi = -\frac{1}{2\tau_{\text{vib}}}\Psi dt + \sqrt{\frac{d_{\text{vib}}k_B}{\tau_{\text{vib}}}}T dW. \quad (2.73)$$

Here τ_{rot} and τ_{vib} denote relaxation times and

$$d_{\text{vib}} = 2\frac{\theta/T}{\exp(\theta/T) - 1}, \quad (2.74)$$

defines the number of vibrational degrees of freedom. The parameter θ denotes a species specific vibrational temperature. The model is constructed, to reproduce the Landau-Teller law as well as the equipartition theorem.

The diffusion coefficient in the translational Fokker-Planck operator (2.54) is adjusted to achieve energy conservation. In addition, the production term (2.61) is recalculated based on McCormacks 17-moment approximation for gases with internal energy modes [112].

Ellipsoidal FP model

Mathiaud et al. [111] proposed a method to describe polyatomic species within the ES FP model. Similar to the method of Gorji et al. [53] described above, rotational energies are modeled as continuous scalars. Therefore, the distribution of internal energies e_{int} is assumed to obey a Fokker-Planck equation. Hence, the microscopic change of internal energies can be described by a stochastic process:

$$dE_{\text{int}} = -\frac{2}{\tau} \left(E_{\text{int}} - \frac{d_{\text{int}}}{2}RT_{\text{rel}} \right) dt + 2\sqrt{RT_{\text{rel}}e_{\text{int}}}dW. \quad (2.75)$$

Here d_{int} denotes the number of internal degrees of freedom and the temperature $T_{\text{rel}} = (1 - \phi)T_{\text{int}} + \phi T$ is composed of the temperature of the internal energy mode T_{int} and the temperature T that the gas would reach if internal modes were equilibrated with translational modes. The parameter ϕ controls the relaxation behavior of internal energies. The model leads to a correct distribution of rotational energies in equilibrium, but is not able to handle vibrational energy states.

Ellipsoidal FP-BGK model

Pfeiffer et al. [122] constructed a method for describing rotational energy modes within the ES FP model. It is worth noting that this method was originally developed for the kinetic BGK method [119] and was only adapted to the kinetic FP framework. The Landau-Teller equation (2.51) is interpreted in the same way as the kinetic BGK model. Hence, the probability that a certain particle relaxes its internal energy state during a time step Δt is given by:

$$P_{\text{rot}} = 1 - \exp\left(-\beta_{\text{rot}} \frac{\Delta t}{\tau_{\text{rot}}}\right). \quad (2.76)$$

Here τ_{rot} denotes the rotational relaxation time. The parameter β_{rot} is a correction factor. It results from the solution of a nonlinear system of equations that can be derived from the requirement that the model reproduces the Landau-Teller relaxation law.

In each time step, Eq. (2.76) is applied to test all particles for internal energy relaxation. Once a particle is selected for relaxation, its internal energy state is resampled using a Boltzmann distribution. In order to describe energy exchange between translational and internal modes, an energy conservation scheme must be applied. For this purpose, rotational and translational energies are rescaled, so that the total energy is retained and each degree of freedom contains the same amount of energy. Rescaling so that each degree of freedom contains the same amount of energy ensures that the gas reaches the correct state of equilibrium.

2.3.4 Models for gas mixtures

This subchapter presents the kinetic FP method of Gorji et al. [51], which is, to the author's knowledge, currently the only method that allows the modelling of gas mixtures within the kinetic FP framework.

Gorji et al. [51] generalized the single species cubic model for describing binary Maxwell gas mixtures. The components of the mixture are referred to by indices α and β . For the sake of simplicity, but without loss of generality, all equations are given only for the α species. The equations for the β species can be obtained by simply exchanging indices.

Similar to monatomic Fokker-Planck models, the set of Boltzmann equations (2.37) is approximated by a set of FP equations in velocity space:

$$\begin{aligned} \frac{\partial f^{(\alpha)}}{\partial t} + v_i \frac{\partial f^{(\alpha)}}{\partial x_i} + \frac{F_i}{m^{(\alpha)}} \frac{\partial f^{(\alpha)}}{\partial v_i^{(\alpha)}} = \\ \underbrace{- \frac{\partial \left(f^{(\alpha)} A_{i|\text{MAX}}^{(\alpha)} \right)}{\partial v_i^{(\alpha)}} + \frac{\partial^2}{\partial v_i^{(\alpha)} \partial v_i^{(\alpha)}} \frac{D^{(\alpha)}{}_{|\text{MAX}}^2}{2} f^{(\alpha)}}_{S_{\text{FP}|\text{MAX}}^{(\alpha)}}. \end{aligned} \quad (2.77)$$

Here $S_{\text{FP}|\text{MAX}}^{(\alpha)}$ represents the Fokker-Planck operator. The drift coefficient $A_{i|\text{MAX}}^{(\alpha)}$ and diffusion coefficient $D_{|\text{MAX}}^{(\alpha)}$ are chosen separately for each species. Similar to the single species model, a cubic ansatz of thermal particle velocities is used for the drift

coefficient:

$$A_{i|\text{MAX}}^{(\alpha)} \equiv b_i^{(\alpha)} + \psi_{ij}^{(\alpha)} c_j^{(\alpha)} + \gamma_i^{(\alpha)} \left(c_j^{(\alpha)} c_j^{(\alpha)} - \frac{1}{n^{(\alpha)}} \langle c_j^{(\alpha)} c_j^{(\alpha)} | f^{(\alpha)} \rangle \right) + \Lambda^{(\alpha)} \left(c_i^{(\alpha)} c_j^{(\alpha)} c_j^{(\alpha)} - \frac{1}{n^{(\alpha)}} \langle c_i^{(\alpha)} c_j^{(\alpha)} c_j^{(\alpha)} | f^{(\alpha)} \rangle \right). \quad (2.78)$$

The constant $\Lambda^{(\alpha)}$ is set to ensure stability of the model [55]. The model parameters $b_i^{(\alpha)}$, $\psi_{ij}^{(\alpha)}$, $\gamma_i^{(\alpha)}$ and the diffusion coefficient $D_{|\text{MAX}}^{(\alpha)}$ are chosen so that the Fokker-Planck operator $S_{\text{FP}|\text{MAX}}^{(\alpha)}$ reproduces Boltzmann production terms upto order three:

$$P_{\text{FP}|\text{MAX}}^{(\alpha)}(X) \stackrel{!}{=} P_{\text{Boltz}}^{(\alpha)}(X), \quad (2.79)$$

$$X \in \left\{ c_i^{(\alpha)}, c_i^{(\alpha)} c_i^{(\alpha)}, c_{<i}^{(\alpha)} c_{j>}^{(\alpha)}, c_i^{(\alpha)} c_j^{(\alpha)} c_j^{(\alpha)} \right\}.$$

It is worth noting, that the right side of expression (2.79) does not vanish for $X = c_i^{(\alpha)}$ and $X = c_i^{(\alpha)} c_i^{(\alpha)}$ since energy and momentum can be transferred between species. The production terms on the right hand side of Eq. (2.79) are evaluated for binary Maxwell mixtures in reference [49]. The parameters $b_i^{(\alpha)}$ and $D_{|\text{MAX}}^{(\alpha)}$ are set, so that the linear part of expression (2.78) satisfies Eq. (2.79) for $X \in \left\{ c_i^{(\alpha)}, c_i^{(\alpha)} c_i^{(\alpha)} \right\}$. The nine remaining model parameters $\psi_{ij}^{(\alpha)}, \gamma_i^{(\alpha)}$ are determined as solution of a system of nine linear equations, that can be derived from Eq. (2.79) for $X \in \left\{ c_{<i}^{(\alpha)} c_{j>}^{(\alpha)}, c_i^{(\alpha)} c_j^{(\alpha)} c_j^{(\alpha)} \right\}$. Similar to the single species model, particle trajectories are calculated by integrating a species depended system of stochastic equations of motion:

$$d\mathbf{X}^{(\alpha)} = \mathbf{V}^{(\alpha)} dt, \quad (2.80)$$

$$d\mathbf{V}^{(\alpha)} = \mathbf{A}_{|\text{MAX}}^{(\alpha)} dt + D_{|\text{MAX}}^{(\alpha)} d\mathbf{W}^{(\alpha)} + \mathbf{F}. \quad (2.81)$$

Due to the similarity to the single species cubic model, the same particle integration as described in Subch. 2.3.2 can be applied.

2.3.5 Applicability of the kinetic Fokker-Planck method

From the user's point of view it is of course very advantageous to know in which dilution range, i.e. in which Knudsen number interval, the kinetic FP method can be applied. From the construction of the FP method it can be deduced that the method delivers correct results in the range of lower Knudsen numbers, in particular it reproduces the results of the Navier-Stokes equations in the Navier-Stokes limit. The applicability of the method for flows with larger Knudsen numbers, on the other hand, cannot simply be considered on the basis of theoretical arguments. Instead, this has to be investigated by examining appropriate numerical test cases:

At this point it should be noted that such numerical applicability studies are generally a complex task, since the applicability of a simulation method depends on many parameters. Important example are the specific test case that is being investigated, the specific type of the FP model parameters that are used, the flow quantities that are being considered, the amount of deviation from the correct solution that is acceptable or simply the definition of the reference length that is used for defining

the Knudsen number. Due to this large number of relevant parameters, the exact application range of a simulation method cannot be specified by a single Knudsen number interval. Instead, the application range of a method has to be re-examined on a case-by-case basis. Hence, in order to examine the applicability of a method across all parameters, many test cases must be investigated.

Due to the novelty of the FP-method, it has not yet been investigated in such depth of detail. Nevertheless, there are a number of publications that investigate the applicability for different types of flows. In the following, the applicability of the cubic FP model is discussed, since this model is the basis for most of the models described in this work.

The cubic FP model has shown good results for some representative zero and one-dimensional test cases. For example, it reproduces very precisely flow velocity, temperature and heat flux distributions for a one-dimensional force-driven Poiseuille flow up to a Knudsen number of two [55].

The model was also examined for more complex two-dimensional flows. For example, it could be shown that for a diluted subsonic cylinder flow with Knudsen number of two, the drag coefficient is only predicted with a deviation of 1.4% compared to DSMC results. Similar good results were achieved when comparing with DSMC results for a lid-driven cavity flow [56].

The applications for hypersonic flows have been studied by Jun et al. [89]. It turns out that the cubic FP model is able to predict shock wave structures ahead of a sphere up to an inflow Mach number of at least two. For an extension of the cubic model, the Entropic-FP model, it was also shown that it delivers good results up to Mach numbers of five in comparison to DSMC calculations [52].

Chapter 3

Modeling of polyatomic species

This chapter describes a new approach for modeling polyatomic species within a kinetic FP framework. The approach employs a master equation for describing the energy structure of molecules. In accordance with the kinetic FP framework, the master equation is not solved directly, but an underlying stochastic process is solved to model microscopic energy states.

For simplicity, all calculations presented in this chapter are performed assuming only a single discrete internal energy mode. However, it is also possible to construct models for multiple energy modes, using the same approach as discussed in this chapter.

The structure of this chapter is as follows. Subchapter 3.1 presents a kinetic model, which employs a master equation to describe the internal energy structure of molecules, while the FP equation is used to model translational velocities. In Subch. 3.2, the kinetic model is translated into a set of microscopic stochastic processes. Subchapter 3.3 describes specific models for the rate coefficients of the master equation. The performance of the master equation model is discussed in Subch. 3.4, based on theoretical considerations. The solution of the stochastic processes is discussed in Subch. 3.5. In Subch. 3.6 various test cases are presented to check the validity of the proposed models. Subchapter 3.7 assesses the computational efficiency of the proposed models. Finally, Subch. 3.8 presents the conclusion of this chapter.

Please note that the main parts of this chapter have been published in reference [75].

3.1 Master equation ansatz

This subchapter employs as master equation to construct a kinetic model for describing polyatomic species. As described in Subch. 2.1.3, the statistical state of the gas is described by the distribution function $f_i(\mathbf{x}, \mathbf{c}, \mathbf{t})$.

The Boltzmann collision operator S_{Boltz} can be separated into an elastic part $S_{\text{Boltz}}^{\text{el}}$ and an inelastic part $S_{\text{Boltz}}^{\text{inel}}$ [114]:

$$S_{\text{Boltz}} = S_{\text{Boltz}}^{\text{el}} + S_{\text{Boltz}}^{\text{inel}}. \quad (3.1)$$

The elastic part describes the impact of elastic particle collisions on the distribution function, while the inelastic part only considers inelastic collisions. As described in Subch. 2.3.1, the elastic part is approximated by a FP operator in velocity space:

$$S_{\text{Boltz}}^{\text{el}} \approx \frac{Z_{\text{tot}} - Z_{\text{inel}}}{Z_{\text{tot}}} \left(-\frac{\partial A_i f_n}{\partial v_i} + \frac{D^2}{2} \frac{\partial^2 f_n}{\partial v_i \partial v_i} \right) = \frac{Z_{\text{tot}} - Z_{\text{inel}}}{Z_{\text{tot}}} S_{\text{FP}}. \quad (3.2)$$

Here Z_{tot} denotes the total number and Z_{inel} the number of inelastic collisions per time and volume. Thus, the factor $(Z_{\text{tot}} - Z_{\text{inel}})/Z_{\text{tot}}$ expresses that only a fraction of all collisions are elastic. For the inelastic part, the following decomposition is assumed:

$$S_{\text{Boltz}}^{\text{inel}} = S_v + S_e. \quad (3.3)$$

The operator S_v models the impact on the distribution function due to particles that change their velocities as a result of inelastic collisions. Similar, the operator S_e models the impact on the distribution function due to particles that change internal energies as a result of inelastic collisions. In accordance with the DSMC models that are described in Subch. 2.2.4, it is supposed that the change of particle velocities in inelastic collisions can be handled similar to in the elastic case. Therefore, it is approximated:

$$S_v \approx \frac{Z_{\text{inel}}}{Z_{\text{tot}}} \left(-\frac{\partial A_i f_n}{\partial v_i} + \frac{D^2}{2} \frac{\partial^2 f_n}{\partial v_i \partial v_i} + K' \frac{\partial^2 f_n}{\partial v_i \partial v_i} \right) = \frac{Z_{\text{inel}}}{Z_{\text{tot}}} \left(S_{\text{FP}} + K' \frac{\partial^2 f_n}{\partial v_i \partial v_i} \right). \quad (3.4)$$

The factor $Z_{\text{inel}}/Z_{\text{tot}}$ takes into account that only a fraction of all collisions are inelastic. The quantity K' is introduced in order to model energy exchange between internal and translational modes. In particular, the diffusion coefficient in the FP operator is modified so that it correctly predicts the gain or loss of translational energy due to inelastic collisions. An expression for K' , that ensures a correct exchange of energy between internal and translational modes is derived later in this subchapter. A master equation model is employed for S_e :

$$S_e = \frac{Z_{\text{inel}}}{Z_{\text{tot}}} \sum_j \left(R'_{jn} f_j - R'_{nj} f_n \right), \quad (3.5)$$

where R'_{jn} and R'_{nj} denote rate coefficients. The product $R'_{jn} dt$ can be interpreted as a probability that a molecule changes from internal energy state j to state n in the time interval dt . For the sake of clarity, the substitutions

$$\frac{Z_{\text{inel}}}{Z_{\text{tot}}} K' \rightarrow K \quad (3.6)$$

$$\frac{Z_{\text{inel}}}{Z_{\text{tot}}} R'_{mn} \rightarrow R_{mn} \quad (3.7)$$

are used in the following. In summary, the following kinetic model is postulated:

$$\frac{\partial f_n}{\partial t} + \frac{\partial f_n}{\partial x_i} v_i = \underbrace{S_{\text{FP}} + K \frac{\partial^2 f_n}{\partial v_i \partial v_i}}_I + \underbrace{\sum_j (R_{jn} f_j - R_{nj} f_n)}_{II} \equiv B_n. \quad (3.8)$$

Please note that the above model neglects the influence of an external force for the sake of simplicity. Expression I in Eq. (3.8) describes the impact on the distribution function caused by a change of particle velocities as a result of elastic and inelastic collisions. In particular, the second term of I models the change of the post-collision translational energy as a result of inelastic energy exchange. Expression II in Eq. (3.8) models the impact on the distribution function due to the change of internal energies as a result of inelastic collisions. The relaxation process of internal energy states is modeled by the rate coefficients R_{mn} , which are discussed in more detail in Subch. 3.3.

As mentioned above, the coefficient K is chosen so that the model conserves energy. A detailed derivation of K , for general rate coefficients R_{ij} , is given in App. B.1. A short summary of these results is presented below, for the special case that internal energy relaxation follows a Landau-Teller law (2.51).

To ensure conservation of energy, it must hold:

$$\sum_n \int d\mathbf{c} B_n \left(\frac{1}{2} m \mathbf{v}^2 + e_n \right) = 0. \quad (3.9)$$

Please note that B_n is defined by Eq. (3.8). When assuming a Landau-Teller relaxation of internal energies, one can find:

$$3Km + \frac{1}{\tau_{\text{int}}} (E_{\text{int}}^{\text{eq}} - E_{\text{int}}) = 0. \quad (3.10)$$

This leads to the following expression for the coefficient K :

$$K = -\frac{1}{3m\tau_{\text{int}}} (E_{\text{int}}^{\text{eq}} - E_{\text{int}}). \quad (3.11)$$

As described above, K modifies the diffusion coefficient D of the FP operator, resulting in an adjustment of translational velocities.

In App. B it is shown that the model (3.8) conserves mass and momentum and the H-Theorem is proven.

The coefficient K may become positive or negative, depending on whether energy is transferred in or out of translational modes. However, in order to be able to interpret the kinetic FP method in a physically meaningful way, all calculated particle velocities must be real numbers. Therefore the diffusion coefficient $\tilde{D} = \sqrt{D^2 + 2K}$ must not become a imaginary number. This leads to the following condition:

$$K > -D^2/2, \quad (3.12)$$

that must hold. For arbitrary coefficients D and K , Eq. (3.12) is difficult to prove. However, when considering the cubic model, which is used in this thesis, the diffusion coefficient (2.57) is known and Eq. (3.12) can be evaluated in more detail:

$$\frac{d_{\text{int}} k_B T}{6m\tau_{\text{int}}} < \frac{k_B T}{\tau m}. \quad (3.13)$$

Here it was used that Eq. (3.11) becomes minimal for $E_{\text{int}} = 0$. Equation (3.13) leads to the following condition for the internal relaxation time τ_{int} :

$$\tau_{\text{int}} > \frac{d_{\text{int}}}{6} \tau. \quad (3.14)$$

This condition is easy to fulfill if the condition $\tau_{\text{int}} \gg \tau$ holds. This is usually the case because the relaxation of internal energy to equilibrium, which happens on a timescale τ_{int} , appears to be a much slower process than the relaxation of particle velocities to equilibrium, which happens on a timescale τ .

3.2 Stochastic equations of motion

Similar to the kinetic FP method that is described in Subch. 2.3.2, Eq. (3.8) can be translated into a system of stochastic processes. Therefore, it is defined:

$$\tilde{S}_{\text{FP}}(f_n) \equiv S_{\text{FP}}(f_n) + K \frac{\partial^2 f_n}{\partial c_i \partial c_i}. \quad (3.15)$$

Hence, Eq. (3.8) can be written as:

$$\frac{\partial f_n}{\partial t} + \frac{\partial f_n}{\partial x_i} v_i = \tilde{S}_{\text{FP}}(f_n) + \sum_j (R_{jn} f_j - R_{nj} f_n). \quad (3.16)$$

For further derivations, it is assumed that the evolution of translational velocities and internal energies can be modeled as independent stochastic processes. As a result, it can be written:

$$f_n(\mathbf{x}, \mathbf{v}, t) = f(\mathbf{x}, \mathbf{v}, t) \cdot g_n(\mathbf{x}, t), \quad (3.17)$$

with distribution functions $f(\mathbf{x}, \mathbf{v}, t)$ and $g_n(\mathbf{x}, t)$. The function $f(\mathbf{x}, \mathbf{v}, t)$ describes the number of particles that can be found in a volume element $d\mathbf{x}$ with velocities in a small range $d\mathbf{v}$, while $g_n(\mathbf{x}, t)$ describes the fraction of particles that are in energy state n . Note that $f(\mathbf{x}, \mathbf{v}, t)$ does not depend on internal energy levels, while $g_n(\mathbf{x}, t)$ is independent of the particle velocities. The validity of this assumption is discussed in Subch. 3.4.1. When inserting Eq. (3.17) in Eq. (3.16) one can find:

$$\frac{1}{f} \left(\frac{\partial f}{\partial t} + \frac{\partial f}{\partial x_i} v_i - \tilde{S}_{\text{FP}}(f) \right) = \frac{1}{g_n} \left(\sum_j (R_{jn} g_j - R_{nj} g_n) - \frac{\partial g_n}{\partial t} - \frac{\partial g_n}{\partial x_i} v_i \right). \quad (3.18)$$

Equation (3.18) must be satisfied for arbitrary distribution functions f and g_n . Thus, the left and right side of the equation must yield the same constant value. In thermal equilibrium f becomes a local Maxwell distribution and the left side of Eq. (3.18) vanishes, determining the constant to zero. Therefore, Eq. (3.18) can be separated:

$$\frac{df}{dt} = \frac{\partial f}{\partial t} + \frac{\partial f}{\partial x_i} v_i = \tilde{S}_{\text{FP}}(f), \quad (3.19)$$

$$\frac{dg_n}{dt} = \frac{\partial g_n}{\partial t} + \frac{\partial g_n}{\partial x_i} v_i = \sum_j (R_{jn} g_j - R_{nj} g_n). \quad (3.20)$$

Equation (3.19) is a FP equation in velocity space with diffusion coefficient $\tilde{D} = \sqrt{D^2 + 2K}$. As described in Subch. 2.3.2, the associated stochastic process may be modeled by the increment $d\mathbf{W}$ of a Wiener process:

$$d\mathbf{X} = \mathbf{V} dt, \quad (3.21)$$

$$d\mathbf{V} = \mathbf{A} dt + \tilde{D} d\mathbf{W}. \quad (3.22)$$

Equation (2.64) and Eq. (2.65) are applied in order to solve the system (3.21) and (3.22). Equation (3.20) describes the change of internal energy states of a moving particle. The term on the right side of Eq. (3.20) is a master equation. The associated stochastic process is a jump process [44] and may be modeled by the increment of a poisson process [83]. This jump process will be discussed in more detail in Subch. 3.5.

3.3 Models for rate coefficients

This subchapter constructs three different models for the rate coefficients of the master equation (3.20). The focus is on providing models that can be used to describe hypersonic flows. This means that the models must handle both continuous and discrete internal energy structures to describe both rotational and vibrational energy modes.

Two of the models are constructed to describe a relaxation of the mean internal energies according to the Landau-Teller law. This is a reasonable requirement since for many applications it is sufficient to model the average internal energies while not requiring detailed knowledge of the microscopic internal energy structure.

A third model, on the other hand, is constructed to also correctly reproduce the relaxation of the microscopic internal energy structure. This model is more complex than those described above, but also allows the calculation of test cases in which the internal energy structure plays an important role.

3.3.1 DLT model

The DLT (discrete energy structure, macroscopic Landau-Teller relaxation) model describes the internal energy structure of a molecule as a set of discrete levels. The model is constructed to reproduce a Landau-Teller relaxation of internal energies and an equilibrium state as described by the quantized harmonic oscillator model [141]. In the following, first basic properties of the quantized harmonic oscillator model are summarized. Subsequently, the rate coefficients for the DLT model are constructed.

For the quantized harmonic oscillator model, the distance $\epsilon = k_B \theta$ between two adjacent energy levels is constant and is expressed by a species-specific characteristic temperature θ . Hence, the energy of the i -th internal level is given by $e_i = \epsilon i$. It should be noted, that e_i is measured relative to the ground state so that the zero-point energy can be neglected. Assuming a Boltzmann distribution for the population of internal energy states in equilibrium, the mean equilibrium energy $E_{\text{int}}^{\text{eq}}$ is given by:

$$E_{\text{int}}^{\text{eq}} = \frac{1}{Q} \sum_i e_i \exp(-\beta e_i) = \frac{\epsilon}{Q} \frac{\exp(-\beta \epsilon)}{(\exp(-\beta \epsilon) - 1)^2}, \quad (3.23)$$

with the inverse temperature $\beta = 1/(k_B T)$. The partition function Q is a normalization factor and defined by:

$$Q \equiv \sum_i \exp(-\beta e_i) = \frac{1}{1 - \exp(-\beta \epsilon)}. \quad (3.24)$$

The equipartition theorem yields the number of internal degrees of freedom d_{int} :

$$d_{\text{int}} = \frac{2\theta/T}{\exp(\theta/T) - 1} \xrightarrow{T \rightarrow \infty} 2. \quad (3.25)$$

Hence, the number of internal degrees of freedom depends on the temperature. In the limiting case for $T \rightarrow \infty$, d_{int} approaches 2.

The rate coefficients for the DLT model are chosen as:

$$R_{ij} \equiv R_j \equiv \frac{1}{\tau_{\text{int}} \cdot Q} \exp(-\beta \epsilon_j). \quad (3.26)$$

The internal relaxation time $\tau_{\text{int}} = Z_{\text{int}}/\nu_{\text{VHS}}$ is calculated based on the equilibrium mean collision frequency ν_{VHS} for particles interacting according to the VHS collision model [10]:

$$\nu_{\text{VHS}} = 4d_{\text{ref}}^2 n \sqrt{\frac{\pi k_B T_{\text{ref}}}{m}} \left(\frac{T}{T_{\text{ref}}}\right)^{1-\omega}. \quad (3.27)$$

The rate coefficients (3.26) fulfill the principle of detailed balance, which leads to a correct prediction of the equilibrium distribution function. For a homogeneous gas in thermal equilibrium, Eq. (3.26) leads to a Landau-Teller relaxation of the mean internal energy $E_{\text{int}} = \sum_i e_i g_i$ to the equilibrium energy (3.23) of a quantized harmonic oscillator:

$$\frac{dE_{\text{int}}}{dt} = \frac{d}{dt} \sum_i e_i g_i = \sum_i e_i \sum_j (R_{ji} g_j - R_{ij} g_i) \quad (3.28)$$

$$= \frac{1}{\tau_{\text{int}}} \sum_i e_i \sum_j \left(\frac{1}{Q} \exp(-\beta \epsilon_i) g_j - \frac{1}{Q} \exp(-\beta \epsilon_j) g_i \right) \quad (3.29)$$

$$= \frac{1}{\tau_{\text{int}}} \sum_i e_i \left(\frac{1}{Q} \exp(-\beta \epsilon_i) - g_i \right) \quad (3.30)$$

$$= \frac{1}{\tau_{\text{int}}} (E_{\text{int}}^{\text{eq}} - E_{\text{int}}). \quad (3.31)$$

When combining Eq. (3.26) and Eq. (3.11) with Eq. (3.19) and Eq. (3.20) one can find the following evolution equations for the distribution functions f and g :

$$\frac{\partial f}{\partial t} + \frac{\partial f}{\partial x_i} v_i = S_{\text{FP}}(f) + \frac{1}{3m\tau_{\text{int}}} (E_{\text{int}}^{\text{eq}} - E_{\text{int}}) \frac{\partial^2 f}{\partial v_i \partial v_i}, \quad (3.32)$$

$$\frac{\partial g_n}{\partial t} + \frac{\partial g_n}{\partial x_i} v_i = \frac{1}{\tau_{\text{int}} \cdot Q} \sum_j \left[\exp(-\beta \epsilon_n) g_j - \exp(-\beta \epsilon_j) g_n \right]. \quad (3.33)$$

The reader should, however, note, that Eq. (3.32) and Eq. (3.33) are not solved directly. Instead stochastic processes are modeled, as described in Subch. 3.2.

3.3.2 CLT model

The CLT (continuous energy structure, macroscopic Landau-Teller relaxation) model describes the internal energy structure of a molecule as a continuous scalar. It is constructed to reproduce the Landau-Teller law and a continuous Boltzmann distribution of internal energies in equilibrium.

Please note, that for the following derivations the discrete distribution functions $f_n(\mathbf{r}, \mathbf{v}, t)$ and g_n are replaced by continuous distributions $f(\mathbf{r}, \mathbf{v}, e, t)$ and $g(e)$, where e denotes the continuous internal energy of a molecule.

Before deriving the rate coefficients of the model, the reader should consider that a continuous Boltzmann distribution for the population of internal energy states at

equilibrium yields the following average equilibrium energy:

$$E_{\text{int}}^{\text{eq}} = \int_0^{\infty} e \beta \exp(-\beta e) de = \frac{1}{\beta}. \quad (3.34)$$

The equipartition theorem, yields the number of internal degrees of freedom d_{int} :

$$d_{\text{int}} = 2. \quad (3.35)$$

Therefore, the Boltzmann distribution can describe, for example, fully excited rotational energies of molecules with linear structure. The same can be expected from the CLT model, which, as will become clear, is based on the Boltzmann distribution at equilibrium.

The rate coefficients of the CLT model are chosen as:

$$R(e, e') \equiv R(e') \equiv \frac{\beta}{\tau_{\text{int}}} \exp(-\beta e'). \quad (3.36)$$

The rate coefficients obey the principle of detailed balance, leading to a Boltzmann distribution in equilibrium. Similar to the DLT model, the rate coefficients (3.36) are designed to reproduce a Landau-Teller relaxation of the mean internal energy to the equilibrium energy (3.34).

$$\frac{dE_{\text{int}}}{dt} = \frac{d}{dt} \int_0^{\infty} e \cdot g(e) de \quad (3.37)$$

$$= \iint_0^{\infty} e (R(e)g(e') - R(e')g(e)) de' de \quad (3.38)$$

$$= \frac{1}{\tau_{\text{int}}} (E_{\text{int}}^{\text{eq}} - E_{\text{int}}). \quad (3.39)$$

As in the discrete case, one can find evolution equations for the distribution functions f and g :

$$\frac{\partial f}{\partial t} + \frac{\partial f}{\partial x_i} v_i = S_{\text{FP}}(f) + \frac{1}{3m\tau_{\text{int}}} (E_{\text{int}}^{\text{eq}} - E_{\text{int}}) \frac{\partial^2 f}{\partial v_i \partial v_i}, \quad (3.40)$$

$$\frac{\partial g_n}{\partial t} + \frac{\partial g_n}{\partial x_i} v_i = \frac{\beta}{\tau_{\text{int}}} \int \left[\exp(-\beta e) g(e') - \exp(-\beta e') g(e) \right] de'. \quad (3.41)$$

Again, the reader should note, that Eq. (3.40) and Eq. (3.41) are not solved directly. Instead stochastic processes are modeled, as described in Subch. 3.2.

3.3.3 DLB model

The DLT and CLT model are designed to reproduce the relaxation of the mean internal energy according to the Landau-Teller law. The relaxation behavior of the internal energy distribution function is not considered. Only a correct prediction of the equilibrium distribution is guaranteed, since both models fulfill the principle of detailed balance. Therefore, the models cannot be expected to provide a correct prediction for the population of internal energy states far from internal equilibrium.

However, when assuming a discrete energy structure and that the relaxation of internal energy states is mainly driven by inelastic collisions, the rate coefficients can

be directly calculated based on microscopic collision cross sections σ^{ij} [116]:

$$R_{ij} = n \int_{c_{r,\min}}^{\infty} \sigma^{ij} f(c_r) c_r dc_r. \quad (3.42)$$

Here $c_{r,\min}$ means the smallest relative collision velocity for which the transition $i \rightarrow j$ is energetically possible:

$$c_{r,\min} = \sqrt{\frac{2(e_j - e_i)}{m}}, \quad (3.43)$$

and σ^{ij} denotes the „cross section“ for an inelastic particle collision, whereby one collision partner changes its internal energy state from state i to state j . The function $f(c_r)$ denotes the distribution function of the relative collision velocities. Assuming thermal equilibrium, it can be approximated by [10]:

$$f(c_r) \approx 4\pi \left(\frac{m}{2\pi k_B T} \right)^{3/2} c_r^2 \exp\left(-\frac{mc_r^2}{2k_B T}\right). \quad (3.44)$$

Since the relaxation time of internal energy states is in general larger than the relaxation time of the velocity distribution function, the assumption of thermal equilibrium is justified for many relevant cases. When rate coefficients are evaluated corresponding to Eq. (3.42) and the assumption of thermal equilibrium (3.44) applies, the master equation is feasible to describe the microscopic distribution of internal energies states, even far from internal equilibrium.

In general, Eq. (3.42) can be evaluated for various microscopic processes. However, the DLB (**d**iscrete energy structure, microscopic **L**arsen-**B**orgnakke relaxation) model is constructed based on DSMC models for inelastic collisions processes. As a results, the DLB model is consistent with the corresponding DSMC models, even when considering the distribution of internal energy states. In particular the DLB model is constructed based on the quantized Larsen-Borgnakke model [6] in combination with the particle selection scheme presented by Zhang et al. [147].

It should be note that the model could also be constructed to reproduce more complex and physical DSMC models on a microscopic scale. However, the DLB model serves as a simple example to demonstrate the capability of the master equation approach. The following subchapter describes the evaluation of Eq. (3.42) for the DLB model in more detail.

With σ_T referring to the total collision cross section for a particle collision, it can be written:

$$\sigma^{ij} = \sigma_T \cdot P_{ij}. \quad (3.45)$$

For particles interacting according to the VHS collision model, the total cross section may be written as [10]:

$$\sigma_T(\mathbf{c}_r) = \sigma_{\text{ref}} \left(\frac{c_{r,\text{ref}}}{|\mathbf{c}_r|} \right)^{2\omega-1}, \quad (3.46)$$

where \mathbf{c}_r means the relative collision velocity and σ_{ref} and $c_{r,\text{ref}}$ are reference values depending on the species of the colliding particles. The quantity P_{ij} denotes the probability that the particle collision is inelastic and one collision partner changes its internal energy state i to state j . This probability depends on the underlying DSMC model for the inelastic collision process. For the quantized Larsen-Borgnakke model

[10] it can be found that:

$$P_{ij}(\mathbf{c}_r) = \frac{1}{Q_{\text{nom}}} \left(1 - \frac{e_j}{\frac{1}{2}m|\mathbf{c}_r|^2 + e_i} \right)^{\frac{3}{2}-\omega} \cdot P_{\text{inel}}. \quad (3.47)$$

Here Q_{nom} is a scaling factor chosen so that $\sum_j P_{ij} = P_{\text{inel}}$, where P_{inel} is the probability that one collision partner performs an arbitrary change of its internal energy state during the collision. An expression for P_{inel} can be extracted from the particle selection scheme, which is described in more detail in App. A.1¹.

$$P_{\text{inel}} = \frac{1}{2} (1 - P_{\text{rot},1}) (1 - P_{\text{rot},2}) (P_{\text{vib},1} + (1 - P_{\text{vib},1}) P_{\text{vib},2}). \quad (3.48)$$

When applying Eq. (3.44) and Eq. (3.43), Eq. (3.42) may be evaluated. For $j > i$ it can be found:

$$R_{ij} = \nu_{\text{VHS}}(T, n) \cdot P_{\text{inel}} \cdot \zeta(i, j, T/\theta). \quad (3.49)$$

Here $\nu_{\text{VHS}}(T, n)$ means the collision frequency of a VHS gas in equilibrium [10] and $\zeta(i, j, T/\theta)$ denotes a function which depends only on the energy states i, j and the temperature ratio T/θ :

$$\zeta(i, j, T/\theta) \equiv \frac{1}{\Gamma(\frac{5}{2}-\omega)} \int_{\frac{\theta}{T}(i-j)}^{\infty} \exp(-x) x^{\frac{3}{2}-\omega} \left(1 - \frac{j}{\frac{T}{\theta}x + i} \right)^{\frac{3}{2}-\omega} \frac{1}{Q_{\text{nom}}} dx, \quad (3.50)$$

Here Γ denotes the gamma function. The reverse rate coefficients can be calculated when applying the principle of detailed balance:

$$R_{ji} = R_{ij} \cdot \exp(-\beta(e_i - e_j)) = \nu_{\text{VHS}}(T, n) \cdot P_{\text{inel}} \cdot \zeta(i, j, T/\theta) \cdot \exp(-\beta(e_i - e_j)). \quad (3.51)$$

The evaluation of Eq. (3.50) is quite time consuming. Thus, to reduce the computational time, a lookup table of $\zeta(i, j, T/\theta)$ is calculated. To estimate the number of

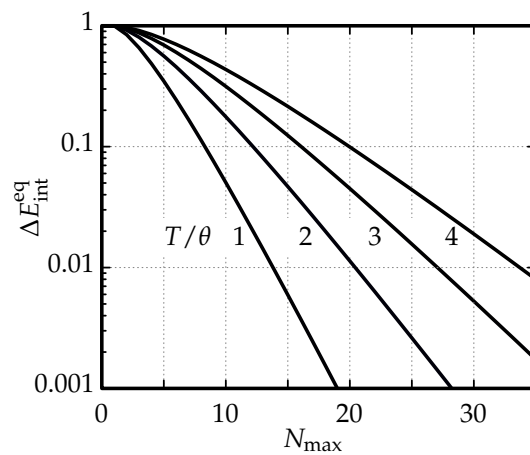


FIGURE 3.1: Relative failure $\Delta E_{\text{int}}^{\text{eq}}$ for different numbers of included energy states and temperatures.

¹Please note that in App. A.1 the scheme for the case of two species α and β is described. For the calculation of Eq. (3.48), however, it was assumed that $\alpha = \beta$.

energy states N_{\max} that should be included into the lookup table, the relative truncation error $\Delta E_{\text{int}}^{\text{eq}}(N_{\max})$, defined by:

$$\Delta E_{\text{int}}^{\text{eq}}(N_{\max}) \equiv \frac{E_{\text{int}}^{\text{eq}} - E_{\text{int}}^{\text{eq}}(N_{\max})}{E_{\text{int}}^{\text{eq}}}, \quad (3.52)$$

is investigated. The total internal equilibrium energy $E_{\text{int}}^{\text{eq}}$ is given by Eq. (3.23) and the expression $E_{\text{int}}^{\text{eq}}(N_{\max})$ is defined by:

$$E_{\text{int}}^{\text{eq}}(N_{\max}) \equiv \frac{1}{Q} \sum_{i=0}^{N_{\max}} e_i \exp(-\beta e_i). \quad (3.53)$$

Figure 3.1 shows the variation of $\Delta E_{\text{int}}^{\text{eq}}(N_{\max})$ for different numbers of included energy states and translational temperatures. The vibrational temperature was set to $\theta = 3000$ K, which is a representative value for many diatomic species. The quantity $\Delta E_{\text{int}}^{\text{eq}}(N_{\max})$ remains smaller than 2% for $T < 4\theta = 12000$ K when including $N_{\max} = 30$ energy states. This is deemed to be sufficient for the test cases shown in this thesis.

The temperature variation of $\zeta(m, l, T/\theta)$ is discretized in 100 equal bins between 0 and 7θ .

3.4 Discussion of the model

This subchapter evaluates the performance of the kinetic model (Eq. (3.8)) based on theoretical considerations. The subchapter is structured into two parts. Subchapter 3.4.1 discusses physical limitations of the model that are induced by the splitting of the distribution function as described by Eq. (3.17). Subchapter 3.4.2 tries to evenuate the performance of the model by investigating production terms.

3.4.1 Separation of the distribution function

A strong assumption made when deriving the stochastic equations of motion in Subch. 3.2 is the separation of the distribution function, as described by Eq. (3.17). This assumption leads to a decoupling of the velocity distribution function, f , and the distribution of internal energies, g . As a result, both distribution functions are only indirectly linked. In particular, the translational velocities are affected only by the coefficient K , which depends on the internal temperature, and internal energies are only affected by the rate coefficients R_{ij} , depending on the translational temperature. Physically this means, that each excited internal energy state features the same velocity distribution. Of course, in general, this assumption is not true for the Boltzmann equation. Even for near continuum approximations of the Boltzmann equation, for example in the context of McCormacks 17-moment approximation [112, 97], the distribution function cannot be clearly separated as given by Eq. (3.17).

On the other hand, when introducing the polyatomic Boltzmann equation, Chang et al. [29] argued, that the distribution function can be divided in two separate parts: One part which describes the particle velocities and a second part which describes the internal energies of the particles. This separation is valid, if the energy exchange between internal and translational modes is slow. This is usually the case, if internal relaxation times are large. Based on this argumentation, the separation as stated in Eq. (3.17) is justified for the special case that internal relaxation times are large.

3.4.2 Moment relaxation

The performance of the model is assessed by comparing the transfer equations for relevant moments [136] induced by the kinetic model (Eq. (3.8)), with those of more established models, e. g. McCormacks 17-moment approximation [112]. Note that McCormack's (Eq. (3.8)) model is a moment model, similar to the Navier-Stokes equations, that describes a polyatomic gas in the Navier-Stokes limit. Hence, this comparison allows assessing the performance of the kinetic model (Eq. (3.8)) for flows with small Knudsen numbers.

Since moment equations are driven by production terms, it is not necessary to compare the full set of moment equations. Instead, only corresponding production terms are compared. In particular, production terms of translational energy $P_{\Psi}(1/2c_i c_i)$, shear stresses $P_{\Psi}(c_{<i} c_{>})$, translational heat fluxes $P_{\Psi}(c_i c_j c_j)$ and internal heat fluxes $P_{\Psi}(c_i e_n)$ are compared with those of McCormacks 17-moment approximation [112]. For the derivations it is assumed, that the distribution function can be separated as described by Eq. (3.17) and that the quantity K is chosen, so that the model (Eq. (3.8)) leads to a Landau-Teller relaxation of internal energies. Since the production terms depend also on the underlying FP operator, the cubic FP model [53] is used here.

When applying the operator from Eq. (3.8) one obtains for the translational energy:

$$P_{B_n} (1/2c_i c_i) = -n \underbrace{\frac{d_{\text{int}}/2k_B}{\tau_{\text{int}}}}_{k_1} (T_{\text{int}}^{\text{eq}} - T_{\text{int}}), \quad (3.54)$$

while McCormacks 17-moment approximation leads to [112]:

$$P_{17\text{-moment}} (1/2c_i c_i) = -\underbrace{2k_B n^2 J_1}_{c_1} (T - T_{\text{int}}). \quad (3.55)$$

Here T denotes the translational temperature, T_{int} the temperature of the internal mode, $T_{\text{int}}^{\text{eq}}$ the internal equilibrium temperature and J_1 a collision integral [112] that depends on the underlying molecular collision model. Identifying that the internal equilibrium temperature $T_{\text{int}}^{\text{eq}}$ in Eq. (3.54) represents the translational temperature T in Eq. (3.55), both production terms display a similar structure. The only differences are coefficients c_1 and k_1 , which describe the rate of relaxation of internal temperatures to equilibrium. While the model in this thesis is formulated to reproduce the Landau-Teller law (2.51) with relaxation time τ_{int} , McCormacks 17-moment approximation is formulated for a general molecular collision potential. However, it is straight-forward to match both coefficients, by adjusting the internal relaxation time τ_{int} in Eq. (3.54).

For the shear stresses, one obtains:

$$P_{B_n} (c_{<i} c_{>}) = P_{\text{FP}} (c_{<i} c_{>}) \stackrel{\text{cubic model}}{=} - \underbrace{\frac{p}{\mu}}_{k_2} \sigma_{ij}. \quad (3.56)$$

Here $P_{\text{FP}} (c_{<i} c_{>})$ denotes the production term of the FP operator that is applied. In case of Gorji's cubic model, this production term can be expressed by the shear stresses. For McCormacks 17-moment approximation one can find:

$$P_{17\text{-moment}} (c_{<i} c_{>}) = \underbrace{\frac{8}{5} n J_4}_{c_2} \sigma_{ij}. \quad (3.57)$$

The collision integral J_4 [112] depends on the underlying molecular collision model. Again, both production terms feature a similar structure, the only differences are relaxation constants k_2 and c_2 . While the production term for the cubic model is adjusted so that the model reproduces a given viscosity μ in the Navier-Stokes limit, McCormacks 17-moment approximation is formulated for general molecular collision models. As for the translational energy, it is straight-forward to match both coefficients, by adjusting the viscosity μ in Eq. (3.56).

For the translational heat fluxes, one obtains:

$$P_{B_n} (c_i c_j) = P_{\text{FP}} (c_i c_j) \stackrel{\text{cubic model}}{=} P_{17\text{-moment}} (c_i c_j). \quad (3.58)$$

Here $P_{\text{FP}} (c_i c_j)$ denotes the production term of the FP operator that is applied. As described in Subch. 2.3.1, the cubic model exactly matches McCormacks 17-moment production term for heat fluxes.

The production term for internal heat fluxes vanishes for the model in this thesis:

$$P_{B_n}(c_i e_n) = 0. \quad (3.59)$$

In contrast, based on McCormacks 17-moment approximation one obtains:

$$P_{17\text{-moment}}(c_i e_n) = -\frac{2n k_B}{3 c_{\text{int}}} J_6 q_{\text{int},i} + \frac{2n}{3} J_7 q_i. \quad (3.60)$$

Here $q_{\text{int},i} = \sum_n \int d\mathbf{c}_i e_n \mathbf{c}$ denotes the internal heat flux, c_{int} the species specific heat capacity per mass and J_6 and J_7 collision integrals [112]. Hence, the production terms for internal heat fluxes do not display the same structure. This suggests incorrect results of the model (Eq. (3.8)) when considering internal heat fluxes. On the other hand, Gorji et al. [53] argued that transport of internal energies is mainly driven by translational mixing, which is determined by the production terms $P_\Psi(m c_i c_j)$. For this reason, Gorji et al. [53] did not include production terms for internal heat fluxes when constructing the diatomic cubic model. Hence, the model (Eq. (3.8)) makes the same assumption. Whether this simplification has an influence on the prediction of internal energies and temperatures is determined by numerical experiments in Subch. 3.6 of the thesis.

In summary the model (Eq. (3.8)) leads to similar production terms for internal energy, shear stresses and translational heat fluxes, compared to McCormacks 17-moment approximation. This also indicates the same macroscopic moment equation and a correct behavior of the model, at least for flows in the Navier-Stokes limit. Differences appear for the production term of internal heat flux. However, as mentioned above, this deviations might have only little influence on the capability of the model for predicting internal energies and temperatures. In contrast, when predicting heat fluxes that are caused by excited internal energy states, results deviating from the McCormack moment approximation are to be expected.

3.5 Solving stochastic equations of motion

This subchapter discusses stochastic jump processes that are described by the master equation (3.20). Depending on the models that are employed for the rate coefficients of the master equation, different algorithms are developed to calculate the temporal evolution of internal energy states for a FP time step Δt . The algorithms are deduced based on Gillespie's *direct simulation method* [46], which is briefly recalled below.

The *direct simulation method* provides an algorithm to simulate the stochastic jump process underlying a master equation. The algorithm is based on the probability density function $P(\tau, i, j)$, which describes the probability that a particle changes its internal energy state i to state j in the time interval $[\tau, \tau + dt]$. The probability density function $P(\tau, i, j)$ can be written as:

$$P(\tau, i, j) = P_1(\tau, i) \cdot P_2(i, j). \quad (3.61)$$

```

/*  $i_{\text{init}}$  → initial energy state */
/*  $i_{\text{final}}$  → final energy state */
/*  $t_{\text{end}}$  → desired simulation time */
Set  $t = 0$ ;
Set  $i = i_{\text{init}}$ ;
while true do
    Sample a reaction time  $\tau$  from  $P_1(\tau, i)$ ;
     $t = t + \tau$ ;
    if  $t > t_{\text{end}}$  then
        Set  $i_{\text{final}} = i$ ;
        break;
    else
        Sample a new internal energy state  $j$  state from  $P_2(i, j)$ ;
        Set  $i = j$ ;
    end
end

```

Algorithm 1: Gillespie's direct simulation method.

Here $P_1(\tau, i) dt$ denotes the probability that an arbitrary transition from state i takes place in the time interval $[\tau, \tau + dt]$ and $P_2(i, j)$ describes the probability that a specific transition results in the excitation of state j . Gillespie found [46]:

$$P_1(\tau, i) = K_i \cdot \exp(-K_i \tau), \quad (3.62)$$

$$P_2(i, j) = \frac{R_{ij}}{K_i}, \quad (3.63)$$

with the definition of $K_i \equiv \sum_j R_{ij}$.

In Alg. 1, the general procedure for Gillespie's direct simulation method is summarized. First, a random reaction time is generated from the distribution function in Eq. (3.62). Afterwards, a new particle state is generated from the distribution (3.63). The calculation is repeated alternately, until the desired simulation time is reached.

3.5.1 DLT model

In this subchapter a kinetic simulation algorithm for the DLT model is constructed. When applying Eq. (3.26), the accumulated rates K_i can be evaluated:

$$K_i = \frac{1}{\tau_{\text{int}} Q} \sum_j \exp(-\beta \epsilon_j) = \frac{1}{\tau_{\text{int}}}. \quad (3.64)$$

For the distribution function $P_1(\tau, i)$ follows:

$$P_1(\tau, i) = P_1(\tau) = \frac{1}{\tau_{\text{int}}} \exp(-\tau / \tau_{\text{int}}), \quad (3.65)$$

while the distribution function $P_2(i, j)$ becomes:

$$P_2(i, j) = P_2(j) = \frac{1}{Q} \exp(-\beta \epsilon_j). \quad (3.66)$$

```

/* Run the following algorithm for each particle */
Calculate a uniformly distributed random number  $\mathbb{R}_1 \in [0, 1]$ ;
if  $\mathbb{R}_1 > P(\Delta t)$ , then
  | Energy state remains unchanged;
else
  | Calculate a uniformly distributed random number  $\mathbb{R}_2 \in [0, 1]$ ;
  | Set the new internal energy state to  $j = -\lfloor \ln(\mathbb{R}_2) \rfloor / (\beta \cdot \epsilon)$ ;
end

```

Algorithm 2: Kinetic simulation algorithm for the DLT model. The brackets $\lfloor \bullet \rfloor$ denote the floor function.

The distribution function $P_2(i, j)$ has the same structure as the equilibrium distribution function of a quantized harmonic oscillator [10]. Hence, sampling a new energy state from $P_2(i, j)$ can be performed similar to the calculation of an equilibrium state for a quantized harmonic oscillator [10].

Since the probability distributions P_1 and P_2 do not depend on the initial transition state, there is no need to perform the entire direct simulation method. Rather, it is sufficient to test if only one transition takes place in the time interval Δt . Therefore, let $P(\Delta t)$ denote the probability that an arbitrary transition takes place during the time step Δt . It can be found:

$$P(\Delta t) = \int_0^{\Delta t} P_1(\tau) d\tau = 1 - \exp(-\Delta t / \tau_{\text{int}}). \quad (3.67)$$

As a result, Alg. 2 to update internal energies for each particle over a time step Δt can be constructed.

3.5.2 CLT model

This subchapter constructs a kinetic simulation algorithm for the CLT model. The algorithm can be constructed similar to the algorithm for the DLT model, only the discrete energy states i and j are replaced by the continuous energies e and e' . For the accumulated rates $R(e)$ it can be found:

$$R(e) = \int_0^{\infty} \frac{\beta}{\tau_{\text{int}}} \exp(-\beta x) dx = \frac{1}{\tau_{\text{int}}}. \quad (3.68)$$

```

/* Run the following algorithm for each particle */
Calculate a uniformly distributed random number  $\mathbb{R}_1 \in [0, 1]$ ;
if  $\mathbb{R}_1 > P(\Delta t)$ , then
  | Energy state remains unchanged;
else
  | Calculate a uniformly distributed random number  $\mathbb{R}_2 \in [0, 1]$ ;
  | Set the new internal energy to  $e' = -\ln(\mathbb{R}_2) / \beta$ .
end

```

Algorithm 3: Kinetic simulation algorithm for the CLT model.

For the probability distribution $P_2(e, e')$ follows:

$$P_2(e, e') = P_2(e') = \beta \cdot \exp(-\beta e'). \quad (3.69)$$

To sample a final transition state from $P_2(e, e')$ a simple inversion method is used. Expression (3.67) also applies to the CLT model. In summary, Alg. 3 to update energy states for each particle can be constructed.

3.5.3 DLB model

This subchapter constructs a kinetic simulation algorithm for the DLB model. The rate coefficients (3.49) for the DLB model depend on the initial and the final transition state. Therefore, the entire direct simulation method must be applied to calculate the time evolution of internal energy states. For the probability distributions (3.62) and (3.63) it can be found that:

$$P_1(\tau, i) = \sum_j R_{ij}(T) \cdot \exp\left(-\sum_j R_{ij}(T) \tau\right), \quad (3.70)$$

$$P_2(i, j) = \frac{R_{ij}(T)}{\sum_j R_{ij}(T)}. \quad (3.71)$$

```

/* Run the following algorithm for each particle */
/* i_init → initial energy state */
/* i_final → final energy state */
Set t = 0;
Set i = i_init;
while true do
  /* Sample new reaction time */
  Calculate a uniformly distributed random number  $\mathbb{R}_1 \in [0, 1]$ ;
  Set  $t = t - \ln(\mathbb{R}_1) / \sum_j R_{ij}$ ;
  if  $t > \Delta t$ , then
    Set  $i_{\text{final}} = i$ ;
    break;
  else
    /* Calculate new energy state by an acceptance-rejection procedure */
    while true do
      Calculate uniformly distributed random numbers  $\mathbb{R}_2 \in [0, 1]$  and
       $\mathbb{R}_3 \in [0, 1]$ ;
      Set  $j = \lfloor N_{\text{max}} \cdot \mathbb{R}_2 \rfloor$ ;
      if  $P_2(i, j) < \mathbb{R}_3$ , then
        Set  $i = j$ ;
        break;
      end
    end
  end
end
end
end

```

Algorithm 4: Kinetic simulation algorithm for the DLB model.

A simple inversion method may be applied to sample a reaction time from the distribution function (3.70). A new internal energy state is sampled from (3.71) through an acceptance-rejection procedure [45]. In summary, Alg. 4 describes the scheme for updating internal energy states for the DLB model. Recall, that N_{\max} denotes the number of energy states, included in the lookup table.

The number of iterations required to complete the algorithm strongly depends on the time step size and the size of the accumulated rates $1/K_i = 1/\sum_j R_{ij}$. Since K_i depend on the initial state i , it is in general a complex task to compute this number. The computational effort for the algorithm is discussed in more detail in Subch. 3.7

3.6 Test cases

The validity of the method has so far only been discussed in the Subch. 3.4 on the basis of theoretical considerations. To expand on these considerations, the following subchapter examines the applicability of the method using numerical test cases. Particular attention is paid to test cases that are representative for the flow phenomena in rarefied hypersonic environment.

It should be noted that this subchapter does not fully examine the validity range of the method. As described in Subch. 2.3.5, this involves a lot of work and is beyond the scope of this thesis. Instead, the applicability of the method is demonstrated for a few, but important test cases.

Please note, that all calculation are performed with the cubic FP model that is described in Subch. 2.3.

All simulations are performed for a molecular nitrogen model with VHS collision parameters as listed in App. F in Tab. F.5 and a characteristic vibrational temperature as listed in Tab. F.2. If not stated otherwise, the internal relaxation numbers listed in Tab. F.5 are used. In order to calculate the viscosity, which is required to evaluate the FP relaxation time τ , the VHS power law (2.49) is used. As reference viscosity

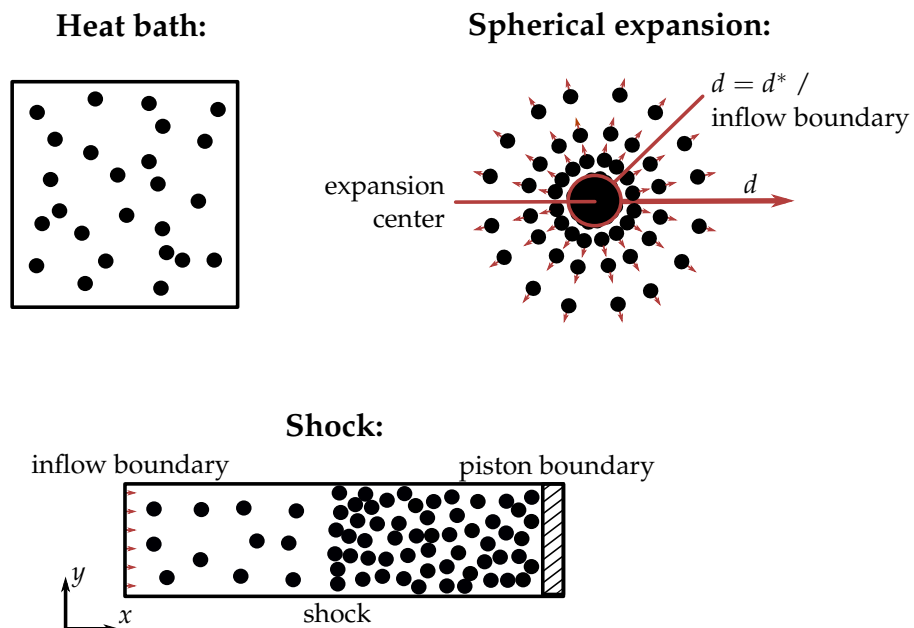


FIGURE 3.2: Illustration of different test cases. Left upper: Heat bath test case as described in Subch. 3.6.1. Right upper: Spherical expansion flow as discussed in Subch. 3.6.2. Bottom: Flow past a shock wave as described in Subch. 3.6.3.

$\mu_{\text{ref}} = 1.656 \cdot 10^{-5} \text{Pa s}$ is applied, which is consistent with the employed VHS collision parameters [10]. Relaxation of rotational energies is modeled by the CLT model and the vibrational relaxation process by the DLT as well as the DLB model.

For reference, DSMC simulations are performed. Rotational relaxation is described by the continuous Larsen-Borgnakke model [14], while the vibrational relaxation process is modeled by the quantized Larsen-Borgnakke model [6]. The scheme presented by Zhang et al. [147] (see App. A) is applied in order to select particle pairs for inelastic collisions. To avoid different results due to numerical discretization, the same spatial and temporal discretization is used for DSMC and kinetic FP simulations, if not stated otherwise.

In order to perform the simulations the stochastic parallel rarefied-gas time-accurate analyzer (SPARTA) is applied [39]. SPARTA is an open source DSMC solver, developed by the Sandia National Laboratories. The author extended the SPARTA code by implementing the kinetic FP methods presented in this chapter and by the selection scheme of Zhang et al. [147].

Figure 3.2 illustrates test cases that are investigated in Subch. 3.6.1 to Subch. 3.6.3.

3.6.1 Heat bath

In order to verify that the proposed models reproduce a correct relaxation behavior, relaxation of internal energies is studied. Therefore, internal energies are initially set according to an internal temperature which is not in equilibrium with the translational temperature. Afterwards, relaxation to equilibrium is studied.

Simulations are performed for a homogeneous, isothermal heat bath (Fig. 3.2). The simulation boundaries are chosen to be periodic in all three space dimensions in order to avoid the influence of particle-wall interactions. At the beginning of each simulation, rotational and vibrational particle energies are set according to a Boltzmann distribution with $T_{\text{rot},0} = T_{\text{vib},0} = 3000 \text{ K}$. The particle velocities are set according to a Maxwell distribution with temperature $T_0 = 9000 \text{ K}$. During the simulation, the particle velocities are scaled in each time step to achieve a constant translational temperature. For the sake of simplicity, the same relaxation numbers $Z_{\text{rot}} = Z_{\text{vib}} = 0.2$ are used for rotational and vibrational relaxation. For each simulation, a single grid cell with 4000 particles is simulated. Since the relaxation process is an unsteady phenomenon, no time averaging can be carried out. Instead, the results of 100 different simulation runs are averaged in order to reduce the statistical scatter of the results. The left side of Fig. 3.3 shows the relaxation process of the rotational temperature towards equilibrium. A good agreement between FP and DSMC results can be observed with both schemes and the rotational temperature reaches the correct equilibrium temperature $T_0 = 9000 \text{ K}$.

The right side of Fig. 3.3 shows five different distribution functions of rotational energies along the relaxation process. The times at which the distribution functions are calculated are marked in the left plot of Fig. 3.3. The equilibrium distribution f_4 obeys a Boltzmann distribution and is correctly predicted by the FP method. In contrast, the non-equilibrium distributions f_1 , f_2 and f_3 can not be described by a Boltzmann distribution. For this case, FP results deviate from DSMC results. This can be expected, since the CLT model is not constructed to reproduce a correct non-equilibrium distribution function. In particular, the CLT model predicts a larger population of high energy states than the DSMC method. This effect may be explained as follows. The Larsen-Borgnakke model distributes new internal energy states due to inelastic particle collisions according to an equilibrium distribution function, with the restriction to conserve the total collision energy. With the rate coefficients (3.36),

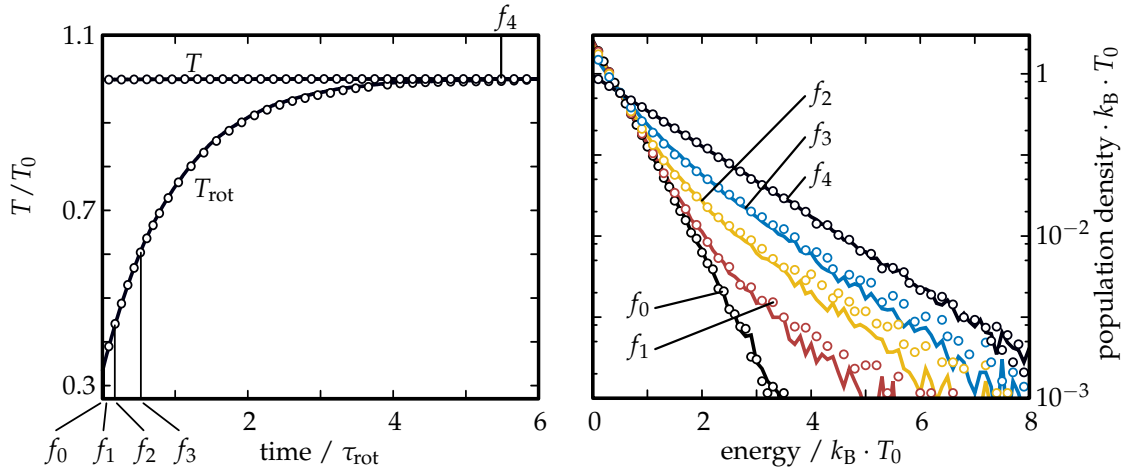


FIGURE 3.3: Left: Relaxation of rotational temperature. Right: Relaxation of rotational energy distribution functions. Note that the unit of the distribution function is the population density, which is defined as $dN/dE/N$, where dN denotes the number of particles that can be found in a small energy interval dE and N is the total number of particles in the simulation. Lines: DSMC results. Symbols: FP/CLT results. Please note that some of the results have been colored to better distinguish one from another.

the FP model also distributes new internal energies according to an equilibrium distribution function. However, since no collisions are modeled in the FP algorithm, new internal particle energies are not constrained by the requirement to obtain a specific total collision energy. Therefore, the CLT model may populate high energy states faster than the DSMC Larsen-Borgnakke model.

The left side of Fig. 3.4 shows the relaxation behavior of the vibrational temperature. Good agreement between FP and DSMC results can be observed. Since the DLT and the DLB model are constructed to obey the Landau-Teller law, both models show an identical relaxation behavior for macroscopic temperatures.

The right side of Fig. 3.4 shows the population of the first three vibrational levels

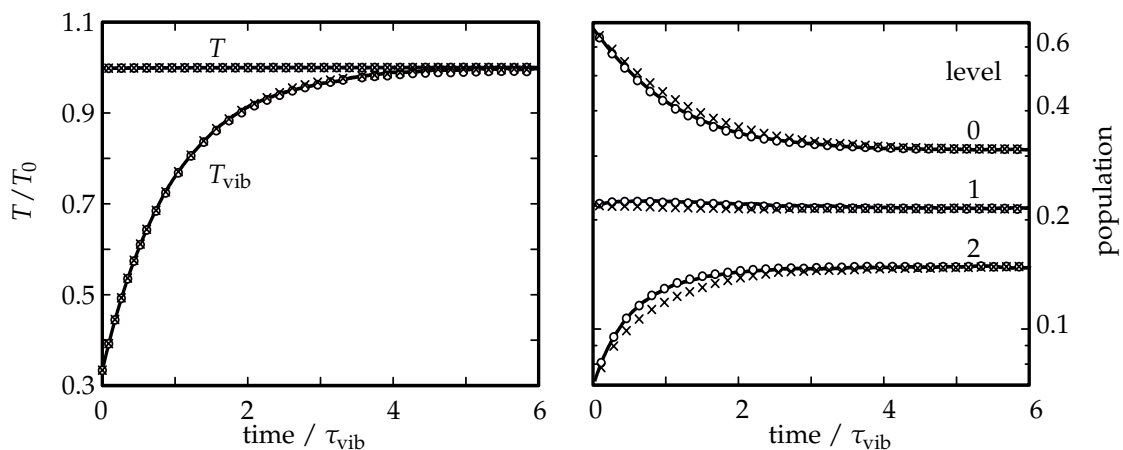


FIGURE 3.4: Left: Relaxation of vibrational temperature. Right: Population of the first three vibrational levels. Lines: DSMC results. Circles: FP-DLB results. Crosses: FP-DLT results.

along the relaxation process. While the equilibrium population at the end of the relaxation process is correctly predicted by both FP models, the non-equilibrium population during the relaxation process is only correctly captured by the DLB model. This result is expected, since only the DLB model is constructed to correctly reproduce microscopic non-equilibrium energy states.

3.6.2 Spherical expansion flow

The spherical expansion flow is investigated [10]. As illustrated in Fig. 3.2, this test case describes the expansion of a gas emerging from a point source. The gas features a strongly decreasing particle density with increasing distance from the expansion center. Hence, this test case provides a good example for checking the performance of the FP models for describing expansion effects, such as freezing of internal energies.

As described by Bird [10], the spherical symmetry of the test case is exploited to employ a one-dimensional calculation. Only the supersonic part of the expansion is modeled. To determine the inflow conditions an isentropic expansion up to the inflow boundary is assumed. Hence, the temperature T^* and particle density n^* at the inflow boundary can be calculated as follows [5]:

$$\frac{T_0}{T^*} = 1 + \frac{\gamma - 1}{2} M^{*2}, \quad (3.72)$$

$$\frac{n_0}{n^*} = \left(1 + \frac{\gamma - 1}{2} M^{*2}\right)^{\frac{1}{\gamma-1}}. \quad (3.73)$$

The quantities T_0 and n_0 denote the reservoir temperature and density, M^* is the Mach number at the inflow boundary and γ denotes specific heat capacity ratio. A Knudsen number may be defined by [10]:

$$\text{Kn} = \frac{\lambda_0}{d^*}, \quad (3.74)$$

with the reservoir mean free path λ_0 and the distance d^* between the inflow boundary and the origin of the expansion.

A typical characteristic of strong expansion flows is the formation of an anisotropic velocity distribution function (see App. E). To characterize this effect, a parallel and perpendicular temperature are introduced:

$$T_{\parallel} \equiv \frac{m}{k_B} \langle \mathbf{c}_{\parallel}^2 | f \rangle, \quad (3.75)$$

$$T_{\perp} \equiv \frac{m}{k_B} \langle \mathbf{c}_{\perp}^2 | f \rangle. \quad (3.76)$$

where \mathbf{c}_{\parallel} and \mathbf{c}_{\perp} refer to the components of the thermal particle velocity parallel and perpendicular to the direction of the expansion. An anisotropic velocity distribution function exists when $T_{\parallel} \neq T_{\perp}$.

As reservoir temperature and particle density, $T_0 = 300$ K and $n_0 = 4 \cdot 10^{22}$ 1/m³ are chosen. The inflow Mach number is set to $M^* = 1.2$, since for $M^* > 1$ a supersonic expansion flow exists. Because of the small temperature, the vibrational excitation is neglected for this test case. Rotational energies are assumed to be fully excited at the inflow boundary. Hence, the specific heat capacity ratio in Eq. (3.72) and Eq. (3.73) becomes $\gamma = 1.4$. Therefore, the inflow temperature and density are set accordingly to $T^* = 233$ K and $n^* = 2.12 \cdot 10^{22}$ 1/m³. The distance between the

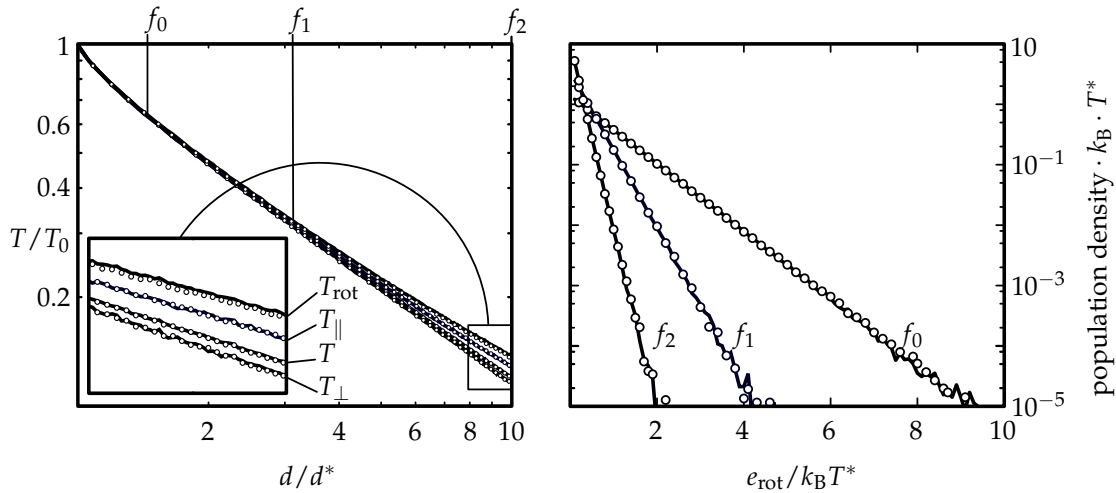


FIGURE 3.5: Left: Temperature distribution along the spherical expansion flow. Right: Rotational energy distribution function along the spherical expansion flow. Note that the unit of the distribution function is the population density, which is defined as $dN/dE/dV/n$, where dN denotes the number of particles that can be found in a small energy interval dE and volume element dV and n is the particle density. Lines: DSMC results. Symbols: FP results.

origin and the inflow boundary is chosen to be $d^* = 0.1$ m. Therefore, the Knudsen number becomes $Kn = 3.24 \cdot 10^{-4}$. Please note that the distance d^* is an input parameter of the simulation and is selected in such a way that a near continuum flow is achieved at the inflow limit. The flow is simulated for a distance of d^* to $10d^*$ from the origin. The domain is divided to 2000 equal-sized grid cells, resulting in an under resolved DSMC-simulation in the inflow area. Therefore, a collision partner selection scheme is applied to obtain meaningful DSMC results [40]. The time step size is set to $\Delta t = 1 \cdot 10^{-7}$ s, which resolves the particle mean collision time in the inflow area. The scaling factor F_N is adjusted to obtain between 140 and 280 particles per cell.

The left side of Fig. 3.5 shows the temperatures distributions of T , $T_{||}$, T_{\perp} and T_{rot} along the expansion. The inflow boundary is located on the left side. On the abscissa the distance from the origin based on the distance d^* is plotted. At the inflow boundary an equilibrium state is assumed. Consequently all temperatures are identical. For a distance greater than approximately $3 \cdot d^*$ from the origin, differences between the temperatures $T_{||}$ and T_{\perp} can be detected, suggesting an anisotropy of the velocity distribution function. In addition, rotational modes become frozen. This effect may be explained by the decreasing particle density and temperature with progressive expansion, which results in a decreasing collision frequency. Therefore, from a certain point in the expansion flow, there are no longer enough inelastic collisions to equalize rotational and translational temperatures. Good agreement between the CLT model and DSMC simulations can be observed. Except of small deviations in the rotational temperature distribution for a distance of $d > 8d^*$ from the origin, different temperature distributions are correctly predicted by the FP method.

The right side of Fig. 3.5 shows three different rotational energy distribution functions f_0 , f_1 and f_2 along the expansion process. The positions in the flow field, where the distribution functions are calculated, are marked in the left part of Fig. 3.5. Good agreement between FP and DSMC results can be observed. In particular, both models show a Boltzmann distribution of internal energies. This can be explained by the special type of the test case: With increasing expansion, inelastic collision become

more and more rare and therefore the internal energies become frozen, which means they change less and less. At the inflow boundary, the internal energies obey a Boltzmann distribution. Since the expansion is not disturbed by any external influences, for example interaction with walls or an interaction with other flows, there is no reason why the internal energies should deviate from the initial Boltzmann distribution. Instead, they freeze in the Boltzmann distribution.

3.6.3 Shock wave

A one dimensional shock wave flow is investigated. Since the thermal temperature increases rapidly across a shock wave, this test case is well suited for investigating the relaxation behavior of internal energy modes in combination with thermal non-equilibrium effects.

Normally, a shock wave forms in front of a surface subjected to supersonic flow. However, a test case in which a surface is simulated is more difficult to interpret than a test case without a simulated surface, since in addition to the physical effects in the shock wave, the interaction of the gas with the surface also has a significant influence on the flow field. For this reason, a very special test case is considered in the following, which allows to simulate a shock wave without the need to consider additional surfaces.

The principle setup of the test case is illustrated in Fig. 3.2. The shock wave is modeled completely in three dimensions. The x-direction is chosen as the flow direction, while periodic boundary conditions are applied for the y- and z-boundaries.

In order for a shock wave to develop, even without the presence of a surface, the boundary conditions at the inflow and outflow surfaces must be set correctly: Particles must be generated on the inflow surface in accordance with the desired flow conditions upstream of the shock wave. On the outflow surface, the piston boundary condition, as defined by Bird [10], should be used. This boundary condition simulates the influence of a moving piston downstream of the shock wave and leads to the generation of a shock wave between the inflow and outflow surfaces. Simply spoken, the piston boundary condition replaces the effect of a surface. To get a stable shock wave, the piston boundary condition must be adapted to the flow condition that develop in the downstream area of the shock wave. In addition, the stabilization algorithm described by Bird [10], which suppress a non-physical random movement of the shock wave, must be used. This algorithm takes the flow conditions in the upstream and downstream area of the shock wave as input parameters. Hence, in summary, the flow conditions up and downstream of the shock wave must be known in advance, to set up the piston boundary condition and the stabilization algorithm.

It should be noted that the entire area of the shock wave is simulated. This means in particular that the entire relaxation process of the internal energies is modelled. Since the inflow temperature is significantly smaller than the characteristic vibrational temperature θ , the vibrational energy mode is not fully excited for this test case. Hence, the heat capacity ratio γ is non-constant over the shock wave and the well known Rankine-Hugoniot equations [5] cannot be applied to link the flow conditions in front of and behind the shock wave. Instead, the flow conditions behind the shock wave are calculated numerically from the inflow conditions, by solving the conservation equations across the shock wave, assuming a temperature dependency

of γ :

$$\gamma(T) = \frac{d_{\text{tot}}(T) + 2}{d_{\text{tot}}(T)} = \frac{7 + d_{\text{vib}}(T)}{5 + d_{\text{vib}}(T)}. \quad (3.77)$$

Here $d_{\text{tot}}(T)$ means the total number of excited degrees of freedom and $d_{\text{vib}}(T)$ the number of excited vibrational degrees of freedom as given by Eq. (3.25).

A shock wave with an upstream Mach number of $M_1 = 10$ is considered. For the upstream density and temperature $n_1 = 10^{20} \text{ 1/m}^3$ and $T_1 = 500 \text{ K}$ are chosen, which leads to a flow speed of $v_1 = 4557 \text{ m/s}$. As described above, the downstream conditions are found numerically. In particular, the values $n_2 = 7.272 \cdot 10^{20} \text{ 1/m}^3$, $T_2 = 8363 \text{ K}$ and $v_2 = 627 \text{ m/s}$ are calculated. The shock wave is simulated over a distance of 1.4 m in flow direction. For the DSMC simulation, the domain is divided in 1000 equal sized grid cells in flow direction, resulting in a grid cell size smaller than the smallest mean free path in the flow. In the FP simulations, the domain is divided in 250 equal sized grid cells. In both cases, the same time step size $\Delta t = 5 \cdot 10^{-7} \text{ s}$ is applied. The scaling factor F_N is adjusted to obtain a number of 20 particles per cell in the upstream area.

Figure 3.6 shows the distributions of translational, rotational and vibrational temperature across the shock wave. Due to the large vibrational relaxation time, the vibrational temperature relaxes only slowly to equilibrium behind the shock wave. In contrast, the rotational temperature closely follows the translational temperature distribution. The FP method accurately reproduces DSMC results, only slight deviations can be observed. However, such deviations are to be expected, since the FP method loses validity in areas of strong thermal non-equilibrium [91, 52]. Again, the DLT and the DLB model show no differences in the distribution of macroscopic temperatures.

The right side of Fig. 3.7 shows the population of the first three vibrational levels. The upstream and downstream equilibrium populations are given by a Boltzmann distribution and are correctly predicted by both FP models. The DLB model also captures non-equilibrium populations during the relaxation process, while the DLT model fails in this area.

The left side of Fig. 3.7 shows three rotational energy distribution functions f_0 , f_1 and

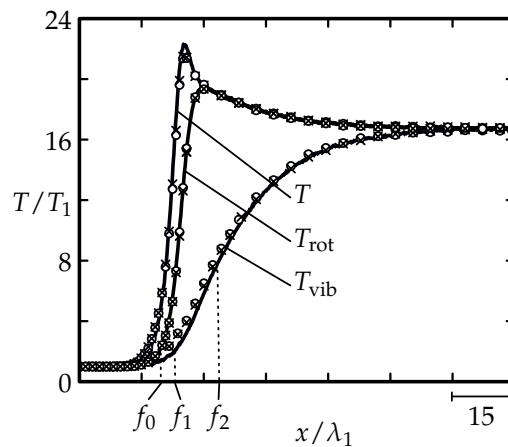


FIGURE 3.6: Translational, rotational and vibrational temperature distributions across the shock wave. Lines: DSMC results. Circles: FP-DLB results. Crosses: FP-DLT results.

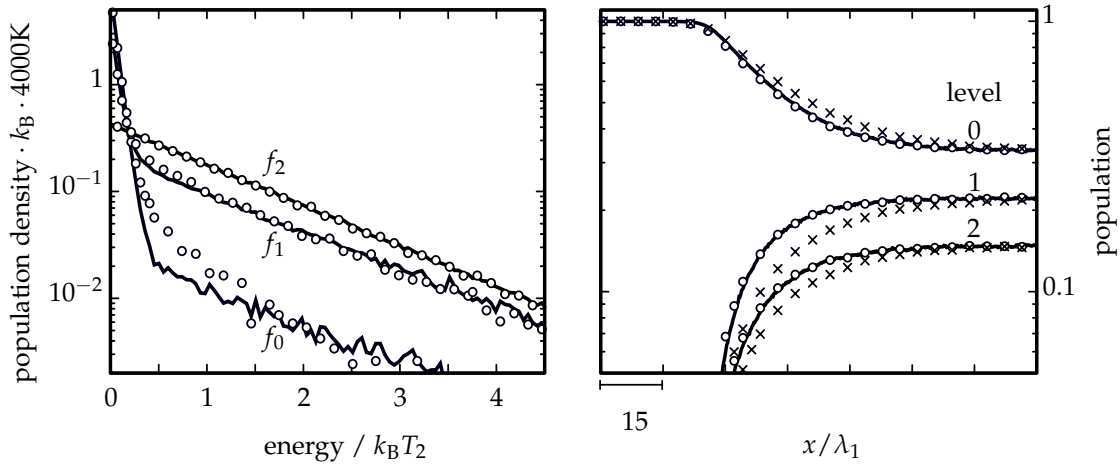


FIGURE 3.7: Left: Rotational energy distributions across the shock wave. Note that the unit of the distribution function is the population density, which is defined as $dN/dE/dV/n$, where dN denotes the number of particles that can be found in a small energy interval dE and volume element dV and n is the particle density. Right: Population of the first three vibrational levels. Lines: DSMC results. Circles: FP-DLB / FP-CLT results. Crosses: FP-DLT results

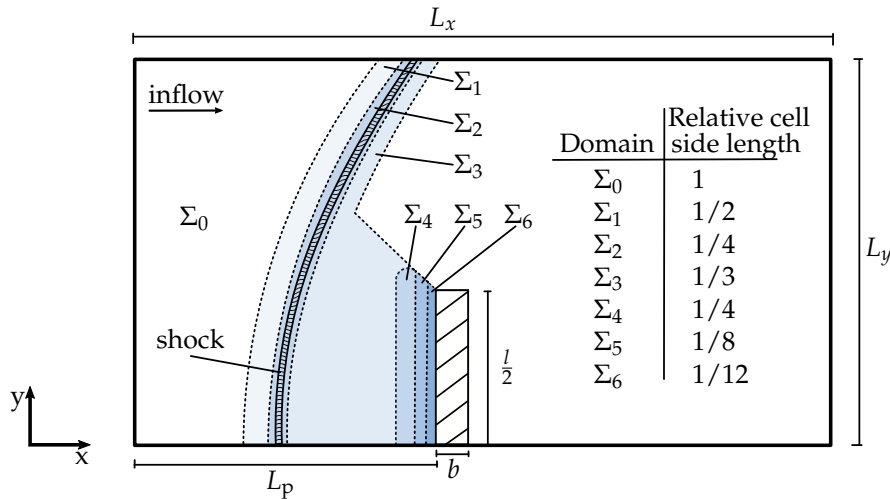


FIGURE 3.8: Computational domain for the FP simulation of the perpendicular flat plate test case.

f_2 recorded at different positions of the flow field, which are marked in Fig. 3.6. For the distribution f_0 , calculated in the upstream area of the shock wave, the FP result deviates from the DSMC result. This can be expected, since the rotational temperatures deviate from the translational temperature in this part of the flow. As described in Subch. 3.6.1, the CLT model is not able to capture such a non-equilibrium energy distribution. The distribution f_1 , calculated where the rotational energy mode is nearly in equilibrium with the translational mode, is much better predicted by the FP method. The distribution f_2 is calculated where translational and rotational temperatures are equalized. In this case the population of rotational energies obeys a Boltzmann distribution, which is accurately predicted by the FP method.

3.6.4 Flow past a perpendicular flat plate

In order to check the performance of the proposed models for a more complex test case, a two-dimensional hypersonic flow over a perpendicular flat plate is considered. This test case features characteristics of the expansion and shock wave test cases, described above. In addition, particle-wall interaction becomes important.

Figure 3.8 shows a sketch of the simulation domain. The length l and the width b of the plate are set to $l = 0.2$ m and $b = 0.02$ m. The domain length in flow direction is set to $L_x = 0.46$ m and in cross direction to $L_y = 0.25$ m. The distance L_p between the inflow boundary and the plate is set to 0.2 m. The symmetry of the problem is exploited and a half-body calculation is performed. For the inflow temperature and number density $T_\infty = 500$ K and $n_\infty = 1.3 \cdot 10^{21} 1/\text{m}^3$ are chosen, resulting in a inflow Knudsen number of $Kn = 0.005$, based on the length of the plate. The inflow velocity is set to $v_\infty = 2278.5$ m/s, leading to an inflow Mach number of $M_\infty = 5$.

In the DSMC simulation the grid cells are adapted step wise to the local mean free path. In the FP simulations the flow domain is divided into areas with different grid resolutions, as indicated in Fig. 3.8. The domain Σ_0 features a mesh with a grid cell size of (2.5×2.5) mm. The sizes in the other domains are refined as indicated in Fig. 3.8. Note that the domains are arranged to properly resolve the shock wave structure and the boundary layer. For the FP and DSMC simulations the same time step size $\Delta t = 2 \cdot 10^{-7}$ s is applied, which resolves the mean collision time in the stagnation point. The scaling factor F_N is adjusted to obtain a minimum number of 10 particles per cell. The FP simulations have converged after 15,000 time steps, while DSMC simulation reaches convergence after 60,000 time steps. Please note that the differences in the convergence behavior are due to the fact that the grid cells in the DSMC simulation are gradually adapted to the mean free path at the beginning of the simulation. Otherwise, the DSMC simulation would converge with the same speed as the FP simulations.

In order to better interpret the following results, the local Knudsen number in the flow field is shown Fig. 3.9. The Knudsen number is calculated based on the length of the plate and the local mean free path as given by Eq. (2.9). In the windward area of the plate, the Knudsen number is in the order of 0.05 and smaller. This is due to the fact that the particle density in front of the plate is increased compared to the

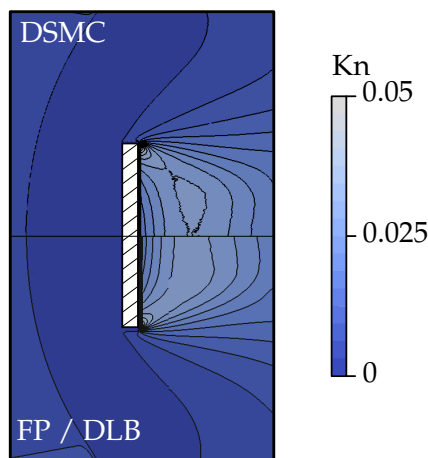


FIGURE 3.9: Local Knudsen number, based on the length of the plate

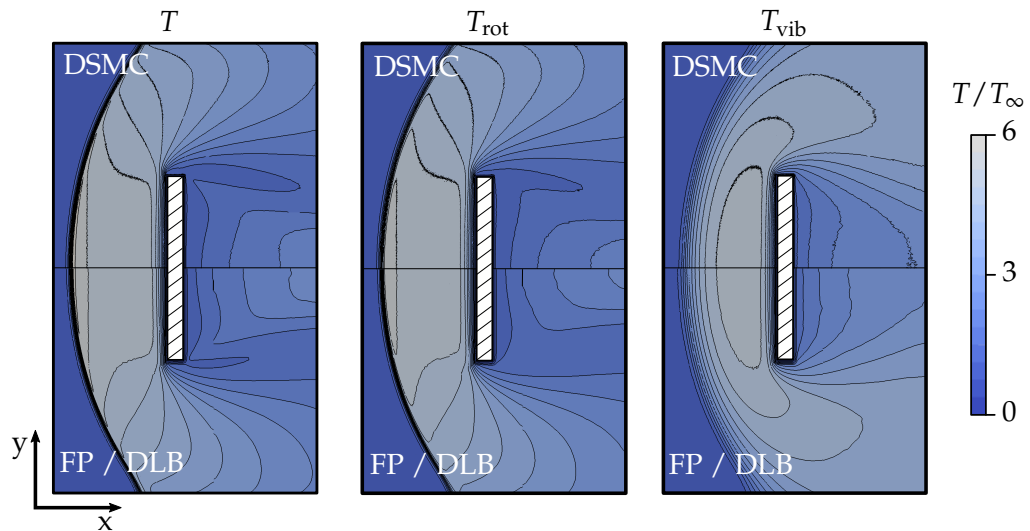


FIGURE 3.10: Translational (left), rotational (middle) and vibrational (right) temperatures for the flat perpendicular plate test case.

inflow area. On the leeward side of the plate, the Knudsen number increases by a factor of 10 compared to the inflow area. This results from the particle density in this area, which decreases to the same extent. In this area, Knudsen numbers of up to 0.05 are reached. It should be noted here, that the Knudsen number is defined based on the length of the plate. If the Knudsen number were defined e.g. based on the width of the plate, then Knudsen numbers up to 0.5 would be achieved. In this respect, the flow in this area can be described as highly rarefied. Fokker-Planck and DSMC simulation produce nearly the same Knudsen number distribution over the flow field. Smaller deviations only occur behind the plate. These can be explained by the strong dilution in this area.

Figure 3.10 shows the translational, rotational and vibrational temperature distributions. Since the DLT and DLB model show no differences in macroscopic temperature distributions, only the results of the DLB model are shown in Fig. 3.10. Larger differences between DSMC and FP results occur only in the wake region behind the plate. This was to be expected since, as mentioned above, this is an area of high

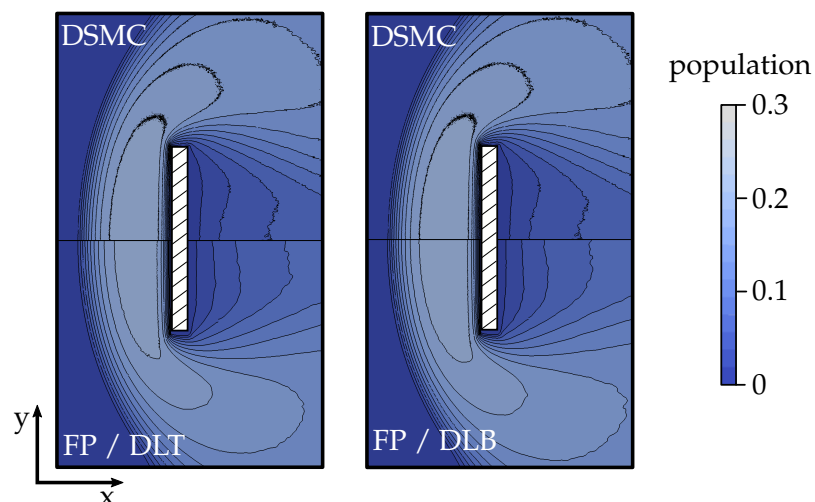


FIGURE 3.11: Population of the first excited vibrational level. Left: DLT model is used for the FP simulation. Right: DLB model is used for the FP simulation

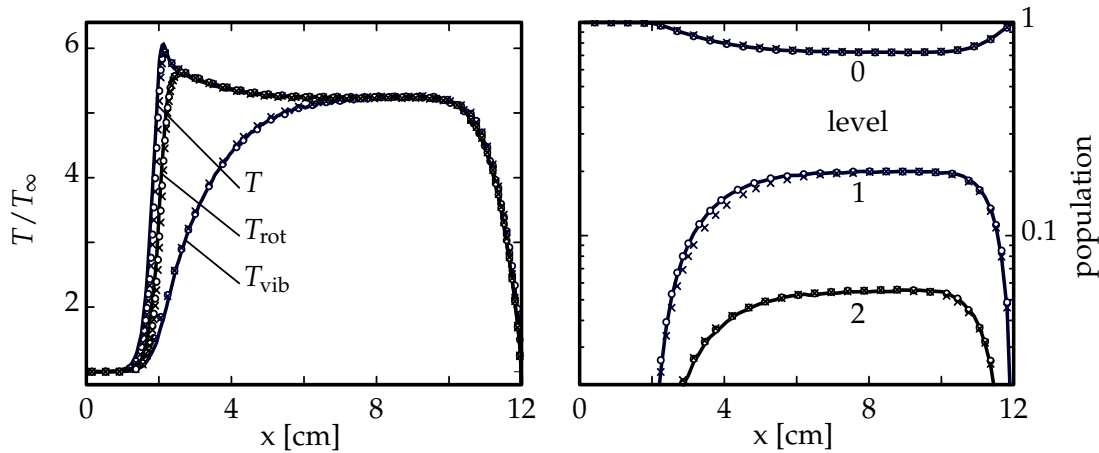


FIGURE 3.12: Temperature distributions and populations of vibrational energy levels along the stagnation line. Lines: DSMC results. Circles: FP-DLB results. Crosses: FP-DLT results

dilution, so the underlying FP method loses its validity. However, in addition to the decreasing validity of the FP operator in this region, the internal energy exchange models developed in this chapter are also based on the assumption of thermal equilibrium and therefore become invalid for highly dilute gases: In the DLT and the CLT model the internal relaxation time $\tau_{int} = Z_{int}/\nu_{coll}$ must be defined, which characterizes the speed of relaxation of internal energies. This relaxation time is defined based on the equilibrium mean collision frequency (Please consider Eq. (3.27) for reference) which is only valid for flows in equilibrium. Similar, for the DLB model an equilibrium distribution of the relative particle velocities is applied to determine the rate coefficient R_{ij} (Please consider Eq. (3.44) for reference). This assumption is also only valid for flows in equilibrium. Therefore, the models for internal energy relaxation lose their validity in areas of strong non-equilibrium, which might contribute to the differences shown in Fig. 3.10.

Figure 3.11 shows the population of the first vibrational level calculated by the two different FP models. Except of the wake region, the DLB model accurately reproduces the DSMC results. The DLT model shows deviations to the DSMC results in the relaxation regime behind the shock wave, which is consistent to the results in Subch. 3.6.3.

The left side of Fig. 3.12 shows the distribution of the translational, rotational and vibrational temperature along the stagnation line. In general, a good agreement between FP and DSMC results can be observed. No significant differences between the DLT and DLB model are detectable.

The right side of Fig. 3.12 shows the population of the first three vibrational levels along the stagnation line. A good agreement between the results of the DLB model and the DSMC results can be observed. The DLT model reveals small deviations to the DSMC results in the relaxation process directly behind the shock wave.

3.7 Efficiency considerations

The following subchapter discusses the efficiency of the proposed method. The first part of the subchapter examines constraints on the overall FP time step size, introduced by the numerical algorithms described in Subch. 3.5. In the second part, the

computational effort of the method is discussed.

3.7.1 Restrictions on the time step size

In order to investigate possible restrictions on the time step size, the heath bath test case described in Subch. 3.6.1 is considered. The relaxation of vibrational energies is calculated by the DLT and DLB model, using different time step sizes. The CLT model is not considered since it features a strong algorithmic similarity to the DLT model and therefore no significant differences between the models are expected.

Figure 3.13 shows the relaxation of vibrational temperatures in an isothermal heat bath with equilibrium temperature T_0 . No differences between the solutions are apparent for different time step sizes. This is due to the the choice of the integration schemes (see Subch. 3.5). These schemes exactly integrate the time evolution of internal energy states for the case that the translational temperature is constant. Since this is the case for an isothermal heat bath, the solutions are independent of the time step size.

For a more challenging investigation, the relaxation of vibrational temperature in an adiabatic heat bath is considered. In contrast to the isothermal heat bath, the translational temperature can change here. Hence, the results are expected to be sensitive to the time step size.

As indicated in Fig. 3.14 numerical results confirm these expectations. While almost no differences between calculations with $\Delta t = 0.1 \tau_{\text{vib}}$ and $\Delta t = 0.2 \tau_{\text{vib}}$ can be detected, deviations for $\Delta t = 0.5 \tau_{\text{vib}}$ clearly emerge.

These results indicate that the time step size Δt is limited by the internal relaxation time τ_{vib} . Although this condition appears to be very restrictive, it should be noted that it is not a major limitation for most applications. When it becomes necessary to model the relaxation behavior of internal energy, the internal relaxation time must be in the same order of magnitude as a characteristic time of the flow τ_c :

$$\tau_{\text{int}} \sim \tau_c. \quad (3.78)$$

Otherwise, the flow could be modeled as frozen or in equilibrium and a detailed modeling of the internal modes as presented in this work would not be necessary. However, the simulation time step Δt should always be limited by a characteristic

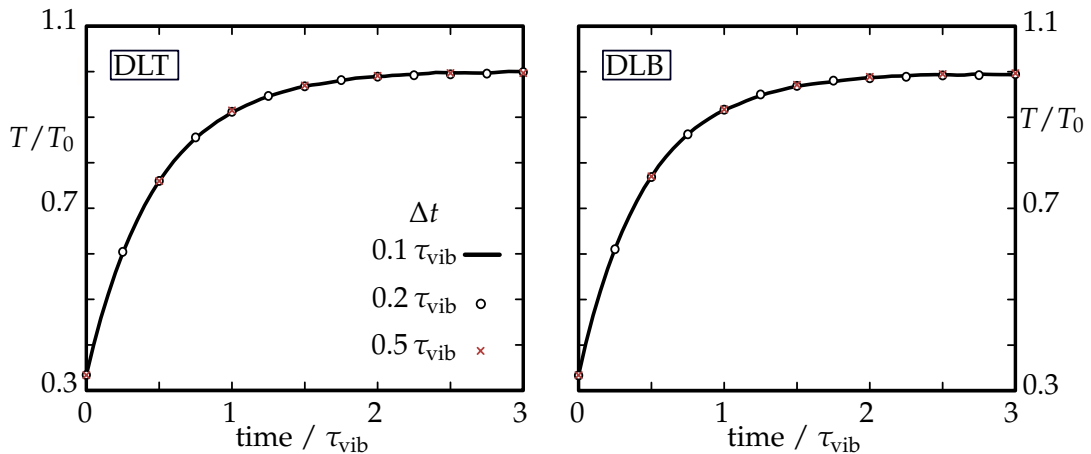


FIGURE 3.13: Relaxation of vibrational temperature in an isothermal heat bath calculated for different time step sizes. Left: DLT model. Right: DLB model.

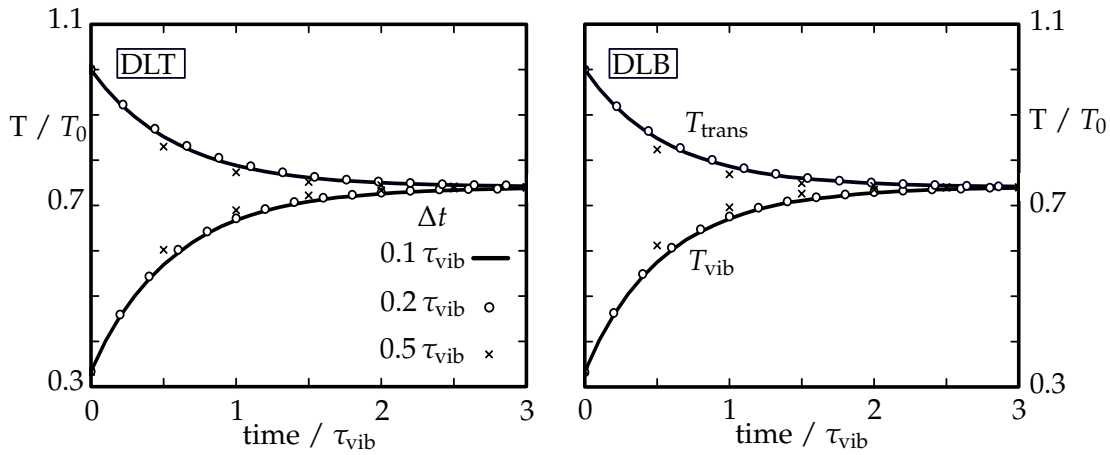


FIGURE 3.14: Relaxation of temperatures in an adiabatic heat bath calculated for different time step sizes. Left: DLT model. Right: DLB model.

flow time τ_c :

$$\Delta t < \tau_c, \quad (3.79)$$

since the simulation could otherwise not resolve important flow structures. When combining Eq. (3.78) and Eq. (3.79) it becomes clear that the time step Δt is naturally limited by the internal relaxation time τ_{int} . Hence, time step limitations that are induced by the DLT and DLB model should not be more restrictive than the time step size required to resolve unsteady flow features.

3.7.2 Computational efficiency

The computational efficiency of the proposed method is investigated. Since other authors [53, 56, 57, 91, 88, 76, 120] already compared the computing effort of the cubic FP model with DSMC calculations for different flows, this is not repeated here. Instead the computational effort of the cubic FP model in combination with the proposed DLB and DLT models is compared to the effort of a pure, monatomic cubic FP calculation.

The computational efficiency of the proposed models is studied by considering the previously described heat bath testcase (see Subch. 3.6.1). Calculations are performed for 100 time steps with varying time step size. Figure 3.15 shows the computing time required to update particle velocities and internal energy states per time step. The y-axis is normalized to the computing time that is required for a monatomic cubic FP calculation.

Since no internal energy states are updated for the monatomic FP calculation, it features the lowest computing time and the results are independent of the time step size. When applying the DLT model, the computing time is approximately 15% higher than that of the monatomic calculations, due to the need for updating internal energy states. The computing time for the DLT model increases only slightly for larger time steps. This results from the scheme for updating internal energy states, as described in Subch. 3.5.1, where each particle is assigned an internal energy state at maximum once per time step.

When applying the DLB model, the computational effort increases with increasing time step size. This is due to the Gillespie algorithm calculating the full evolution of internal energy states over a time step. However, time step sizes that are larger than

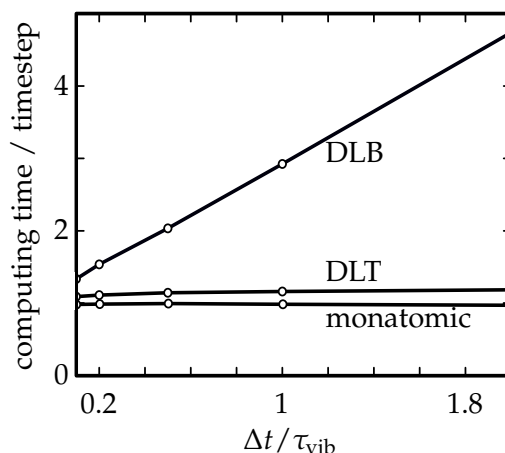


FIGURE 3.15: Relative computational effort per time step for different FP calculations.

the internal relaxation time are unrealistic for well-resolved FP simulations. For a realistic scenario with $\Delta t = 0.2\tau_{\text{vib}}$, the computational effort for the DLB model is about 30% higher than for the monatomic calculations.

3.8 Summary and conclusion

In this chapter, a novel method was described that can be used to extend kinetic Fokker-Planck methods, specifically the cubic kinetic FP method, to simulate internal energy levels of diatomic molecules. The method is based on a master equation, which is used to describe the time evolution of the internal energy levels. The master equation is not solved directly, instead corresponding stochastic processes are simulated. Three different models for the rate coefficients of the master equation are proposed, which can describe the energy levels at different levels of detail: While the CLT and DLT models allow simulating continuous and discrete energy levels relaxing according to the Landau-Teller law, the DLB model is able to describe the microscopic evolution of discrete energy states in accordance with the Larsen-Borgnakke model.

The models were tested against the DSMC method in a series of test cases relevant to hypersonic gas flows using N_2 as test gas. Here, the CLT model is used to model the rotational energy levels, while the DLT and DLB models are used for the vibrational modes. As an important result, it is found that the CLT model describes well the temperature distribution of strongly expanding gases. Relevant phenomena, in particular the freezing of internal energy modes and the formation of an anisotropic velocity distribution, are accurately captured by the models as long as no external influences, such as interaction with walls, disturb the expansion. Furthermore, all models describe the distribution of rotational and vibrational temperatures along a shock wave very accurately for an inflow Mach number of 5. Despite small deviations, the width of the shock wave can be predicted well. With similar accuracy, the distribution of vibrational energy levels can be predicted by the DLB model. Since shock waves with a smaller inflow Mach number tend to have a smaller deviation from equilibrium, it can be assumed that the models can also describe shock waves with a Mach number smaller than 5 with at least the same accuracy.

To assess the usefulness of the master equation model from this chapter, it makes sense to compare it to other models available in the literature for describing internal energies in the context of kinetic FP. In particular, the models of Gorji et al. [53], Pfeiffer [119], and Mathiaud et al. [111] are used below for this comparison: The model of Gorji et al. [53] and Mathiaud et al. [111] make use of a Fokker-Planck equation to describe internal energies, while the model of Pfeiffer [119] is based on the BGK equation and is, in contrast to the others models, also able to describe discrete energy levels. All models have in common that the internal temperatures relax according to the Landau-Teller law. Thus, if the models were compared in a simulation study with the master equation model from this thesis, all would be expected to give very similar results for the distribution of temperature. On the other hand, the master equation model from this chapter uses a fundamentally different mathematical approach than the previously published kinetic FP models. In particular, it is the only model that allows the relaxation behavior to be specified based on rate coefficients. This results in a significant advantage: While the specific form of the models of Pfeiffer [119], Mathiaud et al. [111], and Gorji et al. [53] makes it difficult to fit them to relaxation laws other than the Landau-Teller law,² this is not the case for the master equation model from this chapter. By choosing appropriate rate coefficients, the master equation model can be adapted to a wide range of relaxation phenomena. This was shown by the example of the DLB model, which was constructed to exactly reproduce the relaxation behavior given by corresponding DSMC models.

In general, by a suitable choice of rate coefficients, it is possible to fit the master equation model to any DSMC models describing internal relaxation phenomena. This offers two major advantages. First, it facilitates the coupling of the DSMC method with the kinetic FP method, since consistent physical modeling of both methods can easily be achieved. This is essential for a meaningful coupling of the two methods and a big advantage over classical continuum methods, where a lot of effort has to be spent to achieve such a consistent modeling with DSMC [130]. Second, no fundamentally new models for describing internal energy relaxation need to be developed for the FP method. Instead, already validated DSMC models can simply be integrated into the method. This is a great advantage because it allows the FP method to draw on the wide range of DSMC models that have been developed in recent years. For example, it should be possible to develop models for polyatomic molecules with more than two atoms with relatively little effort by simply referring to corresponding DSMC models.

²The model of Pfeiffer [119] provides only a single parameter to fit the relaxation behavior, while the specific modeling approach of Gorji et al. [53] and Mathiaud et al. [111] makes it hard to fit the models to other relaxation laws than the Landau-Teller law.

Chapter 4

Modeling of hard sphere gas mixtures

This chapter describes an approach for modeling gas mixtures within the kinetic Fokker-Planck method.

The approach is based on the ideas of Gorji et al. [51] (see Subch. 2.3.4) who constructed a kinetic FP model for describing binary gas mixtures, assuming that particles interact according to the mathematically simple but physically unrealistic Maxwell molecular model.

The model presented in this chapter features two major improvements compared to this model. The proposed model can not only describe binary gas mixtures, but also mixtures with any number of species. In addition, particle interaction is modeled using the hard sphere collision model. Compared to the Maxwell molecule model, the HS model is advantageous, since it can better capture transport properties and phenomena for many gases. For example, the HS model is able to model the thermodiffusion effect, which is not the case with the Maxwell molecule model [30]. Also, the HS collision model leads to a square root dependence of viscosity on temperature, while the Maxwell model leads to a linear dependence [10]. The first is a better approximation for some relevant gases in spacecraft related aerodynamics, such as H₂, N₂ or CO [10].

The structure of this chapter is as follows. Subchapter 4.1 describes the construction of the FP operator. In Subch. 4.2 a corresponding stochastic solution algorithm is derived. Test cases to verify the model are presented in Subch. 4.3. Finally, Subch. 4.4 presents the conclusion of this chapter.

Please note that the main parts of this chapter have been published in reference [74].

4.1 Fokker-Planck model for hard sphere mixtures

As described in Subch. 2.3.4, the set of Boltzmann equations (2.37) is approximated by a set of Fokker-Planck equations:

$$\frac{\partial f^{(\alpha)}}{\partial t} + v_i^{(\alpha)} \frac{\partial f^{(\alpha)}}{\partial x_i} + \frac{F_i^{(\alpha)}}{m^{(\alpha)}} \frac{\partial f^{(\alpha)}}{\partial v_i^{(\alpha)}} = \underbrace{-\frac{\partial (f^{(\alpha)} A_i^{(\alpha)})}{\partial v_i^{(\alpha)}} + \frac{\partial^2 (f^{(\alpha)} D^{(\alpha)})}{\partial v_i^{(\alpha)} \partial v_i^{(\alpha)}}}_{S_{\text{FP}}^{(\alpha)}}. \quad (4.1)$$

The FP operator $S_{\text{FP}}^{(\alpha)}$ is a model parameter that should be selected as sensibly as possible¹. In the following it is described how this is constructed.

Please note that a similar approach is followed for the construction of the FP operator as for monatomic gases described in Subch. 2.3.1: The operator is first constructed in such a way that the model delivers correct results in the limit of small Knudsen numbers. Then numerical test cases are used to check whether the resulting model is also suitable for modeling more rarefied gas flows.

In particular, the species specific drift coefficients $A_i^{(\alpha)}$ and the diffusion coefficients $D^{(\alpha)}$ are constructed, so that the Fokker-Planck model correctly predicts species temperature, diffusion velocity, shear stress and heat flux distributions in the limit of small Knudsen numbers. This leads to the conservation of mass, momentum and energy as well as a correct prediction of the transport coefficients for the mixture in the limit of small Knudsen numbers. To fulfill these requirements, the FP operator must reproduce lower order Boltzmann production terms in the limit of small Knudsen numbers:

$$P_{\text{Boltz}}^{(\alpha)}(X) \stackrel{!}{=} P_{\text{FP}}^{(\alpha)}(X), \quad (4.2)$$

$$X \in \left\{ c_i^{(\alpha)}, c_i^{(\alpha)} c_i^{(\alpha)}, c_{<i}^{(\alpha)} c_{>}^{(\alpha)}, c_i^{(\alpha)} c_j^{(\alpha)} c_j^{(\alpha)} \right\}.$$

In order to construct a FP model which satisfies relation (4.2), production terms must be evaluated. Since the FP model is intended to describe particles interacting through the HS collision model, Boltzmann production terms must be derived based on the same assumption. It is worth noting, that calculating production terms for the Boltzmann collision operator is generally a non-trivial task. In particular for the HS collision model, it is not possible to calculate Boltzmann production terms independently of the distribution function.

In this thesis the results of Gupta [63] are applied, who evaluated $P_{\text{Boltz}}^{(\alpha)}(X)$, assuming the HS collision model and a distribution function according to Grad's 13 and 26 moment method. Because Grad's moment method only applies for low Knudsen number gases, the resulting production terms are only valid for near continuum flows. However, since the identity (4.2) must be true only in the limit of small Knudsen numbers, the results of Gupta [63] may be still applied for this work. In App. C.1, these results are discussed in more detail.

For the FP operator, production terms can be calculated independently of the distribution function, which is discussed in more detail in App. C.2.

Similar to the work of Gorji et al. [51], a Fokker-Planck operator with a linear drift coefficient is constructed. This correctly predicts the evolution of the species temperatures and the species mass diffusion in the limit of small Knudsen numbers. In a second step, the drift coefficient is extended by a higher order expression in the thermal particle velocities, which leads to a correct prediction of the species shear stresses and heat fluxes in the limit of small Knudsen numbers.

¹The reader should note that the definition of the diffusion coefficient in the FP operator in Eq. (4.1) differs from the definition of diffusion coefficients in the previous parts of this thesis by a factor of 1/2 and the square root. The different definition was introduced to simplify the following equation and to be consistent with the reference [74].

4.1.1 Linear model

The drift coefficient $A_i^{(\alpha)}$ is chosen so that the model predicts correct diffusion velocities in the limit of small Knudsen numbers. This requirement is satisfied, when expression (4.2) is fulfilled for $X = c_i^{(\alpha)}$. Applying the production terms Eq. (App.C.13) and Eq. (App.C.27), expression (4.2) leads to:

$$- \sum_{\beta=1}^{N_s} \nu^{(\alpha\beta)} \mu^{(\beta)} \left[\frac{5}{3} \rho^{(\alpha)} \left(u_i^{(\alpha)} - u_i^{(\beta)} \right) + \frac{1}{6\hat{\theta}^{(\alpha\beta)}} \left(\hat{h}_i^{(\alpha)} - \frac{\rho^{(\alpha)}}{\rho^{(\beta)}} \hat{h}_i^{(\beta)} \right) \right] \stackrel{!}{=} m^{(\alpha)} \langle A_i^{(\alpha)} | f^{(\alpha)} \rangle \quad (4.3)$$

Recall, that α and β refer to different particle species, $\rho^{(\alpha)}$ means the species density, $\mu^{(\alpha)}$ denotes the reduced mass of a particle, $\nu^{(\alpha\beta)}$ can be interpreted as collision frequency between species, $u_i^{(\alpha)}$ refers to the i -th component of the average flow velocity, $\hat{h}_i^{(\alpha)}$ denotes reduced heatflux and $\hat{\theta}^{(\alpha\beta)}$ can be interpreted as reduced temperature. For more details, please refer to Subch. 2.1.3 and App. C.1. The following choice for the drift coefficient $A_i^{(\alpha)}$ satisfies Eq. (4.3):

$$A_i^{(\alpha)} \equiv - \sum_{\beta=1}^{N_s} \nu^{(\alpha\beta)} \mu^{(\beta)} \left[\frac{5}{3} \left(\hat{c}_i^{(\alpha)} - u_{d,i}^{(\beta)} \right) + \underbrace{\frac{1}{6\hat{\theta}^{(\alpha\beta)}} \left(\frac{1}{\rho^{(\alpha)}} \hat{h}_i^{(\alpha)} - \frac{1}{\rho^{(\beta)}} \hat{h}_i^{(\beta)} \right)}_{(*)} \right] \quad (4.4)$$

$$\equiv -s^{(\alpha)} c_i^{(\alpha)} + K_i^{(\alpha)}, \quad (4.5)$$

Please note, that $\hat{\mathbf{c}}^{(\alpha)}$ denotes the thermal particle velocities as defined by Eq. (2.28). The species heat fluxes $\hat{\mathbf{h}}^{(\alpha)}$ are defined as given by Eq. (App.C.9). The collision frequencies $s^{(\alpha)}$ are given by:

$$s^{(\alpha)} \equiv \frac{5}{3} \sum_{\beta=1}^{N_s} \nu^{(\alpha\beta)} \mu^{(\beta)}, \quad (4.6)$$

where $\nu^{(\alpha\beta)}$ is defined in Eq. (App.C.10). The constants $\mathbf{K}^{(\alpha)}$ are given by:

$$K_i^{(\alpha)} \equiv - \sum_{\beta=1}^{N_s} \nu^{(\alpha\beta)} \mu^{(\beta)} \left[\frac{5}{3} \left(u_i^{(\alpha)} - u_i^{(\beta)} \right) + \underbrace{\frac{1}{6\hat{\theta}^{(\alpha\beta)}} \left(\frac{1}{\rho^{(\alpha)}} \hat{h}_i^{(\alpha)} - \frac{1}{\rho^{(\beta)}} \hat{h}_i^{(\beta)} \right)}_{(*)} \right]. \quad (4.7)$$

The term marked by $(*)$ in Eq. (4.4) and Eq. (4.7) is responsible for the prediction of the thermodiffusion effect as discussed in more detail in Subch. 4.3.3.

The diffusion coefficient is set so that the model predicts the correct evolution of the species temperatures in the Navier-Stokes limit. This requirement is satisfied, when Eq. (4.2) is fulfilled for $X = c_j^{(\alpha)} c_j^{(\alpha)}$. Applying production terms (App.C.17) and (App.C.28), Eq. (4.2) leads to:

$$- 10 \sum_{\beta=1}^{N_s} \nu^{(\alpha\beta)} \mu^{(\beta)} \rho^{(\alpha)} \left[\frac{k_B}{m^{(\alpha)} + m^{(\beta)}} \left(T^{(\alpha)} - T^{(\beta)} \right) - \frac{\mu^{(\beta)}}{3} \left(\mathbf{u}^{(\alpha)} - \mathbf{u}^{(\beta)} \right)^2 \right] \stackrel{!}{=} 2m^{(\alpha)} \langle A_i^{(\alpha)} c_i^{(\alpha)} | f^{(\alpha)} \rangle + 6\rho^{(\alpha)} D^{(\alpha)}. \quad (4.8)$$

When using Eq. (4.5), one can obtain for the diffusion coefficient:

$$D^{(\alpha)} = \frac{10}{6} \sum_{\beta=1}^{N_s} \nu^{(\alpha\beta)} \mu^{(\beta)} \mu^{(\alpha)} \left[\frac{k_B T^{(\alpha)}}{m^{(\alpha)}} + \frac{k_B T^{(\beta)}}{m^{(\beta)}} + \frac{1}{3} \left(\mathbf{u}^{(\alpha)} - \mathbf{u}^{(\beta)} \right)^2 \right]. \quad (4.9)$$

The diffusion coefficient is always positive, which is an essential requirement for a physically meaningful FP model.

4.1.2 Higher order model

In this subchapter, a higher order extension for the drift coefficient (4.5) is constructed, such that the FP model correctly predicts species shear stresses and heat fluxes in the limit of small Knudsen numbers. Similar to the model of Gorji et al. [51], the drift coefficient is extended as follows:

$$A_i^{(\alpha)} \equiv -s^{(\alpha)} c_i^{(\alpha)} + K_i^{(\alpha)} + \underbrace{\psi_{ij}^{(\alpha)} c_j^{(\alpha)} + \gamma_i^{(\alpha)} \left(c_j^{(\alpha)} c_j^{(\alpha)} - \frac{1}{n^{(\alpha)}} \langle c_j^{(\alpha)} c_j^{(\alpha)} | f^{(\alpha)} \rangle \right)}_{N_i^{(\alpha)}(c_i^{(\alpha)})}, \quad (4.10)$$

with a symmetric matrix $\psi_{ij}^{(\alpha)}$ and a vector $\gamma_i^{(\alpha)}$. Gorji's cubic model (2.78) additionally contains a third-order parameter to ensure the stability of the model. This is not included in expression (4.10), mainly because of the author's experience that the model is stable even without a stabilization parameter. If necessary, however, it would be very easy to extend expression (4.10) by an additional third-order parameter.

The model parameters $\psi_{ij}^{(\alpha)}$ and $\gamma_i^{(\alpha)}$ must be chosen so that identity (4.2) holds for $X \in \{c_i^{(\alpha)}, c_i^{(\alpha)} c_i^{(\alpha)}, c_{<i}^{(\alpha)} c_{>}^{(\alpha)}, c_i^{(\alpha)} c_j^{(\alpha)} c_j^{(\alpha)}\}$. For $X = c_i^{(\alpha)}$ expression (4.2) is satisfied since $\langle N_i^{(\alpha)} | f^{(\alpha)} \rangle = 0$ and the linear model already satisfies this requirement. Therefore the parameters $\psi_{ij}^{(\alpha)}$ and $\gamma_i^{(\alpha)}$ are chosen so that:

$$P_{\text{FP}}^{(\alpha)} \left(c_i^{(\alpha)} c_j^{(\alpha)} \right) \stackrel{!}{=} P_{\text{Boltz}}^{(\alpha)} \left(c_{<i}^{(\alpha)} c_{>}^{(\alpha)} \right) + \frac{1}{3} \delta_{ij} P_{\text{Boltz}}^{(\alpha)} \left(c_l^{(\alpha)} c_l^{(\alpha)} \right), \quad (4.11)$$

$$P_{\text{FP}}^{(\alpha)} \left(c_i^{(\alpha)} \mathbf{c}^{(\alpha)} \mathbf{c}^{(\alpha)} \right) \stackrel{!}{=} P_{\text{Boltz}}^{(\alpha)} \left(c_i^{(\alpha)} \mathbf{c}^{(\alpha)} \mathbf{c}^{(\alpha)} \right). \quad (4.12)$$

When using $\sum_i P_{\text{Boltz}}^{(\alpha)} \left(c_{<i}^{(\alpha)} c_{>}^{(\alpha)} \right) = 0$, it can easily be shown that Eq. (4.11) and Eq. (4.12) lead to a fulfillment of Eq. (4.2) for $X \in \{c_i^{(\alpha)} c_i^{(\alpha)}, c_{<i}^{(\alpha)} c_{>}^{(\alpha)}, c_i^{(\alpha)} c_j^{(\alpha)} c_j^{(\alpha)}\}$. Using Eq. (4.11) and Eq. (4.12) and applying Eq. (App.C.29) and Eq. (App.C.30), a system of nine linear equations for the nine parameters $\psi_{ij}^{(\alpha)}$ and γ_i can be deduced, which is discussed in more detail in App. (C.3).

For the diffusion coefficient, the same expression is applied as in the linear model. Note, that in thermal equilibrium the right side of the linear system (App.C.32) and (App.C.31) vanishes, which implies that the model parameters $\psi_{ij}^{(\alpha)}$ and $\gamma_i^{(\alpha)}$ become zero. Consequently, the higher-order model reduces to the linear model.

4.2 Stochastic solution algorithm

In this subchapter a stochastic solution algorithm for the FP operator described in Subch. 4.1.2 is derived. The algorithm is constructed to predict, for the case of a homogeneous gas, a correct evolution of the species temperatures and diffusion velocities, independently of the applied time step size. Consequently, the conservation of energy and momentum is guaranteed.

The stochastic equations of motion that are consistent with the higher order model are:

$$\begin{aligned} \frac{dV_i^{(\alpha)}}{dt} &= A_i^{(\alpha)} + 2\sqrt{D^{(\alpha)}} \frac{dW_i^{(\alpha)}}{dt} \\ &= -s^{(\alpha)}C_i^{(\alpha)} + K_i^{(\alpha)} + N_i^{(\alpha)} \left(C_i^{(\alpha)} \right) + 2\sqrt{D^{(\alpha)}} \frac{dW_i^{(\alpha)}}{dt}, \end{aligned} \quad (4.13)$$

$$\frac{dX_i}{dt} = V_i^{(\alpha)}. \quad (4.14)$$

Here $C_i^{(\alpha)} = V_i^{(\alpha)} - u_i^{(\alpha)}$ denotes the thermal part of the velocity $V_i^{(\alpha)}$. For the temporal evolution of the the species flow velocity $u_i^{(\alpha)}$ follows:

$$\frac{du_i^{(\alpha)}}{dt} = \left\langle \frac{dV_i^{(\alpha)}}{dt} \right\rangle = K_i^{(\alpha)}. \quad (4.15)$$

Combining:

$$\frac{dV_i^{(\alpha)}}{dt} = \frac{d \left(C_i^{(\alpha)} + u_i^{(\alpha)} \right)}{dt} = \frac{d \left(C_i^{(\alpha)} \right)}{dt} + K_i^{(\alpha)}, \quad (4.16)$$

with Eq. (4.13) yields a stochastic equation that determines the thermal particle velocities:

$$\frac{d \left(C_i^{(\alpha)} \right)}{dt} = \underbrace{-s^{(\alpha)}C_i^{(\alpha)} + 2\sqrt{D^{(\alpha)}} \frac{dW_i^{(\alpha)}}{dt}}_{L_i^{(\alpha)}} + N_i^{(\alpha)} \left(C_i^{(\alpha)} \right). \quad (4.17)$$

In order to solve Eq. (4.17), a similar approach as described in reference [56] is applied. The right side of Eq. (4.17) is divided into a linear part $L_i^{(\alpha)}$ and a non-linear part $N_i^{(\alpha)} \left(C_i^{(\alpha)} \right)$. Assuming constant macroscopic coefficients, for the resulting linear equation:

$$\frac{d \left(C_i^{(\alpha)} \right)}{dt} = -s^{(\alpha)}C_i^{(\alpha)} + 2\sqrt{D^{(\alpha)}} \frac{dW_i^{(\alpha)}}{dt}, \quad (4.18)$$

an analytic solution can be found:

$$C_i^{(\alpha),n+1} = C_i^{(\alpha),n} \exp \left(-s^{(\alpha),n} \Delta t \right) + \sqrt{\frac{D^{(\alpha),n}}{s^{(\alpha),n}}} \left(1 - \exp \left(-2s^{(\alpha),n} \Delta t \right) \right) \xi_i^{(\alpha)}. \quad (4.19)$$

The indices n and $n + 1$ refer to the beginning and the end of the time step, Δt denotes the time step size and $\xi_i^{(\alpha)}$ are independent standard normal deviates. For the integration of the non-linear part $N_i^{(\alpha)} \left(C_i^{(\alpha)} \right)$ a simple Euler scheme is applied. In

summary, as solution for Eq. (4.17) can be found:

$$C_i^{(\alpha),n+1} = C_i^{(\alpha),n} \exp(-s^{(\alpha),n} \Delta t) + \Delta t N_i^{(\alpha)} \left(C_i^{(\alpha),n} \right) + \sqrt{\frac{D^{(\alpha),n}}{s^{(\alpha),n}}} (1 - \exp(-2s^{(\alpha),n} \Delta t)) \zeta_i^{(\alpha)}. \quad (4.20)$$

Since the same logic was used for its derivation, expression (4.20) features a strong similarity to the solution (2.64) for the cubic FP model.

The Euler integration of the non-linear part leads to a wrong prediction of the species temperatures. This error can be corrected by a proper scaling of the new particle velocities:

$$\mathbf{C}^{(\alpha),n+1} \rightarrow \Xi \mathbf{C}^{(\alpha),n+1}. \quad (4.21)$$

The scaling parameter Ξ is defines as:

$$\Xi = \sqrt{\frac{3k_B T^{(\alpha),n+1} / m^{(\alpha)}}{\langle C_i^{(\alpha),n+1} C_i^{(\alpha),n+1} | f^{(\alpha)} \rangle / n^{(\alpha)}}}, \quad (4.22)$$

where $T^{(\alpha),n+1}$ denotes the correct species temperatures at the end of the time step. The temperatures $T^{(\alpha),n+1}$ are obtained as solution of a system of differential equation, that is discussed in more detail in App. C.4. The final particle velocity are calculated as:

$$\mathbf{V}^{(\alpha),n+1} = \Xi \cdot \mathbf{C}^{(\alpha),n+1} + \mathbf{u}^{(\alpha),n+1}. \quad (4.23)$$

The species flow velocities $\mathbf{u}^{(\alpha),n+1}$ are also given from the system of differential equations, described in App. C.4.

As described by Eq. (4.23), the final particle velocities are scaled and shifted to adopt the species temperatures $T^{(\alpha),n+1}$ and flow velocities $\mathbf{u}^{(\alpha),n+1}$ at the end of the time step. These quantities are calculated based on the system of differential equations, that is discussed in more detail in App. C.4. This system captures the time evolution of macroscopic quantities for a homogeneous gas. As long as the system is properly integrated, Eq. (4.23) leads to correct species temperatures and flow velocities in a homogeneous flow, regardless of the time step size.

To calculate particle positions, Eq. (4.14) has to be integrated. For the sake of simplicity, the solution as given by Eq. (2.65) is applied. In summary, particle positions and velocities are updated as described in Alg. 5.

1. Evaluate the required statistical moments for every grid cell;
2. Solve the system (App.C.31) and (App.C.32) to obtain the model parameters $\psi_{ij}^{(\alpha)}$ and $\gamma_i^{(\alpha)}$ for every grid cell;
3. Calculate the new thermal particle velocities using equation (4.20);
4. Solve the system (App.C.33) for every grid cell, applying $(\mathbf{u}^{(\alpha),n}, T^{(\alpha),n}, \mathbf{h}^{(\alpha),n})$ as initial condition;
5. Calculate the final particle velocities using equation (4.23);
6. Calculate the final particle positions using equation (2.65);

Algorithm 5: Calculation of new particle positions and velocities.

Due to the simple position integration scheme of Eq. (2.65), the time step should not be much larger than the local mean collision time to avoid errors caused by numerical diffusion. However, this limitation could be avoided by using more accurate, but also more complex integration schemes. For example, integration schemes can be defined that not only lead to correct temperatures and flow velocities in a homogeneous flow, as is the case with the scheme described above, but also to correct higher-order velocity moments, such as shear stress or heat flux [84, 55, 35].

4.3 Testcases

In this subchapter, the proposed method is applied to various test cases in order to discuss its performance for different gas flows. Figure 4.1 illustrates the setup of different test cases. A He-Ar mixture is employed for all simulations. The molecular reference diameters, which are used to calculate the frequencies (App.C.10), are listed in the appendix in Tab. F.1.

For all test cases, reference DSMC simulations using the same hard sphere collision model are performed. To avoid different results due to numerical discretization, the same spatial and temporal discretization is used for DSMC and FP simulations. All simulations are performed using the SPARTA code [39], which is extended by the FP method proposed in this chapter.

4.3.1 Heat bath

The relaxation behavior of diffusion velocities and temperatures to equilibrium is investigated. Therefore, different species are initially assigned to different macroscopic flow velocities and temperatures. Afterwards, the relaxation to equilibrium in a homogeneous, adiabatic heat bath is studied.

The test case setup is illustrated in Fig. 4.1. The simulation boundaries are chosen

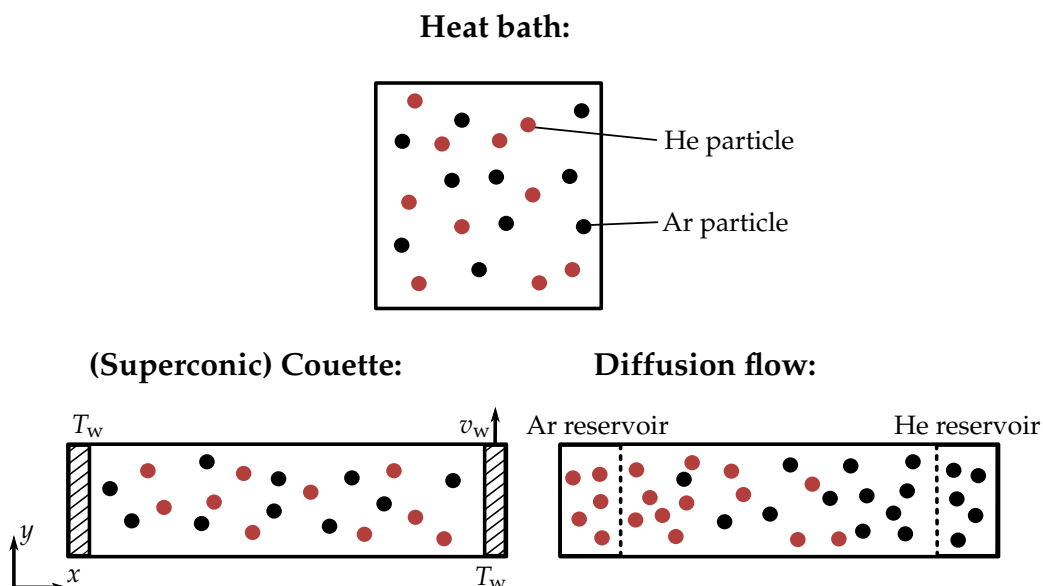


FIGURE 4.1: Illustration of different test cases. Upper: Heat bath test case as discussed in Subch. 4.3.1. Left lower: Couette flow as discussed in Subch. 4.3.2 and Subch. 4.3.3. Right lower: Diffusion flow as discussed in Subch. 4.3.4.

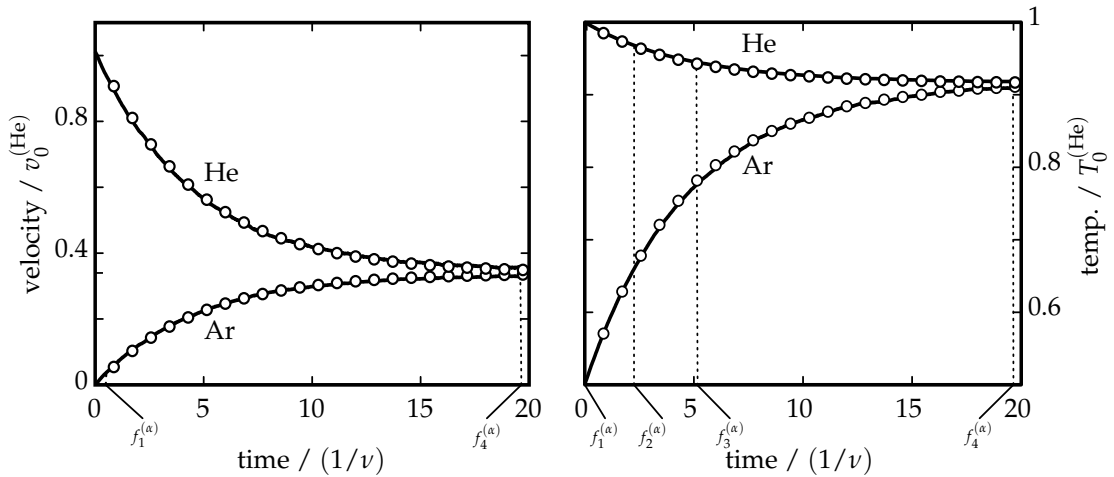


FIGURE 4.2: Left: Relaxation of the species flow velocities in terms of the initial velocity of He $v_0^{(\text{He})}$. Right: Relaxation of the species temperature in terms of the initial He temperature $T_0^{(\text{He})}$. Lines: DSMC results. Circles: FP results.

to be periodic in order to avoid influences of particle-wall interaction. In order to investigate the relaxation process of diffusion velocities, the particle velocities are set at the beginning of the simulation according to a Maxwell distribution with a temperature of $T_{\text{mix}} = 300$ K. The distribution of He velocities is additional shifted by $v_0^{(\text{He})} = 180$ m/s in x direction. To investigate the relaxation process of the species temperatures, the particle velocities are set at the beginning of the simulation according to a Maxwell distribution with a temperature $T_0^{(\text{He})} = 600$ K for the He particles and a temperature $T_0^{(\text{Ar})} = 300$ K for the Ar particles. Please note that the values

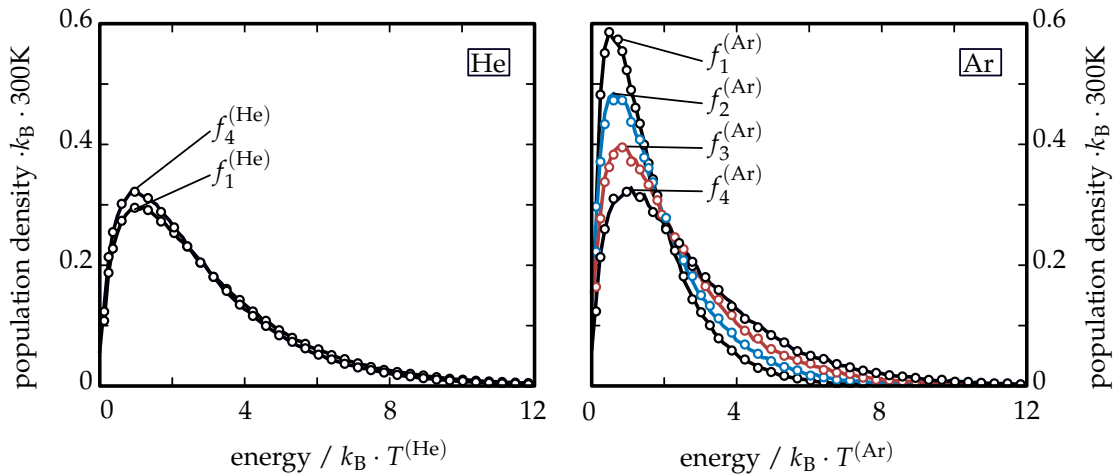


FIGURE 4.3: Left: Relaxation of the energy distribution function for He particles. Right: Relaxation of the energy distribution function for Ar particles. The unit of the distribution functions is the population density, which is defined as $dN/dE/dV/n$, where dN denotes the number of particles that can be found in a small energy interval dE and volume element dV and n is the particle density. Lines: DSMC results. Circles: FP results. Please note that for the sake of clarity, the distribution functions $f_2^{(\text{He})}$ and $f_3^{(\text{He})}$ are not shown in the graphic on the left. Please note that some of the results have been colored to better distinguish one from another.

described above were chosen in order to investigate the relaxation behavior as well as possible. In particular, care was taken to ensure that the initial velocities and temperatures differ sufficiently to achieve a high signal-to-noise ratio. Likewise, the difference should not be too big, otherwise the test case will be unrealistic. For each simulation, a single grid cell with a total number of 5000 particles is simulated. Since both relaxation processes are non-stationary problems, the results of 100 calculations are averaged for each case.

Figure 4.2 shows the relaxation process of the species flow velocities and temperatures. The simulation time t is normalized to an average collision time $\tau = 1/\nu$, with ν defined as:

$$\begin{aligned} \nu &\equiv \frac{1}{2} \left[\nu^{(\text{He-Ar})} (T = 300 \text{ K}) + \nu^{(\text{Ar-He})} (T = 300 \text{ K}) \right] \\ &= \frac{16}{5} \sqrt{\pi} d^{(\text{Ar-He})2} \sqrt{\frac{k_B 300 \text{ K}}{m^{(\text{He})}} + \frac{k_B 300 \text{ K}}{m^{(\text{Ar})}}} n_{\text{mix}}, \end{aligned} \quad (4.24)$$

and $n_{\text{mix}} = n^{(\text{He})} + n^{(\text{Ar})}$. The equilibrium values at the end of the relaxation process, which are given by:

$$v_{\text{eq}} = \frac{\rho^{(\text{He})} v_0^{(\text{He})}}{\rho^{(\text{He})} + \rho^{(\text{Ar})}} = 60 \frac{\text{m}}{\text{s}}, \quad (4.25)$$

$$T_{\text{eq}} = \frac{n^{(\text{He})} T_0^{(\text{He})} + n^{(\text{Ar})} T_0^{(\text{Ar})}}{n^{(\text{He})} + n^{(\text{Ar})}} = 550 \text{ K}, \quad (4.26)$$

are correctly predicted by the FP method. Also, a good agreement between FP and DSMC results during the relaxation process can be observed.

Figure 4.3 shows four different energy distribution functions calculated along the relaxation process of the species temperatures. Times when the distribution functions

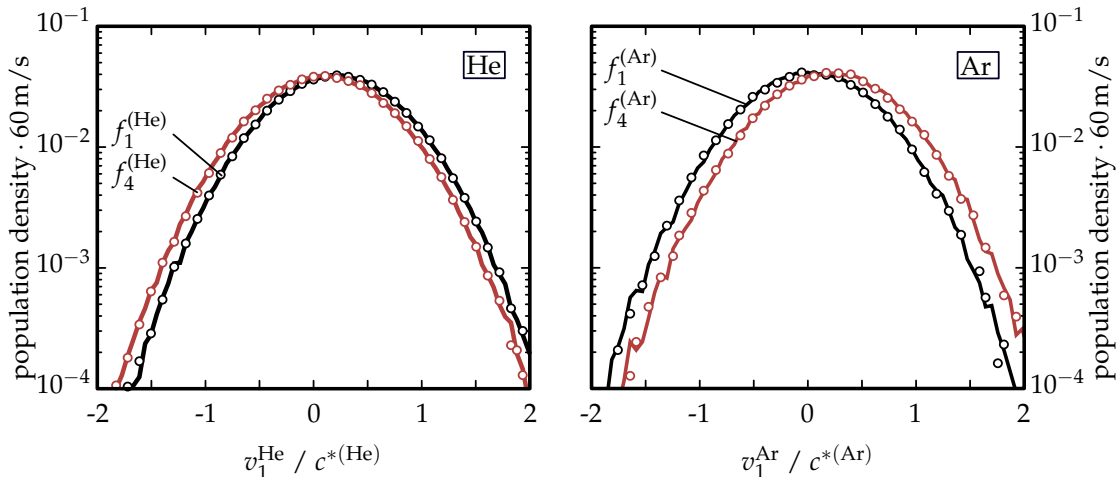


FIGURE 4.4: Left: Relaxation of the velocity distribution function for He particles. Right: Relaxation of the velocity distribution function for Ar particles. The unit of the distribution functions is the population density, which is defined as $dN/dv^{(\alpha)}/dV/n$, where dN denotes the number of particles that can be found in a velocity interval $dv^{(\alpha)}$ and volume element dV and $n^{(\alpha)}$ is the particle density. Lines: DSMC results. Circles: FP results. Please note that some of the results have been colored to better distinguish one from another.

are calculated are marked in the right side of Fig. 4.2. Again, good agreement between FP and the DSMC results can be observed. The equilibrium distribution $f_4^{(\alpha)}$ at the end of the relaxation process as well as the non-equilibrium distributions $f_1^{(\alpha)}$, $f_2^{(\alpha)}$ and $f_3^{(\alpha)}$ along the relaxation process are correctly predicted by the FP method. Figure 4.4 shows two different particle velocity distribution functions at the beginning and at the end of the relaxation process of the flow velocities. The particle velocities are normalized with the most probable speed $c^{*(\alpha)} = \sqrt{2 \frac{k_B 300 \text{ K}}{m^{(\alpha)}}}$. Times at which the distributions are calculated are marked on the right side of Fig. 4.2. Again, good agreement between the results of FP and DSMC simulations can be observed. In summary, the good agreement between FP and DSMC results is unexpected, since production terms used for construction of the method are only valid for near continuum flows, featuring similar species flow velocities and temperatures. This is clearly not the case for the relaxation test cases shown in this subchapter. The key point is the modeling approach used, in which each species is described by a separate distribution function. Thus, the model developed here can easily model different flow conditions for different species, even though the production terms used only apply to species with very similar flow conditions.

4.3.2 Couette flow

A Couette flow as sketched in Fig. 4.1 is investigated. The simplicity of this test case makes it ideal for investigating the performance of the FP method for describing rarefaction phenomena, such as e. g. the slip effects in vicinity of walls.

The flow is modeled in three dimensions. The domain boundaries in x -direction are modeled as fully diffusive walls with a temperature of $T_w = 300 \text{ K}$. The left wall is stationary, while the right wall moves in y -direction with a velocity of $v_w = 300 \text{ m/s}$. The distance between both walls is set to 1 m, which is also used as reference length scale for defining the Knudsen number. The domain boundaries in y - and z -direction are set as periodic. Simulations are performed for different Knudsen numbers $Kn \in \{1, 0.5, 0.25, 0.05\}$ assuming a constant mole fraction $\chi^{(\text{He})} = \chi^{(\text{Ar})} = 0.5$ and for different mole fractions $(\chi^{(\text{He})}, \chi^{(\text{Ar})}) \in \{(0.25, 0.75), (0.5, 0.5), (0.75, 0.25)\}$ assuming a constant Knudsen number $Kn = 0.05$. The domain is divided in 100 equal sized cells in x -direction, resulting in a cell size Δx which is 7 times smaller than the mean free path $\lambda^{(\text{He})}$ and 3 times smaller than $\lambda^{(\text{Ar})}$ for the smallest Knudsen number case.

The time step size is set to $\Delta t = \frac{\Delta x}{5 \cdot c^{*(\text{He})} + 300 \frac{\text{m}}{\text{s}}} \approx 2 \cdot 10^{-6} \text{ s}$, where $c^{*(\text{He})} = \sqrt{2 \frac{k_B 300 \text{ K}}{m^{(\text{He})}}}$ denotes the most probable speed of a He particle. To reduce the amount of statistical fluctuations, the scaling factor f_N is set to obtain a minimum number of 200 particles per cell and per species. A steady flow is achieved after 50000 simulation time steps. Subsequently, the under-relaxation technique as described in Subch. 2.3.2 is applied, using a weighting factor of $\nu = 0.001$. To obtain the final results, averages are taken every 10 time steps to a total number of 90000 averages, with exception of the case with the lowest Knudsen number, where the averages are taken every 100 time steps.

Figure 4.5 shows distributions of species flow velocities for cases with different Knudsen numbers. For the case with the lowest Knudsen number, the flow is almost in the continuum regime. Hence, the shape of the velocity distributions is linear, both species adopt similar flow velocities and slip effects on walls are negligibly

small. As the Knudsen number increases, rarefaction effects become important. Velocity slip on walls can be observed, the velocity distributions adopt a non-linear

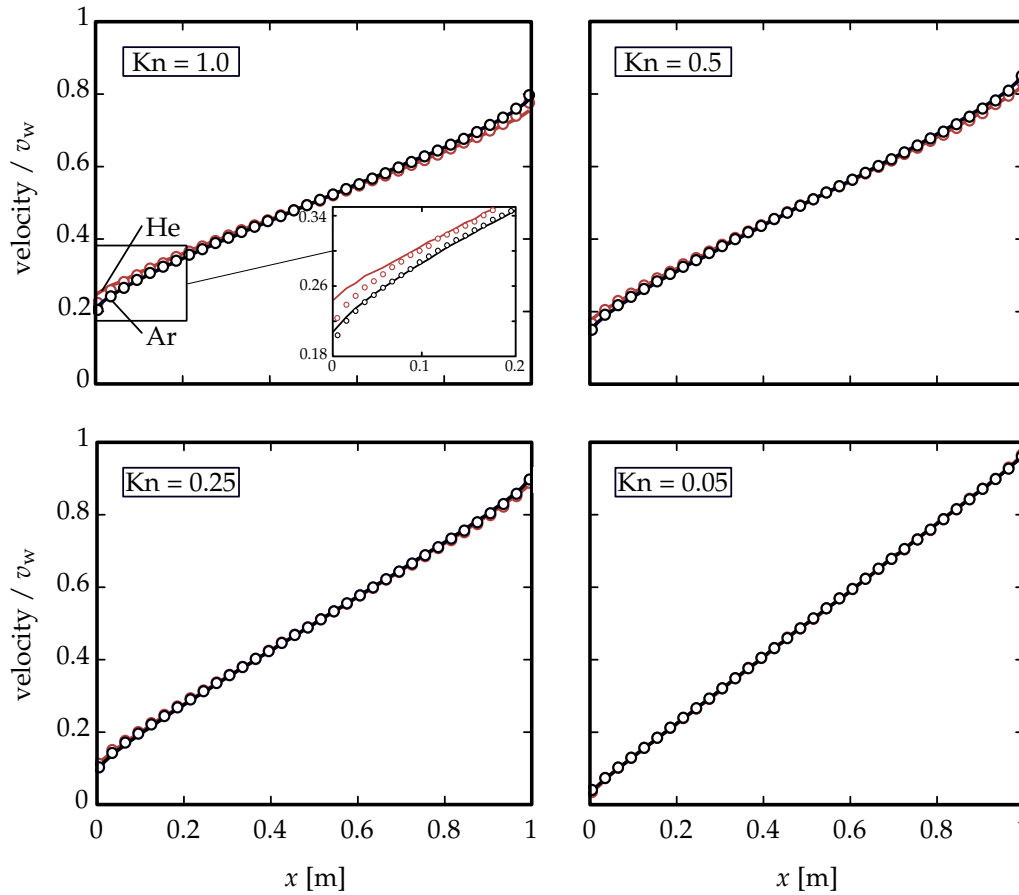


FIGURE 4.5: Species flow velocities of Ar and He in terms of the wall velocity v_w for different Knudsen numbers. Lines: DSMC results; Circles: FP results. (Black: Ar; Red: He) Please note that some of the results have been colored to better distinguish one from another.

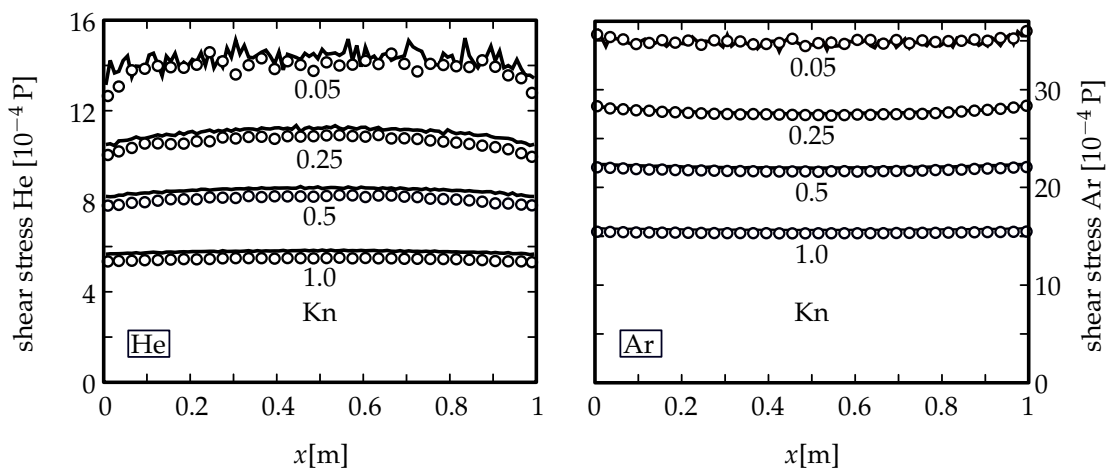


FIGURE 4.6: Left: Species shear stress of He for different Knudsen numbers. Right: Species shear stress of Ar for different Knudsen numbers. Lines: DSMC results. Circles: FP results.

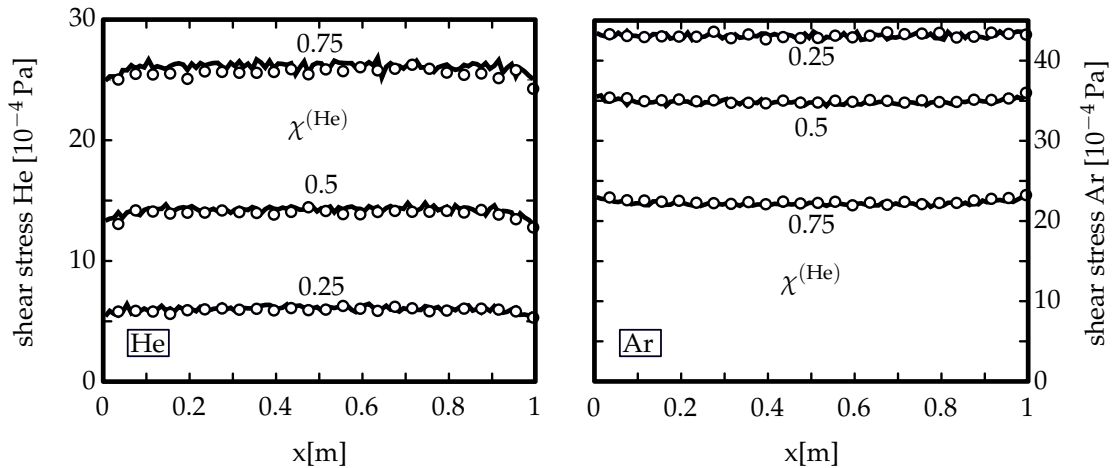


FIGURE 4.7: Left: Species shear stress of He for different mole fractions. Right: Species shear stress of Ar for different mole fractions. Lines: DSMC results. Circles: FP results.

shape and the velocity distributions separate. In particular, the He species shows a larger flow velocity than the Ar species. The FP method accurately predicts slip effects and the non-linear shape of the velocity distribution with increasing Knudsen numbers. Also, the separation of species flow velocities for the largest Knudsen number case is in principal predicted.

Figure 4.6 shows shear stresses of Ar and He for cases with different Knudsen numbers. The large amount of scatter for the lowest Knudsen case may be explained as the following: Because of the small Knudsen number, there are many collisions between particles. Therefore, a particle moves on average a shorter distance in a flow with a small Knudsen number than in a flow with a larger Knudsen number. In extreme cases, with very small Knudsen numbers and many collisions, it can happen that the particles in one grid cell do not exchange with particles in other grid cells over the time interval used for averaging. In such a case, the values that are used for averaging are not independent of each other, which is expressed in greater noise in the final result. The shear stresses decrease with increasing Knudsen numbers due to the decreasing number density and pressure. For the case with the lowest Knudsen number, good agreement is found between FP and DSMC results, whereas for the higher Knudsen number cases the FP method slightly over predicts shear stresses compared to the DSMC simulations.² Such deviations are to be expected, since the FP method is constructed in such a way that it is valid in the limit area of small Knudsen numbers. The behavior of the method far from equilibrium, however, has not been taken into account so far. Deviations are greater for the He species, which can be explained by the large mass ratio $\frac{m^{(Ar)}}{m^{(He)}} \approx 10$, causing the He species to reach thermal non-equilibrium faster.

Figure 4.7 shows species shear stresses for cases with different mole fractions. Due to the decreasing partial pressure, the shear stresses decrease with decreasing mole fraction. Independently of the mixture composition, shear stresses are accurately predicted by the FP method.

² In Fig. 4.6 it can be observed that the absolute deviation between DSMC and FP results remains approximately constant with changing Knudsen number. However, since the shear stress decreases with increasing Knudsen number, it follows that the relative deviation between DSMC and FP increases with increasing Knudsen number.

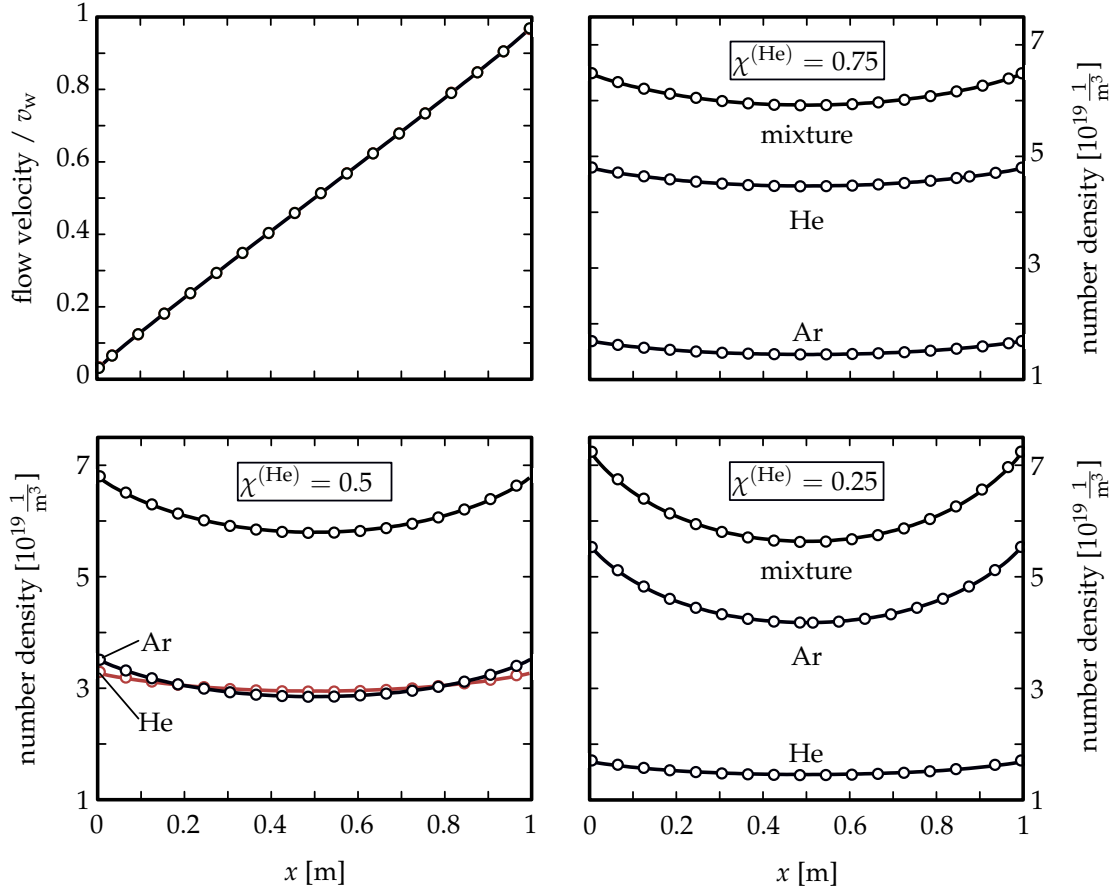


FIGURE 4.8: Left upper: Mixture flow velocity in terms of the wall velocity v_w for a density ratio of $\chi^{(\text{He})} = 0.5$. Other: Density distributions for different mole fractions. Lines: DSMC results. Circles: FP results. (Black: Ar; Red: He.) Please note that some of the results have been colored to better distinguish one from another.

The reader should note, that a correct prediction of shear stresses and flow velocities in the continuum regime, as investigated in this subchapter, leads to a correct prediction of viscosity for the entire mixture.

4.3.3 Supersonic Couette flow

Additionally, a supersonic Couette flow is investigated. In contrast to the subsonic Couette flow studied above, the supersonic Couette flow features a supersonic wall velocity. As a result, strong heat fluxes occur, that allow to study different phenomena such as e. g. thermodiffusion.

The same simulation domain and spatial resolution as described in Subch. 4.3.2 for the subsonic Couette flow is used, only the velocity of the moving wall is changed to $v_w = 1000$ m/s. Simulations are performed for a Knudsen number of $Kn = 0.05$ and three different mole fraction $\chi^{(\text{He})} \in \{0.25, 0.5, 0.75\}$. Later simulation results show, that the species temperature increases up to $T_{\max} \approx 450$ K along the simulation domain. Therefore, the time step size is adjusted to $\Delta t = \frac{\Delta x}{5 \cdot c^{*(\text{He})} + 1000 \frac{\text{m}}{\text{s}}} \approx 1 \cdot 10^{-6}$ s with $c^{*(\text{He})} = \sqrt{2 \frac{k_B 450 \text{ K}}{m^{(\text{He})}}}$. The scaling factor f_N is set to obtain a minimum number 200

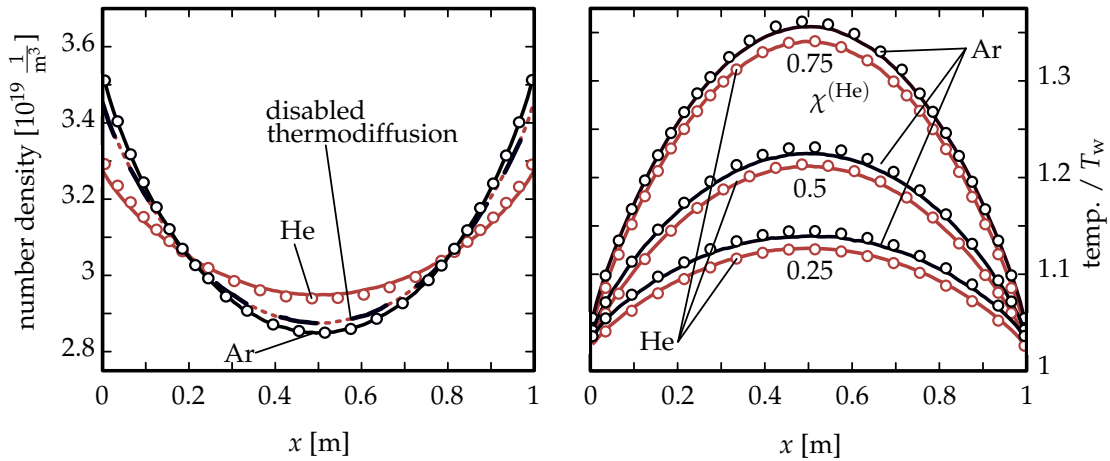


FIGURE 4.9: Left: Species density distributions of Ar and He for a mole fraction of $\chi^{(\text{He})} = 0.5$. Right: Species temperature distributions of Ar and He for different mole fractions. Solid lines: DSMC result; Circles: FP results; Dashed lines: FP results without thermodiffusion. (Black: Ar; Red: He)

particles per cell and per species. A steady flow is reached after 50000 simulation steps, which was checked by observing the development of the flow field over the simulation time. Because of the large signal to noise ratio no under-relaxation technique needs to be applied. To obtain the final result, averages are taken every 20 time steps up to a total number of 90000 averages.

The left upper picture in Fig. 4.8 shows the mixture flow velocity for the case with a mole fraction of $\chi^{(\text{He})} = 0.5$. As in the lowest Knudsen number case described in Subch. 4.3.2, the velocity distribution is linear and slip effects are negligible. The FP result fits very well the DSMC result.

The remaining pictures in Figure 4.8 show density distributions along the simulation domain. The parabolic shape of the distributions is due to the parabolic shape of the temperature distributions (see Fig. 4.9) and a constant pressure along the simulation domain. A good agreement between FP and DSMC results can be detected. It is

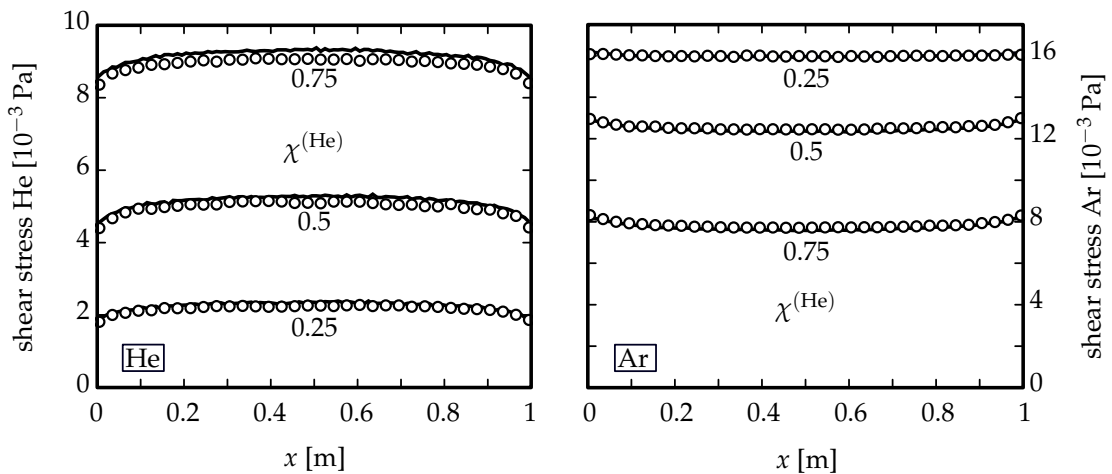


FIGURE 4.10: Left: Species shear stress of He for different mole fractions. Right: Species shear stress of Ar for different mole fractions. Lines: DSMC results; Circles: FP results.

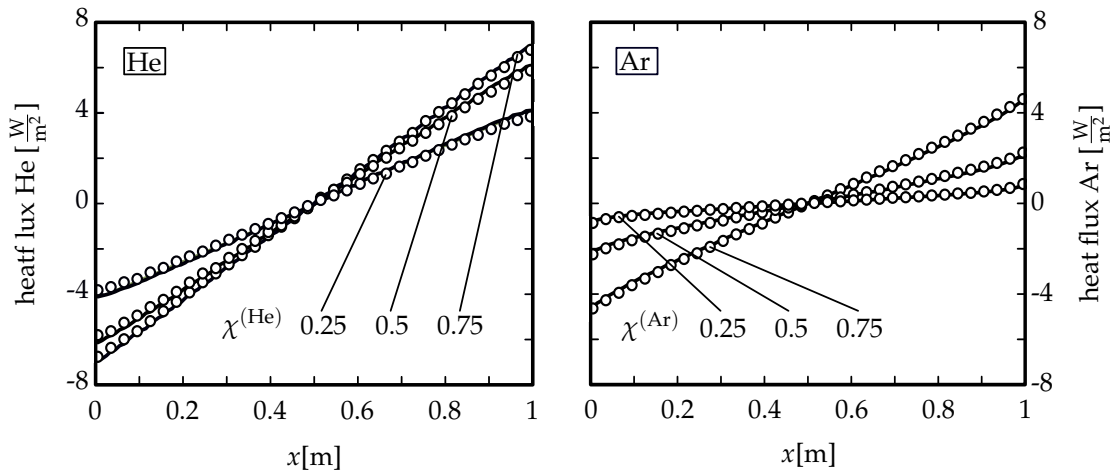


FIGURE 4.11: Left: Species heat flux distributions of He for different mole fractions. Right: Species heat flux distributions of Ar for different mole fractions. Lines: DSMC results; Circles: FP results.

worth noting that a separation of species densities for the case with a mole fraction of $\chi^{(\text{He})} = 0.5$ occurs. Since the binary diffusion coefficient is symmetric [30], this separation can not be caused by classical mass or pressure diffusion. Instead, the separation effect is the result of thermodiffusion [10].

As described by Burgers [22], thermodiffusion is induced by interaction of heat fluxes in production terms $P^{(\alpha)} \left(c_i^{(\alpha)} c_j^{(\alpha)} c_j^{(\alpha)} \right)$. The term marked as (*) in Eq. (4.7) represents such an interaction. To further study this effect, FP calculations *without thermodiffusion* are performed by simply neglecting this term. The left side of Fig. 4.9 shows resulting density distributions for the case with a mole fraction of $\chi^{(\text{He})} = 0.5$. While in the standard FP simulation thermodiffusion induces species separation, the FP simulation with neglected term does not capture thermodiffusion and species separation is consequently not predicted.

The right side of Fig. 4.9 shows the temperature distributions along the simulation domain. The temperature increases with increasing He fraction due to an increase of the dissipated flow energy. In addition, due to the supersonic wall velocity, non-equilibrium effects can be observed. Species temperatures are separated and a significant temperature slip occurs at the walls. With the exception of small deviations, the FP method accurately reproduces the DSMC results.

Figure 4.10 shows the species shear stresses. The shear stresses are non-constant over the domain, indicating a strong degree of thermal non-equilibrium. The boundary layer is clearly indicated by a strong change of shear stresses. The FP method accurately predicts the shear stress distributions expect of small deviations for the case with a mole fraction of $\chi^{(\text{He})} = 0.75$.

Figure 4.11 shows the distributions of the species heat fluxes. The distributions feature a non-linear linear shape, indicating a strong degree of thermal non-equilibrium. The FP method accurately reproduces the DSMC results.

4.3.4 One-dimensional mass diffusion

A one-dimensional diffusion test case is investigated. Since this test case features strong species separation, it is suitable for examining the performance of the FP method to describe diffusion effects.

The test case setup is illustrated in Fig. 4.1. The flow is treated as three-dimensional. The lower x -boundary is modeled as reservoir of Ar particles and the upper x -boundary as reservoir of He particles. Particles are generated at reservoir boundaries as described by the stream boundary condition presented in Subch. 2.2.2, assuming a vanishing flow velocity. For both reservoirs the same temperature $T_0 = 300$ K is set. The distance between the x -boundaries is set to 1 m, which is also used as reference length scale to define the Knudsen number. For the y - and z -boundaries periodic boundary conditions are applied. The reservoir densities are set according to different Knudsen numbers $Kn \in \{0.5, 0.25, 0.1, 0.05\}$ and a constant mole fraction $\chi^{(\text{He})} = \chi^{(\text{Ar})} = 0.5$. The domain is divided in 100 equal sized cells in x -direction resulting in a cell size of Δx which is 7 times smaller than the mean free path $\lambda^{(\text{He})}$ and 3 times smaller than $\lambda^{(\text{Ar})}$ for the smallest Knudsen number case. The simulations show that the He flow velocity increases up to $800 \frac{\text{m}}{\text{s}}$ in x -direction. Therefore, the time step size is set to $\Delta t = \frac{\Delta x}{5 \cdot c^{*(\text{He})} + 800 \frac{\text{m}}{\text{s}}} \approx 2 \cdot 10^{-6} \frac{\text{m}}{\text{s}}$ with $c^{*(\text{He})} = \sqrt{2 \frac{k_B 300 \text{K}}{m^{(\text{He})}}}$. The number of simulated molecules is adjusted to obtain a minimum number of 15 particles per cell and per species. A steady flow is reached after 50000 simulation steps, which was checked by observing the development of the flow field over the simulation time. Because of the large signal to noise ratio no under-relaxation technique is applied. To obtain the final results, averages are taken every 10 time steps

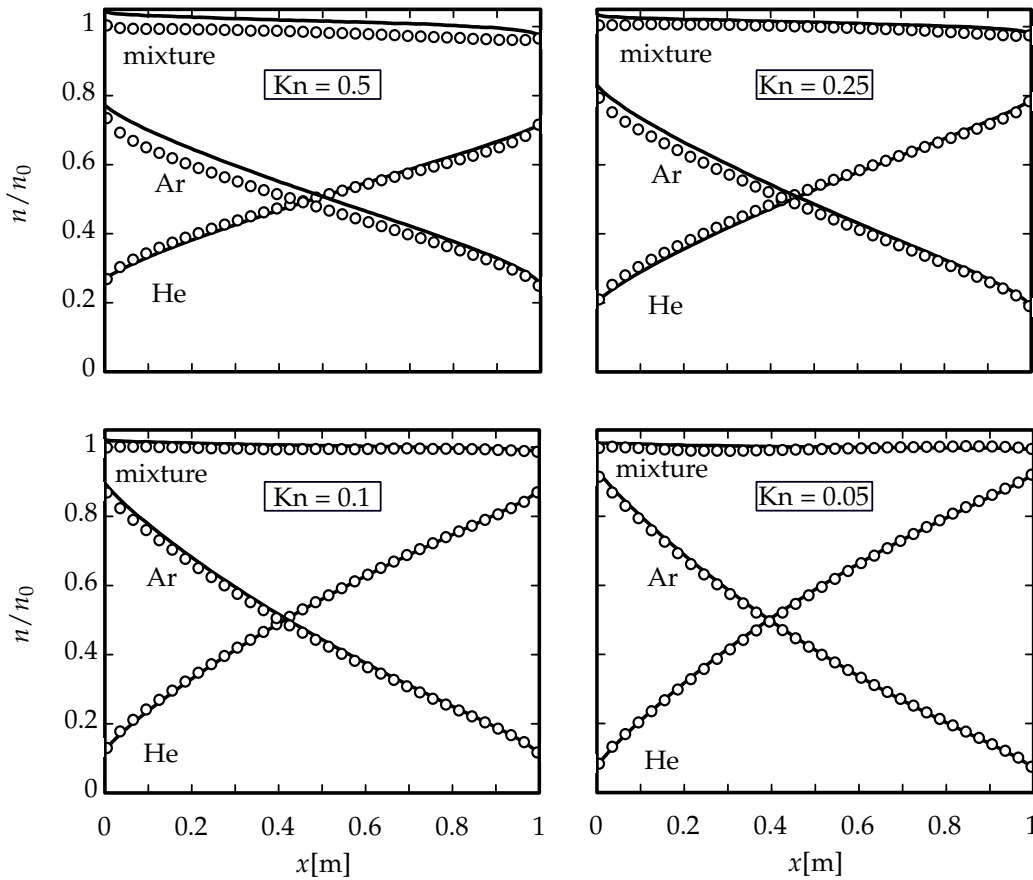


FIGURE 4.12: Number densities of Ar, He and the entire mixture in terms of the reservoir densities n_0 for different Knudsen numbers. Lines: DSMC results; Circles: FP results.

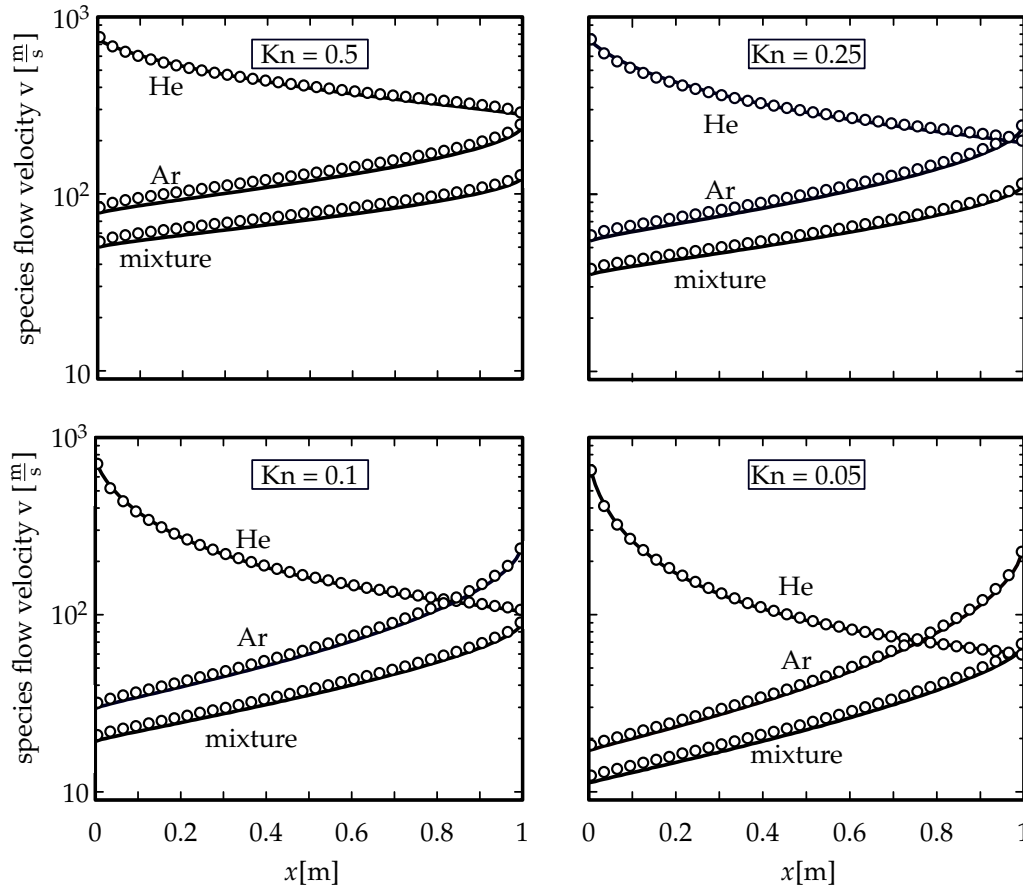


FIGURE 4.13: Magnitude of the flow velocity for Ar, He and the entire mixture for different Knudsen numbers. Lines: DSMD results; Circles: FP results.

up to a total number of 90000 averages.

Figure 4.12 shows distributions of species densities. For the flow with the lowest Knudsen number, good agreement between FP and DSMD results can be found. As the Knudsen number increases, increasing differences can be detected. In particular, the He density becomes over and the Ar density under predicted by the FP method. Figure 4.13 shows the distribution of the species flow velocities. Even for the case with the lowest Knudsen number small deviations between FP and DSMD results can be detected. The reason for this disagreement can be explained by the production terms that have been utilized to construct the FP method. The terms (App.C.1) - (App.C.4) are of linear order. This approximation is only valid if differences between the species flow velocities are small. This approximation is clearly not valid for this test case. Even for the flow with the smallest Knudsen number differences between species flow velocities are dominant.

As the Knudsen number increases differences between DSMD and FP results increase. In particular the He velocity is under predicted and the Ar velocity is over predicted by the FP method. Since the species mass flux must be constant, the deviation in the flow velocities also explains the previously observed deviations in the density distribution.

4.4 Summary and conclusion

In this chapter, a procedure has been developed to simulate gas mixtures with multiple species within the framework of the kinetic FP method. For this purpose, separate FP equations are defined for each species, describing the time evolution of the associated particle distribution functions. The model parameters of the FP equations were set very similarly to the single species model of Gorji et al. [55]. In particular, a polynomial dependence of particle velocities was chosen for the drift coefficient. Analogous to the modeling of the single-species FP methods, the FP equations were not solved directly. Instead, the associated stochastic equations of motion were solved to simulate the microscopic particle motion. For this purpose, an algorithm that guarantees conservation of energy and momentum was proposed.

The capability of the method was investigated against the DSMC method in a series of test cases typical for hypersonic gas flows. An Ar-He mixture was used as the test gas. As an important result, it can be observed that the method is well suited to describe non-equilibrium flows. Even in strong non-equilibrium cases, no major deviations from reference DSMC calculations can be detected. On closer inspection, the capability of the method depends on the degree of dilution. Deviations from the DSMC reference simulations increase with increasing Knudsen number. However, it should be emphasized that important non-equilibrium effects, such as slip effects in the Couette flow, are predicted. Similarly, the capability of the method depends strongly on the parameter under study. For example, the FP method predicts the flow velocity in the the Couette flow well even for high Knudsen numbers. In contrast, deviations are observed for shear stresses. Similarly, the FP method accurately predicts the density distributions for the supersonic Couette flow, while small deviations are again observed for shear stresses. It can be concluded that the performance of the method generally increases for lower order velocity moments. As another result, it can be stated that the FP method is able to describe flows in which different species assume different flow states. For example, the method shows good performance for the diffusion test case where species assume very different flow velocities. This behavior is a result of the modeling approach taken in deriving the FP model. As described above, each species is assumed to adopt its own distribution function and FP equation. As a result, species may assume different flow quantities such as flow velocity or temperature.

Furthermore, it was shown that with the model described here, it is possible to flexibly switch the thermal diffusion effect on or off by simply deleting corresponding terms from the model. This is an interesting feature of the model, as it allows to study the influence of thermal diffusion effect by simply performing calculations with and without this effect. This is not easily possible with, for example, the DSMC method. In Ch. 8 it will be shown how this feature can be applied in practice.

In order to better understand the significance of the model described in this chapter, it makes sense to take a look at the FP models available in the literature for the description of gas mixtures. To the best of the author's knowledge, at the time of writing this chapter, the model of Gorji et al. [51] was the only one that allowed the modeling of gas mixtures in the framework of the kinetic FP method. This model was formulated for binary gas mixtures and adopts the Maxwell molecular model to model molecular collision processes. Thus, although the model of Gorji et al. [51] is an important theoretical contribution in modeling gas mixtures with the kinetic

FP method ³, it is unfortunately unsuitable for many practical applications, since in practice flows with more than two species are often encountered and the Maxwell collision model is often not adequate enough to describe interaction of particles. In contrast, the model of this chapter is formulated for an arbitrary number of species and is based on the realistic HS molecular model, which probably gives it a clear advantage for many applications.

Finally, it should be noted that the HS model has been used as standard in the DSMC method for several decades to describe molecular collision processes [10]. This results in two important advantages for the application of the FP model from this chapter: On the one hand, model parameters for the HS model are known for most relevant species due to the many years of application of the HS model in the DSMC method. These could be easily adopted for a kinetic FP simulation. On the other hand, the DSMC and FP methods can be coupled very easily, since both methods are based on the same molecular collision model. Thus, it is trivial to achieve a consistent physical modeling of both methods, which is mandatory for a coupled simulation. This is a big advantage compared to many other simulation methods, where for more complex gases a lot of effort has to be spent to create a consistent modeling of both methods in coupled simulations [130].

³This model served as a template for the work from this chapter

Chapter 5

Modeling of variable hard sphere gas mixtures

In the previous chapter, a FP method was developed to describe gas mixtures based on the HS collision model. However, the HS collision model is not suitable for describing many gas species, since it leads for these species to unrealistic transport coefficients, such as viscosity or thermal conductivity, in the Navier-Stokes limit. For this reason, as described in Subch. 2.2.4, the more realistic variable hard sphere (VHS) model [11] was developed.

In this chapter, the previously described HS-FP method is generalized for describing particle interaction by the VHS collision model. The chapter is structured into three parts. In Subch. 5.1, the VHS-FP method is constructed. Subchapter 5.2 examines various test cases to analyze the validity of the model. Finally, Subch. 5.3 presents the conclusion of this chapter.

Please note that the main parts of this chapter have been published in reference [73].

5.1 Fokker-Planck method for a VHS gas mixture

Similar as described in Ch. 4, the VHS-FP model is constructed based on production terms. The calculation of Boltzmann production terms for the VHS model is a non-trivial task. However, in [64, 109] Boltzmann production terms for binary gas mixtures, assuming a general molecular interaction potential and a distribution function according to Grad's 13 moment method are evaluated. Appendix D.1 discusses how these results can be applied to derive Boltzmann production terms for the VHS collision model and for any number of species.

Due to the similarity of the HS and VHS collision model, both collision models lead to similar Boltzmann production terms. In particular, VHS production terms (App.D.13) - (App.D.16) feature the same structure than HS production terms (App.C.1) - (App.C.4). Only differences are terms $\text{VHS}[i]$ ($i \in \{1, 2, 3, 4, 5, 6\}$), that depend on the VHS collision parameters. Therefore, the VHS-FP model can be derived similar to the HS-FP model that is described in Ch. 4. For clarity, this derivation is not repeated. Instead, only the final results are presented. In the following, the terms $\text{VHS}[i]$ are marked in red color in order to indicate differences from the HS-FP model. For the special case of HS molecules, these parameters become one and the VHS-FP model reproduces the HS-FP model.

For the diffusion coefficient the following expression can be found:

$$D_{|\text{VHS}}^{(\alpha)} = \frac{10}{6} \text{VHS}[1] \sum_{\beta=1}^{N_s} \nu_{|\text{VHS}}^{(\alpha\beta)} \mu^{(\beta)} \mu^{(\beta)} \left[\frac{k_B T^{(\alpha)}}{m^{(\alpha)}} + \frac{k_B T^{(\beta)}}{m^{(\beta)}} + \frac{1}{3} \left(\mathbf{v}^{(\alpha)} - \mathbf{v}^{(\beta)} \right)^2 \right]. \quad (5.1)$$

The parameter VHS[1] is defined in Eq. (App.D.18) while the frequency $\nu_{|\text{VHS}}^{(\alpha\beta)}$ is given by expression (App.D.17). Note the similar structure of the diffusion coefficient (5.1) and the diffusion coefficient (4.9) for the HS-FP model. For the drift coefficient, the following ansatz is made:

$$A_i^{(\alpha)} \equiv -s_{|\text{VHS}}^{(\alpha)} c_i^{(\alpha)} + K_{i|\text{VHS}}^{(\alpha)} + \psi_{ij|\text{VHS}}^{(\alpha)} c_j^{(\alpha)} + \gamma_{i|\text{VHS}}^{(\alpha)} \left(c_j^{(\alpha)} c_j^{(\alpha)} - \frac{1}{n^{(\alpha)}} \langle c_j^{(\alpha)} c_j^{(\alpha)} | f^{(\alpha)} \rangle \right), \quad (5.2)$$

The frequencies $s_{|\text{VHS}}^{(\alpha)}$ are given by:

$$s_{|\text{VHS}}^{(\alpha)} = \frac{5}{3} \text{VHS}[1] \sum_{\beta=1}^{N_s} \nu_{|\text{VHS}}^{(\alpha\beta)} \mu^{(\beta)}, \quad (5.3)$$

while the constants $K_{i|\text{VHS}}^{(\alpha)}$ are defined by:

$$K_{i|\text{VHS}}^{(\alpha)} = - \sum_{\beta=1}^{N_s} \nu_{|\text{VHS}}^{(\alpha\beta)} \mu^{(\beta)} \left[\frac{5}{3} \text{VHS}[1] \left(u_i^{(\alpha)} - u_i^{(\beta)} \right) + \underbrace{\frac{1}{6\hat{\theta}^{(\alpha)}} \text{VHS}[2] \left(\frac{1}{\rho^{(\alpha)}} \hat{h}_i^{(\alpha)} - \frac{1}{\rho^{(\beta)}} \hat{h}_i^{(\beta)} \right)}_* \right]. \quad (5.4)$$

The parameter VHS[2] is defined in Eq. (App.D.19). Again, note the similarity of the drift coefficient (5.2) to the drift coefficient of the higher order HS-FP model (4.10). As described in Subch. 4.3.3, the marked term in expression (5.4) is related to the thermodiffusion effect. The nine model parameters $\psi_{ij|\text{VHS}}^{(\alpha)}$ and $\gamma_{i|\text{VHS}}^{(\alpha)}$ are chosen, such that:

$$P_{\text{FP}}^{(\alpha)} \left(c_i^{(\alpha)} c_j^{(\alpha)} \right) \stackrel{!}{=} P_{\text{VHS}}^{(\alpha)} \left(c_{<i}^{(\alpha)} c_{>j}^{(\alpha)} \right) + \frac{1}{3} \delta_{ij} P_{\text{VHS}}^{(\alpha)} \left(c_i^{(\alpha)} c_i^{(\alpha)} \right), \quad (5.5)$$

$$P_{\text{FP}}^{(\alpha)} \left(c_i^{(\alpha)} \mathbf{c}^{(\alpha)} \mathbf{c}^{(\alpha)} \right) \stackrel{!}{=} P_{\text{VHS}}^{(\alpha)} \left(c_i^{(\alpha)} \mathbf{c}^{(\alpha)} \mathbf{c}^{(\alpha)} \right). \quad (5.6)$$

Since the drift coefficients (5.2) and (4.10) have the same structure, the expressions (5.5) and (5.6) lead to the same system of linear equations as discussed in App. C.3 for the HS-FP model, only the right-hand production terms need to be adapted accordingly.

To integrate the corresponding stochastic equations of motion, the same algorithm as discussed in Subch. 4.2 for the HS-FP model can be used. Simply the right side of the system of differential equations (App.C.33) needs to be adapted to the VHS production terms.

5.2 Test cases

In the following subchapter, the proposed method is applied to different test cases. Simulations are performed for a He-Ar mixture. Collision parameters, that are used to calculate the quantities (App.D.17) - (App.D.23), are listed in Tab. F.3. For all test cases, reference DSMC simulations are performed, assuming the same VHS collision model. For an additional comparison, also simulations assuming an equivalent HS collision model are performed. Therefore, similar collisions parameters as for the VHS model are used, but the viscosity exponent is adjusted to $\omega^{(\alpha\beta)} = 0.5$. To avoid different results due to numerical discretization, the same spatial and temporal resolution is used for the DSMC and the FP simulations, unless stated otherwise. All

simulations are performed using the SPARTA code [39] that has been extended by the proposed FP method.

5.2.1 Supersonic Couette flow

In order to check the performance of the FP method for describing shear stresses, heat fluxes and the thermodiffusion effect, the supersonic Couette flow is investigated. Therefore, the same simulation setup as described in Subch. 4.3.3 is applied. Simulations are performed for a Knudsen number of $Kn = 0.05$ assuming a constant mole fraction $\chi^{(\text{He})} = \chi^{(\text{Ar})} = 0.5$. Figure 5.1 compares FP and DSMC results.

The upper left plot of Fig. 5.1 shows the density distributions of He and Ar along the simulation domain. As described in Subch. 4.3.3, thermodiffusion induces species separation. The separation effect is slightly larger for the HS molecule model, indicating a smaller thermal-diffusion ratio [97] for the VHS molecule model.

The upper right graph of Fig. 5.1 shows temperature distributions of He and Ar. As for the HS-FP method, a significant temperature slip occurs at walls. In addition, species temperatures are separated, indicating a strong degree of thermal non-equilibrium. Differences between the HS and the VHS method are only small. In

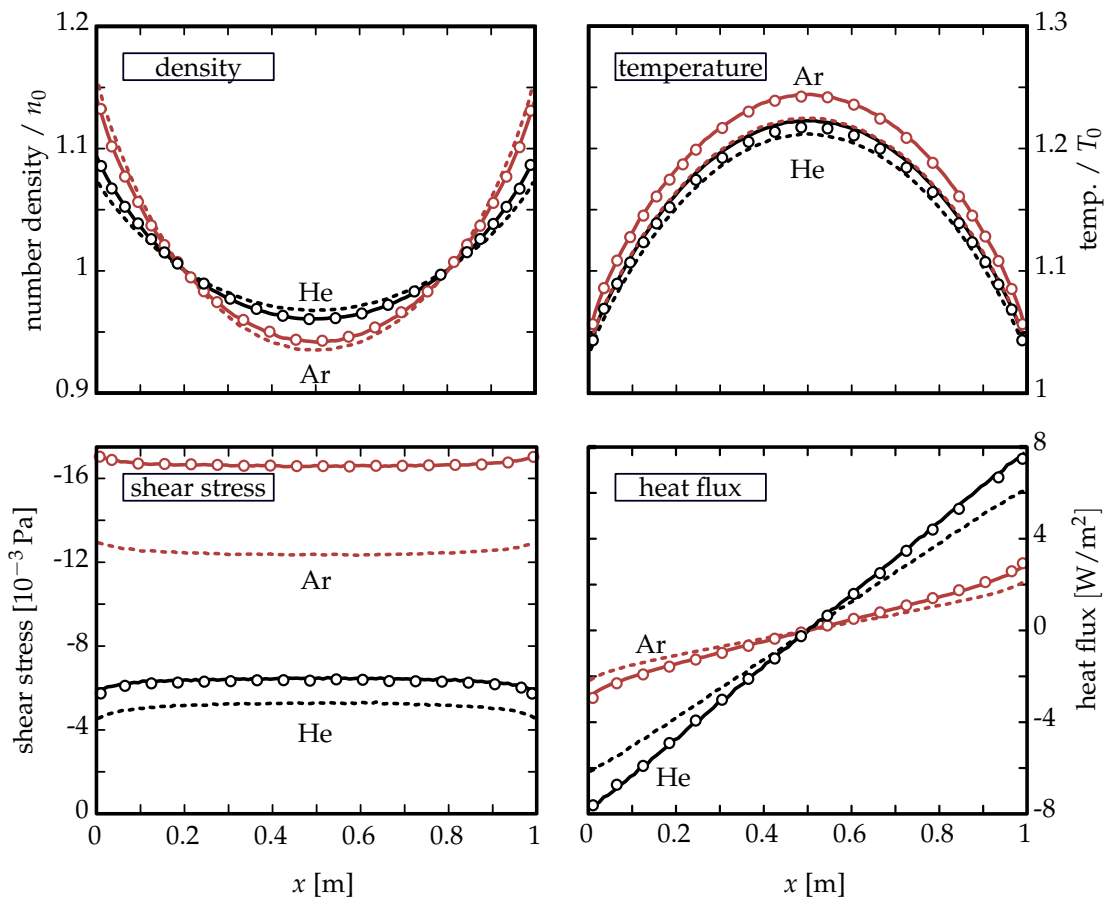


FIGURE 5.1: Species density, temperature, shear stress and heat flux distributions for a supersonic Couette flow. Lines: DSMC / VHS results. Circles: FP / VHS results. Dashed lines: DSMC / HS results. (Black: He; Red: Ar).

particular, the molecular model appears to have little influence on the slip temperature.

The lower left plot of Fig. 5.1 shows shear stress distributions of He and Ar along the simulation domain. While shear stresses are nearly constant in the bulk flow, they adopt a non-constant shape in the boundary layer. As expected, the collision model strongly influences the shear stress distributions. In particular, the HS model leads to a smaller shear stress compared to the VHS model.

The lower right graph of Fig. 5.1 shows heat flux distributions of He and Ar along the simulation domain. In the bulk flow, the heat flux distributions are nearly linear, while they adopt a non-linear shape in the boundary layer.

In general, very good agreement between VHS-FP results and the reference DSMC simulations can be found. Species separation in density and temperature distributions as well as shear stress and heat flux distributions are correctly predicted.

5.2.2 Diffusion flow

In order to check the performance of the method for predicting diffusion phenomena, the one-dimensional diffusion test case is investigated. The same setup as described in Subch. 4.3.4 is applied.

Reservoir densities are chosen according to a Knudsen number of $Kn = 0.05$ assuming a constant mole fraction $\chi^{(\text{He})} = \chi^{(\text{Ar})} = 0.5$. Figure 5.2 compares FP and DSMC results.

The left graph of Fig. 5.2 shows the species density distributions. Interestingly, no differences between HS and VHS results can be determined which indicates a weak dependence of the diffusion coefficient on the molecular collision model.

The right side of graph Fig. 5.2 shows the species velocity distributions. Again, there are only minor differences between different collision models. In general, the FP model accurately reproduces DSMC results.

5.2.3 Flat plate

In order to check the performance of the method for a more complex test case, a two-dimensional, hypersonic flow over a flat plate is considered.

The simulation parameters are adopted from the test case that is described in Subch. 3.6.4.

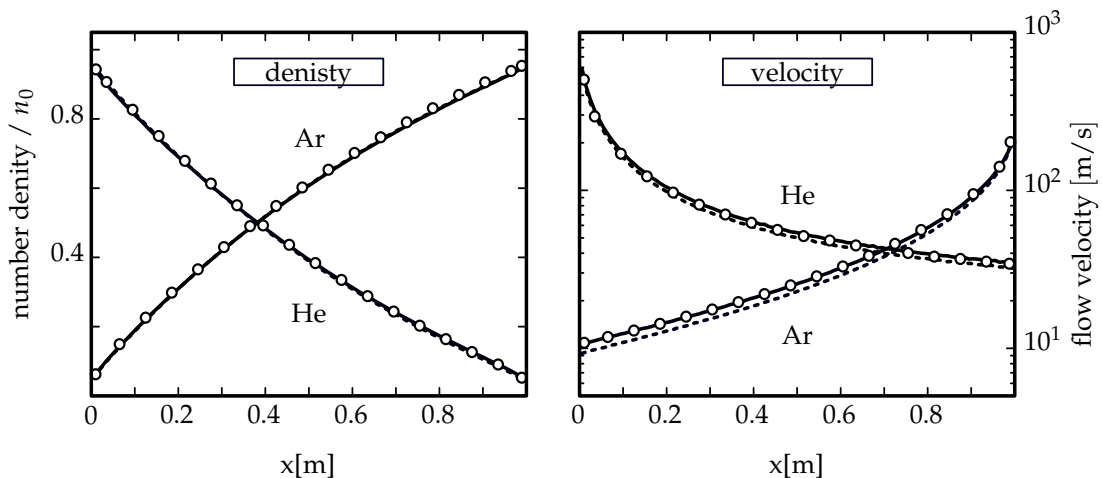


FIGURE 5.2: Species density and velocity distributions for a diffusion flow. Lines: DSMC / VHS results. Circles: FP / VHS results. Dashed lines: DSMC / HS results.

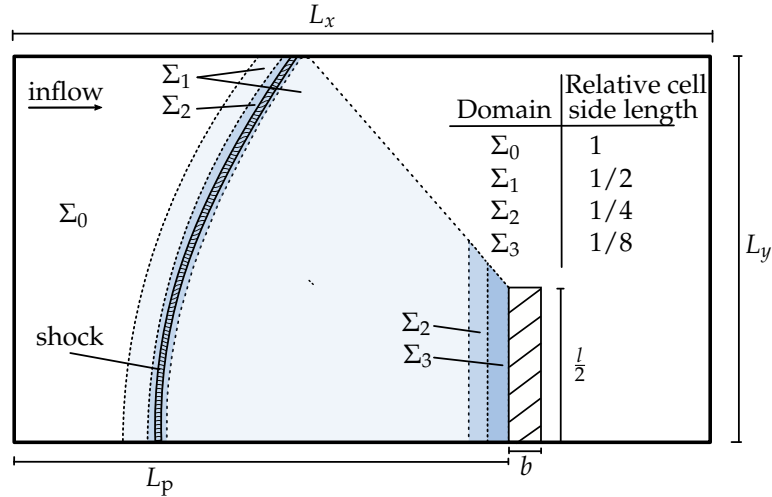


FIGURE 5.3: Computational domains for the FP simulation of the flat plate test case.

Only the size of the simulation domain in flow direction is adjusted to $L_x = 0.6$ m, since the distance between shock wave and plate becomes larger for the He-Ar mixture compared to a pure N_2 gas. The mole fraction on the inflow is set to $\chi_\infty^{(\text{He})} = \chi_\infty^{(\text{Ar})} = 0.5$. For the DSMC simulation, the grid cells are adapted step wise to the local mean free path. For the FP simulation, the flow domain is divided into areas with different grid resolutions, as shown in Fig. 5.3. The domain Σ_0 features a mesh with a cell size of (2.5×2.5) mm. Note that the grid geometry is arranged to properly resolve the shock wave structure and the boundary layer. For the FP and DSMC simulations the same time step size $\Delta t = 2 \cdot 10^{-7}$ s is applied, which resolves the mean collision time in the stagnation point. The scaling factor F_N between the number of real to simulated molecules is adjusted to obtain a number of 30 particles per cell and per species in the inflow region. To obtain the final results, averages are taken every 5 time steps up to a total number of 2400 averages.

Figure 5.4 shows the temperature distributions of He and Ar in the simulation domain. For the He species, the shock wave width is larger than for the Ar species. This effect can be explained by the small mass of the He particles, leading the He species to adopt a larger mean free path compared to the Ar species, as discussed

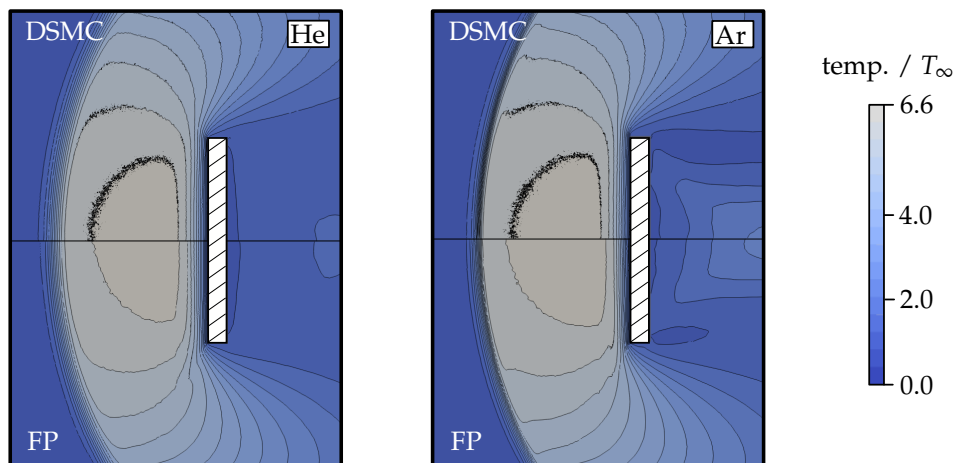


FIGURE 5.4: Temperature distributions of He and Ar for the flat plate test case.

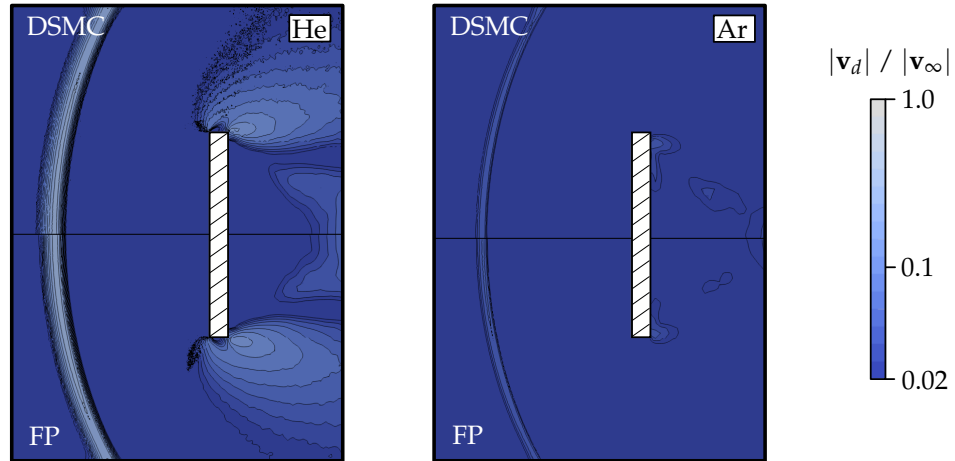


FIGURE 5.5: Normalized magnitude of diffusion velocity of He and Ar for the flat plate test case.

in Subch. 2.1.3. The larger mean free path means that a thermal non equilibrium is reached more quickly, which leads to a larger shock wave width. The FP method accurately reproduces DSMC results for the He species. The shock wave width as well as the width of the boundary layer are correctly predicted. For the Ar species, small deviations between FP and DSMC results can be observed. In particular, deviations occur in the relaxation structure behind the plate.

Figure 5.5 shows the normalized absolute value of the diffusion velocities for He and Ar in the simulation domain. Due to thermal non-equilibrium, diffusion becomes dominant in the shock wave and the expansion structure behind the plate. Because of the large mass ratio $m^{(\text{Ar})}/m^{(\text{He})} \approx 10$, the diffusion velocity is much large for the He species than for the Ar species. The FP method accurately reproduces DSMC results for both species.

Figure 5.6 shows the mole fractions for He and Ar in the simulation domain. Species separation occurs in the shock wave, behind the plate and in the boundary layer.

The deviations between FP and DSMC methods described above are to be expected,

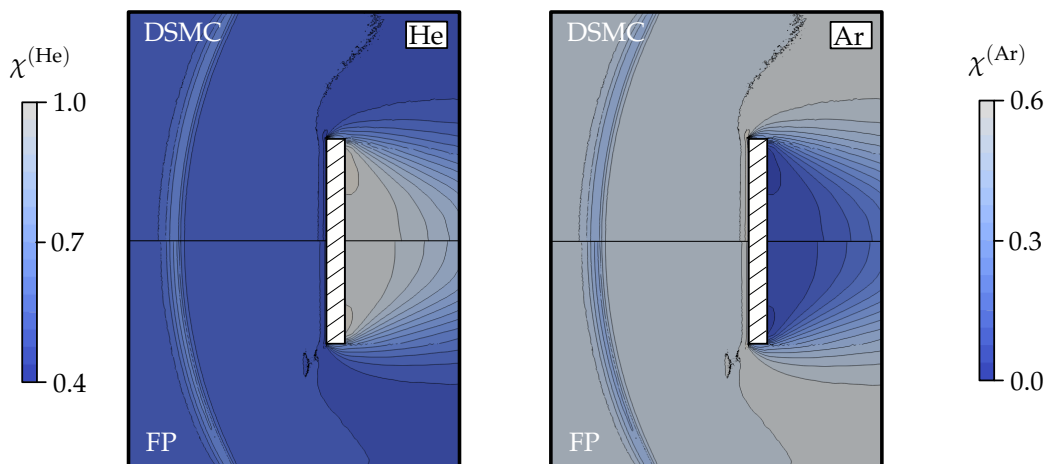


FIGURE 5.6: Distributions of mole fractions of He and Ar for the flat plate test case.

since the FP method constructed in this chapter is essentially based on the same assumptions as Gorjic's cubic model for single species gases (see Subch. 4.1) which has already shown similar deviations from the DSMC method (see Subch. 3.6.4).

5.3 Summary and conclusion

In this chapter, it was demonstrated how the FP method described in Ch. 4 can be extended so that molecular interaction is described by the VHS collision model. It can be seen that due to the algorithmic similarity of the VHS and HS collision models, the FP model developed in this chapter is very similar to the model in Chap. 4. In particular, the drift and diffusion coefficients have the same structure and the same numerical algorithm can be used for the simulation method to calculate the particle trajectories. In the limiting case, the model from Ch. 4 is included in the model developed here.

To evaluate the performance of the FP method, two of the test cases discussed in Subch. 4.3 are repeatedly simulated using the VHS-FP method from this chapter. Overall, a good performance of the VHS-FP method can be observed. Temperature, density, heat flux, and shear stress distributions agree well with results from DSMC calculations. The algorithmic similarity with the HS FP method from Ch. 4 suggests that the VHS-FP method would also show similar results for the other test cases studied in Ch. 4.

To investigate the applicability of the VHS-FP method for a more complex supersonic flow, a Mach 5 flow around a flat plate was also simulated. Apart from small deviations, temperature distributions, flow velocities and density distributions of the different species are predicted well compared to DSMC reference calculations.

To understand the importance of the VHS extensions that are described in this chapter, it makes sense to consider the importance of the VHS collision model for the DSMC method. Since the VHS model is only slightly more complex compared to the HS model, but offers one additional model parameter, it has become established in the DSMC community as a standard for modeling molecular collision processes. For example, using the Google Scholar engine [50] shows that the original publication by Bird [11], in which the VHS model was first introduced, has now been referenced over 600 times. Accordingly, VHS model parameters for many species were determined over the last years. By extending the FP model to the VHS collision model, this large set of model parameters is also available for simulations with the FP method, which is a great advantage in practice. As another advantage the VHS-FP model can be coupled very easily with DSMC methods that use the VHS model. Since for most DSMC users the VHS model is the standard collision model, this makes the FP method interesting for this large group of potential users.

Finally, this chapter has shown that it is in principle possible to extend the FP method derived in the last chapter to more complex molecular collision models, as long as appropriate production terms are known. For example, it would be conceivable to derive an FP model based on the Lennard-Jones model or other realistic collision models in a similar way as presented in this chapter. This could greatly expand the applicability range of the FP method, even in areas of fluid mechanics outside of the rarefied hypersonic flows that are discussed in this thesis.

Chapter 6

Modeling of polyatomic variable hard sphere gas mixtures

Chapter 3 introduced a kinetic FP method for describing polyatomic gases, while Ch. 4 and Ch. 5 presented methods for describing gas mixtures within the kinetic FP approach. The present chapter combines both approaches in order to construct a method for describing gas mixtures with diatomic species. The method presented in this chapter features a similar structure compared to the methods described in the former parts of this thesis. For the sake of clarity, however, some concepts are also repeated in this chapter.

The structure of this chapter is as follows. Subchapter 6.1 adopts the master equation approach, that is described in Subch. 3.1, for modeling gas mixtures featuring polyatomic species. Subchapter 6.2 discusses the corresponding stochastic processes. In Subch. 6.3, models for the rate coefficients of the master equation are constructed. Finally, Subch. 6.4 presents various test cases to check the ability of the proposed method to simulate typical phenomena that occur in hypersonic flows, such as shock waves and expansion flows. Finally, Subch. 6.5 presents the conclusion of this chapter.

6.1 Fokker-Planck model

For the following derivations, the statistical state of species α in internal energy state i is described by the distribution function $f_i^{(\alpha)}(\mathbf{x}, \mathbf{v}^{(\alpha)}, t)$. A master equation is applied in order to model the relaxation behavior of internal energies. When using a similar argumentation as presented in Subch. 3.1, the following governing equation for the distribution function $f_i^{(\alpha)}(\mathbf{x}, \mathbf{c}, t)$ can be postulated:

$$\begin{aligned} \frac{\partial f_n^{(\alpha)}}{\partial t} + \frac{\partial f_n^{(\alpha)}}{\partial x_i} v_i^{(\alpha)} = & \overbrace{\frac{\partial}{\partial v_i^{(\alpha)}} A_i^{(\alpha)} f_n^{(\alpha)} + \frac{\partial^2}{\partial v_k^{(\alpha)} \partial v_k^{(\alpha)}} \frac{D^{(\alpha)2}}{2} f_n^{(\alpha)}}^{S_{FP}^{(\alpha)}} \\ & + K^{(\alpha)} \frac{\partial^2 f_n}{\partial v_i^{(\alpha)} \partial v_i^{(\alpha)}} + \underbrace{\sum_j \left(R_{jn}^{(\alpha)} f_j^{(\alpha)} - R_{nj}^{(\alpha)} f_n^{(\alpha)} \right)}_{S_{MA}^{(\alpha)}} \equiv B_n^{(\alpha)} \end{aligned} \quad (6.1)$$

The reader should note that the definition of the diffusion coefficient in the FP operator in Eq. (6.1) differs from the definition of diffusion coefficients in Eq. (4.1) by a factor of 1/2 and the square root. The different definition was introduced to regain consistency with the nomenclature in Ch. 3. Therefore, the species specific diffusion

coefficient $D^{(\alpha)2}/2$ is defined as in Eq. (5.1), while the and the drift coefficients $A_i^{(\alpha)}$ is defined as in Eq. (5.2).

The species specific rate coefficients $R_{ij}^{(\alpha)}$ present model parameters, describing the relaxation process of internal energies. They are discussed in more detail in Subch. 6.3. The conservation of mass and momentum can be proven similar as described in App. B.1 for the single species model. The constant $K^{(\alpha)}$ leads to a modification of the diffusion coefficient $D^{(\alpha)}$ and is adjusted to ensure energy conservation for the model. This is discussed in more detail below.

For the single species model, the coefficient K was chosen, so that energy which leaves an internal mode due to inelastic collisions is transferred to the translational mode. In a similar way, the species specific coefficient $K^{(\alpha)}$ must be constructed for the mixture model. However, since a mixture may include many particle species, it is a-priori not clear in which way energy that leaves the internal modes due to inelastic collisions is transferred to translational modes of different species. In particular, for the case that different species adopt very different collision frequencies, energy might not be distributed evenly across translational modes of all species.

However, since elastic collisions are in general much more frequent than inelastic collisions, redistribution of translational energy across species is a much faster process than transformation of internal energy to translational energy. Therefore, energy that is transferred from the internal to the translational modes due to inelastic collisions is rapidly redistributed evenly across all species due to elastic collisions. In summary, it is therefore justified to assume an even distribution of energy that is transferred from internal to translational modes. Based on this argumentation, the coefficient $K^{(\alpha)}$ is constructed below.

In order to ensure conservation of energy, the following expression must be fulfilled:

$$\sum_{\alpha=1}^{N_s} \sum_n \int B_n^{(\alpha)} \left(\frac{1}{2} m^{(\alpha)} \mathbf{v}^{(\alpha)} \mathbf{v}^{(\alpha)} + e_n^{(\alpha)} \right) d\mathbf{c}^{(\alpha)} = 0. \quad (6.2)$$

Because of the energy conservation of the VHS mixture model, it holds:

$$\sum_{\alpha=1}^{N_s} \sum_n \int S_{FP}^{(\alpha)} m^{(\alpha)} \mathbf{v}^{(\alpha)} \mathbf{v}^{(\alpha)} d\mathbf{c}^{(\alpha)} \equiv 0. \quad (6.3)$$

Similar to the derivation that is described in App. B.1 for the single species model, it can be found:

$$\sum_{\alpha=1}^{N_s} 3K^{(\alpha)} m^{(\alpha)} n^{(\alpha)} + \sum_{\alpha=1}^{N_s} \sum_j H_j^{(\alpha)} n_j^{(\alpha)} \equiv 0, \quad (6.4)$$

that must be fulfilled in order to conserve energy. Please note, that $H_j^{(\alpha)}$ is defined as:

$$H_j^{(\alpha)} \equiv \sum_n R_{jn}^{(\alpha)} \left(e_n^{(\alpha)} - e_j^{(\alpha)} \right). \quad (6.5)$$

The following choice for $K^{(\alpha)}$ satisfies Eq. (6.4):

$$K^{(\alpha)} = -\frac{1}{3m^{(\alpha)}n^{(\alpha)}N_s} \sum_{\beta=1}^{N_s} \sum_j H_j^{(\beta)} n_j^{(\beta)}. \quad (6.6)$$

As in the single species model, $H_j^{(\alpha)}$ is a quantity that only depends on the structure of the internal energy states. Hence, at the beginning of each simulation a lookup table of $H_j^{(\alpha)}$ is calculated in order to efficiently evaluate Eq. (6.6).

For the case that the rate coefficients obey the Landau-Teller law (6.14), a simpler expression for $K^{(\alpha)}$ may be derived. In this case, it can be written:

$$\sum_j H_j^{(\beta)} n_j^{(\beta)} = \frac{n^{(\beta)}}{\tau_{\text{int}}^{(\beta)}} \left(E_{\text{int}}^{(\beta)\text{eq}} - E_{\text{int}}^{(\beta)} \right). \quad (6.7)$$

When combining Eq. (6.7) with Eq. (6.6) it can be found that:

$$K^{(\alpha)} = -\frac{1}{3m^{(\alpha)}n^{(\alpha)}N_s} \sum_{\beta=1}^{N_s} \frac{m^{(\beta)}}{\tau_{\text{int}}^{(\beta)}} \left(E_{\text{int}}^{(\beta)\text{eq}} - E_{\text{int}}^{(\beta)} \right). \quad (6.8)$$

As in the single species model, the species specific diffusion coefficients $\tilde{D}^{(\alpha)} = \sqrt{D^{(\alpha)2} + 2K^{(\alpha)}}$ that occur in the set of the FP equations (6.1) must be a real number. This leads to the condition:

$$K^{(\alpha)} > -D^{(\alpha)2}/2, \quad (6.9)$$

that must hold for each coefficient. Because of the complexity of the coefficient $D^{(\alpha)}$, Eq. (6.9) is difficult to prove. However, in numerical practice a violation of Eq. (6.9) is highly unrealistic, since this would mean that during one time step the entire energy of the system is transferred to internal modes.

Considering the change of the translation energy of species α with the model described above, the following expression can be derived:

$$\frac{dE_{\text{tr}}^{(\alpha)}}{dt} = 3K^{(\alpha)}m^{(\alpha)}n^{(\alpha)} = -\frac{1}{N_s} \sum_{\beta=1}^{N_s} \sum_j H_j^{(\beta)} n_j^{(\beta)}. \quad (6.10)$$

From this it can be seen that the change in translational energy is the same for all species. This corresponds to the assumption discussed at the beginning of the subchapter.

6.2 Stochastic equations of motion

Similar as described in Subch. 3.2 for the single species model, Eq. (6.1) can be translated into a consistent system of stochastic processes.

With a similar argumentation as described in Subch. 3.4.1, the distribution function can be written as:

$$f_n^{(\alpha)}(\mathbf{x}, \mathbf{c}, t) = f^{(\alpha)}(\mathbf{x}, \mathbf{c}, t) \cdot g_n^{(\alpha)}(\mathbf{x}, t). \quad (6.11)$$

The function $f^{(\alpha)}(\mathbf{x}, \mathbf{c}, t)$ does not depend on internal energy states, while $g_n^{(\alpha)}(\mathbf{x}, t)$ is independent of particle velocities. With a similar calculation as shown in Subch. 3.2, Eq. (6.1) can be separated into:

$$\frac{df^{(\alpha)}}{dt} = \frac{\partial f^{(\alpha)}}{\partial t} + \frac{\partial f^{(\alpha)}}{\partial x_i} c_i^{(\alpha)} = S_{FP}^{(\alpha)} + \frac{K^{(\alpha)2}}{2} \frac{\partial^2 f^{(\alpha)}}{\partial v_i^{(\alpha)} \partial v_i^{(\alpha)}}, \quad (6.12)$$

$$\frac{dg_n^{(\alpha)}}{dt} = \frac{\partial g_n^{(\alpha)}}{\partial t} + \frac{\partial g_n^{(\alpha)}}{\partial x_i} c_i^{(\alpha)} = \sum_j \left(R_{jn}^{(\alpha)} g_j^{(\alpha)} - R_{nj}^{(\alpha)} g_n^{(\alpha)} \right). \quad (6.13)$$

Equation (6.12) is a FP equation in velocity space with diffusion coefficient $\tilde{D}^{(\alpha)} = \sqrt{D^{(\alpha)2} + 2K^{(\alpha)}}$. The associated stochastic processes is a diffusion process. Corresponding solution algorithms have been discussed in Subch. 4.2. Equation (6.13) is a master equation. The associated stochastic process is a jump process. The solution of the process will be discussed in the following subchapters.

6.3 Models for rate coefficients

The following subchapters present models for the rate coefficients of the master equation (6.13). The models are constructed similar as for the single species case, that is described in Ch. 3. For the sake of simplicity, the same temperature $T = T^{(\alpha)}$ is assumed for all species. This assumption is physically justified if the relaxation time of internal energy modes is significantly greater than the characteristic relaxation time of translational energy modes. Please note, that this is the case for many realistic relaxation processes [10].

The models are constructed to obey a Landau-Teller relaxation of internal energies. Therefore, Eq. (2.51) can be generalized for multi species gases. Since collisions between any species particle can occur, the following relaxation law for species α is obtained:

$$\begin{aligned} \frac{dE_{\text{int}}^{(\alpha)}}{dt} &= \sum_{\beta} \frac{N_{\beta}}{\tau_{\text{int}}^{(\alpha\beta)}} \left(E_{\text{int}}^{(\alpha)\text{eq}} - E_{\text{int}}^{(\alpha)} \right), \\ &= \frac{1}{\tau_{\text{int}}^{(\alpha)}} \left(E_{\text{int}}^{(\alpha)\text{eq}} - E_{\text{int}}^{(\alpha)} \right). \end{aligned} \quad (6.14)$$

The parameter $\tau_{\text{int}}^{(\alpha\beta)}$ describes the impact of inelastic reactions between α and β particles to the overall relaxation time $\tau_{\text{int}}^{(\alpha)}$ of species α . Similar to the single species case, $E_{\text{int}}^{(\alpha)}$ denotes the average internal energy of species α , $E_{\text{int}}^{(\alpha)\text{eq}}$ the corresponding equilibrium energy, $\tau_{\text{int}}^{(\alpha\beta)} = Z_{\text{int}}^{(\alpha\beta)} / \nu_{\text{coll}}^{(\alpha\beta)}$ the internal relaxation time with the mean collision frequency $\nu_{\text{coll}}^{(\alpha\beta)}$ and a relaxation number $Z_{\text{int}}^{(\alpha\beta)}$.

6.3.1 DLT model

As in the single species case, the internal energy structure of a molecule is modeled as a set of discrete levels of a quantized harmonic oscillator.

Derivations can be made similar as in Subch. 3.3. For this reason only final results

are presented. Here for the rate coefficients $R_{ij}^{(\alpha)}$, it is chosen:

$$R_{ij}^{(\alpha)} \equiv R_j^{(\alpha)} \equiv \frac{1}{\tau_{\text{int}}^{(\alpha)} \cdot Q^{(\alpha)}} \exp\left(-\beta e_j^{(\alpha)}\right). \quad (6.15)$$

Here $e_i^{(\alpha)} = \epsilon^{(\alpha)} i$ denotes the energy of the i -th internal energy level of a species α . The species specific spacing between two adjacent energy levels $\epsilon^{(\alpha)} = k_B \theta^{(\alpha)}$ is typically expressed by a species-specific characteristic temperature $\theta^{(\alpha)}$. $Q^{(\alpha)}$ denotes a partition function:

$$Q^{(\alpha)} \equiv \sum_i \exp\left(-\beta e_i^{(\alpha)}\right) = \frac{1}{1 - \exp\left(-\beta \epsilon^{(\alpha)}\right)}. \quad (6.16)$$

The internal relaxation time $1/\tau_{\text{int}}^{(\alpha)} = \sum_{\beta=1}^{N_s} \nu_{\text{VHS}}^{(\alpha\beta)} / Z_{\text{int}}^{(\alpha\beta)}$ is calculated from the equilibrium mean collision frequency $\nu_{\text{VHS}}^{(\alpha\beta)}$ for particles interacting according to the VHS collision model [10]:

$$\nu_{\text{VHS}}^{(\alpha\beta)} = 4\bar{a}_{\text{ref}}^{(\alpha\beta)2} n^{(\beta)} \sqrt{\frac{\pi k_B T_{\text{ref}}^{(\alpha\beta)}}{m_r^{(\alpha\beta)}}} \left(\frac{T}{T_{\text{ref}}^{(\alpha\beta)}}\right)^{1-\omega^{(\alpha\beta)}}. \quad (6.17)$$

Here $m_r^{(\alpha\beta)} = \left(m^{(\alpha)} \cdot m^{(\beta)}\right) / \left(m^{(\alpha)} + m^{(\beta)}\right)$ denotes the reduced mass. Expression (6.15) is designed to lead to a Landau-Teller relaxation (6.14) of the total internal energy $E_{\text{int}}^{(\alpha)} = \sum_i e_i^{(\alpha)} g_i^{(\alpha)}$. The principle of detailed balance is easy to check for the model, ensuring a correct prediction of the equilibrium distribution function.

Due to the algorithmic similarity of the rate coefficients (6.15) and (3.26), the resulting stochastic equations of motion can be solved in the same way as described in Alg. 2.

6.3.2 CLT model

In the CLT model, the internal energy structure of a molecule is described as a continuous scalar. For the continuous rate coefficients it is chosen:

$$R(e^{(\alpha)}, e^{(\alpha)'}) \equiv R(e^{(\alpha)'}) \equiv \frac{\beta}{\tau_{\text{int}}^{(\alpha)}} \exp(-\beta e^{(\alpha)'}). \quad (6.18)$$

As for the discrete case, the rate coefficients (6.18) are designed to lead to a Landau-Teller relaxation of the total internal energy. The principle of detailed balance is checked easily.

Due to the algorithmic similarity of the rate coefficients (6.18) and (3.36), the resulting stochastic equations of motion can be solved in the same way as described in Alg. 3.

6.3.3 DLB model

As in the single species case, the DLT and the CLT model are designed to reproduce a relaxation behavior according to the Landau-Teller law. The relaxation behavior of internal energy states is not considered. Therefore, the DLB model is constructed to predict the relaxation behavior of internal energy states according to the quantized

Larsen-Borgnakke model [6] in combination with the particle selection scheme represented by Zhang et al. [147].

The rate coefficients for the DLB model are constructed for $i < j$ as follows:

$$R_{ij}^{(\alpha)} = \sum_{\beta=1}^{N_s} n^{(\beta)} \underbrace{\int_{c_{r,\min}^{(\alpha\beta)}}^{\infty} \sigma_{ij}^{(\alpha\beta)} f(c_r^{(\alpha\beta)}) c_r^{(\alpha\beta)} dc_r^{(\alpha\beta)}}_{R_{ij}^{(\alpha\beta)}}. \quad (6.19)$$

The rates $R_{ij}^{(\alpha\beta)}$ in expression (6.19) can be calculated similar as for the single species model. As a result, for $i > j$ follows:

$$R_{ij}^{(\alpha)} = \sum_{\beta=1}^{N_s} n_{\beta} v_{\text{VHS}}^{(\alpha\beta)} \cdot P_{\text{inel}}^{(\alpha\beta)} \cdot \zeta^{(\alpha\beta)}(i, j, T/\theta^{(\alpha)}), \quad (6.20)$$

The rate coefficients for $j > i$ are obtained from the requirement that the principle of detailed balance is fulfilled:

$$R_{ji}^{(\alpha)} = \sum_{\beta=1}^{N_s} n_{\beta} v_{\text{VHS}}^{(\alpha\beta)} \cdot P_{\text{inel}}^{(\alpha\beta)} \cdot \zeta^{(\alpha\beta)}(i, j, T/\theta^{(\alpha)}) \cdot \exp(-\beta(e_i^{(\alpha)} - e_j^{(\alpha)})). \quad (6.21)$$

When using the replacement $\omega \rightarrow \omega^{(\alpha\beta)}$, the function $\zeta^{(\alpha\beta)}(i, j, T/\theta^{(\alpha)})$ is defined similar as in Eq. (3.50). The probability $P_{\text{inel}}^{(\alpha\beta)}$ can be derived similar as Eq. (3.48) for the single species case. Note, that the probabilities $P_{\text{rot},i}$ and $P_{\text{vib},i}$ in Eq. (3.48) depend in general on the particle species, as described in App. A

Due to the algorithmic similarity of the rate coefficients (6.20) and (3.49), the resulting stochastic equations of motion can be solved in the same way as described in Alg. 4.

6.4 Test cases

In the following subchapters, the performance of the proposed method is investigated for various test cases. Simulations are carried out for a N₂-O₂ mixture. The corresponding model parameters are listed in Tab. F.4. While the VHS collision parameters are adapted from reference [10], the relaxation numbers are not realistic and only chosen in order to demonstrate the capability of the proposed method. Relaxation of rotational energies is modeled by the CLT model and the vibrational relaxation process by the DLT as well as the DLB model.

For reference, DSMC simulations are performed. To be consistent with the FP method, the same VHS collision model is used for the DSMC simulations. Rotational relaxation is described by the continuous Larsen-Borgnakke model [14], while the vibrational relaxation process is modeled by the quantized Larsen-Borgnakke model [6]. The scheme presented by Zhang et al. [147] (see App. A) is applied in order to select particle pairs for inelastic collisions. To avoid different results due to numerical discretization, the same spatial and temporal discretization is used for DSMC and kinetic FP simulations, if not stated otherwise.

All simulations are carried out using the SPARTA code [39], which has been extended by the proposed FP method.

6.4.1 Adiabatic heat bath

In order to verify that the proposed models obey the Landau-Teller law, the relaxation behavior of internal energies is studied. Therefore, internal energies are initially set according to an internal temperature which is not equalized with the translational temperature. Afterwards, relaxation to equilibrium is studied.

Simulations are performed for a homogeneous, adiabatic heat bath. The simulation boundaries are chosen to be periodic in order to avoid influences of particle-wall interaction. The species densities are set to $n^{(\text{N}_2)} = n^{(\text{O}_2)} = 2 \cdot 10^{19} \text{1/m}^3$. For each simulation a single grid cell with 9000 particles is simulated. At the beginning of each simulation, rotational and vibrational particle energies are set according to a Boltzmann distribution with $T_{\text{rot},0}^{(\alpha)} = T_{\text{vib},0}^{(\alpha)} = 3000 \text{ K}$. The particle velocities are set according to a Maxwell distribution with temperature $T_0^{(\alpha)} = 9000 \text{ K}$. Averaging over 100 simulations is performed for each case, given the unsteady nature of the problem.

The left part of Fig. 6.1 shows the relaxation behavior of rotational and translational temperatures. The time is normalized by an average VHS collision time [10] which is defined by:

$$1/\tau \equiv 4a_{\text{ref}}^{(\text{N}_2\text{O}_2)^2} \left(n^{(\text{O}_2)} + n^{(\text{N}_2)} \right) \sqrt{\frac{\pi k_B T_{\text{ref}}^{(\text{N}_2\text{O}_2)}}{m_r^{(\text{N}_2\text{O}_2)}} \left(\frac{T_0}{T_{\text{ref}}^{(\text{N}_2\text{O}_2)}} \right)^{1-\omega^{(\text{N}_2\text{O}_2)}}}. \quad (6.22)$$

Here $m_r^{(\text{N}_2\text{O}_2)}$ denotes the reduced mass of a N_2 and O_2 particle. In general, good agreement between FP and DSMC results can be observed. Small deviations in the translational temperature distributions can only be detected at the beginning of the relaxation process. Here, the DSMC method predicts a separation of translational temperatures, while the FP method predicts equal species temperatures. This is due to the choice of Eq. (6.6) for the coefficient $K^{(\alpha)}$. As described above, this choice leads

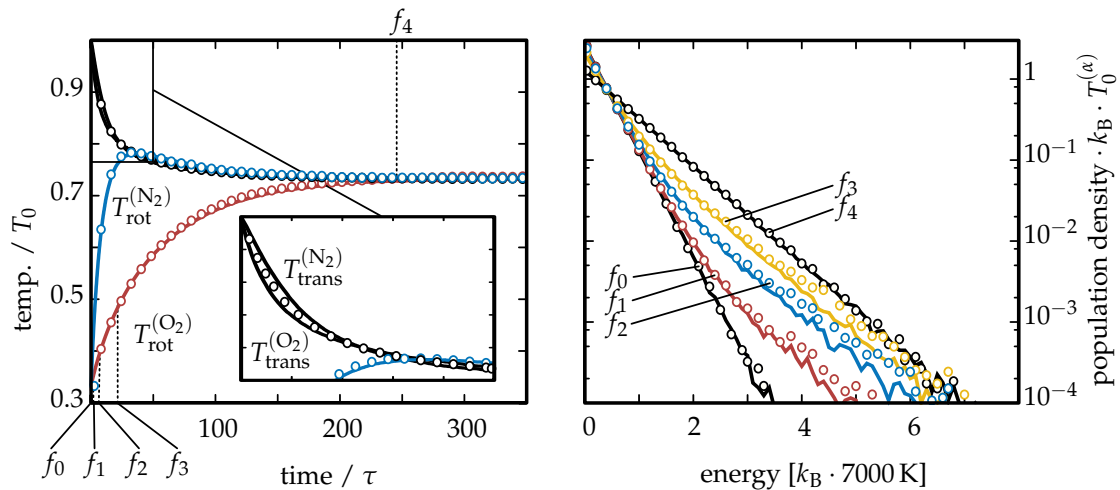


FIGURE 6.1: Left: Relaxation of rotational and translational temperatures to equilibrium. Right: Relaxation of the rotational energy distribution function of O_2 to equilibrium. The unit of the distribution function is the population density, which is defined as $dN/dE/dV/n$, where dN denotes the number of particles that can be found in a small energy interval dE and volume element dV and n is the particle density. Lines: DSMC results. Symbols: FP results. Please note that some of the results have been colored to better distinguish one from another.

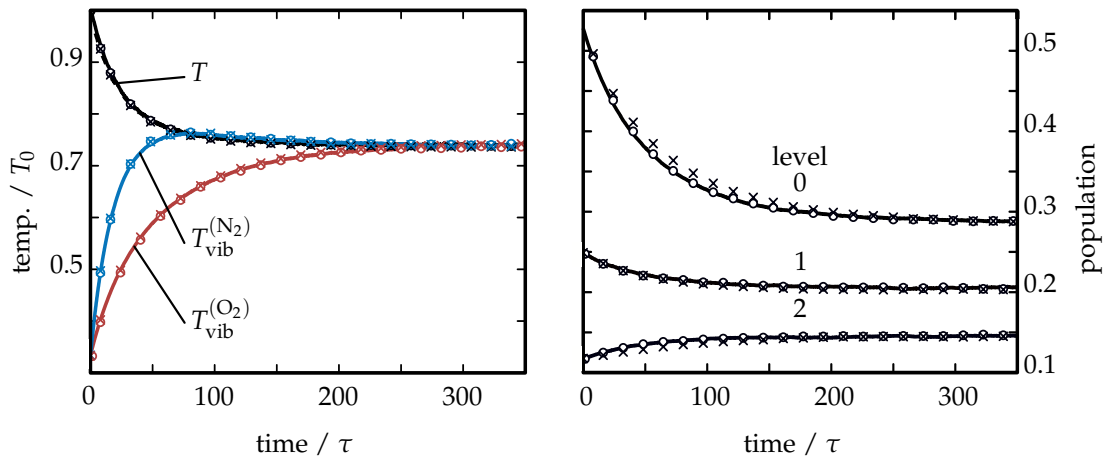


FIGURE 6.2: Left: Relaxation of vibrational and translational temperatures to equilibrium. Right: Relaxation of the first three vibrational levels of O_2 to equilibrium. Lines: DSMC results. Circles: FP-DLB results. Crosses: FP-DLT results. Please note that some of the results have been colored to better distinguish one from another.

to an even distribution of energy which is transferred from internal to the translational modes. In contrast, in the DSMC approach different species adopt different inelastic collision frequencies, which leads to a species-specific energy distribution that is transferred to translational modes. This effect results in a separation of translational temperatures as predicted by the DSMC algorithm. However, since the frequency of inelastic collisions is much smaller than the frequency of elastic collisions, this separation, and also deviations to the FP results, are only small. Here it should be noted that most realistic relaxation processes tend to have a longer internal relaxation time than the test case examined here. It is therefore to be expected that the observed deviations are irrelevant for most practical cases.

The right graph of Fig. 6.1 shows five different rotational energy distribution functions of O_2 over the relaxation process. The times when the distribution functions are calculated, are marked in the left plot of Fig. 6.1. The equilibrium distribution f_4 is correctly predicted by the FP method. For the non-equilibrium distributions f_1 , f_2 and f_3 , the FP method predicts a larger population of high energy states than the DSMC algorithm. This effect may be explained similar as for the single species method, discussed in Subch. 3.6.1: The Larsen-Borgnakke model, which is used in the DSMC algorithm, distributes new internal energy states due to inelastic particle collisions according to an equilibrium distribution function, with the restriction to conserve the total collision energy. The FP model also distributes new internal energies according to an equilibrium distribution function. However, since no collisions are modeled in the FP algorithm, new internal particle energies are not constrained by the requirement to obtain a specific total collision energy. Therefore, the CLT model may populate high energy states faster than the DSMC Larsen-Borgnakke model.

The left plot of Fig. 6.2 shows the relaxation of vibrational temperatures to equilibrium. A separation of translational temperatures, as for the rotational modes, is not observed. This is due to the large vibrational relaxation times, resulting in small vibrational collision frequencies. As a result, energy transfer between vibrational and

translational modes is so slow, that no significant separation occurs. Good agreement between FP and the DSMC results can be observed. Furthermore, no differences between the DLT and the DLB model are detectable.

The right plot of Fig. 6.2 exemplary shows the population of the first three vibrational levels of O_2 over the relaxation process. While the equilibrium population at the end of the relaxation process is correctly predicted by both models, the non-equilibrium populations during the relaxation process are correctly predicted only by the DLB model. This result is expected, as explained in Subch. 6.3.3.

6.4.2 Spherical expansion flow

The spherical expansion flow is investigated. As described in Subch. 3.6.2, this test case provides a good example to check the performance of the FP method for describing expansion effects, such as freezing of internal energies.

The test case is set up as described in Subch. 3.6.2. Due to the low translational temperatures, the vibrational excitation for this test case is neglected. Rotational modes are assumed to be fully excited at the inflow boundary. When assuming thermal equilibrium at the inflow boundary, the species temperatures are given by $T^{*(N_2)} = T^{*(O_2)} = T^* = 233$ K. The inflow number densities are set to $n^{*(N_2)} = n^{*(O_2)} = 0.5n^* = 0.5 \cdot 2.12 \cdot 10^{22}$. The ratio between the number of real to simulated molecules is adjusted to obtain between 70 and 140 particles per cell and per species. The left part of Fig. 6.3 shows species specific rotational temperature distributions and components of the translational mixture temperature along the expansion line. The inflow boundary is located on the left, the abscissa reveals the distance to the origin normalized with the distance d^* . At the inflow boundary an equilibrium flow is assumed, therefore, all temperatures are identical. Already at the beginning of the expansion process the internal mode of O_2 freezes. This effect is caused by small rotational relaxation numbers $Z_{rot}^{(O_2O_2)}$ and $Z_{rot}^{(O_2N_2)}$ (see Tab. F.4), which greatly reduce the number of inelastic collisions. For that reason, rotational and translational

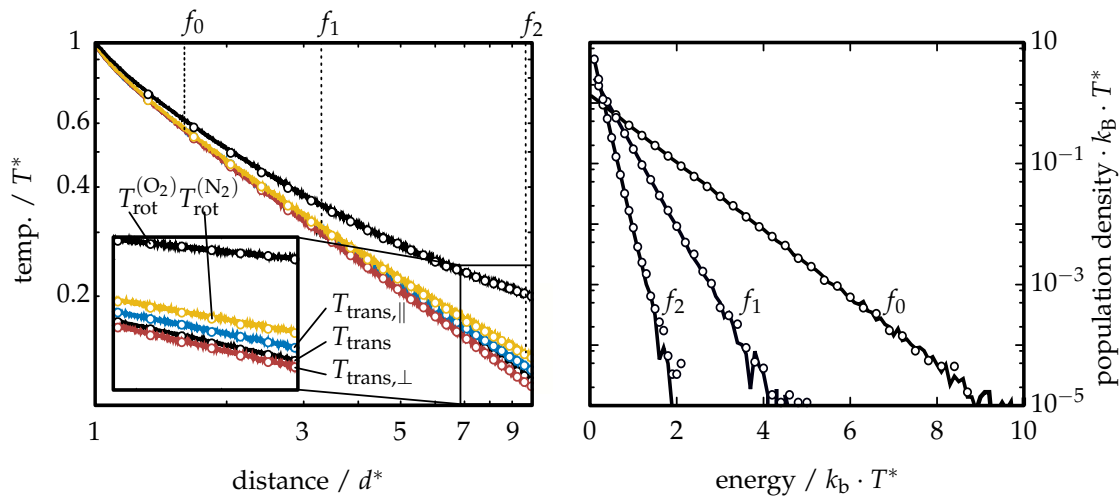


FIGURE 6.3: Left: Distribution of rotational and translational temperatures along the expansion line. Right: Relaxation of the rotational energy distribution function of O_2 during the expansion process. Note that the unit of the distribution function is the population density, which is defined as $dN/dE/dV/n$, where dN denotes the number of particles that can be found in a small energy interval dE and volume element dV and n is the particle density. Lines: DSMC results. Symbols: FP results. Please note that some of the results have been colored to better distinguish one from another.

temperatures do not equalize during the simulation. The reader should recall, that the rotational relaxation numbers used are not necessarily realistic, but were only used to demonstrate the performance of the FP method. For distances greater than $3 \cdot d^*$ from the origin, additional deviations between T_{\parallel} and T_{\perp} can be determined, suggesting an anisotropy of the velocity distribution function. In addition, the rotational mode of N_2 becomes frozen. In general, good agreement between FP and DSMC results can be observed. The FP method correctly predicts the separation process of translational and rotational temperatures.

The right part of Fig. 6.3 shows different rotational energy distribution functions f_0 , f_1 and f_2 of O_2 along the expansion process. The positions in the flow field where the distribution functions are evaluated, are marked in the plot side of Fig. 6.3. Very good agreement between FP and DSMC results can be observed.

6.4.3 One-dimensional flow past a shock wave

A one dimensional flow past a shock wave is investigated. As described in Subch. 3.6.3, this test case is well suited for investigating the relaxation behavior of internal energy modes in combination with thermal non-equilibrium effects.

The test case is set up as described in Subch. 3.6.3. In order to apply the piston boundary condition and the stabilization algorithm, the flow conditions in front of and downstream the shock wave must be known. Since the vibrational energy modes are not fully excited for this test case, the heat capacity ratio γ is non-constant over the shock wave. Hence, the well known Rankine-Hugoniot equations [5] cannot be applied to link the flow conditions across the shock wave. Instead, the flow conditions downstream the shock wave are calculated numerically by equating the conservation equations in front of and behind the shock wave and considering a temperature dependency of γ :

$$\gamma(T) = \frac{n(N_2)c_p^{(N_2)}(T) + n(O_2)c_p^{(O_2)}(T)}{n(N_2)c_v^{(N_2)}(T) + n(O_2)c_v^{(O_2)}(T)}, \quad (6.23)$$

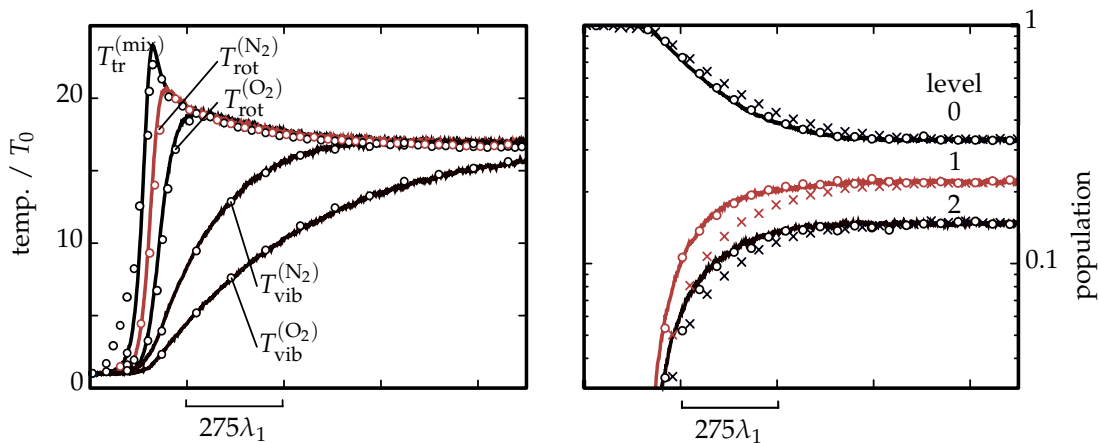


FIGURE 6.4: Left: Distribution of vibrational, rotational and mixture translational temperature across the shock wave. Right: Population of the first three vibrational levels of O_2 across the shock wave. Lines: DSMC results. Circles: FP-DLB results. Crosses: FP-DLT results. Please note that some of the results have been colored to better distinguish one from another.

with the heat capacities:

$$c_p^{(\alpha)}(T) \equiv \frac{(7 + d_{\text{vib}}^{(\alpha)}(T))}{2} \cdot \frac{k_B}{m^{(\alpha)}}, \quad (6.24)$$

$$c_v^{(\alpha)}(T) \equiv \frac{(5 + d_{\text{vib}}^{(\alpha)}(T))}{2} \cdot \frac{k_B}{m^{(\alpha)}}. \quad (6.25)$$

$$(6.26)$$

Here $f_{\text{vib}}^{(\alpha)}(T)$ denotes the number of excited vibrational degrees of freedom:

$$d_{\text{vib}}^{(\alpha)}(T) = 2 \frac{\theta^{(\alpha)}/T}{\exp(\theta^{(\alpha)}/T) - 1}. \quad (6.27)$$

A shock wave with an upstream Mach number of $M = 8$ is considered. For the upstream densities and temperatures $n_1^{(\text{N}_2)} = n_1^{(\text{O}_2)} = 5 \cdot 10^{19} \text{ 1/m}^3$ and $T_1^{(\text{N}_2)} = T_1^{(\text{O}_2)} = 500 \text{ K}$ are chosen, leading to a flow speed of $v_1^{(\text{N}_2)} = v_1^{(\text{O}_2)} = 4403.42 \text{ m/s}$. For the downstream conditions $n_2^{(\text{N}_2)} = n_2^{(\text{O}_2)} = 7.272 \cdot 10^{20} \text{ 1/m}^3$, $T_2^{(\text{N}_2)} = T_2^{(\text{O}_2)} = 8363.03 \text{ K}$ and $v_2^{(\text{N}_2)} = v_2^{(\text{O}_2)} = 605.50 \text{ m/s}$ are determined. The shock wave is simulated for a distance of 5 m in streamwise direction. The domain is divided in 2500 equal sized grid cells in flow direction, which resolves the smallest mean free path in the flow. The time step size is set to $\Delta t = 7 \cdot 10^{-7} \text{ s}$, which resolve the mean collision time behind the shock wave. The ratio between the number of real to simulated molecules is adjusted to obtain a number of 20 particles per cell and per species in the upstream area.

The left plot of Fig. 6.4 shows distributions of translational, rotational and vibrational temperature across the shock wave. Since no differences between the DLB and DLT model for macroscopic temperatures occur, only results of the DLB model are shown. The x-axis is normalized to the mean free path λ_1 in front of the shock wave. Since only slight differences are found in the distribution of the translational temperatures for different species, only the translational temperature for the entire mixture is shown. Due to the large vibrational relaxation times, the vibrational temperatures relax only slowly to equilibrium behind the shock wave. In contrast, the rotational temperatures follow the translational temperature distribution more closely. The N_2 species relaxes faster to equilibrium, which is consistent with results obtained above. In general, very good agreement between FP and DSMC results can be observed. Only small deviations in the temperature distributions just ahead of the shock wave are found. Note, that this area features strong thermal non-equilibrium, so that the validity of the FP method can not be expected.

The right plot of Fig. 6.4 shows the population of the first three vibrational levels of O_2 . The upstream and downstream equilibrium populations are correctly predicted by both FP models. However, only the DLB model is able to correctly predict the non-equilibrium populations along the relaxation process.

6.4.4 Flow past a perpendicular flat plate

To check the performance of the CLT, DLT and DLB models for a complex test case, a supersonic, two-dimensional flow over a perpendicular flat plate is considered. The dimensions of the plate, the inflow conditions and the numerical setup are adapted from Subch. 3.6.4, while the mole fractions at the inflow are set to $\chi_\infty^{(\text{N}_2)} =$

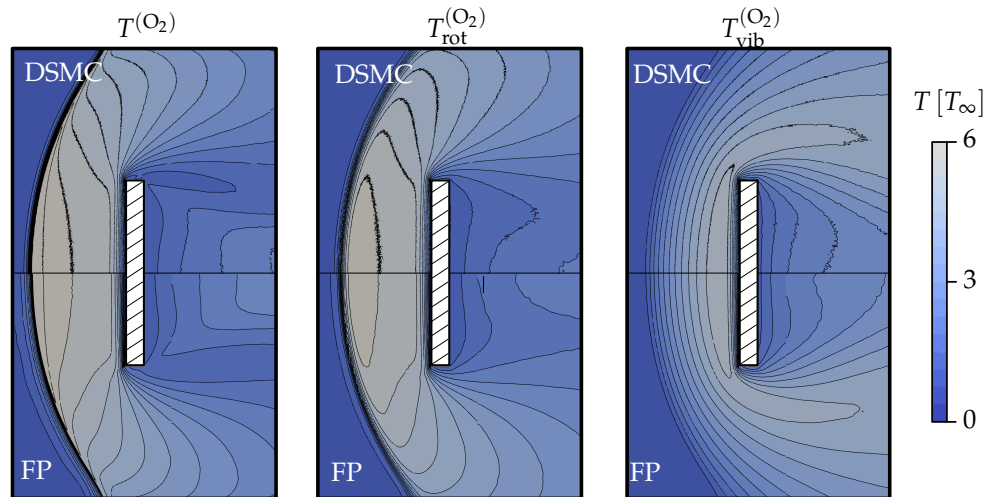


FIGURE 6.5: Translational (left), rotational (mid) and vibrational (right) temperature of O_2 . Result of the DLB model are shown.

$\chi_{\infty}^{(O_2)} = 0.5$. Two different FP simulations using the DLT and DLB model are performed. For reasons of clarity, only results for the O_2 species are shown. It should be mentioned, that the author also examined results for the N_2 species and that they are of a similar quality as the results for the O_2 species.

Figure 6.5 shows distributions of translational, rotational and vibrational temperature normalized to the inflow temperature $T_{\infty} = 500$ K. As described in the test cases above, no differences in temperature distributions can be detected for the DLT and the DLB model. Hence, only results of the DLB FP calculation are shown in Fig. 6.5. Small deviations between FP and DSMC results can be observed in the shock wave structure and in the boundary layer, whereas larger differences occur only in the region behind the plate. Similar as in the single species case described in Subch. 3.6.4, these deviations are caused by local thermal non-equilibrium effects, that can not be captured by the FP algorithm.

Figure 6.6 exemplary shows the population of the first vibrational level. Except of the region behind the plate, the DLB model accurately reproduces the DSMC results. For the DLT model deviations to the DSMC results can be detected in the relaxation

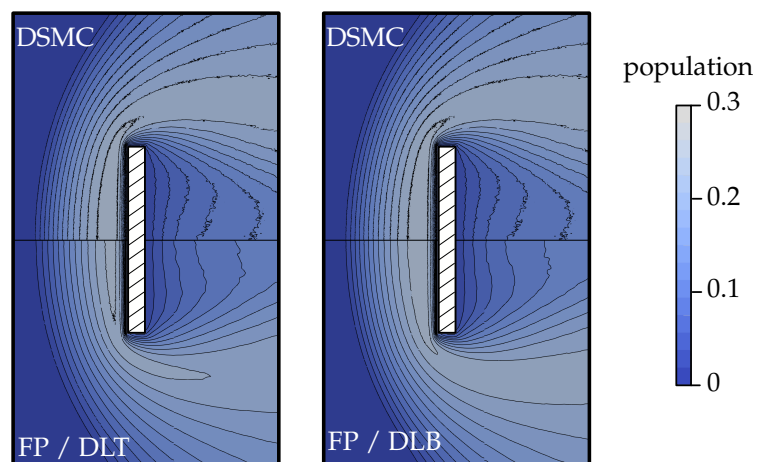


FIGURE 6.6: Population of the first vibrational level of O_2 .

behind the shock wave. In particular, the DLT model predicts a slower relaxation behavior, which is consistent with the results shown Subch. 6.4.3.

6.5 Summary and conclusion

In this chapter, the methods previously developed in Chap. 3 and Chap. 5 have been combined to develop a FP method suitable for describing gas mixtures with excited internal energies. Similarly, as described in Chap. 3, the relaxation of the internal energies was modeled by a master equation and three models, the CLT, DLT, and DLB model, were developed for the rate coefficients of the master equation. As a key assumption in the derivation of the method, the energy converted to translational energy by inelastic collisions is assumed to be uniformly distributed among all species. This assumption is justified because the relaxation process of internal energies, and thus the conversion of internal to translational energy, is a much slower occurring process than the equalization of translational energy between different species. Comparisons of FP results with DSMC results for a relaxation test case support this assumption, since only negligible deviations from DSMC reference calculations can be observed.

In order to test the performance of the models, different test cases relevant for hypersonic flows are investigated. A binary N_2 - O_2 mixture is used as the test gas. For an isolated shock and expansion flow, the FP results fit well with reference DSMC calculations. In particular, the relaxation behavior of the internal energies on the lee side of the shock wave and during expansion is correctly predicted compared to DSMC. Similarly, the FP method shows good results for a Mach 5 flow around a flat plate compared to reference DSMC simulations.

The work in this chapter further demonstrated the applicability of the previously discussed models. On the one hand, it shows that the master equation model from Ch. 3 is formulated in such a general way that it can also be generalized to several species. On the other hand, the shock and expansion test cases demonstrate that the mixture models from Ch. 4 and Ch. 5 also provide good results in such type of flows.

Finally, the reader should note, that this chapter gains importance from the fact that most real flow problems in hypersonic aerothermodynamics involve gases that feature both, multiple species and internal energies in non-equilibrium. Combining the models discussed in the previous chapters to an FP method that can handle gas mixtures with internal energies in non-equilibrium is therefore the next logical, but also necessary step to a kinetic FP method which is applicable in practice. In particular, to the best of the author's knowledge, at the time this chapter was written, no other kinetic FP models had been published that allow simulating gas mixtures with internal energies in non-equilibrium.

Chapter 7

Efficiency considerations

The kinetic FP methods presented in Ch. 5 and Ch. 6 have shown that they can reproduce shock waves, expansion flows and surface interactions in hypersonic flows compared to DSMC simulations. Therefore, they meet the basic properties to simulate hypersonic flows. However, the computational efficiency of the proposed methods has not yet been examined.

The most computationally intensive part of the kinetic particle algorithm, is the solution of the system of differential equations, as describe in point 4 of Alg. 5. For that reason, the set of differential equations is linearized in the following chapter. The resulting linear system of differential equations can be solved very efficiently.

In addition, an efficiency study of the FP methods from Ch. 5 is carried out. Different strategies for a meaningful application of these methods are discussed.

The structure of the present chapter is as follows. Subchapter 7.1 describes the linearization of the set of differential equations. In Subch. 7.2, test cases are investigated in order to check the validity of the linear system. Subchapter 7.3 discusses the efficiency of the proposed FP methods. Finally, Subch. 7.4 presents the conclusion of this chapter.

7.1 Linear system of evolution equations

In order to calculate the particle trajectories for the methods in Ch. 5 and Ch. 6, the coupled system of differential equations (App.C.33) must be solved, as described in point 4 of Alg. 5. In particular, the system must be integrated over a time interval corresponding to the size of a time step in the FP method. For example, a higher order Runge Kutta method can be used for this purpose. However, such a solution can quickly become computational expensive. This is due to the fact that the system (App.C.33) describes the relaxation of velocity moments over time. This relaxation takes place on time scales of the inverse collision frequency $1/\nu^{(\alpha\beta)}$ (see also Eq. (App.D.5)). Accordingly the temporal discretization in the Runge-Kutta method must be able to resolve this time scale. Hence, for FP time steps much greater than $1/\nu^{(\alpha\beta)}$, many steps in the Runge-Kutta method are necessary, which makes the calculation time-consuming.

In order to avoid this problem, the system (App.C.33) is linearized in the present subchapter. As a result, a more efficient integration method can be used that is independent of the time interval to be integrated and thus also independent of the size of an FP time step.

The linearization is of course connected with a number of assumptions which are discussed in the following. The error that is made by the linearization in comparison to the non-linearized method is also examined for representative test cases.

All derivations are made for the VHS collision model. In addition, thermodiffusion is neglected. It is worthwhile to mention, that this assumption is not necessary for the linearization. However, if thermodiffusion is neglected, heat fluxes can be excluded in the system (App.C.33), since they do not effect the production term (App.D.13) anymore. As a result, the number of equations that must be handled becomes smaller, making its solution even faster.

When neglecting thermodiffusion and reformulating system (App.C.33) based on velocities $\hat{\mathbf{c}}^{(\alpha)}$, it reduces to:

$$\frac{d}{dt} u_i^{(\alpha)} = -\frac{5}{3} \text{VHS}[1] \sum_{\beta=1}^{N_s} v_{|\text{VHS}}^{(\alpha\beta)} \mu^{(\beta)} \left(u_i^{(\alpha)} - u_i^{(\beta)} \right) \quad , i \in [0, 1, 2], \quad (7.1)$$

$$\frac{d}{dt} \hat{\theta}^{(\alpha)} = -\frac{10}{3} \text{VHS}[1] \sum_{\beta=1}^{N_s} v_{|\text{VHS}}^{(\alpha\beta)} \mu^{(\beta)} \left(\mu^{(\alpha)} \hat{\theta}^{(\alpha)} - \mu^{(\beta)} \hat{\theta}^{(\beta)} \right). \quad (7.2)$$

Equation (7.1) represents $3 \cdot N_s$ and Eq. (7.2) N_s differential equations. Equation (7.1) and Eq. (7.2) are not independent, since the frequencies $v_{|\text{VHS}}^{(\alpha\beta)}$ depend on the reduced temperatures $\hat{\theta}^{(\alpha)}$. Because this dependency is non-linear, Eq. (7.1) and Eq. (7.2) represent a non-linear system of differential equations.

To linearize Eq. (7.1) and Eq. (7.2) it is assumed that the frequencies $v_{|\text{VHS}}^{(\alpha\beta)}$ do not change with time:

$$v_{|\text{VHS}}^{(\alpha\beta)} \approx v_{|\text{VHS}|_{t=0}}^{(\alpha\beta)} = \text{const.} \quad (7.3)$$

This assumption is not true in general, since the frequencies depend on reduced temperatures $\hat{\theta}^{(\alpha)}$ that change over time. However, for near equilibrium flows, differences between species temperatures are small and the approximation is applicable.

As a result, Eq. (7.1) and Eq. (7.2) become independent and linear. In particular, Eq. (7.1) can be written as:

$$\frac{d}{dt} \mathbf{u}_i = A \cdot \mathbf{u}_i. \quad (7.4)$$

Similar, Eq. (7.2) reduces to:

$$\frac{d}{dt} \hat{\boldsymbol{\theta}} = B \cdot \hat{\boldsymbol{\theta}}. \quad (7.5)$$

In the equations above, the vectors \mathbf{v}_i and $\hat{\boldsymbol{\theta}}$ are defined with respect to the particle species:

$$\mathbf{u}_i \equiv \begin{pmatrix} u_i^{(1)} \\ u_i^{(2)} \\ \dots \end{pmatrix}, \hat{\boldsymbol{\theta}} \equiv \begin{pmatrix} \hat{\theta}^{(1)} \\ \hat{\theta}^{(2)} \\ \dots \end{pmatrix}. \quad (7.6)$$

A and B are $N_s \times N_s$ matrices. They are given by:

$$A_{lm} = \begin{cases} -\frac{5}{3} \text{VHS}[1] \sum_{\beta \neq l}^{N_s} v_{|\text{VHS}}^{(l\beta)} \mu^{(\beta)}, & \text{if } l = m \\ \frac{5}{3} \text{VHS}[1] v_{|\text{VHS}}^{(lm)} \mu^{(m)}, & \text{if } l \neq m \end{cases}, \quad (7.7)$$

$$B_{lm} = \begin{cases} -\frac{10}{3} \text{VHS}[1] \sum_{\beta \neq l}^{N_s} v_{|\text{VHS}}^{(l\beta)} \mu^{(l)} \mu^{(\beta)}, & \text{if } l = m \\ \frac{10}{3} \text{VHS}[1] v_{|\text{VHS}}^{(lm)} \mu^{(m)} \mu^{(m)}, & \text{if } l \neq m \end{cases}. \quad (7.8)$$

Equation (7.4) and Eq. (7.5) can be solved by standard methods for solving linear systems of differential equations. In this thesis, an eigenvalue method is applied [3]. Algorithm 6 schematically summarizes the application of this method for solving the system Eq. (7.5).

1. Calculate the eigenvalues λ_l^B and eigenvectors \mathbf{v}_l^B of B ;
2. Construct the solution $\hat{\boldsymbol{\theta}}(t) = \sum_l c_l \mathbf{v}_l^B \exp(\lambda_l^B t)$;
3. Solve the condition $\hat{\boldsymbol{\theta}}(t=0) = \hat{\boldsymbol{\theta}}_0$ to calculate the constants c_l . Here $\hat{\boldsymbol{\theta}}_0 = (\hat{\theta}^{(1),n}, \hat{\theta}^{(2),n}, \dots)$ denotes the reduced temperatures at the beginning of the integration step;
4. Evaluate $\hat{\theta}^{(1),n+1} = (\hat{\boldsymbol{\theta}}(\Delta t))_0, \hat{\theta}^{(2),n+1} = (\hat{\boldsymbol{\theta}}(\Delta t))_1, \dots$;

Algorithm 6: Solution method for the linear system of Eq. (7.4) and Eq. (7.5).

7.2 Validity considerations

This subchapter studies the validity of the linear integration method that has been proposed in the previous subchapter. In a first study, the relaxation behavior of a gas in an adiabatic heat bath is studied. Therefore, not the entire kinetic FP algorithm is applied. Instead, only solutions of the non-linear system are directly compared with solutions of the proposed linear system of differential equations. In a second study, the full linear kinetic FP algorithm is applied to a supersonic Couette flow test case. In the following, the phrases *linear* and *non-linear* kinetic FP refer to a kinetic FP simulation, where either the linear system of Eq. (7.4) and Eq. (7.5) or the full system of differential equations is solved.

7.2.1 Relaxation of flow quantities

The relaxation behavior of flow velocity and temperature, as described by the non-linear system, is compared to the relaxation behavior of the linear system. For this, the non-linear system (Eq. (7.1) and Eq. (7.2)) and the linear system (Eq. (7.4) and Eq. (7.5)) are solved with different initial conditions and the result is compared. From this comparison it can then be deduced how severe the error is that is made by the linearization described above.

	condition 1	condition 2
$u^{(\text{He}),0}$	100 m/s	0 m/s
$u^{(\text{Ar}),0}$	-10 m/s	0 m/s
$\hat{T}^{(\text{He}),0}$	300 K	300 K
$\hat{T}^{(\text{Ar}),0}$	300 K	600 K

TABLE 7.1: Initial conditions.

Calculations are performed for a He-Ar mixture. The same model parameters as described in Tab. F.5 are employed. Two different initial conditions, as described in Tab. 7.1, are considered, in order to investigate the relaxation process of species temperatures and diffusion velocities separately. The non-linear system is solved by a fourth order Runge-Kutta method with adaptive step size control [129], while the linear system is solved as described in Alg. 6.

The upper left plot of Fig. 7.1 shows the relaxation behavior of the species diffusion velocities, when applying initial condition 1. In general, very good agreement between the linear and the non-linear system can be found. In order to further analyze these results, relative deviations $|u_{\text{non-linear}}^{(\alpha)} - u_{\text{linear}}^{(\alpha)}| / |u_{\text{non-linear}}^{(\alpha)}|$ between non-linear

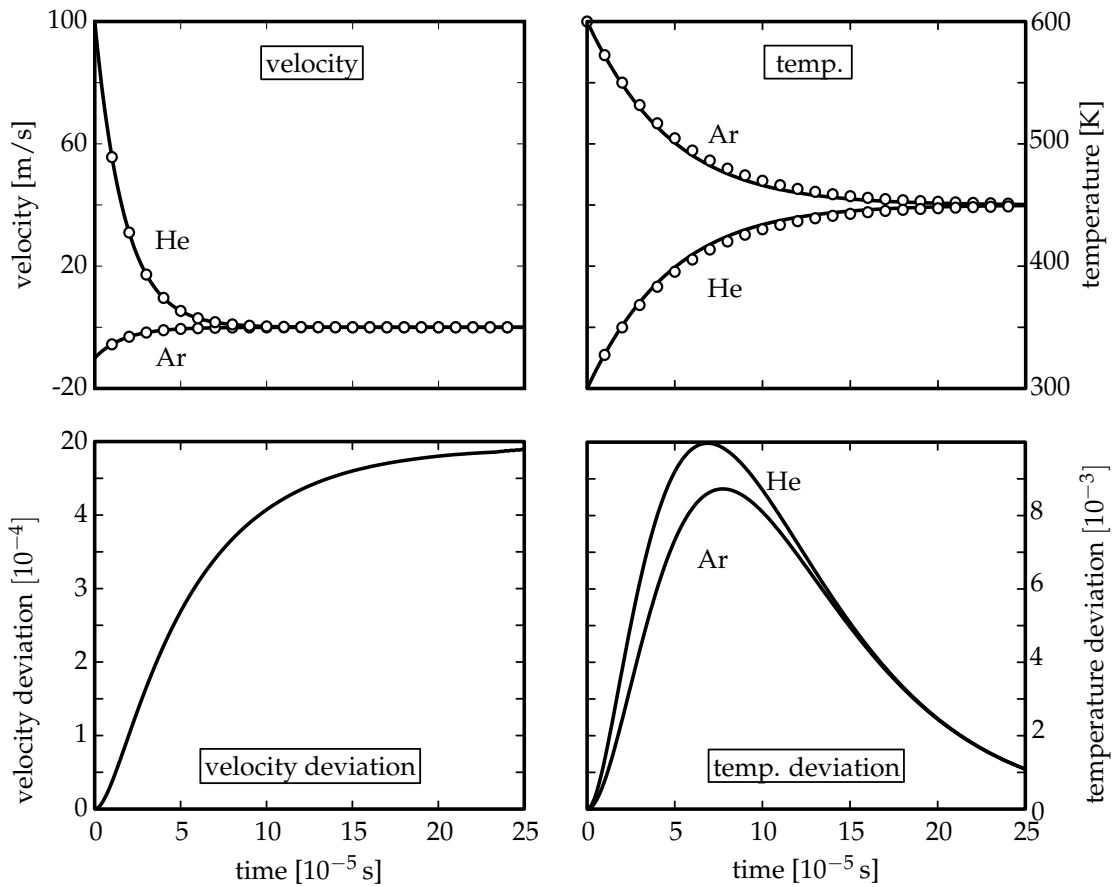


FIGURE 7.1: Upper row: Solutions of the non-linear system (lines) and the linear system (symbols). Lower row: Relative deviations between non-linear and linear solutions. Left column: Results for initial condition 1. Right column: Results for initial condition 2.

and linear results are shown in the lower left plot of Fig. 7.1. The maximum relative deviation is observed to be less than 0.2%. Such small deviations are to be expected, since initial condition 1 features no temperature separation for different species. Hence, the species temperatures change only slightly over the relaxation process and the assumption of constant frequencies $\nu_{\text{VHS}}^{(\alpha\beta)}$, as assumed when deriving the linear system, is justified.

The upper right plot of Fig. 7.1 shows the relaxation process of species temperatures, when applying initial condition 2. Small deviations between the linear and the non-linear system can be detected. In particular, the non-linear system leads to a faster relaxation of species temperatures. Relative deviations $|\hat{T}_{\text{non-linear}}^{(\alpha)} - \hat{T}_{\text{linear}}^{(\alpha)}| / \hat{T}_{\text{non-linear}}^{(\alpha)}$ are shown in the lower right plot of Fig. 7.1. The maximum relative deviation is around 1% and larger than for the diffusion velocities. This was to be expected, since initial condition 2 features a temperature separation for different species. As a result, temperatures change during the relaxation process and the assumption of constant frequencies $\nu_{\text{VHS}}^{(\alpha\beta)}$ is invalid.

All in all, a relatively small discrepancy between the results of the linear and non-linear system can be determined. This suggests that there are no major differences to

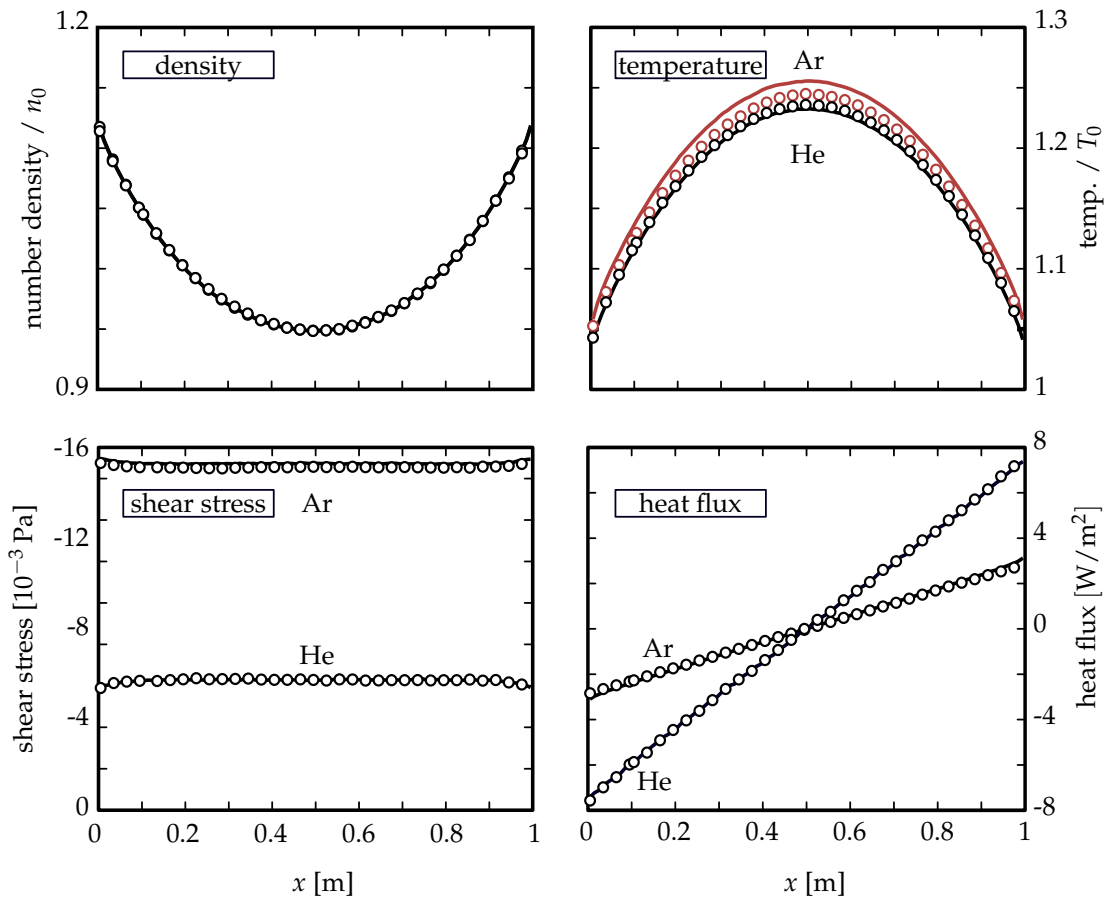


FIGURE 7.2: Species densities, temperatures, shear stresses and heat fluxes for a supersonic Couette flow. Lines: FP results with exact integration. Circles: FP results with linear integration. Please note that some of the results have been colored to better distinguish one from another.

be expected for a full FP simulation either. This is examined in the following chapter.

7.2.2 Supersonic Couette flow

In order to further study the performance of the linear integration algorithm for a full kinetic FP simulation, the supersonic Couette flow is investigated.

The same test case as described in Subch. 5.2.1 is considered. Two FP simulations, using the linear and the non-linear integration algorithm, are performed. To be consistent with the linear FP simulation, the non-linear integration is performed without thermodiffusion.

Figure 7.2 compares linear and non-linear FP results. In general, very good agreement between linear and non-linear FP results are detected. Smaller differences can be observed only in the species temperature distributions. In particular, separation of species temperatures is slightly under-predicted by the linear FP algorithm. Deviations in species temperatures were to be expected, since similar deviations were observed in the relaxation test case, as described above.

7.3 Efficiency considerations

After constructing a linearized FP method in the last subchapter, this subchapter examines the computational efficiency of this linearized FP algorithm, as well as the efficiency of the non-linearized FP method from the previous chapters.

First it should be noted, that due to the algorithmic similarity of the HS FP method and the VHS FP method, it is expected that both show the same computational efficiency. In addition, the impact on the computation time when the method from Ch. 3 is used to describe internal energies has already been discussed in detail in Subch. 3.7. For these reasons, the present subchapter only discusses the computational efficiency of the VHS FP method. In particular, the computational effort of the kinetic VHS FP method is compared to the effort of the DSMC algorithm.

The computational complexity of a kinetic particle method depends on various properties such as the Knudsen number, the surface geometry or the signal-to-noise ratio of flow quantities. Hence, a satisfactory efficiency study is a complex task. However, when using a simple position scheme for the kinetic FP algorithm, as described by Eq. (2.65), and when moving particles based on a Euler scheme, as describe in Fig. 2.7, the only algorithmic difference between DSMC and kinetic FP is how particle velocities are updated.

Due to this strong algorithmic similarity between the two methods, only the computational time for the calculation of the particle velocities will be compared in the following. This comparison is not performed for a complex test case, but for a simple heat bath. This heat bath can be understood as a small section of a more "complex" simulation. As will be discussed below, this allows very general statements to be made about the relative computational efficiency of DSMC and kinetic FP.

A three-dimensional box with side length of $5 \cdot l$ is simulated. The box is divided in $5 \times 5 \times 5$ grid cells featuring a side length of l . Calculations are made for a hypothetical, monatomic N_2 - O_2 mixture. The species temperatures are set to $T^{(\alpha)} = 300$ K. The scaling f_N is adjusted to obtain 6000 particles in the simulation. Calculations are performed for 100 time steps using the DSMC algorithm and the kinetic FP method. Different combinations of time step sizes Δt and mean free paths λ are simulated, and for each simulation the time needed to update the particle velocities is stored.

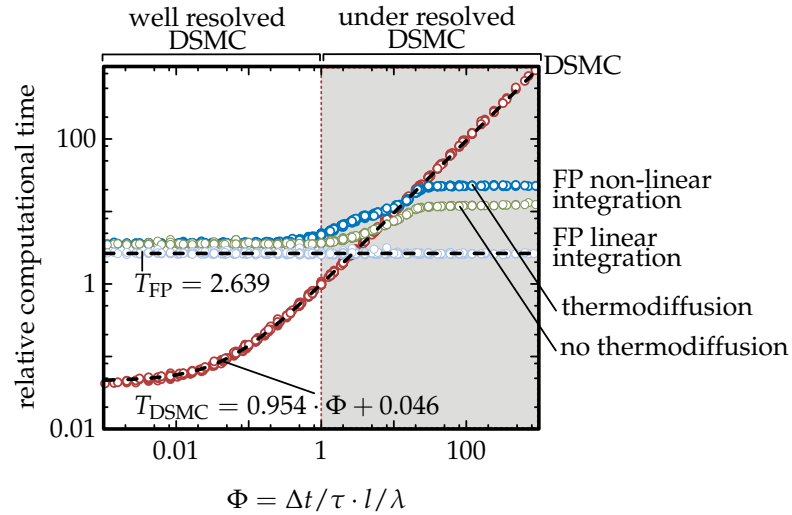


FIGURE 7.3: Computational effort required to update particle velocities within DSMC and kinetic FP, depending on time step size and mean free path. All times are normalized with the time which is required for a DSMC simulation with $\Phi = 1$. Note the double logarithmic scaling of the axes.

Variations in the mean free path λ are realized by changing the species densities. The computing time for kinetic FP and DSMC changes similar when changing Δt and $1/\lambda$. Hence, the two dimensional parameter space $(\Delta t, \lambda)$ is reduced to a one dimensional parameter space $(\Delta t \cdot 1/\lambda)$. Figure 7.3 shows the resulting computing time to update particle velocities per particle, per grid cell and per time step for different values of $\Phi \equiv \Delta t/\tau \cdot l/\lambda$. Note, that τ denotes the average time, a particle needs to travel along the cell side length l :

$$\tau \equiv \frac{l}{\sqrt{2 \frac{k_B 300 \text{K}}{m(\text{N}_2)}}} \quad (7.9)$$

The computational time is normalized with the computing effort which is required for a DSMC simulation with $\Phi = 1$.

The computational time required to update particles velocities within a DSMC simulation scales linear with Φ . This is due to a linear increase in the number of calculated particle collisions with increasing time step size Δt or increasing particle density. The following scaling law is found for the SPARTA DSMC solver used in this work:

$$T_{\text{DSMC}}(\Phi) = 0.954 \cdot \Phi + 0.046. \quad (7.10)$$

Note, that Eq. (7.10) depends on the particular DSMC implementation. The small offset in Eq (7.10) is due to algorithmic operations that are performed independently of the time step size and the particle density, for example the calculation of the number of required particle collisions.

When using the linear integration algorithm as discussed in Subch. 7.1, the computational time to update velocities within the kinetic FP algorithm is independent of Φ . This is because no collisions or any other processes that depend on the time step size or on the gas density need to be resolved.

When the non-linear integration algorithm is applied, the computational time to update particle velocities within kinetic FP is not independent of Φ . Instead, the computational time increases with increasing Φ and reaches a steady value for $\Phi \gtrsim 20$.

This behavior is due to the integration scheme which is utilized to solve the system of differential equations (App.C.33). Therefore, a Runge–Kutta scheme with adaptive temporal discretization technique [129] is applied. For small values of Φ , the solution of the system (App.C.33) varies only slightly. Hence, the time required for the numerical integration is negligible small. When increasing Φ , the solution starts to change. As a result, the Runge–Kutta scheme uses a small temporal discretization, which leads to an increasing computational time. For $\Phi \gtrsim 20$ a steady state is reached. Thus, the Runge–Kutta scheme applies a large temporal discretization, leading to a time step independent solution for large values of Φ . When thermodiffusion is neglected, heat fluxes can be excluded from the non-linear system (App.C.33), resulting in a simpler system of equation (Eq. (7.1) and Eq. (7.2)). As a result, the computing time to solve the system reduces.

When comparing the computing effort of kinetic FP with DSMC, two perspectives are possible. In one perspective, a kinetic FP simulation may be compared with an under resolved DSMC simulation.¹ This perspective corresponds to the right side of Fig. 7.3. When increasing Φ , DSMC becomes more computational expensive, while the effort for kinetic FP stays roughly constant. For a certain value of Φ , a kinetic FP simulation will be more efficient than a DSMC simulation. As an example, it can be found $T_{\text{DSMC}}(\Phi) > T_{\text{FP}}$ for $\Phi > 2.72$. Consequently, kinetic FP will be more efficient than an under resolved DSMC simulation when choosing for example a resolution of $\Delta t = \tau$ and $l > 2.72\lambda$ for both methods.

In a different perspective, a FP simulation may be compared with a well resolved DSMC simulation. This perspective corresponds to the left side of Fig. 7.3. In this situation, the DSMC algorithm is less computational expensive than the kinetic FP algorithm when considering a single grid cell. Nevertheless, kinetic FP holds the potential to be more efficient than DSMC, since the kinetic FP method must not resolve the particle mean free path. Hence, larger grid cell sizes can be used in a FP simulation than in a DSMC simulation.

For example, traditionally the condition $\Delta t_{\text{DSMC}} = 0.3 \tau$, $l_{\text{DSMC}} = 0.3 \lambda \Rightarrow \Phi = 0.09$ is assumed for a very well resolved DSMC simulation. For this condition it can be found that $T_{\text{FP}}(\Phi) \approx 20 \cdot T_{\text{DSMC}}$. Consequently, a kinetic FP simulation would be more efficient than a very well resolved DSMC simulation, if the kinetic FP simulation uses at least 20 times less grid cells than the DSMC simulation. In a 2-d case, and assuming a very well resolved DSMC simulation, this could be achieved by using a cell size of $\Delta x_{\text{FP}} = 1.34\lambda = 4.47\Delta x_{\text{DSMC}}$ for the FP simulation.²

In this case, additional speed up for the kinetic FP algorithm can be expected, due to two effects which are not represented in Fig. 7.3. Due to the smaller number of simulation cells which are used in the kinetic FP algorithm, a smaller number of particles can be used for the simulation. As a result, computational time which is required to move the particles and to perform averages is additionally decreased.

When a proper position integration for the kinetic FP algorithm is applied also larger

¹ This comparison is justified because, due to the limited computing power available, especially in the case of large simulations, an at least partially under-resolved DSMC simulation is carried out from time to time.

² This argumentation is based on the assumption that a reduction in the number of cells and particles in the FP method leads to a reduction in the time required to calculate the particle velocities to the same extent. This is a reasonable assumption, since all computational operations are performed separately for each cell and each particle.

time step sizes can be used, resulting in an even faster convergence of the simulation. For example, algorithms could be derived that correctly describe not only the temporal evolution of energy and flow velocities over a time step, but also of higher-order velocity moments and joint velocity moments. For monatomic gases such algorithms were derived from Jenny et al. [84] or Gorji et al. [55], for example.

7.4 Summary and conclusion

In this chapter, the computational efficiency of the previously developed kinetic FP method is assessed. In particular, the computational cost of the VHS-FP method from Ch. 5, without including internal energy level modeling, is examined, since the impact due to internal energy level modeling has already been discussed in Subch. 3.7³.

In the first part of this chapter, an efficient algorithm for updating the particle velocities for the VHS-FP method is derived. This is achieved by linearizing a system of differential equations that must be solved for each time step and grid cell for the VHS-FP method. This linearization makes the computational cost of solving the system of differential equations, and hence the cost of the entire FP method, independent of the FP time step size. However, some assumptions must be made about the time evolution of the velocity moments. To investigate the error introduced by these assumptions, the relaxation behavior of the linearized system is compared with the relaxation of the original differential equation system. Also, a supersonic Couette flow is simulated using the linearized and the original algorithm. For these test cases, only minor differences are observed between the results of the full and linearized algorithms.

In the second part of this chapter, the computational effort of the kinetic VHS-FP method is compared with the computational effort of the DSMC method. For the comparison it is exploited that both methods differ only in the scheme of how the particle velocities are updated in each time step. This allows a very general comparison of the computational effort. For this purpose, a simple heat bath test case is simulated with both methods for 100 time steps. The computational effort per time step used by both methods to update the particle velocities is then compared. The comparison is made for different particle densities and time step sizes. In this way, the cost of both methods can be estimated for a small, homogeneous computational domain.

It can be observed that the computational effort of the linearized FP algorithm is independent of the time step size, while the effort for the original algorithm increases slightly for time step sizes greater than the mean collision time, but becomes constant again for larger time steps. The latter observation is a result of the Runge-Kutta solver used to solve the system of differential equations. As expected, the FP method is less efficient than DSMC when the particle density or the time step size is small. However, for large time step sizes and particle densities FP becomes more efficient than DSMC. In addition, FP has the potential to be more efficient than DSMC because it can use a coarser temporal and spatial numerical resolution. The results can be used to assess at which numerical resolution the use of the FP method becomes

³In Subch. 3.7, the impact of modeling internal energy levels on the computational time for the one species cubic FP method was discussed. However, due to the analogous mathematical formulation, it can be assumed that the same conclusions are valid for the FP models for gas mixtures as well.

advantageous compared to DSMC. For the specific implementation in this work, it can be stated that FP becomes more efficient than a well-resolved DSMC simulation when the grid cell size is at least 1.34 times the mean free path.

Through the efficiency study in this chapter, it could be shown that the kinetic FP method, from a certain numerical resolution which is only slightly coarser than the resolution of the DSMC method, computes faster than the DSMC method. Therefore, in many cases, it makes sense from a computational time perspective to use the kinetic FP method instead of DSMC. Since it is expected that the kinetic FP method will directly compete with the DSMC method in many cases, this is an important result that justifies the model developments of this thesis so far.

The results of this chapter can be used by future users of the FP method to assess whether it makes sense from the point of view of computing time to work with the FP method instead of the DSMC method. Of course, the study in this chapter does not allow an exact statement of how much computing time is saved compared to the DSMC method, since only the time for calculating the particle velocities is evaluated, while many other factors, such as the calculation of the particle positions, are not taken into account. However, at least a rough estimation can be made, from which numerical resolution on the FP method can be expected to be more efficient than DSMC. However, it is to be noted of course that the results from this chapter refer to a specific implementation of the DSMC and FP method. A potential user should therefore repeat such a study with his own code if in doubt.

Chapter 8

Gas expansion into a vacuum environment

In the latter parts of this thesis, models have been developed to simulate gases with multiple species and excited internal energies using the kinetic FP method. As described in Subch. 1.4, these are Phase 2 studies, i.e., studies in which the feasibility of such modeling has been demonstrated. In order to construct a simulation method that is fully functional in practice, it is necessary to conduct additional Phase 3 studies that further investigate the applicability of the developed models. However, to provide motivation for such Phase 3 studies, a complex Phase 4 test case is already simulated in this chapter. It should be clear to the reader, however, that the primary purpose of the studies from this chapter is to demonstrate the applicability of the methods developed so far for a complex test case. The investigation of the physical flow phenomena, on the other hand, is of only secondary importance.

To this end, this chapter applies the previously constructed kinetic FP methods to numerically reproduce an experimental study of expanding air from an axially symmetric orifice into a vacuum environment, that was carried out in the DLR high-vacuum plume test facility for chemical thrusters (Simulationsanlage Treibstrahlen Göttingen für chemische Triebwerke / **STG-CT**) at the German Aerospace Center (DLR), Göttingen. Numerical results are compared with experimental measurements of the total reservoir mass flow and experimentally measured angular mass flux profiles in the far field.

Please note, that such a Free jet expansion flow is one of the most basic experimental test cases that can be used to study physical effects in strong expanding gases. Therefore, such flows were intensively studied experimentally [67, 127], numerically [88] and theoretically [134, 66], in recent decades.

The structure of this chapter is as follows. Subchapter 8.1 and Subch. 8.2 describe the experimental and numerical set up. Results of numerical simulations and comparison with experimental measurements are described in Subch. 8.3. Subchapter 8.4 presents the conclusion of this chapter.

8.1 Test case description and experimental setup

Measurements are performed in the high-vacuum plume test facility Göttingen for chemical thrusters (STG-CT) at the German Aerospace Center (DLR) in Göttingen [59]. The STG-CT features a vacuum chamber with a diameter of 1.6 m and a length of 5 m. The walls of the test section can be cooled to about 4.7 K, employing evaporating helium. Consequently, the test section works as a cryogenic pump which is sufficient to maintain a ratio of reservoir to background pressure of $p_0/p_{\text{back}} > 10^{10}$

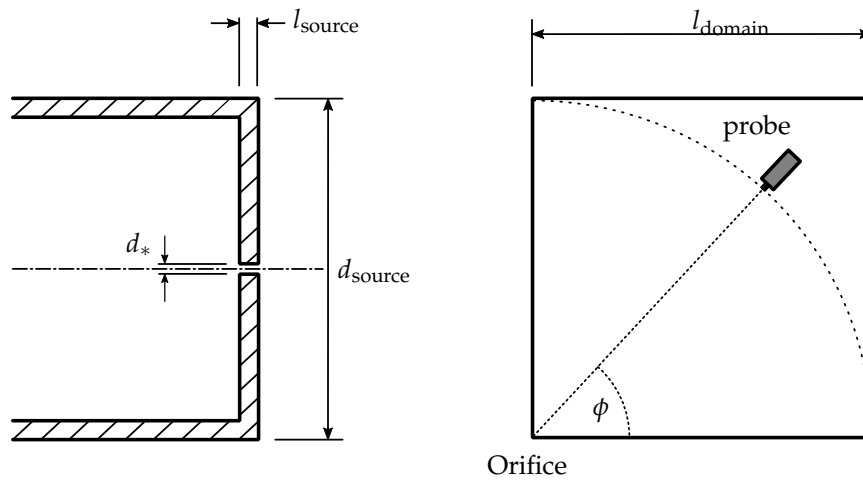


FIGURE 8.1: Left: Sketch of axially symmetrical flat-faced orifice. Right: The flow source can be rotated which leads to different polar angles Φ between the mass spectrometer (probe) and the flow source.

upto mass fluxes in the order of grams per second which enter the chamber.

The STG-CT was used to study the expansion of a gas from an axisymmetric orifice in a vacuum environment. These experiments were performed as part of a test of a new mass spectrometer that will be used to measure angular profiles of species-specific mass fluxes. The original goal of this experiment was to demonstrate the functionality of the mass spectrometer. However, the measurements are also well suited to demonstrate the functionality of the numerical models described in the previous chapters of this thesis.

The gas expands out of a sonic source featuring a flat-faced cylinder, as schematically drawn in the left part of Fig. 8.1. An axially symmetrical orifice is machined centrally into the face of the cylindrical shape. The diameter is $d_* = 0.6$ mm and the length of the face is $l_{\text{source}} = 0.8$ mm. The outer source diameter is given by $d_{\text{source}} = 16.6$ mm. A heater assembly is located upstream of the flow source in order to control the reservoir temperature $T_0 = 284$ K, while controlling the reservoir pressure and keeping it at a constant value of $p_0 = 11000$ Pa. The mass flow rate $\dot{m}_{\text{exp}} = 5.814 \cdot 10^{-6}$ kg/s is adjusted manually by a dedicated flow controller. Synthetic air with 78.43 % N_2 , 19.61 % O_2 and 1.96 % H_2 is used for this study.

The spectrometer is installed in a distance of $l_{\text{domain}} = 2$ m from the orifice. The flow source is installed so that it can be rotated in a plane. As a result, the mass spectrometer can measure angular profiles, while its position stays constant. The mass spectrometer provides a signal for each species in the gas. The height of the signal is proportional to the mass flux of the corresponding species. Using the law of mass conservation, angular profiles of the species-specific mass fluxes can be calculated from the mass flow rate through the reservoir.

8.2 Numerical setup

In contrast to the previous chapters of this thesis, only the FP method is used to calculate the expansion. DSMC calculations for comparison are not performed, since

the calculation of this test case with DSMC was not possible with the available computational resources. This is mainly due to the high particle density in the reservoir, which makes it necessary to use very small time steps and cell sizes for a DSMC simulation.

The VHS-FP method for diatomic molecules, as described in Ch. 6, is applied to calculate the test case. Rotational relaxation is modeled by the CLT model while, due to the low reservoir temperature, vibrational relaxation is neglected. Table F.5 lists the employed species model parameters. The interspecies model parameters $d^{(ij)}$, $\omega^{(ij)}$, $T_{\text{ref}}^{(ij)}$ and $Z_{\text{rot}}^{(ij)}$ are calculated by simply averaging the species parameters.

The symmetry of the test case is exploited to perform an axially symmetrical simulation. The upper part of Fig 8.2 shows the structure of the simulation domain in direct vicinity to the orifice. All walls are assumed to be fully diffusive with a temperature of $T_w = 300$ K. For the inflow boundaries, a uniform inflow condition with vanishing flow velocity, temperature $T_0 = 284$ K and mixture number density

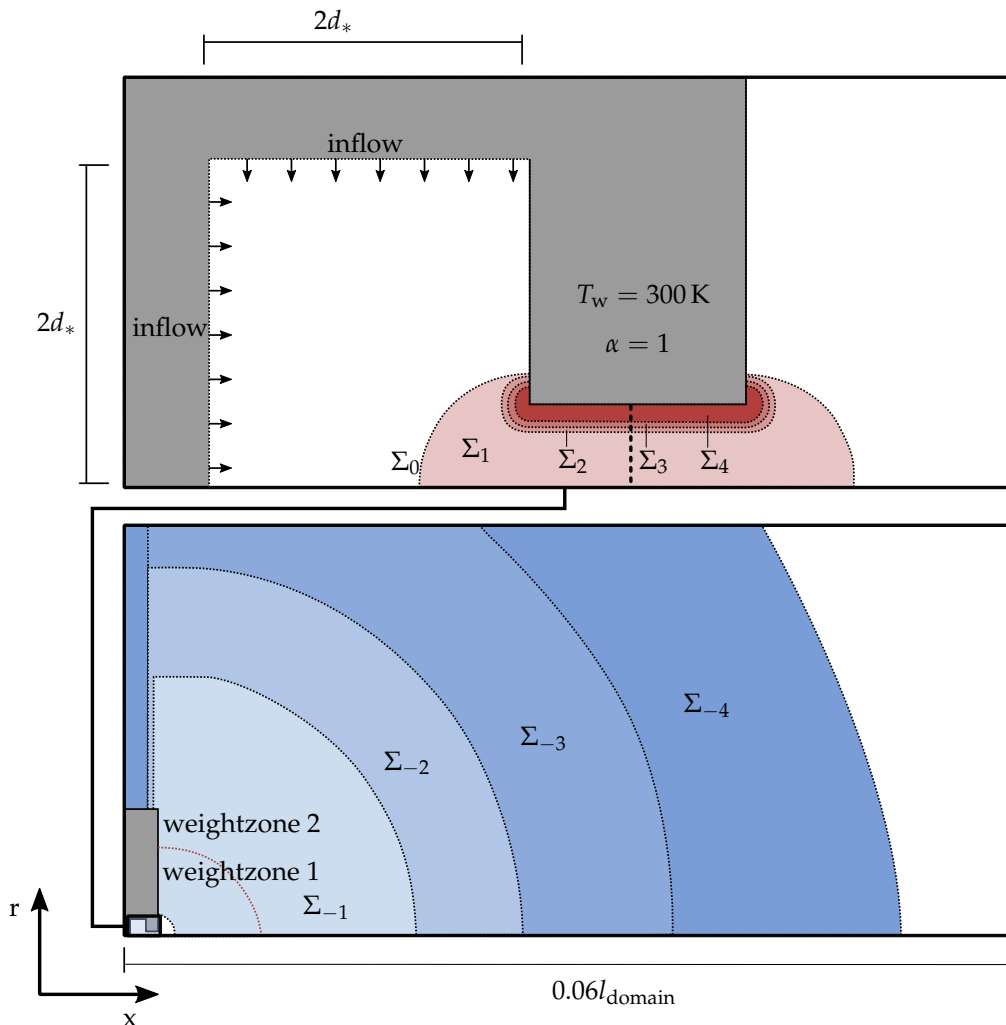


FIGURE 8.2: Setup of the simulation domain in vicinity of the orifice (upper schematic) and in the far field (lower schematic). Blue and red areas indicate regions with different grid resolutions. The lower picture shows only a small part of the entire simulation domain. The red line in the lower picture indicates the zones with different weighting factors. The black dotted line in the upper picture indicates the plane at which the mass flux is calculated in order to judge the quality of the grid resolution, as described in Subch. 8.3.1.

$n_0 = p_0/k_B/T_0 = 2.81 \cdot 10^{24} \text{1/m}^3$ is set. These parameters correspond to the reservoir pressure $p_0 = 11000 \text{ Pa}$ which is experimentally measured. Note, that only a small part of the entire reservoir is simulated. In Subch. 8.3.2 it is confirmed, that the size of the simulated reservoir is sufficiently large, so that the assumption of uniform inflow conditions is justified. Radial weighting factors are used to compensate for the decreasing number of particles in vicinity of the symmetry line caused by the assumption of axial symmetry [10].

Since any particle that reaches the far field has to pass the channel, it is of great importance to properly resolve this area of the flow. Therefore, the computational grid is gradually adapted to the channel boundary as indicated in the upper schematic of Fig 8.2. The cell size Δx_i in region Σ_i is given by $\Delta x_i = \Delta x_0/2^i$. The initial cell size Δx_0 is estimated in Subch. 8.3.1 by a grid adaptation study.

The lower part of Fig 8.2 shows a small part of the simulation domain in the far field. Note, that the entire simulation domain features an area of $l_{\text{domain}} \times l_{\text{domain}}$ in the (x, r) space. The outer edges of the simulation domain are formulated as vacuum boundary conditions, which means that particles are removed when they hit these edges. This leads to a free expansion flow, since expanding particles are not scattered back but removed from the simulation as soon as they reach the edges of the simulation domain. This assumption seems to be justified, since in STG-CT the cryogenic test section ensures that expanding particles are not scattered back, but freeze on the walls of the test section.

As the distance to the orifice increases, the particle density and the number of particles per cell decreases. Therefore, the grid cells are gradually coarsened with increasing distance to the orifice in order to compensate for the decreasing number of simulation particles. In addition, cell-specific weighting factors are used. Therefore, different *weighting zones*, featuring similar particle weighting factors, are defined. These zones feature a spherical shape and the weighting factors decrease with increasing distance to the orifice. Hence, particles that move away from the orifice are cloned as they move across the interface between different weighting zones.

In order to handle large differences in relevant time scales, a local time stepping technique is applied. For this purpose, the scheme describe by Wu et al. [145] is used, since it is very stable and allows to define different time steps for any computational cell. Time steps are estimated based on the Courant-Friedrichs-Lewy (CFL) criterion [31], which leads to an increasing time step size with increasing distance to the orifice.

Different species weighting factors $g^{(i)}$ are employed, to handle the small portion of H_2 in the mixture. Table F.5 lists the employed weighting factors. These are chosen, so that the number of simulation particles in the reservoir are identical for each species. Although this is not a mandatory prerequisite for the simulation, it is an advantage, as it resolves every species equally well in the reservoir.

8.3 Results

8.3.1 Grid convergence study

A grid convergence study is carried out to determine a grid resolution that is fine enough to sufficiently resolve the flow source.

To save computational time, simulations are not performed for the entire flow domain. Instead, only a small region of the flow domain directly around the slit, as shown in the upper part of Fig. 8.2, is simulated. To justify this assumption, the upper part of Fig. 8.4 shows the ratio between flow velocity and thermal velocity of N_2 .

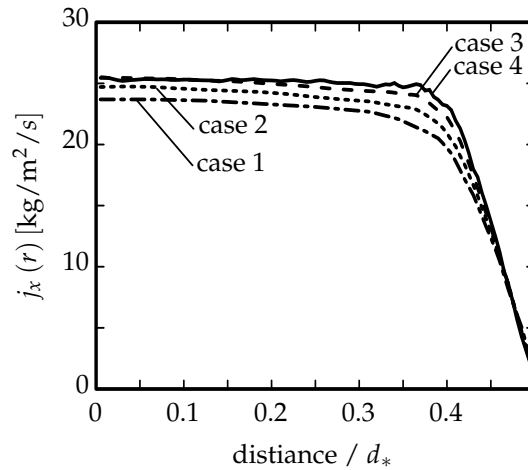


FIGURE 8.3: Distribution of mass flux density in x-direction along the channel for different grid resolutions.

It can be seen that at the outflow from the simulation area the flow velocity of N_2 exceeds the thermal velocity by far. Therefore, information flow back to the slit is very unlikely and the area around the slit can be treated separately from the rest of the expansion area.

The grid features a structure as described in Subch. 8.2. Four simulation cases with different cell sizes x_0 , as shown in Tab. 8.1, are performed. To judge the quality of

	case 1	case 2	case 3	case 4
x_0	$d_*/8$	$d_*/16$	$d_*/32$	$d_*/64$

TABLE 8.1: Cell size Σ_0 for different simulation cases.

the solution, the mass flux emitted by the flow source is calculated.

Figure 8.3 shows the local mass flux density $j_x(r) = \rho(r)v_x(r)$ in x-direction along the radius r of the channel. The plane, where the profile is calculated, is marked by the black dotted line in the upper schematic of Fig. 8.2. While there are clear differences in the mass flux distribution in the middle part of the slit between cases 1 and 2 and cases 2 and 3, no such difference can be recognized between cases 3 and 4 anymore. Possible deviations between cases 3 and 4 in the middle part of the slit are in the order of magnitude of the statistical fluctuations. Very slight deviations between case 3 and case 4 only occur in the vicinity of the boundary layer. However, these deviations are considered to be negligibly small for the following calculations. Therefore, the resolution of case 3 is applied for the following simulations.

The total mass flow for case 3 is $\dot{m}_{\text{num}} = 5.674 \cdot 10^{-6} \text{kg/s}$ which leads to a relative deviation of $|\dot{m}_{\text{num}} - \dot{m}_{\text{exp}}| / \dot{m}_{\text{exp}} = 2.4\%$ from the experimentally measured value.

8.3.2 Reservoir size

The size of the simulated reservoir must be sufficiently large, so that the assumption of homogeneous inflow conditions at the reservoir boundaries is justified. In order to check this requirement, simulations of the flow source are performed as described

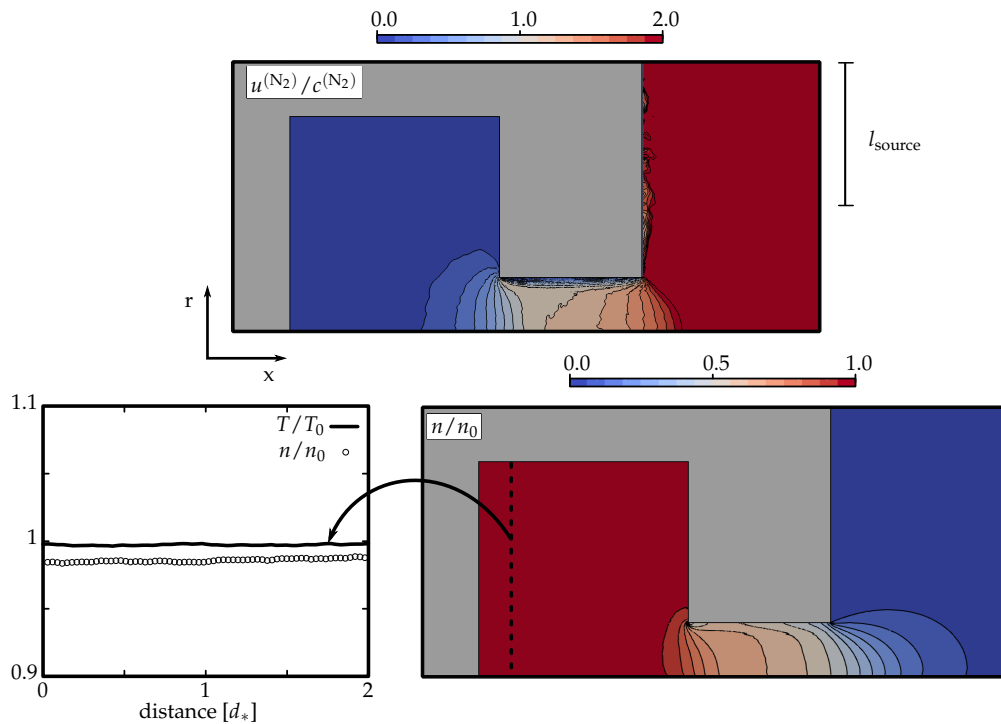


FIGURE 8.4: Above: Normalized flow velocity of N_2 . Left: Normalized number density and temperature across the reservoir. Right: Contours of normalized number density.

above. The simulation results are then checked for a correct prediction of flow quantities inside of the reservoir.

In the lower right part of Fig. 8.4 contours of the normalized number density n/n_0 are plotted. While the number density decreases strongly along the channel, it remains almost constant inside the reservoir.

To further study these results, in the lower left part of Fig. 8.4 the normalized number density n/n_0 and temperature T/T_0 along the reservoir are plotted. The temperature reaches the desired reservoir value, deviation are in the order of magnitude of statistical fluctuations. In contrast, the computed number density is slightly lower than the corresponding reservoir value. This result was to be expected: The boundary condition used for the reservoir generates a continuous particle flow based on a particle density n_0 at the inflow surface. In addition, particles that hit the inflow surface leave the simulation. If the reservoir were closed, such a boundary condition leads to a reservoir density of n_0 . However, the reservoir is not closed and particles can leave the reservoir through the slit, which slightly reduces the reservoir density compared to the inflow density n_0 . However, the deviation is assumed to be tolerable small for this test case.

In summary, no non-physical interaction between the inflow boundaries and the channel flow can be detected. In addition, the reservoir density and temperature assume the correct values, within the bounds of expectations. Hence, the size of the simulated reservoir appears to be sufficiently large.

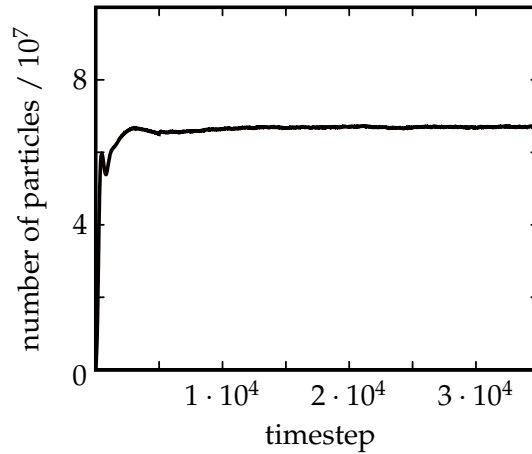


FIGURE 8.5: Number of particles in the simulation vs. the number of simulated time steps.

8.3.3 Numerical considerations

All simulations are performed on the SCART computing cluster [128]. For the calculations of the entire flow field, 80 CPUs were used. The recursive coordinate bisectioning method, which is implemented by default in SPARTA, was used to distribute the computation evenly across each processor [125]. The calculations were performed over a period of 11 hours, corresponding to a usage of 880 CPU hours.

The convergence of the simulation was evaluated based on a visual inspection the flow field and the number of particles in the simulation domain. The variation of the latter is shown in Fig. 8.5. The periodic pattern in the number of simulation particles at the beginning of the simulation can be attributed to the processes involved when initial filling the simulation region with particles. Convergence can be observed from a computation time of 10^4 time steps. Slight variations in the number of particles after this time step are due to the stochastic nature of the Monte-Carlo simulation combined with the use of local weighting factors¹. At the end of the calculation, there were approximately $6.7 \cdot 10^7$ particles in the simulation domain.

Final results are calculated as mean value, as described in Sec.2.2.5. Values that are used to calculate the averages are gathered from time step $1.5 \cdot 10^4$ every 20 time steps. In total, the simulation is performed up to time step $3.5 \cdot 10^4$, which corresponds to 1000 values that are used for the final calculation of the mean values.

8.3.4 Comparison with experiments

Figure 8.6 compares experimentally measured and numerically calculated mass flux distributions versus the polar angle Φ , in a distance of $l_{\text{domain}} = 2$ m from the source. The experimental results are normalized with the experimentally measured total mass flow \dot{m}_{exp} , while numerical results are normalized with the numerically calculated total mass flow \dot{m}_{num} . Since axial symmetry is assumed for the kinetic FP calculations, the numerical results are symmetric. Experimental measurements were

¹Experience has shown that the use of local weighting factors amplifies the stochastic fluctuations of flow variables.

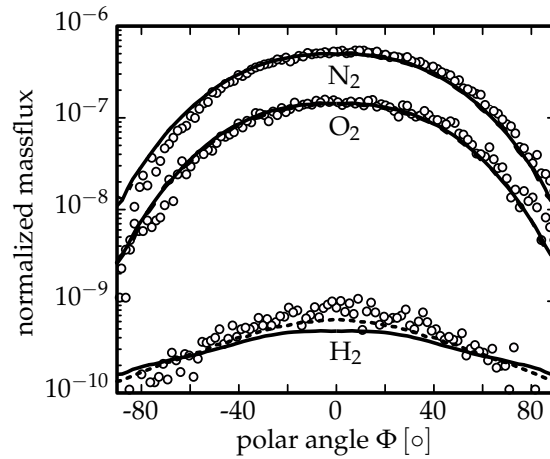


FIGURE 8.6: Normalized mass flux distributions of H_2 , N_2 , and O_2 versus polar angle Φ . Circles: Experiments. Full lines: FP results with thermodiffusion. Dotted lines: FP results without thermodiffusion.

taken for polar angles in a range of $-90^\circ \leq \Phi \leq 90^\circ$.

The experimentally measured N_2 and O_2 mass flux distributions feature a slight asymmetry. This effect might be caused by an asymmetric orifice, for example, and can not be reproduced by numerical simulations. Apart from these deviations, numerical results accurately reproduce experimentally measured N_2 and O_2 mass fluxes distributions. Deviations are in the order of magnitude of the statistical noise of the experimental measurements.

While mass flux distributions of N_2 and O_2 feature a similar shape, the mass flux distribution of H_2 is more flattened. This is due to the small molecular mass of H_2 compared to the molecular masses of N_2 and O_2 . Hence, the H_2 particles feature a larger thermal velocity component, which results in a larger amount of particles that are scattered away from the direction of expansion. This behavior is predicted by both, the numerical simulations and the experiments. However, numerical simulations are predicting a slightly more flattened distribution compared to experimental measurements.

From a numerical perspective, the deviations for the H_2 species might have different reasons. For example, the particle-wall interaction model or interspecies collision parameters might be not realistic. On the other side, an unrealistic particle-wall interaction model is expected to influence results for all species and not only for the H_2 species. Wrong interspecies collision parameters would also influence the results for any species, since these parameters are obtained with a similar technique for all species [10]. It is therefore unlikely that a wrong particle-wall interaction model or wrong collision parameters are responsible for the deviation.

From the author's point of view, the most likely reason for the discrepancy between numerical and experimental results is the assumption of a free expansion flow that is made for the numerical simulations. This assumption might not be true for the experimental measurements.

As described above, experimental measurements were taken in the STG-CT vacuum chamber. This chamber utilizes a cryogenic test sub-chamber in order to generate a high vacuum environment. However, gas that freezes on cryogenic surfaces is expected to evaporate back into the chamber [27]. This effect generates a non-zero

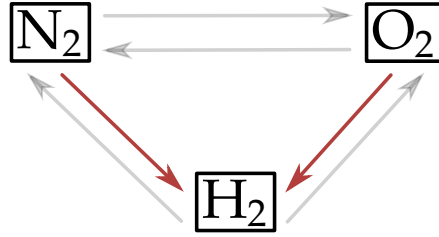


FIGURE 8.7: Potential impact of thermodiffusion on different species. Grey arrows: Thermodiffusion is negligible. Red arrows: Thermodiffusion is relevant.

background-pressure in the test sub-chamber, which is determined by the amount of particles that evaporate back into the chamber. In general, this evaporation process is a very complicated, non-steady phenomena. However, when assuming equilibrium conditions, the background pressure $p_{\text{back}}^{(\alpha)}$ of species α can be approximated by the species-specific vapor-pressure curve $p_{\text{vp}}^{(\alpha)}(T)$ [27]:

$$p_{\text{back}}^{(\alpha)} \approx p_{\text{vp}}^{(\alpha)}(T_w) = p_{\text{vp}}^{(\alpha)}(4.7 \text{ K}). \quad (8.1)$$

For the N_2 and O_2 species, this background pressure is negligible small. In contrast, it can become important for the H_2 species. For instance, when calculating a Knudsen number, based on the diameter of the STG-CT test sub-chamber and the background pressure $p_{\text{back}}^{(\text{H}_2)}$, one obtains:

$$Kn_{\text{STG-CT}}^{(\text{H}_2)} \approx 0.1. \quad (8.2)$$

To calculate this Knudsen number, vapor-pressure data provided by reference [80] was used. Hence, the test sub-chamber might feature a H_2 background gas with a significant pressure, generated by evaporating ice on the cryogenic surfaces. In particular, this background gas can not be assumed as free molecular. For this reason, the background gas could have a significant impact on the expansion behavior of the H_2 species. Since the N_2 and O_2 species feature a larger mass than the H_2 species, their expansion behavior is influenced much less by the light background gas. In order to verify this assumption, a numerical calculation of the entire STG-CT test-section would be required. However, such a comprehensive study lies beyond the scope of this work.

8.3.5 Impact of thermodiffusion

As described in Ch. 4, it is possible to explicitly neglect thermodiffusion in the proposed kinetic FP methods. This subchapter uses that feature, to investigate the impact of thermodiffusion on the expansion test case described above.

Thermodiffusion always occurs between different species. Figure 8.7 shows the potential effects of thermodiffusion on a given species caused by another species. Thermodiffusion between the N_2 and O_2 species is expected to be negligible small, since thermodiffusion becomes only relevant between species that feature large differences in mass and size. Because the mole fraction of H_2 is small for this test case, the impact of thermodiffusion on N_2 and O_2 , caused by the H_2 species, is also expected to be negligible. Therefore, it is expected that only for H_2 species an influence of thermodiffusion can be detected.

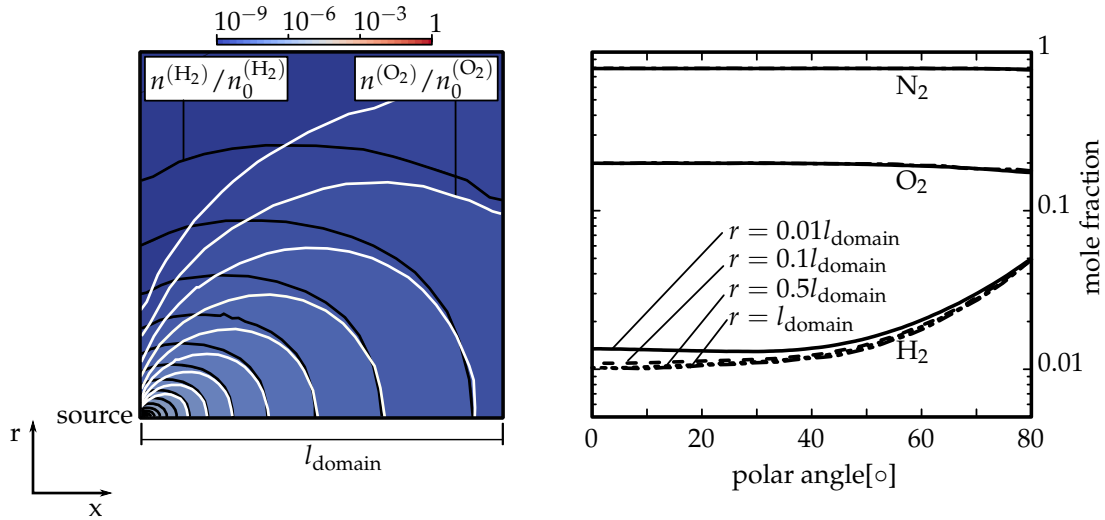


FIGURE 8.8: Left: Contours of normalized O_2 density (colored background and white lines) and normalized H_2 density (black lines). Right: Mole fraction of N_2 , O_2 and H_2 against the polar angle ϕ for different distances r from the slit. The reader should note that there is no significant difference in the mole fractions for N_2 and O_2 . Therefore, the different lines lie on top of each other.

The simulation results, shown in Fig 8.6, confirm these assumption. Thermodiffusion only influences the H_2 species. In particular, it leads to a more flattened distribution of the mass flux. The following subchapter tries to explain this effect by analyzing the flow fields, obtained by numerical simulations.

Large differences in the spatial scales of the flow make it difficult to analysis the entire flow field. For example, the total size l_{domain} of the simulation domain is $l_{\text{domain}}/d_* \approx 3333$ times larger than the channel size d_* . However, most of the important physical processes take place near the flow source. Far from the source, the low number density leads to a free molecular particle transport, which results in self-similarities of flow structures.

To clarify this effect, in the left part of Fig. 8.8 contours of the normalized O_2 and H_2 number densities in the complete far field are plotted. As expected, contours feature a similar shape at different distances from the source. To investigate this phenomena in more detail, in the right part of Fig. 8.8 H_2 , N_2 and O_2 mole fractions over the polar angle for different distances from the flow source are plotted. The N_2 and O_2 mole fractions do not change for the plotted distances. The distribution of the H_2 mole fraction changes near to the flow source, but stays also constant for distances large than $\approx 0.1l_{\text{domain}}$. Hence, particle-particle and particle-wall collisions, that lead to a change in the mole fraction must take place in direct vicinity of the flow source. Therefore, only this area of the flow will be considered in the further analysis.

Thermodiffusion is driven by temperature gradients [97]. In general, the large particles of the mixture diffuse to cold areas and the small particles to hot areas. For species that feature a similar temperature, it can be shown, that thermodiffusion leads to a diffusion velocity, that is proportional to $\nabla \ln(T)$ [10]:

$$\mathbf{u}_{d,\text{thermo}}^{(\alpha)} \sim k_{\text{thermo}}(\alpha) \cdot \nabla \ln(T). \quad (8.3)$$

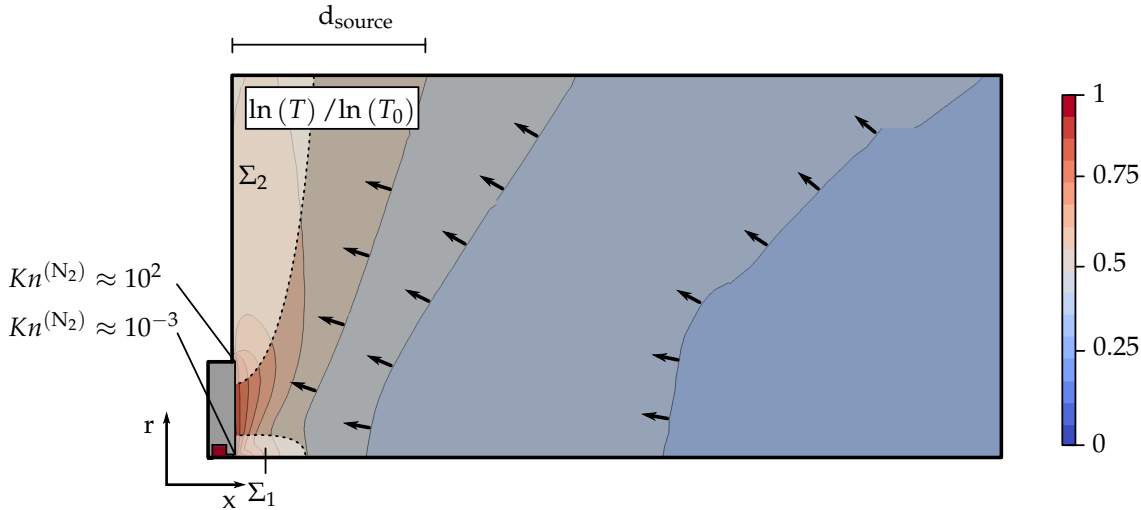


FIGURE 8.9: Logarithmic temperature contours in the vicinity of the flow source. Black arrows mark the impact of thermodiffusion on the H_2 species. Since H_2 is the smallest species in the mixture, thermodiffusion drives the H_2 particles to areas with large temperature. Accordingly, the arrows point in the direction of increasing temperature. To demonstrate the strong dilution, the Knudsen number for N_2 , based on the diameter d^* , was calculated for two locations in the flow field as an example.

The constant k_{thermo} in Eq. (8.3) depends on the species attributes. To study the impact of thermodiffusion on the H_2 species, in Fig. 8.9 the logarithmic mixture temperature distribution in the vicinity of the flow source is plotted. The particle density in the area Σ_2 is small ², so that mass diffusion effects that occur in this region can be neglected. Since the area Σ_1 is small ³, the average residence time of particles in this area is short. Because thermodiffusion is a rather slow process, diffusion effects which occur in this region can also be neglected. In all remaining areas of the flow, black arrows represent gradients of $\ln(T)$, indicating the direction of the diffusion effect, that is induced by thermodiffusion.

Thermodiffusion contributes to the total mass flux that tends away from the flow source. As indicated in Fig. 8.9, thermodiffusion reduces the x -component and increases the r -component of this flux. Therefore, H_2 particles are driven to larger radii by the thermodiffusion effect. This results in more flattened distribution of the H_2 mass flux when enabling thermodiffusion, as shown in Fig. 8.6.

8.4 Summary and conclusion

In this chapter, the applicability of the kinetic FP method to a complex test case was demonstrated. For this purpose, the expansion of a gas out of an axially symmetric orifice into a vacuum environment was simulated. A mixture consisting of N_2 , O_2 , and H_2 was used as the test gas, with H_2 as a trace species. The diameter of the orifice was 0.6 mm, but an area up to 2 m away from the expansion center was simulated. Local weighting factors and time steps were used to cope with the large

² The Knudsen number for the N_2 species is around 10^{-3} at the outlet of the slit, but around 10^2 at the outer source wall, as indicated in Fig. 8.9.

³ The area Σ_1 feature a dimension of d_{source} which is 120 times smaller that the distance between slit and mass spectrometer.

differences in the relevant time and length scales. Similarly, species-specific weighting factors were used to simulate sufficient numbers of particles for the H_2 species. For the calculation, the VHS-FP model from Ch. 5 was used in conjunction with the CLT model discussed in Ch. 6 to model rotational energies.

Species-specific mass flux distributions were compared with experimental measurements recorded at the STG-CT vacuum chamber at DLR Göttingen. The comparison with the experimental measurements shows good results for the mass flux distributions of N_2 and O_2 . For H_2 , on the other hand, deviations occur, specifically the numerical simulation predicts larger mass fluxes at high polar angles compared to the measurements. However, these deviations can be well explained by the finite H_2 background pressure in the STG-CT vacuum chamber, which is not modeled by the numerical simulation.

In addition, the effects of thermodiffusion were investigated by performing simulations without thermodiffusion, as described in Ch. 4. It was observed that thermodiffusion affects the expansion behavior of the H_2 species. In particular H_2 particles are scattered to larger polar angles due to the thermodiffusion effect during expansion. This results in numerical results deviating more from experimental measurements when thermodiffusion is modeled than when thermodiffusion is excluded. It should be noted, however, that this does not mean that the modeling approach with thermodiffusion is less realistic. Rather, thermodiffusion leads to a similar effect on the expansion as the assumption of a negligible low background pressure in the vacuum chamber.

In order to be able to classify the results of this chapter, it is important to understand that the numerical calculation of strongly expanding flows is a highly non-trivial problem. This is because the far field of the expansion usually has to be computed with DSMC due to strong dilution, while DSMC cannot be used in the reservoir because the particle density and thus the computational time would be too large. Therefore, classical approaches couple continuum solvers in the reservoir with DSMC in the far field [142, 58]. However, such couplings are technically difficult to implement. This is because the physical models used in the DSMC method must be adapted to the models used in the continuum method, but also because the interface between the two methods, due to the fundamentally different modeling approach, is difficult to handle.

In this chapter, it was shown that such complex expansion flows can be calculated with relatively little effort using the kinetic FP method. This is due to the fact that the kinetic FP method could be used to calculate the entire flow field, i.e. for the reservoir as well as for the far field. Thus, no complex coupling between two different numerical methods had to be performed. This shows that with the kinetic FP method a powerful tool is given to analyze such strong expansion flows.

At this point it is important to point out that the kinetic FP method is of course not applicable for arbitrary rarefied gases. However, it is the case that the method provides the correct solution for the limiting case of small Knudsen numbers as well as for the limiting case of large Knudsen numbers. Thus, the FP method can be used for continuum flows as well as for strongly rarefied flows, only in the transition regime between these two limit cases it loses its validity. For strong expansion flows, the flow field is essentially determined by regions of very strong dilution and by regions in the continuum, which is why the FP method gives very good results even without coupling with DSMC. In other cases, where the transition region between the two limiting cases is more relevant, coupling with the DSMC method probably

cannot be dispensed with. However, even if this should become necessary, it has been shown for monatomic FP methods that the kinetic FP method and DSMC can be coupled very easily due to algorithmic similarity [57, 76]. This is also true for the FP methods used here, since they have the same algorithmic similarity to the DSMC method and are based on the same physical models as DSMC.

Furthermore, it could be demonstrated in this chapter that with the developed models it is possible to investigate the influence of thermodiffusion by systematically switching off or adding this effect in simulations. Thus, a greater understanding of the processes in the expansion could be achieved. Such an analysis is not possible with the DSMC method, because here thermodiffusion can not be easily switched of.

However, the most important conclusion of this chapter is that the methods developed in this thesis can also be applied to large simulation cases: While all previous simulations were performed on a local computer with only one computational core, this calculation was performed on a computational cluster with 80 CPUs over 11 hours. Nevertheless, the calculation ran stable and no unexpected problems occurred, neither for the models for VHS gas mixtures nor for the models for internal energies. It can be concluded that the developed models can also be used for large-scale flow cases. This finding may be trivial from the point of view of theoretical development. However, for many potential users of a numerical method, it is important to know in advance that the method can not only handle academic test cases, but can also be applied to large-scale real-world problems. And exactly this could be shown for the kinetic FP method in this chapter.

Chapter 9

Conclusion and Outlook

9.1 Summary

In this work, several kinetic FP methods are developed to describe complex physical phenomena in rarefied hypersonic gasflows. More specifically, FP models are developed for the treatment of polyatomic molecules as well as for gas mixtures. All methods are investigated in terms of their computational efficiency and tested for representative hypersonic gas flows. Finally, a large simulation case is performed to also demonstrate the suitability of the proposed methods for realistic applications.

The relaxation of internal energies of polyatomic species is modeled by a master equation. In agreement with the kinetic Fokker-Planck model, the master equation is not solved directly, but instead the microscopic energy states are simulated by solving stochastic jump processes. The well-known Gillespie algorithm is used to solve the jump processes, resulting in a simple solution algorithm. Three different models for the rate coefficients of the master equation are developed, allowing to model both continuous and discrete internal energy structures. The models each describe the relaxation process at different levels of detail: While the CLT and DLT models lead to a relaxation of the temperatures according to the Landau-Teller law, the DLB model can describe the relaxation of specific energy levels in accordance with the well-known Larsen-Borgnakke model.

Gas mixtures are modeled by introducing separate distribution functions and Fokker-Planck equations for each species. The model parameters of these Fokker-Planck equations are set very similar to the single species model of Gorji et al. [55]. In particular, a polynomial dependence on particle velocities was chosen for the drift coefficients. Analogous to the single-species case, the FP equations were not solved directly. Instead, the associated stochastic equations of motion were solved to simulate the microscopic particle motion. An algorithm was developed to solve the equations of motion that guarantees conservation of energy and momentum independent of the applied time step size.

The kinetic FP method for gas mixtures has been developed to be consistent with Grad's moment equations for HS particles in the limiting case of small Knudsen numbers. Based on this method, another kinetic FP method is constructed but based on the VHS interaction potential. Due to the similarity of the HS and VHS interaction potentials, the original HS-FP method needs only minor modification for this purpose. In particular, the HS-FP method is included as a limiting case in the kinetic

VHS-FP method.

The VHS-FP method for gas mixtures and the model for polyatomic molecules are combined in order to construct a kinetic FP model that is capable of describing multi species, polyatomic gases. Similar as for the single species case, three different models for the rate coefficients of the master equation were constructed. These models allow to describe the relaxation behavior of continuous, as well as discrete internal energy states and are consistent with the Landau-Teller equation and the Larsen Borgnakke model.

Updating particle velocities within the proposed multi species kinetic Fokker-Planck algorithms requires solving a system of differential equations for each grid cell in each time step. The system is linearized to increase the efficiency of the particle algorithm. Errors that can occur due to the assumptions of the linearization are examined in two representative test cases.

The computational effort of the proposed FP methods is compared with that of the DSMC algorithm by performing zero-dimensional heat bath calculations with both methods. Based on this study, it was shown that the proposed kinetic FP methods are indeed more efficient than DSMC in simulating time and length scales above the mean free path and mean collision time. Based on these results, different strategies are derived to efficiently apply the kinetic Fokker-Planck algorithm.

The expansion behavior of synthetic air from an axially symmetric orifice is studied to test the practical applicability of some of the proposed methods. Local time stepping and local weighting factors are used to handle large differences in spatial and temporal scales of the test case. The numerical simulations capture several magnitudes of Knudsen numbers, from the high pressure reservoir up to the free molecular far field. Numerical results are compared with experimental measurements of species-specific mass fluxes that were taken in the DLR high-vacuum plume test facility for chemical thrusters (STG-CT) at the German Aerospace Center (DLR), Göttingen. For N_2 and O_2 good agreement between numerical results and experimental measurements is observed. For H_2 differences between measurements and simulation results can be detected. However, these deviations can be explained by the finite background pressure in the test section of the STG-CT, which is not modeled by the numerical simulations.

9.2 Conclusion

The modeling of rarefied hypersonic gas flows requires the calculation of flows where both translational and internal energies are far from the equilibrium state of the Boltzmann distribution. Since the kinetic FP method has proven to be a powerful tool for modeling such flows, the extension of this method is discussed in this thesis. Attention is paid to the modeling of phenomena which are of great importance for the practical applicability in hypersonic gas flows.

Polyatomic molecules are found in almost all practical applications of hypersonic aerothermodynamics. Since such flows are usually accompanied by either very high

temperatures or very low temperatures, rotational and vibrational processes are either strongly excited or frozen. Both effects have a great influence on the aerothermodynamic behavior of the flow. Therefore, this work first investigated how the combination of the kinetic FP model with a master equation leads to a simulation method that can describe such excited polyatomic molecules.

Even though the modeling of excited internal energies with the kinetic FP method has already been discussed in other publications [53, 111, 122], the approach of this work brings the advantage over these publications that it can be flexibly adapted to a wide variety of relaxation cases. In particular, by choosing the rate coefficients of the master equation appropriately, it is possible to tune the model from this thesis such that specific internal energy levels relax according to specific specifications. This was demonstrated by the example of the DLB model, which was constructed to fit the relaxation behavior of individual energy levels to the Larsen-Borgnakke model. Because of this flexibility, it is also readily possible, to adjust the model from this thesis to other DSMC models. This is a major advantage for two reasons: first, it greatly simplifies the coupling of kinetic FP with DSMC, since both methods use consistent physical modeling. Second, this approach eliminates the need to design entirely new models for the FP method when it comes to relaxation of internal energies. Instead, one of the many DSMC models developed in recent years can simply be adapted to the FP method.

Another important capability for the practical applicability of the FP method is the modeling of gases with multiple species. Therefore, a kinetic FP model for the description of gas mixtures was developed in this thesis. This method is, to the best of the author's knowledge, at the time this thesis was written, besides the model of Gorji et al. [51], the only kinetic FP method which can model gas mixtures. However, the model of Gorji et al. [51] was defined only for binary gas mixtures and is based on the less realistic Maxwell molecular model. In contrast, the model from this thesis is defined for an arbitrary number of species and is based on the realistic HS model to describe the particle interaction. This is a great advantage because in practice many flows consist of more than two species. In particular, however, the use of the HS collision model leads to two further advantages: First, it greatly simplifies a possible coupling with the DSMC method, since the HS model can be easily implemented there as well. On the other hand, the large pool of HS model parameters, which has accumulated over the many years in which the HS model was used as a standard in the DSMC method, can be used for simulations with the FP method from this thesis. In sum, the applicability of kinetic FP is greatly enhanced by the multi-species model developed in this thesis.

Even though the application of the HS model already has a number of important advantages, the VHS model has become more widely used in recent years. This is mainly due to the fact that the VHS model provides an additional model parameter and can thus be better adapted to the properties of many gases, while being only slightly more complex than the HS model. Therefore, an FP model for VHS gas mixtures was developed, based on the FP model for HS gas mixtures.

In addition to the advantage of having another model parameter, this development is important for two other reasons: first, the VHS model has become the standard in the DSMC method since several years. Hence, with the development of a FP method based on the VHS model, the FP method becomes interesting for all DSMC users, who couple the DSMC method with continuum methods, e.g. to investigate flows with local areas with very small Knudsen numbers. This is because such a coupling

becomes trivial with the VHS FP method described here, since it is based on the same physical models as DSMC. Second, by extending the FP model to the VHS collision model, it was shown that it is in principle possible to extend the proposed FP model to other molecular interaction potentials as long as the corresponding production terms are known. Accordingly, it would be conceivable, for example, to include more complex interaction potentials, e.g., the Lennard-Jones potential. This would significantly increase the applicability of the FP method, even for applications away from dilute hypersonic flows.

In order to justify the use of the FP methods developed in this thesis in comparison to the DSMC method, it is essential to show that the FP methods compute faster than the DSMC method. This was shown in the context of an efficiency study. Since a representative, one-dimensional test case was considered in the efficiency study, another application of this study opens up: future users of the FP method can use the study to estimate with relatively little effort whether the simulation for a specific test case can be performed faster with the FP method than with DSMC. Of course, this statement can only be made for the specific implementations of the DSMC and FP methods used in this work. However, it should be easy for a potential user to perform analogous investigations for his own implementations of the DSMC and FP method.

In order to demonstrate the practical applicability of the developed methods, it is indispensable to apply the methods at least exemplarily to a large test case, which goes beyond purely academic investigations in terms of complexity. This seems to be a trivial investigation from a theoretical point of view, but in practice it has been shown that many numerical difficulties only arise in large application cases and thus the applicability of a method can only be finally assessed in such large simulations. Therefore, a number of the developed methods were applied to a complex expansion test case. It could be shown that no unexpected numerical problems occur and the good comparison with experimental measurements underlines the quality of the modeling.

As much as this work has extended the scope of the kinetic FP method, some important aspects have fallen by the wayside due to time constraints. For example, in modeling polyatomic molecules, only the energy exchange between rotation and translation or between rotation and vibration was modeled. In contrast, a direct energy exchange between rotation and vibration cannot be modeled with the proposed CLT, DLT and DLB models. In a more realistic approach, however, this direct energy exchange between rotation and vibration could be considered. At this point it should be noted that such a modeling is also possible with the master equation model proposed here. In this case, however, the rate coefficients of the models for vibrational and rotational energies would have to be matched accordingly.

Another important aspect in the description of space-relevant gas flows, which is not addressed in this thesis, is the modeling of chemically reacting gases. This usually becomes relevant at very high temperatures, as they occur during re-entry in front of very fast objects or in the exhaust plume of chemical thrusters. It should be noted, however, that this work has laid the foundation for future modeling of chemical reactions using the kinetic FP method by developing FP models for gas mixtures and excited molecules. This is because chemical reactions always occur in association with several species, and the modeling of reactions, such as dissociation,

usually refers to the excited state of a molecule. Both can be modeled in detail with the approach described in this work.

For the numerical calculation of particle positions and velocities in the FP method, the simplest conceivable approach was implemented for the models developed in this thesis. In particular, the particle positions were calculated based on a linear displacement similar to the DSMC method, and a simple Euler method was used for the integration of the particle velocities. It follows that the time steps should not be chosen much larger than the mean time between particle collisions, otherwise strong numerical diffusion is expected. This was not a strong limitation for this thesis, since the FP method was mainly used for test cases with hypersonic flows. There, the time step is primarily determined by the need to resolve the large flow velocities, so the above limitation becomes negligible. For future users, however, this limitation could lead to serious restrictions in the applicability of the FP method, for example when simulating the reservoir of a thruster. However, since this limitation is not a fundamental problem of the FP method, but only due to the numerical implementation, it would be useful to develop higher order methods for the integration of particle motions in the future. For the case of a single species, this has also already been investigated by various authors [84, 55, 35].

To validate the developed models and to motivate potential users to deal with the models, representative test cases were simulated at the end of each chapter and some of the models were also applied to a large test case in Ch. 8. However, due to the focus of this thesis as a feasibility study, many detailed questions remain about the applicability of the models. First, there is the question of a parameter space in which the FP methods are applied with still acceptable errors. For example, for already established models, such as the Navier-Stokes equations, the Knudsen number is traditionally used as a parameter to characterize the applicability [5]. Similar analyses would be useful for the methods presented here, as this would greatly facilitate the question of the applicability of FP methods to a particular test case. Another question that a potential user might ask is how the methods developed here behave to other established continuum methods, such as the Navier-Stokes equations or the R13 equations. Such comparisons could help a potential user decide whether to use the FP method.

Appendix A

DSMC

A.1 Particle selection scheme

The particle selection scheme proposed by Zhang et al. [147] determines particles for inelastic energy exchange in DSMC collisions. The scheme allows only one collision partner to change its internal energy during a collision. This restriction is of course not correct and the scheme is thus not suitable to model the population of individual energy states correctly, i.e. in agreement with experimental measurements. However, if it is not necessary to model the relaxation of individual energy levels, then the scheme offers some valuable algorithmic advantages. For example, it can be easily generalized to describe gas mixtures and it leads to a relaxation of the internal energies corresponding to the Landau-Teller law.

Figure A.1 illustrates the particle selection process with a particle 1 of species α and a particle 2 of species β . Once a particle pair is selected for an elastic collision, collision

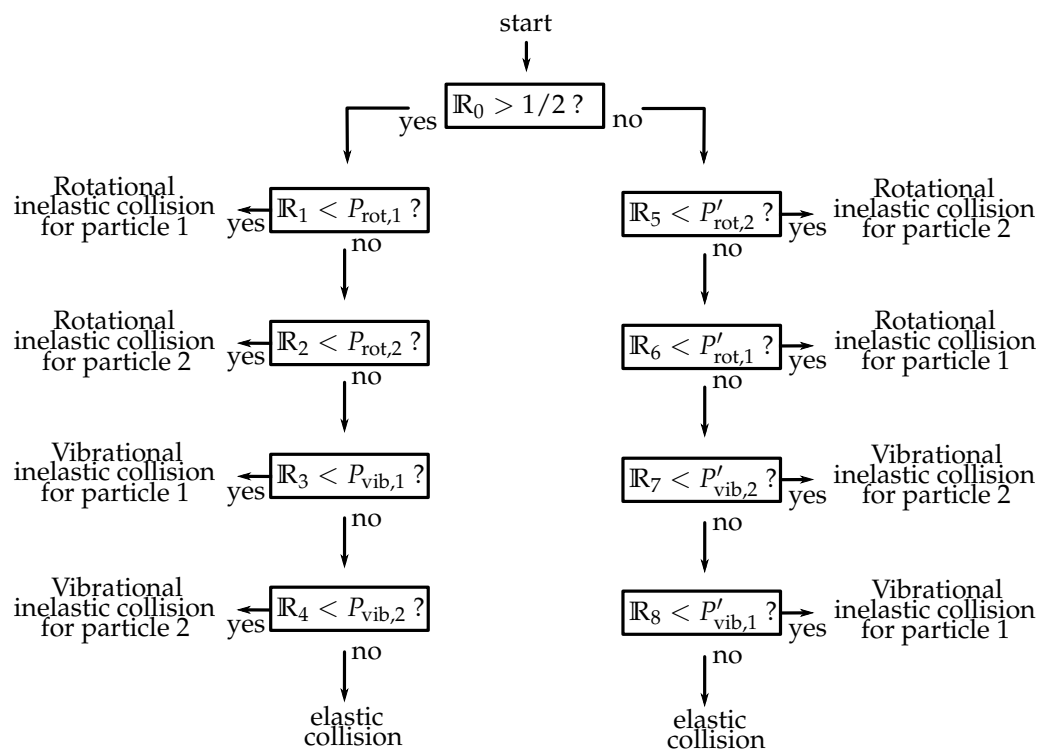


FIGURE A.1: Decision tree for selecting particles that experience inelastic energy exchange during a DSMC collision according to [147]. Particle 1 is of species α , while particle 2 is of species β . Random numbers $\mathbb{R}_i \in [0, 1]$ are uniformly distributed.

partners are sequentially tested for internal energy exchange. When internal energy exchange takes place, the internal energy of the selected particle and the translational collision energy is redistributed according to the Larsen-Borgnakke model. Otherwise, standard DSMC procedures for elastic collisions are performed.

The probabilities in Fig. A.1 are defined as:

$$P_{\text{rot},1} = F_{\text{rot}}^{(\alpha)}, \quad (\text{App.A.1})$$

$$P_{\text{rot},2} = \frac{F_{\text{rot}}^{(\beta)}}{1 - F_{\text{rot}}^{(\alpha)}}, \quad (\text{App.A.2})$$

$$P_{\text{vib},1} = \frac{F_{\text{vib}}^{(\alpha)}}{1 - F_{\text{rot}}^{(\alpha)} - F_{\text{rot}}^{(\beta)}}, \quad (\text{App.A.3})$$

$$P_{\text{vib},2} = \frac{F_{\text{vib}}^{(\beta)}}{1 - F_{\text{rot}}^{(\alpha)} - F_{\text{rot}}^{(\beta)} - F_{\text{vib}}^{(\beta)}}, \quad (\text{App.A.4})$$

$$P'_{\text{rot},2} = F_{\text{rot}}^{(\beta)}, \quad (\text{App.A.5})$$

$$P'_{\text{rot},1} = \frac{F_{\text{rot}}^{(\alpha)}}{1 - F_{\text{rot}}^{(\beta)}}, \quad (\text{App.A.6})$$

$$P'_{\text{vib},2} = \frac{F_{\text{vib}}^{(\beta)}}{1 - F_{\text{rot}}^{(\beta)} - F_{\text{rot}}^{(\alpha)}}, \quad (\text{App.A.7})$$

$$P'_{\text{vib},1} = \frac{F_{\text{vib}}^{(\alpha)}}{1 - F_{\text{rot}}^{(\beta)} - F_{\text{rot}}^{(\alpha)} - F_{\text{vib}}^{(\alpha)}}. \quad (\text{App.A.8})$$

In the following, equations will be only shown for the α species. Equations for the β species can be obtained by simply exchanging indices. Expressions for $F_{\text{vib}}^{(\alpha)}$ and $F_{\text{rot}}^{(\alpha)}$ are given by:

$$F_{\text{vib}}^{(\alpha)} = Z_{\text{vib}}^{(\alpha\beta)} \cdot \frac{\zeta_{\text{t}}^{(\alpha\beta)} + \frac{\exp(\theta^{(\alpha)}/T)}{2} d_{\text{vib}}^{(\alpha)2}}{d_{\text{trans}}^{(\alpha\beta)}}, \quad (\text{App.A.9})$$

$$F_{\text{rot}}^{(\alpha)} = Z_{\text{rot}}^{(\alpha\beta)} \cdot \frac{f_{\text{t}}^{(\alpha\beta)} + d_{\text{rot}}^{(\alpha)}}{d_{\text{trans}}^{(\alpha\beta)}}. \quad (\text{App.A.10})$$

Here $d_{\text{trans}}^{(\alpha\beta)} = 5 - 2\omega^{(\alpha\beta)}$ denotes the number of the translational degrees of freedom during a particle collision according to the VHS interaction model. $d_{\text{vib}}^{(\alpha)}$ and $d_{\text{rot}}^{(\beta)}$ denote the number of vibrational and rotational degrees of freedom:

$$d_{\text{vib}}^{(\alpha)} = \frac{2\theta^{(\alpha)}/T}{\exp(\theta^{(\alpha)}/T) - 1}, \quad (\text{App.A.11})$$

$$d_{\text{rot}}^{(\alpha)} = 2. \quad (\text{App.A.12})$$

Note that $\theta^{(\alpha)}$ refers to a species specific characteristic vibrational temperature.

Appendix B

Internal energies

B.1 Conservation equation

This subchapter proves the conservation equations for the model equation (3.8). Assuming that the underlying Fokker-Planck operator already satisfies the conservation equations, the following relationships apply:

$$\int d\mathbf{c} S_{\text{FP}} = 0, \quad (\text{App.B.1})$$

$$\int d\mathbf{c} S_{\text{FP}} \mathbf{c} = 0, \quad (\text{App.B.2})$$

$$\int d\mathbf{c} S_{\text{FP}} \mathbf{c}^2 = 0. \quad (\text{App.B.3})$$

B.1.1 Mass conservation

With the nomenclature introduced in Eq. (3.8), conservation of mass is expressed by $\sum_n \int d\mathbf{c} B_n = 0$. Expanding the integrand, it can be found that:

$$\sum_n \int d\mathbf{c} B_n = \sum_n \left(\underbrace{\int d\mathbf{c} S_{\text{FP}}}_i + \underbrace{\int d\mathbf{c} K \frac{\partial f_n}{\partial v_i \partial v_i}}_{ii} + \underbrace{\sum_j \left(R_{jn} \int d\mathbf{c} f_j - R_{nj} \int d\mathbf{c} f_n \right)}_{iii} \right). \quad (\text{App.B.4})$$

Expression (i) vanishes because of the mass conservation of S_{FP} . Expression (ii) vanishes since $K = K(\mathbf{r}, t)$ does not depend on \mathbf{c} (see Eq. (App.B.15)). When defining $n_i \equiv \int d\mathbf{c} f_i$, expression (iii) reduced to:

$$\sum_n (iii) = \sum_{nj} (R_{jn} n_j - R_{nj} n_n) = \sum_{nj} R_{jn} n_j - \sum_{nj} R_{nj} n_n = \sum_{nj} R_{jn} n_j - \sum_{nj} R_{jn} n_j = 0. \quad (\text{App.B.5})$$

and therefore:

$$\sum_n \int d\mathbf{c} B_n = 0. \quad (\text{App.B.6})$$

B.1.2 Momentum conservation

With the nomenclature introduced in Eq. (3.8), conservation of momentum is expressed by $\sum_n \int d\mathbf{c} B_n \mathbf{c} = 0$. Expanding the integrand, it can be found that:

$$\sum_n \int d\mathbf{c} B_n \mathbf{c} = \sum_n \left(\underbrace{\int d\mathbf{c} S_{\text{FP}} \mathbf{c}}_i + \underbrace{\int d\mathbf{c} K \frac{\partial f_n}{\partial v_i \partial v_i} \mathbf{c}}_{ii} + \underbrace{\sum_j \left(R_{jn} \int d\mathbf{c} f_j \mathbf{c} - R_{nj} \int d\mathbf{c} f_n \mathbf{c} \right)}_{iii} \right) \quad (\text{App.B.7})$$

Expression (i) vanishes since S_{FP} conserves momentum and expression (ii) vanishes because $K = K(\mathbf{r}, t)$ does not depend on \mathbf{c} (see Eq. (App.B.15)). Expression (iii) vanishes after a similar calculation as in B.1.1. Hence, it follows:

$$\sum_n \int d\mathbf{c} B_n \mathbf{c} = 0. \quad (\text{App.B.8})$$

B.1.3 Energy conservation

With the nomenclature introduced in Eq. (3.8), conservation of energy is expressed by $\sum_n \int d\mathbf{c} B_n \left(\frac{1}{2} m \mathbf{v}^2 + e_n \right) = 0$. Expanding the integrand, it can be found that:

$$\begin{aligned} \sum_n \int d\mathbf{c} B_n \left(\frac{1}{2} m \mathbf{v}^2 + e_n \right) = \\ \sum_n \left(\underbrace{\int d\mathbf{c} S_{\text{FP}} \frac{1}{2} m \mathbf{v}^2}_i + \underbrace{\int d\mathbf{c} K \frac{\partial f_n}{\partial v_i \partial v_i} \frac{1}{2} m \mathbf{v}^2}_{ii} + \underbrace{\sum_j \left(R_{jn} \int d\mathbf{c} f_j \frac{1}{2} m \mathbf{v}^2 - R_{nj} \int d\mathbf{c} f_n \frac{1}{2} m \mathbf{v}^2 \right)}_{iii} \right) + \\ \sum_n \left(\underbrace{\int d\mathbf{c} S_{\text{FP}} e_n}_{iv} + \underbrace{\int d\mathbf{c} K \frac{\partial f_n}{\partial v_i \partial v_i} e_n}_v + \underbrace{\sum_j \left(R_{jn} \int d\mathbf{c} f_j e_n - R_{nj} \int d\mathbf{c} f_n e_n \right)}_{vi} \right). \end{aligned} \quad (\text{App.B.9})$$

Expression (i) vanishes since S_{FP} conserves energy and expression (iii) vanishes after a similar calculation as in B.1.1. Expression (iv) becomes zero since S_{FP} conserves mass and expression (v) vanishes because $K = K(\mathbf{r}, t)$ does not depend on \mathbf{c} . Using integration by parts and assuming that K does not depend on \mathbf{c} , term (ii) reduces to:

$$(ii) = 3 K m n. \quad (\text{App.B.10})$$

Applying the definition $\Delta e_{jn} \equiv e_n - e_j$, expression (vi) becomes:

$$\begin{aligned} \sum_n (vi) &= \sum_{nj} \left(R_{jn} \int d\mathbf{c} f_j e_n - R_{nj} \int d\mathbf{c} f_n e_n \right), \\ &= \sum_{nj} (R_{jn} n_j e_n - R_{nj} n_n e_n), \end{aligned} \quad (\text{App.B.11})$$

$$= \sum_{nj} R_{jn} n_j e_j + \sum_{nj} R_{jn} n_j \Delta e_{jn} - \sum_{nj} R_{nj} n_n e_n, \quad (\text{App.B.12})$$

$$= \sum_{nj} R_{jn} n_j \Delta e_{jn} = \sum_j H_j n_j, \quad (\text{App.B.13})$$

with:

$$H_j \equiv \sum_n R_{jn} \Delta e_{jn}. \quad (\text{App.B.14})$$

To satisfy the energy conservation, the following expression for the coefficient K must hold:

$$K = -\frac{1}{3m n} \sum_j H_j n_j(\mathbf{r}, t). \quad (\text{App.B.15})$$

The coefficient K is used in order to describe energy exchange between internal and translational modes. H_j is a constant that depends only on the energy structure of the system. Therefore, at the beginning of each simulation a lookup table of H_j is calculated for efficiently evaluating Eq. (App.B.15). However, for the three proposed models in Subch. 3.3, a simpler expression for K may be derived. Because all models are satisfying the Landau-Teller relaxation, term (vi) in Eq. (App.B.9) can be written as:

$$\sum_n (vi) = \frac{n}{\tau_{\text{int}}} (E_{\text{int}}^{\text{eq}} - E_{\text{int}}). \quad (\text{App.B.16})$$

Therefore, it follows that:

$$K = -\frac{1}{3 m \tau_{\text{int}}} (E_{\text{int}}^{\text{eq}} - E_{\text{int}}). \quad (\text{App.B.17})$$

B.2 H-Theorem

In this subchapter the H-theorem for the model Eq. (3.8) is proven, under the assumptions that the operator S_{FP} satisfies the H-theorem and that translational velocities are in equilibrium. The reader should note, that the H-theorem has not been proven for the cubic FP operator, which is used throughout this work. However, the model Eq. (3.8) could also be constructed with different FP operators that satisfy the H-theorem, for example the ES-FP model [110, 111].

In the following, the entropy function $H(t)$ is defined as:

$$H(t) \equiv \int d\mathbf{c} \sum_n \ln(f_n) f_n. \quad (\text{App.B.18})$$

Hence, for a homogeneous system, the following relationships must hold:

$$\frac{dH(t)}{dt} \leq 0, \quad (\text{App.B.19})$$

$$\frac{dH(t)}{dt} = 0 \quad \text{when} \quad f = f_{\text{eq}}, \quad (\text{App.B.20})$$

where f_{eq} denotes the equilibrium distribution function.

In the following, Eq. (App.B.19) is proven. Let f_n be an arbitrary distribution function. For a homogeneous system it can be found that:

$$\frac{dH(t)}{dt} = \int d\mathbf{c} \sum_n \ln(f_n) \frac{df_n}{dt} \quad (\text{App.B.21})$$

$$= \int d\mathbf{c} \sum_n \ln(f_n) S_{\text{FP}}(f_n) + \int d\mathbf{c} \sum_n \ln(f_n) K \frac{\partial f_n}{\partial v_i \partial v_i} + \int d\mathbf{c} \sum_n \ln(f_n) \left(\sum_j R_{jn} f_j - R_{nj} f_n \right). \quad (\text{App.B.22})$$

As described in Subch. 3.2, $f_n(\mathbf{c}, t)$ may be written as:

$$f_n(\mathbf{c}, t) = g_n(t) \cdot f(\mathbf{c}, t). \quad (\text{App.B.23})$$

Hence, it follows:

$$\begin{aligned} \frac{dH}{dt} &= \underbrace{\int d\mathbf{c} \sum_n \ln(g_n) S_{\text{FP}}(f) g_n}_i + \underbrace{\int d\mathbf{c} \sum_n \ln(f) S_{\text{FP}}(f) g_n}_{ii} + \underbrace{\int d\mathbf{c} \sum_n g_n \ln(g_n) K \frac{\partial f}{\partial v_i \partial v_i}}_{iii} \\ &+ \underbrace{\int d\mathbf{c} \sum_n g_n \ln(f) K \frac{\partial f}{\partial v_i \partial v_i}}_{iv} + \underbrace{\int d\mathbf{c} f \sum_n \ln(g_n) \left(\sum_j R_{jn} g_j - R_{nj} g_n \right)}_v \\ &+ \underbrace{\int d\mathbf{c} f \sum_n \ln(f) \left(\sum_j R_{jn} g_j - R_{nj} g_n \right)}_{vi}. \end{aligned} \quad (\text{App.B.24})$$

Expression (i), expression (iii) and expression (vi) vanish as described in App. B.1. Expression (ii) is negative since S_{FP} fulfills the H-theorem. Using Eq. (App.B.15) and Eq. (App.B.11), for expression (iv) it is found that:

$$(iv) = -C K = \frac{C}{3m} \sum_{nj} (R_{jn} g_j - R_{nj} g_n) \epsilon_n, \quad (\text{App.B.25})$$

$$C = \int d\mathbf{c} \sum_i \left(\frac{\partial f}{\partial v_i} \right)^2 \frac{1}{f} > 0. \quad (\text{App.B.26})$$

Next, it is defined that:

$$g_n^{\text{eq}} \equiv \frac{1}{Z} \exp \left(-\frac{C}{3m} e_n \right). \quad (\text{App.B.27})$$

Note that in thermal equilibrium $f(\mathbf{c})$ becomes a Maxwell distribution. Hence, Eq. (App.B.26) can be evaluated. It follows that $g_n^{\text{eq}} = \frac{1}{Z} \exp(-\frac{e_n}{kT})$. Thus, g_n^{eq} can be interpreted as a Boltzmann distribution function. Further it is written:

$$(iv) = - \sum_{nj} (R_{jn} g_j - R_{nj} g_n) (\ln(g_n^{\text{eq}}) + \ln(Z)). \quad (\text{App.B.28})$$

It follows:

$$\begin{aligned} (iv) + (v) &= \sum_{nj} (R_{jn} g_j - R_{nj} g_n) \left(\ln \left(\frac{g_n}{g_n^{\text{eq}}} \right) - \ln(Z) \right) \\ &= \sum_{nj} (R_{jn} g_j - R_{nj} g_n) \ln \left(\frac{g_n}{g_n^{\text{eq}}} \right) \\ &= \sum_{nj} R_{jn} \left(g_j \ln \left(\frac{g_n}{g_n^{\text{eq}}} \right) - g_j \ln \left(\frac{g_j}{g_j^{\text{eq}}} \right) \right) \\ &= \sum_{nj} R_{jn} g_j^{\text{eq}} \left(\frac{g_j}{g_j^{\text{eq}}} \ln \left(\frac{g_n}{g_n^{\text{eq}}} \right) - \frac{g_j}{g_j^{\text{eq}}} \ln \left(\frac{g_j}{g_j^{\text{eq}}} \right) \right) \\ &= \sum_{nj} R_{jn} g_j^{\text{eq}} (x_j \ln(x_n) - x_j \ln(x_j)), \end{aligned} \quad (\text{App.B.29})$$

with $x_j \equiv g_j/g_j^{\text{eq}}$. With the definition of $\Psi(x) \equiv x \ln(x) - x$ and $\frac{d\Psi(x)}{dx} = \ln(x)$ it can be formulated:

$$(iv) + (v) = \sum_{nj} R_{jn} g_j^{\text{eq}} \left(x_j \frac{d\Psi(x_n)}{dx} - x_j \frac{d\Psi(x_j)}{dx} \right). \quad (\text{App.B.30})$$

Assuming the principle of detailed balance $R_{jn} g_j^{\text{eq}} = R_{nj} g_n^{\text{eq}}$ and for arbitrary numbers ψ_n follows:

$$\begin{aligned} & \sum_{nj} R_{jn} g_j^{\text{eq}} (\psi_n - \psi_j) \\ &= \sum_{nj} R_{jn} g_j^{\text{eq}} \psi_n - \sum_{nj} R_{jn} g_j^{\text{eq}} \psi_j \\ &= \sum_{nj} R_{jn} g_j^{\text{eq}} \psi_n - \sum_{nj} R_{nj} g_n^{\text{eq}} \psi_n \\ &= \sum_{nj} R_{jn} g_j^{\text{eq}} \psi_n - \sum_{nj} R_{jn} g_j^{\text{eq}} \psi_n \\ &= 0. \end{aligned}$$

As a result, it can be written:

$$\sum_{nj} R_{jn} g_j^{\text{eq}} \psi_n - \sum_{nj} R_{jn} g_j^{\text{eq}} \psi_j = 0. \quad (\text{App.B.31})$$

Let now $\psi_n \equiv \Psi(x_n) - x_n \frac{d\Psi(x_n)}{dx}$. Then the addition of Eq. (App.B.31) and Eq. (App.B.30) results in:

$$(iv) + (v) = \sum_{nj} R_{jn} g_j^{\text{eq}} \left(x_j \frac{d\Psi(x_n)}{dx} - x_j \frac{d\Psi(x_j)}{dx} + \Psi(x_n) - x_n \frac{d\Psi(x_n)}{dx} - \Psi(x_j) + x_j \frac{d\Psi(x_j)}{dx} \right) \quad (\text{App.B.32})$$

$$= \sum_{nj} R_{jn} g_j^{\text{eq}} \left((x_j - x_n) \frac{d\Psi(x_n)}{dx} + \Psi(x_n) - \Psi(x_j) \right) \quad (\text{App.B.33})$$

$\Psi(x)$ is a concave function. Because of geometrical considerations the expression $\left((x_j - x_n) \frac{d\Psi(x_n)}{dx} + \Psi(x_n) - \Psi(x_j) \right)$ is negative for arbitrary concave functions [92]. Therefore, it follows that:

$$\frac{dH}{dt} = (ii) + (iv) + (v) < (iv) + (v) < 0. \quad (\text{App.B.34})$$

In the following, Eq. (App.B.20) is proven. Let f_n be the equilibrium distribution function. Then g_n takes the form of a Boltzmann distribution. Hence, the internal energy e_{int} in Eq. (App.B.17) equalizes to the equilibrium energy $e_{\text{int}}^{\text{eq}}$ leading to $K = 0$. Following expression (iv) in Eq. (App.B.24) vanishes. Using Eq. (App.B.15)

and Eq. (App.B.11), for expression (v) in Eq. (App.B.24) it is found that:

$$(v) = \sum_{nj} \left(\ln \left(\frac{1}{Z} \right) - \frac{e_n}{k_B T} \right) (R_{jn} g_j - R_{nj} g_n) \quad (\text{App.B.35})$$

$$= -\frac{1}{k_B T} \underbrace{\sum_{nj} e_n (R_{jn} g_j - R_{nj} g_n)}_{3mK} \quad (\text{App.B.36})$$

$$= 0 \quad (\text{App.B.37})$$

Term (ii) in Eq. (App.B.24) vanishes since S_{FP} fulfills the H-Theorem, hence it follows that:

$$\frac{dH}{dt} = 0. \quad (\text{App.B.38})$$

Appendix C

HS mixtures

C.1 HS-Boltzmann production terms

Gupta [63] calculated Boltzmann production terms based on the HS collision model assuming a distribution function according to Grad's 13 and 26 moment method[61, 136]. In contrast to Eq. (4.2), Gupta evaluated production terms based on the thermal velocities $\hat{\mathbf{c}}^{(\alpha)}$ as defined in Eq. (2.28). Therefore, in the following, all quantities marked by $\hat{\cdot}$ are calculated on the basis of $\hat{\mathbf{c}}^{(\alpha)}$ instead of $\mathbf{c}^{(\alpha)}$. In particular, lower order production terms are given as:

$$P_{\text{Boltz}}^{(\alpha)} \left(\hat{\mathbf{c}}_i^{(\alpha)} \right) = - \sum_{\beta=1}^{N_s} \nu^{(\alpha\beta)} \mu^{(\beta)} \left[\frac{5}{3} \rho^{(\alpha)} \left(u_i^{(\alpha)} - u_i^{(\beta)} \right) + \frac{1}{6\hat{\theta}^{(\alpha\beta)}} \left(\hat{h}_i^{(\alpha)} - \frac{\rho^{(\alpha)}}{\rho^{(\beta)}} \hat{h}_i^{(\beta)} \right) \right], \quad (\text{App.C.1})$$

$$P_{\text{Boltz}}^{(\alpha)} \left(\hat{\mathbf{c}}^{(\alpha)} \hat{\mathbf{c}}^{(\alpha)} \right) = - \sum_{\beta=1}^{N_s} \nu^{(\alpha\beta)} \mu^{(\beta)} \left[10\rho^{(\alpha)} \hat{\theta}^{(\alpha\beta)} \Delta\hat{\theta} - \frac{10}{3} \left(\mu^{(\alpha)} - \mu^{(\beta)} \right) \rho^{(\alpha)} u_i^{(\alpha)} u_i^{(\beta)} \right], \quad (\text{App.C.2})$$

$$P_{\text{Boltz}}^{(\alpha)} \left(\hat{c}_{<i}^{(\alpha)} \hat{c}_{>j}^{(\alpha)} \right) = \sum_{\beta=1}^{N_s} \nu_{\alpha\beta} \mu^{(\beta)} \left[4\mu^{(\alpha\beta)} \left\{ \hat{\sigma}_{ij}^{(\alpha)} + \frac{1}{3} \left(\hat{\sigma}_{ij}^{(\alpha)} - \frac{\rho^{(\alpha)}}{\rho^{(\beta)}} \hat{\sigma}_{ij}^{(\beta)} \right) \right\} + \frac{10}{3} \left(\mu^{(\alpha)} - \mu^{(\beta)} \right) \hat{\sigma}_{ij}^{(\alpha)} \right], \quad (\text{App.C.3})$$

$$P_{\text{Boltz}}^{(\alpha)} \left(\hat{c}_i^{(\alpha)} \hat{\mathbf{c}}^{(\alpha)} \hat{\mathbf{c}}^{(\alpha)} \right) = - \sum_{\beta=1}^{N_s} \nu^{(\alpha\beta)} \mu^{(\beta)} \left[\frac{16}{3} \mu^{(\beta)} \hat{h}_i^{(\alpha)} + 10 \left(\mu^{(\alpha)} - \mu^{(\beta)} \right) \hat{h}_i^{(\alpha)} + \frac{2}{6} \mu^{(\beta)} \left(5 + 27\mu^{(\beta)} \right) \left(\hat{h}_i^{(\alpha)} - \frac{\rho^{(\alpha)}}{\rho^{(\beta)}} \hat{h}_i^{(\beta)} \right) + \frac{10}{3} \mu^{(\beta)} \left(5 + \mu^{(\beta)} \right) \rho^{(\alpha)} \hat{\theta}^{(\alpha\beta)} \left(u_i^{(\alpha)} - u_i^{(\beta)} \right) \right]. \quad (\text{App.C.4})$$

The quantities $\mu^{(\alpha)}$, $\hat{\theta}^{(\alpha)}$, $\hat{\theta}^{(\alpha\beta)}$, $\Delta\hat{\theta}^{(\alpha\beta)}$ and $\nu^{(\alpha\beta)}$ are defined as:

$$\mu^{(\alpha)} \equiv \frac{m^{(\alpha)}}{m^{(\alpha)} + m^{(\beta)}}, \quad (\text{App.C.5})$$

$$\hat{\theta}^{(\alpha)} \equiv \frac{k_B \hat{T}^{(\alpha)}}{m^{(\alpha)}}, \quad (\text{App.C.6})$$

$$\hat{\theta}^{(\alpha\beta)} \equiv \frac{\hat{\theta}^{(\alpha)} + \hat{\theta}^{(\beta)}}{2}, \quad (\text{App.C.7})$$

$$\Delta\hat{\theta}^{(\alpha\beta)} \equiv \frac{\mu^{(\alpha)}\hat{\theta}^{(\alpha)} - \mu^{(\beta)}\hat{\theta}^{(\beta)}}{\hat{\theta}^{(\alpha\beta)}}, \quad (\text{App.C.8})$$

$$\hat{\mathbf{h}}^{(\alpha)} \equiv \hat{\mathbf{q}}^{(\alpha)} - \frac{5}{2}\rho^{(\alpha)}\hat{\theta}^{(\alpha)}\mathbf{u}_d^{(\alpha)}, \quad (\text{App.C.9})$$

$$\nu^{(\alpha\beta)} \equiv \frac{16}{5}\sqrt{\pi}n^{(\beta)}d_{\text{ref}}^{(\alpha\beta)^2}\sqrt{\hat{\theta}^{(\alpha\beta)}}, \quad (\text{App.C.10})$$

where $d_{\text{ref}}^{(\alpha\beta)}$ denotes the reference diameter between species α and β . Note, that $d_{\text{ref}}^{(\alpha\beta)}$ is a model parameter within the HS collision potential.

The production terms Eq. (App.C.1) - Eq. (App.C.4) contain only terms with linear dependency in the quantities $\hat{\theta}^{(\alpha)}$, $\hat{\mathbf{u}}^{(\alpha)}$, $\hat{\mathbf{h}}^{(\alpha)}$, $\hat{\sigma}_{ij}^{(\alpha)}$ with the exception of Eq. (App.C.2), which additionally contains a quadratic term $u_i^{(\alpha)}u_i^{(\beta)}$. Since for low Knudsen number flows only linear terms are relevant, higher order terms are not required for capturing a correct Navier-Stokes limit. However, the additional term in production term Eq. (App.C.2) is necessary for deriving a FP model with a positive diffusion coefficient, as described in Subch. 4.1.1. Using the identities:

$$\hat{\mathbf{c}}^{(\alpha)} = \mathbf{c}^{(\alpha)} + \mathbf{u}_d^{(\alpha)}, \quad (\text{App.C.11})$$

$$P\left(\mathbf{c}_i^{(\alpha)}\right) = P\left(\hat{\mathbf{c}}_i^{(\alpha)}\right) = 0, \quad (\text{App.C.12})$$

the production terms can be transformed into a \mathbf{c} basis:

$$P^{(\alpha)}\left(\mathbf{c}_i^{(\alpha)}\right) = P^{(\alpha)}\left(\hat{\mathbf{c}}_i^{(\alpha)}\right), \quad (\text{App.C.13})$$

$$P^{(\alpha)}\left(\mathbf{c}^{(\alpha)}\mathbf{c}^{(\alpha)}\right) = P^{(\alpha)}\left(\hat{\mathbf{c}}^{(\alpha)}\hat{\mathbf{c}}^{(\alpha)}\right) - 2u_{d_i}^{(\alpha)}P^{(\alpha)}\left(\hat{\mathbf{c}}_i^{(\alpha)}\right), \quad (\text{App.C.14})$$

$$P^{(\alpha)}\left(\mathbf{c}_{<i}^{(\alpha)}\mathbf{c}_{>}^{(\alpha)}\right) = P^{(\alpha)}\left(\hat{\mathbf{c}}_{<i}^{(\alpha)}\hat{\mathbf{c}}_{>}^{(\alpha)}\right) - u_{d_{<j}}^{(\alpha)}P^{(\alpha)}\left(\hat{\mathbf{c}}_{i>}^{(\alpha)}\right) - u_{d_{<i}}^{(\alpha)}P^{(\alpha)}\left(\hat{\mathbf{c}}_{j>}^{(\alpha)}\right), \quad (\text{App.C.15})$$

$$P^{(\alpha)}\left(\mathbf{c}_i^{(\alpha)}\mathbf{c}^{(\alpha)}\mathbf{c}^{(\alpha)}\right) = P^{(\alpha)}\left(\hat{\mathbf{c}}_i^{(\alpha)}\hat{\mathbf{c}}^{(\alpha)}\hat{\mathbf{c}}^{(\alpha)}\right) - 2u_{d_j}^{(\alpha)}P^{(\alpha)}\left(\hat{\mathbf{c}}_i^{(\alpha)}\hat{\mathbf{c}}_j^{(\alpha)}\right) + u_{d_j}^{(\alpha)}u_{d_j}^{(\alpha)}P^{(\alpha)}\left(\hat{\mathbf{c}}_i^{(\alpha)}\right) - u_{d_i}^{(\alpha)}P^{(\alpha)}\left(\hat{\mathbf{c}}_i^{(\alpha)}\hat{\mathbf{c}}^{(\alpha)}\hat{\mathbf{c}}^{(\alpha)}\right) + 2u_{d_i}^{(\alpha)}u_{d_j}^{(\alpha)}P^{(\alpha)}\left(\hat{\mathbf{c}}_j^{(\alpha)}\right). \quad (\text{App.C.16})$$

When neglecting the second term in Eq. (App.C.1), Eq. (App.C.14) can be written as:

$$P^{(\alpha)}\left(\mathbf{c}^{(\alpha)}\mathbf{c}^{(\alpha)}\right) = -10\sum_{\beta=1}^{N_s}\nu^{(\alpha\beta)}\mu^{(\beta)}\rho^{(\alpha)}\left[\frac{k_B}{m^{(\alpha)}+m^{(\beta)}}\left(T^{(\alpha)}-T^{(\beta)}\right) - \frac{\mu^{(\beta)}}{3}\left(\mathbf{u}^{(\alpha)}-\mathbf{u}^{(\beta)}\right)^2\right]. \quad (\text{App.C.17})$$

Eq. (App.C.17) is employed in Subch. 4.1.1 for constructing the linear FP operator. Since Eq. (App.C.17) is only approximately valid, namely exactly when the second term in Eq. (App.C.1) can be neglected, the linear FP operator does not lead exactly to the correct production term. The quadratic FP operator, however, described in Subch. 4.1.2, reproduces the full production term (App.C.14), since here the agreement of the production terms is ensured by solving a linear system of equations.

C.2 Fokker-Planck production terms

For the FP-operator, production terms can be calculated independently of a distribution function. For the following derivations it is only assumed that $D^{(\alpha)}$ does not depend on microscopic particle velocities $\mathbf{v}^{(\alpha)}$ and that the distribution function tends to zero for large velocities *sufficiently fast*:

$$\lim_{v_i^{(\alpha)} \rightarrow \infty} f^{(\alpha)} = 0, \quad (\text{App.C.18})$$

$$\lim_{v_i^{(\alpha)} \rightarrow \infty} \frac{\partial f^{(\alpha)}}{v_i^{(\alpha)}} = 0. \quad (\text{App.C.19})$$

The meaning of *sufficiently fast* depends on the production term and will be discussed later in this subchapter. The following expression can be derived:

$$P_{\text{FP}}^{(\alpha)}(X) = -m^{(\alpha)} \underbrace{\int \frac{\partial}{\partial v_j^{(\alpha)}} \left(f^{(\alpha)} A_j^{(\alpha)} \right) X \, d^3 c^{(\alpha)}}_I + m^{(\alpha)} D^{(\alpha)} \underbrace{\int \frac{\partial^2 f^{(\alpha)}}{\partial v_j^{(\alpha)} \partial v_j^{(\alpha)}} X \, d^3 c^{(\alpha)}}_{II}. \quad (\text{App.C.20})$$

Term I can be written as:

$$I = \frac{\partial}{\partial v_j^{(\alpha)}} \left(f^{(\alpha)} A_j^{(\alpha)} X \right) - \frac{\partial X}{\partial v_j^{(\alpha)}} A_j^{(\alpha)} f^{(\alpha)}, \quad (\text{App.C.21})$$

and similar term II can be written as:

$$II = \frac{\partial}{\partial v_j^{(\alpha)}} \left(\frac{\partial f^{(\alpha)}}{\partial v_j^{(\alpha)}} X \right) - \frac{\partial X}{\partial v_j^{(\alpha)}} \frac{\partial f^{(\alpha)}}{\partial v_j^{(\alpha)}}, \quad (\text{App.C.22})$$

$$= \frac{\partial}{\partial v_j^{(\alpha)}} \left(\frac{\partial f^{(\alpha)}}{\partial v_j^{(\alpha)}} X \right) - \frac{\partial}{\partial v_j^{(\alpha)}} \left(f^{(\alpha)} \frac{\partial X}{\partial v_j^{(\alpha)}} \right) + f^{(\alpha)} \frac{\partial^2 X}{\partial v_j^{(\alpha)} \partial v_j^{(\alpha)}}. \quad (\text{App.C.23})$$

Hence, one obtains:

$$\begin{aligned} P_{\text{FP}}^{(\alpha)}(X) &= -m^{(\alpha)} f^{(\alpha)} A_j^{(\alpha)} X \Big|_{-\infty}^{\infty} + m^{(\alpha)} \int \frac{\partial X}{\partial v_j^{(\alpha)}} A_j^{(\alpha)} f^{(\alpha)} \, d^3 c^{(\alpha)} \\ &+ m^{(\alpha)} D^{(\alpha)} \frac{\partial f^{(\alpha)}}{\partial v_j^{(\alpha)}} X \Big|_{-\infty}^{\infty} - m^{(\alpha)} D^{(\alpha)} f^{(\alpha)} \frac{\partial X}{\partial v_j^{(\alpha)}} \Big|_{-\infty}^{\infty} + m^{(\alpha)} D^{(\alpha)} \int f^{(\alpha)} \frac{\partial^2 X}{\partial v_j^{(\alpha)} \partial v_j^{(\alpha)}} \, d^3 c^{(\alpha)}. \end{aligned} \quad (\text{App.C.24})$$

Assuming that the distribution function and its derivative vanish sufficiently fast for large velocities, the first, third and fourth term in Eq. (App.C.24) can be neglected. *Sufficiently fast* means, that the distribution function vanishes faster for large velocities than the terms $A_j^{(\alpha)} X$, X and $\partial X / \partial v_j^{(\alpha)}$ might increase. This assumption is in general difficult to prove. However, in this work $A_j^{(\alpha)} X$, X and $\partial X / \partial v_j^{(\alpha)}$ feature a simple polynomial form. In addition, only production terms for low Knudsen number flows are relevant. Hence, the distribution function:

$$f^{(\alpha)} \sim \exp \left(-c_i^{(\alpha)} c_i^{(\alpha)} \right), \quad (\text{App.C.25})$$

can be expand around a Maxwell distribution [63] and features an exponential dependency on microscopic velocities. As a result, the first, third and fourth term in Eq. (App.C.24) vanish. For the production terms follow:

$$P_{\text{FP}}^{(\alpha)}(X) = m^{(\alpha)} \left\langle \frac{\partial X}{\partial v_j^{(\alpha)}} A_j^{(\alpha)} \middle| f^{(\alpha)} \right\rangle + m^{(\alpha)} D^{(\alpha)} \left\langle \frac{\partial X}{\partial v_j^{(\alpha)} \partial v_j^{(\alpha)}} \middle| f^{(\alpha)} \right\rangle. \quad (\text{App.C.26})$$

In particular, it can be found that:

$$P_{\text{FP}}^{(\alpha)}(c_i^{(\alpha)}) = m^{(\alpha)} \langle A_i^{(\alpha)} | f^{(\alpha)} \rangle, \quad (\text{App.C.27})$$

$$P_{\text{FP}}^{(\alpha)}(\mathbf{c}^{(\alpha)} \mathbf{c}^{(\alpha)}) = 2m^{(\alpha)} \langle A_i^{(\alpha)} c_i^{(\alpha)} | f^{(\alpha)} \rangle + 6\rho^{(\alpha)} D^{(\alpha)} \quad (\text{App.C.28})$$

$$P_{\text{FP}}^{(\alpha)}(c_i^{(\alpha)} c_j^{(\alpha)}) = m^{(\alpha)} \langle A_i^{(\alpha)} c_j^{(\alpha)} | f^{(\alpha)} \rangle + m^{(\alpha)} \langle A_j^{(\alpha)} c_i^{(\alpha)} | f^{(\alpha)} \rangle + 2\delta_{ij}\rho^{(\alpha)} D^{(\alpha)}, \quad (\text{App.C.29})$$

$$P_{\text{FP}}^{(\alpha)}(c_i^{(\alpha)} \mathbf{c}^{(\alpha)} \mathbf{c}^{(\alpha)}) = m^{(\alpha)} \langle A_i^{(\alpha)} c_j^{(\alpha)} c_j^{(\alpha)} | f^{(\alpha)} \rangle + 2m^{(\alpha)} \langle A_j^{(\alpha)} c_j^{(\alpha)} c_i^{(\alpha)} | f^{(\alpha)} \rangle. \quad (\text{App.C.30})$$

C.3 Linear system of equations

The nine model parameters $\gamma_i^{(\alpha)}$ and $\psi_{ij}^{(\alpha)}$ occurring in the drift coefficient (Eq. (4.10)) of the higher-order model are calculated as solution of a linear system of equations. Combining Eq. (4.12) with Eq. (App.C.30) results in three linear equations:

$$\begin{aligned} & K_i^{(\alpha)} \langle c_j^{(\alpha)} c_j^{(\alpha)} | f^{(\alpha)} \rangle + 2K_j^{(\alpha)} \langle c_i^{(\alpha)} c_j^{(\alpha)} | f^{(\alpha)} \rangle - 3s^{(\alpha)} \langle c_i^{(\alpha)} c_j^{(\alpha)} c_j^{(\alpha)} | f^{(\alpha)} \rangle \\ & + \psi_{il}^{(\alpha)} \langle c_l^{(\alpha)} c_j^{(\alpha)} c_j^{(\alpha)} | f^{(\alpha)} \rangle + 2\psi_{jl}^{(\alpha)} \langle c_j^{(\alpha)} c_l^{(\alpha)} c_i^{(\alpha)} | f^{(\alpha)} \rangle \\ & + \gamma_i^{(\alpha)} \left[\langle c_l^{(\alpha)} c_l^{(\alpha)} c_j^{(\alpha)} c_j^{(\alpha)} | f^{(\alpha)} \rangle - \frac{1}{n^{(\alpha)}} \langle c_l^{(\alpha)} c_l^{(\alpha)} | f^{(\alpha)} \rangle \langle c_j^{(\alpha)} c_j^{(\alpha)} | f^{(\alpha)} \rangle \right] \\ & + 2\gamma_j^{(\alpha)} \left[\langle c_l^{(\alpha)} c_l^{(\alpha)} c_j^{(\alpha)} c_i^{(\alpha)} | f^{(\alpha)} \rangle - \frac{1}{n^{(\alpha)}} \langle c_l^{(\alpha)} c_l^{(\alpha)} | f^{(\alpha)} \rangle \langle c_j^{(\alpha)} c_i^{(\alpha)} | f^{(\alpha)} \rangle \right] \\ & = \frac{1}{m^{(\alpha)}} P_{\text{Boltz}}^{(\alpha)}(c_i^{(\alpha)} \mathbf{c}^{(\alpha)} \mathbf{c}^{(\alpha)}). \end{aligned} \quad (\text{App.C.31})$$

Combing Eq. (4.11) with Eq. (App.C.29) yields six linear equations:

$$\begin{aligned} & -2s^{(\alpha)} \langle c_i^{(\alpha)} c_j^{(\alpha)} | f^{(\alpha)} \rangle + \psi_{il}^{(\alpha)} \langle c_j^{(\alpha)} c_l^{(\alpha)} | f^{(\alpha)} \rangle + \psi_{jl}^{(\alpha)} \langle c_i^{(\alpha)} c_l^{(\alpha)} | f^{(\alpha)} \rangle \\ & + \gamma_i^{(\alpha)} \langle c_j^{(\alpha)} c_l^{(\alpha)} c_l^{(\alpha)} | f^{(\alpha)} \rangle + \gamma_j^{(\alpha)} \langle c_i^{(\alpha)} c_l^{(\alpha)} c_l^{(\alpha)} | f^{(\alpha)} \rangle + 2\delta_{ij} D^{(\alpha)} \\ & = \frac{1}{m^{(\alpha)}} \left(P_{\text{Boltz}}^{(\alpha)}(c_{<i}^{(\alpha)} c_{j>}^{(\alpha)}) + \frac{1}{3} \delta_{ij} P_{\text{Boltz}}^{(\alpha)}(\mathbf{c}^{(\alpha)} \mathbf{c}^{(\alpha)}) \right). \end{aligned} \quad (\text{App.C.32})$$

In a kinetic FP simulation, the nine linear equations Eq. (App.C.31) and Eq. (App.C.32) are solved at each time step and each grid cell, to calculate the model parameters $\psi_{ij}^{(\alpha)}$ and $\gamma_i^{(\alpha)}$.

C.4 Time evolution of moments

In order to integrate the stochastic equation of motion (Eq. (4.13)), the species velocities and temperatures at the end of the integration process must be known. When assuming a homogeneous systems, the rate of change of velocity moments is given by the production terms [65]. Hence, the system:

$$\frac{d}{dt} \begin{pmatrix} u_0^{(\alpha)} \\ u_1^{(\alpha)} \\ u_2^{(\alpha)} \\ T^{(\alpha)} \\ q_0^{(\alpha)} \\ q_1^{(\alpha)} \\ q_1^{(\alpha)} \end{pmatrix} = \begin{pmatrix} \frac{1}{\rho^{(\alpha)}} P_{\text{Boltz}}^{(\alpha)} \left(c_0^{(\alpha)} \right) \\ \frac{1}{\rho^{(\alpha)}} P_{\text{Boltz}}^{(\alpha)} \left(c_1^{(\alpha)} \right) \\ \frac{1}{\rho^{(\alpha)}} P_{\text{Boltz}}^{(\alpha)} \left(c_2^{(\alpha)} \right) \\ \frac{1}{3n^{(\alpha)} k_B} P_{\text{Boltz}}^{(\alpha)} \left(\mathbf{c}^{(\alpha)} \mathbf{c}^{(\alpha)} \right) \\ \frac{1}{2} P_{\text{Boltz}}^{(\alpha)} \left(c_0^{(\alpha)} \mathbf{c}^{(\alpha)} \mathbf{c}^{(\alpha)} \right) \\ \frac{1}{2} P_{\text{Boltz}}^{(\alpha)} \left(c_1^{(\alpha)} \mathbf{c}^{(\alpha)} \mathbf{c}^{(\alpha)} \right) \\ \frac{1}{2} P_{\text{Boltz}}^{(\alpha)} \left(c_2^{(\alpha)} \mathbf{c}^{(\alpha)} \mathbf{c}^{(\alpha)} \right) \end{pmatrix}, \quad (\text{App.C.33})$$

of ordinary differential equations can be deduced for each species. Note, that the right side of Eq. (App.C.33) depends on all species in the mixture. Hence, Eq. (App.C.33) defines a system of $7 \times N_{\text{species}}$ differential equations, where N_{species} denotes the number of species. The evolution equations for the heat fluxes are included in the system Eq. (App.C.33), since the production terms Eq. (App.C.1) also depend on heat fluxes. When the vector $(\mathbf{u}^{(\alpha),n}, T^{(\alpha),n}, \mathbf{q}^{(\alpha),n})$ is employed as initial condition, solving of Eq. (App.C.33) yields the species flow velocities and temperatures $(\mathbf{u}^{(\alpha),n+1}, T^{(\alpha),n+1}, \mathbf{q}^{(\alpha),n+1})$ at the end of the Fokker-Planck time step.

Within this thesis, the system Eq. (App.C.33) is solved by a fourth order Runge-Kutta method with adaptive time step size control [129].

Appendix D

VHS mixtures

D.1 VHS Boltzmann production terms

References [64, 109] calculated linear production terms for binary gas mixtures assuming a general interaction potential. These results can be extended to mixtures with an arbitrary number of species. When reordering the binary terms and summing them up with respect to the particle species, one obtains:

$$P_{\text{GEN}}^{(\alpha)} \left(\hat{c}_i^{(\alpha)} \right) = - \sum_{\beta=1}^{N_s} \nu_{|\text{gen}}^{(\alpha\beta)} \mu^{(\beta)} \left[\frac{10}{3} \rho^{(\alpha)} \left(u_i^{(\alpha)} - u_i^{(\beta)} \right) \frac{\Sigma_{\alpha,\beta}^{1,1}}{\Sigma_{\alpha,\beta}^{2,2}} - \frac{2}{\hat{\theta}^{(\alpha\beta)}} \left(\frac{5}{6} \frac{\Sigma_{\alpha,\beta}^{1,1}}{\Sigma_{\alpha,\beta}^{2,2}} - \frac{1}{3} \frac{\Sigma_{\alpha,\beta}^{1,2}}{\Sigma_{\alpha,\beta}^{2,2}} \right) \right] \left(\hat{h}_i^{(\alpha)} - \hat{h}_i^{(\beta)} \right), \quad (\text{App.D.1})$$

$$P_{\text{GEN}}^{(\alpha)} \left(\hat{c}^{(\alpha)} \hat{c}^{(\alpha)} \right) = - \sum_{\beta=1}^{N_s} 20 \nu_{|\text{gen}}^{(\alpha\beta)} \mu^{(\beta)} \rho^{(\alpha)} \left(\mu^{(\alpha)} \hat{\theta}^{(\alpha)} - \mu^{(\beta)} \hat{\theta}^{(\beta)} \right) \frac{\Sigma_{\alpha,\beta}^{1,1}}{\Sigma_{\alpha,\beta}^{2,2}}, \quad (\text{App.D.2})$$

$$P_{\text{GEN}}^{(\alpha)} \left(\hat{c}_i^{(\alpha)} \hat{c}_j^{(\alpha)} \right) = - \sum_{\beta=1, \beta \neq \alpha}^{N_s} \nu_{|\text{gen}}^{(\alpha\beta)} \mu^{(\beta)} \left[2 \hat{\sigma}_{ij}^{\alpha} + \frac{2}{3} \mu^{(\beta)} \frac{10 \Sigma_{\alpha,\beta}^{1,1} - 3 \Sigma_{\alpha,\beta}^{2,2}}{\Sigma_{\alpha,\beta}^{2,2}} \left(\hat{\sigma}_{ij}^{\alpha} - \hat{\sigma}_{ij}^{\beta} \right) + \frac{2}{3} \frac{10 \Sigma_{\alpha,\beta}^{1,1} - 3 \Sigma_{\alpha,\beta}^{2,2}}{\Sigma_{\alpha,\beta}^{2,2}} \left(\mu^{(\alpha)} - \mu^{(\beta)} \right) \hat{\sigma}_{ij}^{\alpha} \right] - \nu_{|\text{gen}}^{\alpha\alpha} \hat{\sigma}_{ij}^{\alpha}, \quad (\text{App.D.3})$$

$$P_{\text{GEN}}^{(\alpha)} \left(\hat{c}_i^{(\alpha)} \hat{c}^{(\alpha)} \hat{c}^{(\alpha)} \right) = - \sum_{\beta=1, \beta \neq \alpha}^{N_s} \nu_{|\text{gen}}^{(\alpha\beta)} \mu^{(\beta)} \left[\frac{8}{3} \hat{h}_i^{(\alpha)} + \frac{20}{3} \hat{\theta}^{(\alpha\beta)} \mu^{(\beta)} \frac{5 \mu^{(\alpha)} \Sigma_{\alpha,\beta}^{1,1} + 2 \mu^{(\beta)} \Sigma_{\alpha,\beta}^{1,2}}{\Sigma_{\alpha,\beta}^{2,2}} \left(u_i^{\alpha} - u_i^{\beta} \right) + \frac{4}{3} \left(\mu^{(\alpha)} - \mu^{(\beta)} \right) \frac{15 \Sigma_{\alpha,\beta}^{1,1} - 2 \Sigma_{\alpha,\beta}^{2,2}}{\Sigma_{\alpha,\beta}^{2,2}} \hat{h}_i^{(\alpha)} + \frac{2}{3} \mu^{(\beta)} \frac{1}{\Sigma_{\alpha,\beta}^{2,2}} \left(5 \mu^{(\alpha)} \left(5 \Sigma_{\alpha,\beta}^{1,1} - 2 \Sigma_{\alpha,\beta}^{1,2} \right) \right) + 2 \mu^{(\beta)} \left(-15 \Sigma_{\alpha,\beta}^{1,1} + 5 \Sigma_{\alpha,\beta}^{1,2} - 2 \Sigma_{\alpha,\beta}^{1,3} + 4 \Sigma_{\alpha,\beta}^{2,2} \right) \left(h_i^{(\alpha)} - h_i^{(\beta)} \right) \right] - \frac{4}{3} \nu_{|\text{gen}}^{\alpha\alpha} \hat{h}_i^{(\alpha)}. \quad (\text{App.D.4})$$

The collisions frequencies $\nu_{|\text{gen}}^{(\alpha\beta)}$ are defined by [63]:

$$\nu_{|\text{gen}}^{(\alpha\beta)} \equiv \frac{16}{5} \sqrt{\pi} n^{(\beta)} \sqrt{\hat{\theta}^{(\alpha\beta)}} \Sigma_{\alpha,\beta}^{2,2}, \quad (\text{App.D.5})$$

and the collision integrals are given by [97]:

$$\Sigma_{\alpha,\beta}^{l,r} \equiv \int_0^\infty \exp(-\gamma^2) \gamma^{2r+3} Q_{\alpha\beta}^{(l)}(\gamma) d\gamma, \quad (\text{App.D.6})$$

with the effective cross sections:

$$Q_{\alpha\beta}^{(l)}(c) \equiv \int_0^\infty (1 - \cos^l \chi) b_{\alpha\beta}(c, \chi) db. \quad (\text{App.D.7})$$

The quantity $b_{\alpha\beta}$ denotes the impact parameter of a colliding α and β particle, χ is the deflection angle, $\gamma = c / (2\sqrt{\hat{\theta}^{(\alpha\beta)}})$ a non-dimensional velocity and c the magnitude of the relative collision velocity. In the following deviation, production terms Eq. (App.D.1) - Eq. (App.D.4) are evaluated for the VHS interaction potential.

For the VHS model, the following relationship between impact parameter and deflection angle can be found [10]:

$$\begin{aligned} b_{\alpha\beta}(c, \chi) &= d_{\text{ref}}^{(\alpha\beta)} \left(\frac{c_{\text{ref}}^{(\alpha\beta)}}{c} \right)^{\nu^{(\alpha\beta)}} \cos\left(\frac{\chi}{2}\right) \\ \Leftrightarrow b_{\alpha\beta}(c, \chi) db &= -\frac{1}{4} d_{\text{ref}}^{(\alpha\beta)2} \left(\frac{c_{\text{ref}}^{(\alpha\beta)}}{c} \right)^{2\nu^{(\alpha\beta)}} \sin(\chi) d\chi, \end{aligned} \quad (\text{App.D.8})$$

with a reference diameter $d_{\text{ref}}^{(\alpha\beta)}$. In practical applications, it is common practice to express the velocity exponent $\nu^{(\alpha\beta)}$ and the reference velocity $c_{\text{ref}}^{(\alpha\beta)}$ by a viscosity exponent $\omega^{(\alpha\beta)}$ and a reference temperature $T_{\text{ref}}^{(\alpha\beta)}$:

$$\nu^{(\alpha\beta)} = \omega^{(\alpha\beta)} - \frac{1}{2}, \quad (\text{App.D.9})$$

$$c_{\text{ref}}^{(\alpha\beta)2\nu^{(\alpha\beta)}} = \frac{1}{\Gamma(2 - \nu^{(\alpha\beta)})} \left(\frac{2k_B T_{\text{ref}}^{(\alpha\beta)}}{m_r^{(\alpha\beta)}} \right)^{\nu^{(\alpha\beta)}}, \quad (\text{App.D.10})$$

where $m_r^{(\alpha\beta)}$ denotes the reduced mass of an α and a β particle. Note, that $d_{\text{ref}}^{(\alpha\beta)}$, $\omega^{(\alpha\beta)}$ and $T_{\text{ref}}^{(\alpha\beta)}$ are model parameters within the VHS collision potential.

Applying Eq. (App.D.8), Eq. (App.D.7) can be evaluated as follows:

$$Q_{\alpha\beta}^{(l)}(c) = \frac{d_{\text{ref}}^{(\alpha\beta)2}}{4} \left(\frac{c_{\text{ref}}^{(\alpha\beta)}}{c} \right)^{2\nu^{(\alpha\beta)}} \left(2 - \frac{1}{l+1} (1 + (-1)^l) \right). \quad (\text{App.D.11})$$

For the collision integral Eq. (App.D.6) follows:

$$\begin{aligned} \Sigma_{\alpha,\beta}^{l,r} &= \frac{d_{\text{ref}}^{(\alpha\beta)2}}{8} c_{\text{ref}}^{(\alpha\beta)2\nu^{(\alpha\beta)}} \left(2 - \frac{1}{l+1} (1 + (-1)^l) \right) \\ &\quad \left(2\hat{\theta}^{(\alpha)} + 2\hat{\theta}^{(\beta)} \right)^{-\nu^{(\alpha\beta)}} \Gamma(r + 2 - \nu^{(\alpha\beta)}). \end{aligned} \quad (\text{App.D.12})$$

Hence, the production terms Eq. (App.D.1) - Eq. (App.D.4) can be calculated for the VHS collision model:

$$P_{\text{VHS}}^{(\alpha)} \left(\hat{c}_i^{(\alpha)} \right) = - \sum_{\beta=1}^{N_s} \nu_{|\text{VHS}}^{(\alpha\beta)} \mu^{(\beta)} \left[\frac{5}{3} \rho^{(\alpha)} \mathbf{VHS}[1] \left(u_i^{(\alpha)} - u_i^{(\beta)} \right) + \frac{1}{6\hat{\theta}^{(\alpha\beta)}} \mathbf{VHS}[2] \left(\hat{h}_i^{(\alpha)} - \frac{\rho^{(\alpha)}}{\rho^{(\beta)}} \hat{h}_i^{(\beta)} \right) \right], \quad (\text{App.D.13})$$

$$P_{\text{VHS}}^{(\alpha)} \left(\hat{\mathbf{c}}^{(\alpha)} \hat{\mathbf{c}}^{(\alpha)} \right) = - \sum_{\beta=1}^{N_s} \nu_{|\text{VHS}}^{(\alpha\beta)} \mu^{(\beta)} \mathbf{VHS}[1] 10 \rho^{(\alpha)} \hat{\theta}^{(\alpha\beta)} \Delta \hat{\theta}^{(\alpha\beta)}, \quad (\text{App.D.14})$$

$$P_{\text{VHS}}^{(\alpha)} \left(\hat{c}_i^{(\alpha)} \hat{c}_j^{(\alpha)} \right) = - \sum_{\beta=1}^{N_s} \nu_{|\text{VHS}}^{(\alpha\beta)} \mu^{(\beta)} \left[4 \mu^{(\beta)} \left\{ \hat{\sigma}_{ij}^{(\alpha)} + \frac{1}{3} \mathbf{VHS}[3] \left(\hat{\sigma}_{ij}^{(\alpha)} - \frac{\rho^{(\alpha)}}{\rho^{(\beta)}} \hat{\sigma}_{ij}^{(\beta)} \right) \right\} + \frac{10}{3} \mathbf{VHS}[1] \left(\mu^{(\alpha)} - \mu^{(\beta)} \right) \hat{\sigma}_{ij}^{(\alpha)} \right], \quad (\text{App.D.15})$$

$$P_{\text{VHS}}^{(\alpha)} \left(\hat{c}_i^{(\alpha)} \hat{\mathbf{c}}^{(\alpha)} \hat{\mathbf{c}}^{(\alpha)} \right) = - \sum_{\beta=1}^{N_s} \nu_{|\text{VHS}}^{(\alpha\beta)} \mu^{(\beta)} \left[\frac{16}{3} \mu^{(\beta)} \hat{h}_i^{(\alpha)} + 10 \mathbf{VHS}[1] \left(\mu^{(\alpha)} - \mu^{(\beta)} \right) \hat{h}_i^{(\alpha)} + \frac{2}{6} \mu^{(\beta)} \mathbf{VHS}[4] \left(5 + 27 \mu^{(\beta)} \right) \left(\hat{h}_i^{(\alpha)} - \frac{\rho^{(\alpha)}}{\rho^{(\beta)}} \hat{h}_i^{(\beta)} \right) + \frac{10}{3} \mu^{(\beta)} \mathbf{VHS}[5] \left(5 + \mu^{(\beta)} \right) \rho^{(\alpha)} \hat{\theta}^{(\alpha\beta)} \left(u_i^{(\alpha)} - u_i^{(\beta)} \right) \right], \quad (\text{App.D.16})$$

with the VHS-collision frequencies:

$$\nu_{|\text{VHS}}^{(\alpha\beta)} = \frac{16}{5} \mathbf{VHS}[6] \sqrt{\pi} n^{(\beta)} d_{\text{ref}}^{(\alpha\beta)^2} \sqrt{\hat{\theta}^{(\alpha\beta)}}. \quad (\text{App.D.17})$$

The VHS-scaling parameters are given by:

$$\mathbf{VHS}[1] = 3 \frac{\Gamma(3.5 - \omega^{(\alpha\beta)})}{\Gamma(4.5 - \omega^{(\alpha\beta)})}, \quad (\text{App.D.18})$$

$$\mathbf{VHS}[2] = 6 - 15 \frac{\Gamma(3.5 - \omega^{(\alpha\beta)})}{\Gamma(4.5 - \omega^{(\alpha\beta)})}, \quad (\text{App.D.19})$$

$$\mathbf{VHS}[3] = \frac{15}{2} \frac{\Gamma(3.5 - \omega^{(\alpha\beta)})}{\Gamma(4.5 - \omega^{(\alpha\beta)})} - \frac{3}{2}, \quad (\text{App.D.20})$$

$$\begin{aligned} \text{VHS[4]} = & -\frac{1}{5 + 27\mu^{(\beta)}} \left[10\mu^{(\alpha)} \left(\frac{15}{2} \frac{\Gamma(3.5 - \omega^{(\alpha\beta)})}{\Gamma(4.5 - \omega^{(\alpha\beta)})} - 3 \right) \right. \\ & \left. + 4\mu^{(\beta)} \left(\frac{23}{2} - \frac{45}{2} \frac{\Gamma(3.5 - \omega^{(\alpha\beta)})}{\Gamma(4.5 - \omega^{(\alpha\beta)})} - 3 \frac{\Gamma(5.5 - \omega^{(\alpha\beta)})}{\Gamma(4.5 - \omega^{(\alpha\beta)})} \right) \right], \quad (\text{App.D.21}) \end{aligned}$$

$$\text{VHS[5]} = \frac{1}{5 + \mu^{(\beta)}} \left[15 \frac{\Gamma(3.5 - \omega^{(\alpha\beta)})}{\Gamma(4.5 - \omega^{(\alpha\beta)})} \mu^{(\alpha)} + 6\mu^{(\beta)} \right], \quad (\text{App.D.22})$$

$$\text{VHS[6]} = \frac{1}{6} c_{\text{ref}}^{2\nu^{(\alpha\beta)}} \Gamma(4.5 - \omega^{(\alpha\beta)}) \left(2\hat{\theta}^{(\alpha)} + 2\hat{\theta}^{(\beta)} \right)^{0.5 - \omega^{(\alpha\beta)}}. \quad (\text{App.D.23})$$

Gupta et al. [64] calculated production terms based on the thermal velocities $\hat{\mathbf{c}}$. Similar, as described for the HS model in App. C, the production terms can be transformed into a \mathbf{c} basis.

Note, that the VHS production terms Eq. (App.D.13) - Eq. (App.D.16) and the collision frequency Eq. (App.D.17) feature a similar structure than the HS production terms and frequency described in App. C.1. Differences are only the scaling parameters Eq. (App.D.18) - Eq. (App.D.23), which adopt the value 1 in the case of hard sphere molecules ($\omega^{(\alpha\beta)} = 0.5$).

Appendix E

Expansion flows

E.1 Temperature anisotropy in free molecular expansion

In this subchapter, the formation of an anisotropic temperature distribution due to free molecular expansion processes is explained using a simple and illustrative model. For the following explanations, a free molecular transport of particles is considered. The flow is assumed to feature a vanishing macroscopic velocity, while each particle exhibits a thermal velocity component.

As shown in Fig. E.1 particles with different velocity vectors can move into a region G , far away from the expansion axis. Because of the large distance to the expansion axis, these particles must all have a much larger velocity v_{\perp} perpendicular to the direction of expansion, than the velocity v_{\parallel} parallel to the direction of expansion. Consequently the region G includes a large number of particles which all have a high velocity v_{\perp} and a much lower velocity v_{\parallel} . From this it can be concluded that the thermal velocity c_{\perp} should also be on average much higher than the thermal velocity c_{\parallel} .

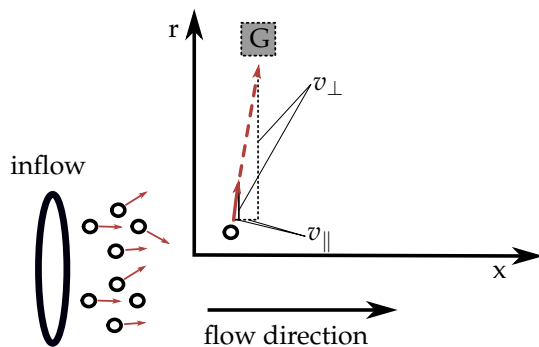


FIGURE E.1: Free molecular transport of particles into an area G , at a large distance from the expansion axis. Only particles with a sufficiently large velocity ratio v_{\perp}/v_{\parallel} can reach G .

As a result, the temperature component T_{\perp} , as defined in Eq. (3.76), becomes large, while the temperature component T_{\parallel} , as defined in (3.75), becomes small in this region. Analogous considerations can be made for the case when G is close to the expansion axis. In this case, the temperature component T_{\parallel} becomes large. In summary, the distribution of T_{\perp} features its maximum away from the expansion axis, while the distribution of T_{\parallel} features its maximum on the expansion axis.

Appendix F

Collision parameters

The following tables list model parameters that are used for the numerical studies in this thesis.

species α	species β	$d^{(\alpha\beta)}$ [10^{-10} m]
He	He	2.33
He	Ar	3.25
Ar	Ar	4.17

TABLE F.1: HS collision parameters for a He-Ar mixture [10].

species	θ [K]
N ₂	3371
O ₂	2256

TABLE F.2: Vibrational temperatures for N₂ and O₂.

species α	species β	$d^{(\alpha\beta)}$ [10^{-10} m]	$\omega^{(\alpha\beta)}$	$T_{\text{ref}}^{(\alpha\beta)}$ [K]
He	He	2.33	0.66	273.15
He	Ar	3.25	0.735	273.15
Ar	Ar	4.17	0.81	273.15

TABLE F.3: VHS collision parameters for a He-Ar mixture [10].

species α	species β	$d^{(\alpha\beta)}$ [10^{-10} m]	$\omega^{(\alpha\beta)}$	$T_{\text{ref}}^{(\alpha\beta)}$ [K]	$Z_{\text{rot}}^{(\alpha\beta)}$	$Z_{\text{vib}}^{(\alpha\beta)}$
N ₂	N ₂	4.17	0.74	273.15	0.05	0.001
N ₂	O ₂	4.12	0.755	273.15	0.02	0.002
O ₂	N ₂	4.12	0.755	273.15	0.15	0.003
O ₂	O ₂	4.07	0.77	273.15	0.2	0.004

TABLE F.4: VHS collision parameters and internal relaxation times for a N₂-O₂ mixture[10].

species α	$d^{(\alpha)}$ [10^{-10} m]	$\omega^{(\alpha)}$	$T_{\text{ref}}^{(\alpha)}$ [K]	$Z_{\text{rot}}^{(\alpha)}$	$Z_{\text{vib}}^{(\alpha)}$	$g^{(i)}$
N ₂	4.07	0.74	273.15	0.2	0.02	0.7846
O ₂	3.96	0.77	273.15	0.2	0.02	0.1961
H ₂	2.92	0.67	273.15	0.2	0.02	0.0196

TABLE F.5: VHS collision parameters, internal relaxation times [10] and species specific weights $g^{(i)}$ for a H₂-N₂-O₂ mixture.

Bibliography

- [1] I. Adamovich, S. Macheret, W. Rich, and C. Treanor. "Vibrational relaxation and dissociation behind shock waves part 1: Kinetic rate models". In: *AIAA Journal* 33.6 (1995), pp. 1064–1069. ISSN: 0001-1452. DOI: 10.2514/3.12528.
- [2] I. Adamovich, S. Macheret, W. Rich, and C. Treanor. "Vibrational relaxation and dissociation behind shock waves Part 2: Master equation modeling". In: *AIAA Journal* 33.6 (1995), pp. 1070–1075. ISSN: 0001-1452. DOI: 10.2514/3.48339.
- [3] S. Ahmad and A. Ambrosetti. *First order linear differential equations*. Springer International Publishing, 2015, pp. 1–14. ISBN: 978-3-319-16408-3.
- [4] H. Akhlaghi, E. Roohi, and S. Stefanov. "A new iterative wall heat flux specifying technique in DSMC for heating/cooling simulations of MEMS/NEMS". In: *International Journal of Thermal Sciences* 59 (2012), pp. 111–125. DOI: 10.1016/j.ijthermalsci.2012.04.002.
- [5] J. Anderson. *Hypersonic and high-temperature gas dynamics, second edition (AIAA Education)*. AIAA, 2006. ISBN: 978-1-56347-780-5.
- [6] F. Bergmann. "Gaskinetical simulation of near-continuum hypersonic flow with consideration of wall-catalysis". PhD thesis. Technische Universität München, 1994.
- [7] P. L. Bhatnagar, E. P. Gross, and M. Krook. "A model for collision processes in gases. I. Small amplitude processes in charged and neutral one-component systems". In: *Physical Review* 94.3 (1954), pp. 511–525. DOI: 10.1103/PhysRev.94.511.
- [8] G. A. Bird. "Approach to translational equilibrium in a rigid sphere gas". In: *Physics of Fluids* 6.10 (1963), p. 1518. DOI: 10.1063/1.1710976.
- [9] G. A. Bird. *Molecular gas dynamics*. Clarendon Press, 1976. ISBN: 0 19 856120 2.
- [10] G. A. Bird. *Molecular gas dynamics and the direct simulation of gas flows (Oxford Engineering Science Series)*. Clarendon Press, 1994. ISBN: 0-19-856195-4.
- [11] G. A. Bird. "Monte-Carlo simulation in an engineering context". In: *Progress in Astronautics and Aeronautics* 74 (1981), pp. 239–255. DOI: 10.2514/5.9781600865480.0239.0255.
- [12] G.A. Bird. "Sophisticated DSMC". In: *Notes prepared for a short course at the DSMC07 meeting, Santa Fe, USA*. 2007.
- [13] S. V. Bogomolov. "On Fokker-Planck model for the Boltzmann collision integral at the moderate Knudsen numbers". In: *Mathematical Models and Computer Simulations* 1.6 (2009), pp. 739–744. DOI: 10.1134/s2070048209060088.
- [14] C. Borgnakke and P. S. Larsen. "Statistical collision model for Monte-Carlo simulation of polyatomic gas mixture". In: *Journal of Computational Physics* 18.4 (1975), pp. 405–420. DOI: 10.1016/0021-9991(75)90094-7.

- [15] I. D. Boyd. "Analysis of rotational nonequilibrium in standing shock waves of nitrogen". In: *AIAA Journal* 28 (1990), pp. 1997–1999. DOI: 10.2514/3.10511.
- [16] I. D. Boyd. "Analysis of vibrational-translational energy transfer using the direct simulation Monte-Carlo method". In: *Physics of Fluids A: Fluid Dynamics* 3.7 (1991), pp. 1785–1791. DOI: 10.1063/1.857959.
- [17] I. D. Boyd. "Relaxation of discrete rotational energy distributions using a Monte-Carlo method". In: *Physics of Fluids A: Fluid Dynamics* 5.9 (1993), pp. 2278–2286. DOI: 10.1063/1.858531.
- [18] I. D. Boyd, G. Chen, and G. V. Candler. "Predicting failure of the continuum fluid equations in transitional hypersonic flows". In: *Physics of Fluids* 7.1 (1995), pp. 210–219. DOI: 10.1063/1.868720.
- [19] K. Breuer, E. Piekos, and D. Gonzales. "DSMC simulations of continuum flows". In: *30th Thermophysics Conference*. American Institute of Aeronautics and Astronautics, 1995. DOI: 10.2514/6.1995-2088.
- [20] S. Bruschi, S. Lehner, T. Fritz, M. Soccorsi, A. Soloviev, and B. van Schie. "Ship surveillance with TerraSAR-X". In: *IEEE Transactions on Geoscience and Remote Sensing* 49.3 (2011), pp. 1092–1103. DOI: 10.1109/TGRS.2010.2071879.
- [21] C. Buet. "A discrete-velocity scheme for the Boltzmann operator of rarefied gas dynamics". In: *Transport Theory and Statistical Physics* 25.1 (1996), pp. 33–60. DOI: 10.1080/00411459608204829.
- [22] J. M. Burgers. *Flow equations for composite gases*. Tech. rep. Maryland university college park institute for fluid dynamics and applied mathematics, 1969.
- [23] J. M. Burgers. "The boltzmann equation for flows with chemical reactions". In: *Planetary and Space Science* 3 (1961), pp. 4–11. DOI: 10.1016/0032-0633(61)90218-5.
- [24] J. Burt and I. Boyd. "A low diffusion particle method for simulating compressible inviscid flows". In: *39th AIAA Thermophysics Conference*. American Institute of Aeronautics and Astronautics, 2007. DOI: 10.2514/6.2007-4259.
- [25] J. Burt and I. Boyd. "Evaluation of a particle method for the ellipsoidal statistical Bhatnagar-Gross-Krook equation". In: *44th AIAA Aerospace Sciences Meeting and Exhibit* (2006). DOI: 10.2514/6.2006-989.
- [26] J. M. Burt and I. D. Boyd. "A hybrid particle approach for continuum and rarefied flow simulation". In: *Journal of Computational Physics* 228.2 (2009), pp. 460–475. DOI: 10.1016/j.jcp.2008.09.022.
- [27] C. Cercignani. *Rarefied Gas Dynamics: From basic concepts to actual calculations (Cambridge Texts in Applied Mathematics)*. Cambridge University Press, 2000. ISBN: 0-521-65008-9.
- [28] C. Cercignani and M. Lampis. "Kinetic models for gas-surface interactions". In: *Transport Theory and Statistical Physics* 1.2 (1971), pp. 101–114. DOI: 10.1080/00411457108231440.
- [29] C.S. Wang Chang and G.E. Uhlenbeck. "Transport phenomena in polyatomic gases". In: *Research Rep. CM-681. University of Michigan Engineering* (1951).
- [30] S. Chapman and T. G. Cowling. *The mathematical theory of non-uniform gases*. The Syndics of the Cambridge University Press, 1960.
- [31] R. Courant, K. Friedrichs, and H. Lewy. "Über die partiellen Differenzgleichungen der mathematischen Physik". In: *Mathematische Annalen* 100.1 (1928), pp. 32–74. DOI: 10.1007/BF01448839.

- [32] A. Einstein. "Zur Theorie der Brownschen Bewegung". In: *Annalen der Physik* 324.2 (1906), pp. 371–381.
- [33] D. Enskog. *Kinetische Theorie der Wärmeleitung: Reibung und Selbst-Diffusion in gewissen verdichteten Gasen und Flüssigkeiten*. Almqvist & Wiksells boktryckeri-a.-b., 1922.
- [34] F. Fei and J. Fan. "A diffusive information preservation method for small Knudsen number flows". In: *Journal of Computational Physics* 243 (2013), pp. 179–193. ISSN: 0021-9991. DOI: 10.1016/j.jcp.2013.03.012.
- [35] F. Fei, Z. Liu, J. Zhang, and C. Zheng. "A particle Fokker-Planck algorithm with multiscale temporal discretization for rarefied and continuum gas flows". In: *Communications in Computational Physics* 22.02 (2017), pp. 338–374. DOI: 10.4208/cicp.oa-2016-0134.
- [36] F. Filbet and C. Mouhot. "Analysis of spectral methods for the homogeneous Boltzmann equation". In: *Transactions of the American Mathematical Society* 363.04 (2011), pp. 1947–1947. DOI: 10.1090/S0002-9947-2010-05303-6.
- [37] F. Filbet and G. Russo. "High order numerical methods for the space non-homogeneous Boltzmann equation". In: *Journal of Computational Physics* 186.2 (2003), pp. 457–480. DOI: 10.1016/S0021-9991(03)00065-2.
- [38] A. D. Fokker. "Die mittlere Energie rotierender elektrischer Dipole im Strahlungsfeld". In: *Annalen der Physik* 348.5 (1914), pp. 810–820. DOI: 10.1002/andp.19143480507.
- [39] M. A. Gallis, J. R. Torczynski, S. J. Plimpton, D. J. Rader, and T. Koehler. "Direct simulation Monte-Carlo: The quest for speed". In: *AIP Conference Proceedings*. Vol. 1628. 1. AIP, 2014, pp. 27–36. DOI: 10.1063/1.4902571.
- [40] M. A. Gallis and J. Torczynski. "Effect of collision-partner selection schemes on the accuracy and efficiency of the direct simulation Monte-Carlo method". In: *International Journal for Numerical Methods in Fluids* 67.8 (2011), pp. 1057–1072. DOI: 10.1002/flid.2409.
- [41] M. A. Gallis and J. R. Torczynski. "Investigation of the ellipsoidal-statistical Bhatnagar–Gross–Krook kinetic model applied to gas-phase transport of heat and tangential momentum between parallel walls". In: *Physics of Fluids* 23.3 (2011), p. 030601. DOI: 10.1063/1.3558869.
- [42] M. A. Gallis and J. K. Harvey. "The modeling of chemical reactions and thermochemical nonequilibrium in particle simulation computations". In: *Physics of Fluids* 10.6 (1998), pp. 1344–1358. DOI: 10.1063/1.869660.
- [43] A. L. Garcia and B. J. Alder. "Generation of the Chapman–Enskog distribution". In: *Journal of Computational Physics* 140 (1998), pp. 66–70. ISSN: 0021-9991. DOI: 10.1006/jcph.1998.5889.
- [44] C. W. Gardiner. *Handbook of stochastic methods for physics, chemistry, and the natural sciences (Springer series in synergetics)*. Springer-Verlag, 1983. ISBN: 0-387-11357-6.
- [45] J. E. Gentle. *Random number generation and Monte-Carlo methods*. Springer Science & Business Media, 2006. ISBN: 978-1-4757-2960-3.
- [46] D. T. Gillespie. "A General method for numerically simulating the stochastic time evolution of coupled chemical reactions". In: *Journal of Computational Physics* 22.4 (1976), pp. 403–434. DOI: 10.1016/0021-9991(76)90041-3.

- [47] S. Gimelshein, I. Boyd, Q. Sun, and M. Ivanov. "DSMC modeling of vibration-translation energy transfer in hypersonic rarefied flows". In: *33rd Thermophysics Conference* (1999). DOI: 10.2514/6.1999-3451.
- [48] O. Gnedin and J. P. Ostriker. "Destruction of the galactic globular cluster system". In: *The Astrophysical Journal* 474.1 (1997), p. 223. DOI: 10.1086/303441.
- [49] E. Goldman. "Equations for gas mixtures". In: *Physics of Fluids* 10.9 (1967), p. 1928. DOI: 10.1063/1.1762389.
- [50] *Google Scholar*. <https://scholar.google.com/>. Accessed: 2021-12-10.
- [51] H. Gorji and P. Jenny. "A kinetic model for gas mixtures based on a Fokker-Planck equation". In: *Journal of Physics: Conference Series* 362 (2012), p. 012042. DOI: 10.1088/1742-6596/362/1/012042.
- [52] H. Gorji and M. Torrilhon. "Entropic Fokker-Planck kinetic model". In: *Journal of Computational Physics* 430 (2021), p. 110034. DOI: 10.1016/j.jcp.2020.110034.
- [53] M. H. Gorji and P. Jenny. "A Fokker-Planck based kinetic model for diatomic rarefied gas flows". In: *Physics of Fluids* 25.6 (2013), p. 062002.
- [54] M. H. Gorji and P. Jenny. "A gas-surface interaction kernel for diatomic rarefied gas flows based on the Cercignani-Lampis-Lord model". In: *Physics of Fluids* 26.12 (2014), p. 122004. ISSN: 1070-6631. DOI: 10.1063/1.4903004.
- [55] M. H. Gorji, M. Torrilhon, and P. Jenny. "Fokker-Planck model for computational studies of monatomic rarefied gas flows". In: *Journal of Fluid Mechanics* 680 (2011), pp. 574–601. ISSN: 0022-1120. DOI: 10.1017/jfm.2011.188.
- [56] M. Hossein Gorji and P. Jenny. "An efficient particle Fokker-Planck algorithm for rarefied gas flows". In: *Journal of Computational Physics* 262 (2014), pp. 325–343. DOI: 10.1016/j.jcp.2013.12.046.
- [57] M. Hossein Gorji and P. Jenny. "Fokker-Planck-DSMC algorithm for simulations of rarefied gas flows". In: *Journal of Computational Physics* 287 (2015), pp. 110–129. DOI: 10.1016/j.jcp.2015.01.041.
- [58] M. Grabe. "Modellierung der Treibstrahl-Wechslewirkung von Kleintriebwerken unter Hochvakuumbedingungen". PhD thesis. Universität Stuttgart, 2017.
- [59] M. Grabe. "STG-CT: High-vacuum plume test facility for chemical thrusters". In: *Journal of large-scale research facilities JLSRF* 2 (2016). DOI: 10.17815/jlsrf-2-139.
- [60] M. Grabe, G. Dettleff, C. Hepp, and K. Hannemann. "Effect on source geometry on fully expanding jets". In: *Effect on source geometry on fully expanding jets* 2132 (2019), p. 030001. DOI: 10.1063/1.5119526.
- [61] H. Grad. "On the kinetic theory of rarefied gases". In: *Communications on Pure and Applied Mathematics* 2.4 (1949), pp. 331–407. DOI: 10.1002/cpa.3160020403.
- [62] H. Grad. "Principles of the kinetic theory of gases". In: *Handbuch der Physik / Encyclopedia of Physics* (1958), pp. 205–294. DOI: 10.1007/978-3-642-45892-7_3.
- [63] V. K. Gupta. "Mathematical modeling of rarefied gas-mixtures". PhD thesis. RWTH Aachen, 2015.

- [64] V. K. Gupta and M. Torrillon. *Automated Boltzmann collision integrals for moment equations*. 2012. DOI: 10.1063/1.4769474.
- [65] V. Kumar Gupta and M. Torrillon. "Reprint of: Comparison of relaxation phenomena in binary gas-mixtures of Maxwell molecules and hard spheres". In: *Computers & Mathematics with Applications* 72.2 (2016), pp. 271–287. ISSN: 0898-1221. DOI: 10.1016/j.camwa.2016.04.020.
- [66] B. B. Hamel. "Kinetic theory of source flow expansion with application to the free jet". In: *Physics of Fluids* 9.5 (1966), p. 829. DOI: 10.1063/1.1761783.
- [67] B. B. Hamel, B. L. Maguire, and E. P. Muntz. "Some characteristics of exhaust plume rarefaction". In: *AIAA Journal* 8.9 (1970), pp. 1651–1658. DOI: 10.2514/3.5960.
- [68] A. Haselbacher, F. M. Najjar, and J. P. Ferry. "An efficient and robust particle-localization algorithm for unstructured grids". In: *Journal of Computational Physics* 225.2 (2007), pp. 2198–2213. DOI: 10.1016/j.jcp.2007.03.018.
- [69] H. A. Hassan and D. B. Hash. "A generalized hard-sphere model for Monte-Carlo simulation". In: *Physics of Fluids A: Fluid Dynamics* 5.3 (1993), pp. 738–744. DOI: 10.1063/1.858656.
- [70] S. Heinz. "Molecular to fluid dynamics: The consequences of stochastic molecular motion". In: *Physical Review E* 70.3 (2004), p. 036308. DOI: 10.1103/PhysRevE.70.036308.
- [71] C. Hepp. "Modeling of internal energy relaxation in a kinetic Fokker-Planck solver". DSMC 2019 Conference, Santa Fe. 2019.
- [72] C. Hepp. "Modeling of rarefied gas flows with particle methods". Department of Mechanical Engineering, University of New Mexico, Invited by Dr. D. T. Banuti. 2019.
- [73] C. Hepp, M. Grabe, and K. Hannemann. "A kinetic Fokker-Planck approach for modeling variable hard-sphere gas mixtures". In: *AIP Advances* 10.8 (2020), p. 085219. DOI: 10.1063/5.0017289.
- [74] C. Hepp, M. Grabe, and K. Hannemann. "A kinetic Fokker-Planck approach to model hard-sphere gas mixtures". In: *Physics of Fluids* 32.2 (2020), p. 027103. DOI: 10.1063/1.5141909.
- [75] C. Hepp, M. Grabe, and K. Hannemann. "Master equation approach for modeling diatomic gas flows with a kinetic Fokker-Planck algorithm". In: *Journal of Computational Physics* 418 (2020), p. 109638. DOI: 10.1016/j.jcp.2020.109638.
- [76] C. Hepp, M. Grabe, and K. Hannemann. "Non-equilibrium parameter for a hybrid Fokker-Planck/DSMC scheme". In: *AIP Conference Proceedings*. Vol. 2132. 1. AIP Publishing. 2019, p. 070002. DOI: 10.1063/1.5119556.
- [77] D. Hinkley. "A novel cold gas propulsion system for nanosatellites and picosatellites". In: *Small Satellite Conference*. 2008.
- [78] J. O. Hirschfelder, C. F. Curtiss, and R. B. Bird. *Molecular theory of gases and liquids*. Wiley New York, 1964. ISBN: 978-0-471-40065-3.
- [79] L. H. Holway. "New statistical models for kinetic theory: Methods of construction". In: *Physics of Fluids* 9.9 (1966), p. 1658. DOI: 10.1063/1.1761920.

- [80] A. Van Itterbeek, O. Verbeke, F. Theewes, K. Staes, and J. De Boelpaep. "The difference in vapour pressure between normal and equilibrium hydrogen. Vapour pressure of normal hydrogen between 20 K and 32 K". In: *Physical* 30.6 (1964), pp. 1238–1244. DOI: 10.1016/0031-8914(64)90114-4.
- [81] M. S. Ivanov and S. V. Rogazinskii. "Comparative analysis of algorithms of the direct statistical simulation method in rarefied gas dynamics". In: *USSR Computational Mathematics and Mathematical Physics* 28 (1988), pp. 63–71. DOI: 10.1016/0041-5553(88)90112-7.
- [82] M. S. Ivanov and S. V. Rogazinskii. "Theoretical analysis of traditional and modern schemes of the DSMC method". In: *Rarefied gas dynamics; Proceedings of the 17th International Symposium*, VCH Verlagsgesellschaft mbH, 1991, pp. 629–642.
- [83] K. Jacobs. *Stochastic processes for physicists: Understanding noisy systems*. Cambridge University Press, 2010. ISBN: 9780521765428.
- [84] P. Jenny, M. Torrillon, and S. Heinz. "A solution algorithm for the fluid dynamic equations based on a stochastic model for molecular motion". In: *Journal of Computational Physics* 229.4 (2010), pp. 1077–1098. ISSN: 0021-9991. DOI: 10.1016/j.jcp.2009.10.008.
- [85] P. Jenny, S. Küchlin, and H. Gorji. "Controlling the bias error of Fokker-Planck methods for rarefied gas dynamics simulations". In: *Physics of Fluids* 31.6 (2019), p. 062005. DOI: 10.1063/1.5097884.
- [86] P. Jenny, M. Muradoglu, K. Liu, S. B. Pope, and D. A. Caughey. "PDF simulations of a bluff-body stabilized flow". In: *Journal of Computational Physics* 169.1 (2001), pp. 1–23. ISSN: 0021-9991. DOI: 10.1006/jcph.2001.6704.
- [87] Y. Jiang, Z. Gao, and C. Lee. "Particle simulation of nonequilibrium gas flows based on ellipsoidal statistical Fokker-Planck model". In: *Computers & Fluids* 170 (2018), pp. 106–120. ISSN: 0045-7930. DOI: 10.1016/j.compfluid.2018.04.034.
- [88] E. Jun. "Cubic Fokker-Planck-DSMC hybrid method for diatomic rarefied gas flow through a slit and an orifice". In: *Vacuum* 159 (2019), pp. 125–133. DOI: 10.1016/j.vacuum.2018.10.028.
- [89] E. Jun, M. Pfeiffer, L. Mieussens, and M. H. Gorji. "A comparative study between cubic and ellipsoidal Fokker-Planck kinetic models". In: *AIAA Journal* 57 (2019), pp. 1–10. ISSN: 0001-1452. DOI: 10.2514/1.j057935.
- [90] E. Jun, I. Boyd, and J. Burt. "Assessment of an all-Particle hybrid method for hypersonic rarefied flow". In: *51st AIAA Aerospace Sciences Meeting including the New Horizons Forum and Aerospace Exposition* (2013). DOI: 10.2514/6.2013-1203.
- [91] E. Jun, M. H. Gorji, M. Grabe, and K. Hannemann. "Assessment of the cubic Fokker-Planck-DSMC hybrid method for hypersonic rarefied flows past a cylinder". In: *Computers & Fluids* 168 (2018), pp. 1–13. ISSN: 0045-7930. DOI: 10.1016/j.compfluid.2018.03.059.
- [92] N. G. Van Kampen. *Stochastic processes in physics and chemistry*. Vol. 1. Elsevier, 1992, p. 112.
- [93] J. G. Kirkwood. "The statistical mechanical theory of transport processes I. General theory". In: *The Journal of Chemical Physics* 14.3 (1946), pp. 180–201. DOI: 10.1063/1.1724117.

- [94] A. Kolmogoroff. "Über die analytischen Methoden in der Wahrscheinlichkeitsrechnung". In: *Mathematische Annalen* 104.1 (1931), pp. 415–458.
- [95] K. Koura and H. Matsumoto. "Variable soft sphere molecular model for air species". In: *Physics of Fluids A: Fluid Dynamics* 4.5 (1992), pp. 1083–1085. DOI: 10.1063/1.858262.
- [96] K. Koura and H. Matsumoto. "Variable soft sphere molecular model for inverse-power-law or Lennard-Jones potential". In: *Physics of Fluids A: Fluid Dynamics* 3.10 (1991), pp. 2459–2465. DOI: 10.1063/1.858184.
- [97] G. M. Kremer. *An introduction to the Boltzmann equation and transport processes in gases*. Springer Berlin Heidelberg, 2010.
- [98] E.V. Kustova and E.A. Nagnibeda. "Transport properties of a reacting gas mixture with strong vibrational and chemical nonequilibrium". In: *Chemical Physics* 233.1 (1998), pp. 57–75. DOI: 10.1016/S0301-0104(98)00092-5.
- [99] U. Kvell et al. "Nanosatellite orbit control using MEMS cold gas thrusters". In: *Proceedings of the Estonian Academy of Sciences* 63.2S (2014), pp. 279–285. DOI: 10.3176/proc.2014.2S.09.
- [100] S. Kuchlin. "Stochastic computation of rarefied gas flows using the Fokker-Planck-DSMC Method: Theory, algorithms, and parallel implementation". PhD thesis. ETH Zürich, 2018.
- [101] S. Kuchlin and P. Jenny. "Parallel Fokker-Planck-DSMC algorithm for rarefied gas flow simulation in complex domains at all Knudsen numbers". In: *Journal of Computational Physics* 328 (2017), pp. 258–277. ISSN: 0021-9991. DOI: 10.1016/j.jcp.2016.10.018.
- [102] G. LeBeau, K. Jacikas, and F. Lumpkin. "Virtual sub-cells for the direct simulation Monte-Carlo method". In: 2003, p. 1031. DOI: 10.2514/6.2003-1031.
- [103] J. L. Lebowitz, H. L. Frisch, and E. Helfand. "Nonequilibrium distribution functions in a fluid". In: *Physics of Fluids* 3.3 (1960), p. 325.
- [104] R. Lerner. *Encyclopedia of physics*. Wiley-VCH, 1990. ISBN: 0-89573-752-3.
- [105] C. R. Lilley and M. N. Macrossan. "Methods for implementing the stream boundary condition in DSMC computations". In: *International Journal for Numerical Methods in Fluids* 42.12 (2003), pp. 1363–1371. DOI: 10.1002/flid.603.
- [106] W. Liou and Y. Fang. "Implicit boundary conditions for direct simulation Monte-Carlo method in MEMS flow predictions". In: *Computer Modeling in Engineering & Science* 1.4 (2000), pp. 119–128. DOI: 10.3970/cmcs.2000.001.571.
- [107] R. G. Lord. "Some extensions to the Cercignani-Lampis gas-surface scattering kernel". In: *Physics of Fluids A: Fluid Dynamics* 3 (1991), p. 706. DOI: 10.1063/1.858076.
- [108] F. E. Lumpkin, B. L. Haas, and I. D. Boyd. "Resolution of differences between collision number definitions in particle and continuum simulations". In: *Physics of Fluids A: Fluid Dynamics* 3.9 (1991), pp. 2282–2284. DOI: 10.1063/1.857964.
- [109] *mathcces.rwth-aachen*. <https://web.mathcces.rwth-aachen.de/CollisionIntegrals/>. Accessed: 2022-02-14.
- [110] J. Mathiaud and L. Mieussens. "A Fokker-Planck Model of the Boltzmann equation with correct prandtl number". In: *Journal of Statistical Physics* 162.2 (2015), pp. 397–414. DOI: 10.1007/s10955-015-1404-9.

- [111] J. Mathiaud and L. Mieussens. "A Fokker–Planck model of the Boltzmann equation with correct prandtl number for polyatomic gases". In: *Journal of Statistical Physics* 168.5 (2017), pp. 1031–1055. DOI: 10.1007/s10955-017-1837-4.
- [112] F. J. McCormack. "Kinetic equations for polyatomic gases: The 17-moment approximation". In: *Physics of Fluids* 11.12 (1968), p. 2533. DOI: 10.1063/1.1691855.
- [113] A. Mohammadzadeh, A. Rana, and H. Struchtrup. "DSMC and R13 modeling of the adiabatic surface". In: *International Journal of Thermal Sciences* 101 (2016), pp. 9–23. DOI: 10.1016/j.ijthermalsci.2015.10.007.
- [114] T. F. Morse. "Kinetic model for gases with internal degrees of freedom". In: *Physics of Fluids* 7.2 (1964), p. 159. DOI: 10.1063/1.1711128.
- [115] L. Pareschi and B. Perthame. "A Fourier spectral method for homogeneous boltzmann equations". In: *Transport Theory and Statistical Physics* 25.3-5 (1996), pp. 369–382. DOI: 10.1080/00411459608220707.
- [116] C. Park. *Nonequilibrium hypersonic aerothermodynamics*. Wiley-Interscience, 1990. ISBN: 0-471-51093-9.
- [117] R. F. Pawula. "Approximation of the Linear Boltzmann equation by the Fokker–Planck equation". In: *Physical Review* 162.1 (1967), pp. 186–188. DOI: 10.1103/physrev.162.186.
- [118] A. G. Peeters and D. Strintzi. "The Fokker-Planck equation, and its application in plasma physics". In: *Annalen der Physik* 17.2-3 (2008), pp. 142–157. DOI: 10.1002/andp.200710279.
- [119] M. Pfeiffer. "Extending the particle ESBGK method to diatomic molecules including quantized vibrational energies". In: *Physics of Fluids* 30.11 (2018), p. 116103. ISSN: 1070-6631. DOI: 10.1063/1.5054961.
- [120] M. Pfeiffer and M. H. Gorji. "Adaptive particle–cell algorithm for Fokker–Planck based rarefied gas flow simulations". In: *Computer Physics Communications* 213 (2017), pp. 1–8. DOI: 10.1016/j.cpc.2016.11.003.
- [121] M. Pfeiffer and P. Nizenkov. "Coupled ellipsoidal statistical BGK-DSMC simulations of a nozzle expansion". In: *AIP Conference Proceedings* 2132 (2019), p. 070019. DOI: 10.1063/1.5119573.
- [122] M. Pfeiffer, A. Mirza, and P. Nizenkov. "Evaluation of particle-based continuum methods for a coupling with the direct simulation Monte-Carlo method based on a nozzle expansion". In: *Physics of Fluids* 31.7 (2019), p. 073601. DOI: 10.1063/1.5098085.
- [123] M. Pfeiffer, P. Nizenkov, and S. Fasoulas. "Extension of particle-based BGK models to polyatomic species in hypersonic flow around a flat-faced cylinder". In: *AIP Conference Proceedings* 2132 (2019), p. 1000001. DOI: 10.1063/1.5119596.
- [124] M. Planck. "Über einen Satz der statischen Dynamik und seiner Erweiterung in der Quantentheorie". In: *Sitzungsbericht der preussischen Akademie der Wissenschaften* (1917), pp. 324–341.
- [125] S. J. Plimpton et al. "Direct simulation Monte-Carlo on petaflop supercomputers and beyond". In: *Physics of Fluids* 31.8 (2019), p. 086101. DOI: 10.1063/1.5108534.

- [126] F. Rogier and J. Schneider. "A direct method for solving the Boltzmann equation". In: *Transport Theory and Statistical Physics* 23.1-3 (1994), pp. 313–338. DOI: 10.1080/00411459408203868.
- [127] D. E. Rothe. "Electron beam studies of the diffusive separation of Helium-Argon mixtures". In: *Physics of Fluids* 9.9 (1966), p. 1643. DOI: 10.1063/1.1761919.
- [128] Scart. <https://scart.dlr.de/site/index.php>. Accessed: 2021-12-27.
- [129] P. O. J. Scherer. *Computational physics*. Springer International Publishing, 2013. DOI: 10.1007/978-3-319-00401-3.
- [130] T. E. Schwartzentruber and I. D. Boyd. "Progress and future prospects for particle-based simulation of hypersonic flow". In: *Progress in Aerospace Sciences* 72 (2015), pp. 66–79. ISSN: 0376-0421. DOI: 10.1016/j.paerosci.2014.09.003.
- [131] Scopus. <https://www.scopus.com>. Accessed: 2019-10-28.
- [132] E. M. Shakhov. "Generalization of the Krook kinetic relaxation equation". In: *Fluid Dynamics* 3.5 (1972), pp. 95–96. DOI: 10.1007/BF01029546.
- [133] M. Sh. Shavaliyev. "Super-Burnett corrections to the stress tensor and the heat flux in a gas of Maxwellian molecules". In: *Journal of Applied Mathematics and Mechanics* 57.3 (1993), pp. 573–576. DOI: 10.1016/0021-8928(93)90137-B.
- [134] F. S. Sherman. "Hydrodynamical theory of diffusive separation of mixtures in a free jet". In: *Physics of Fluids* 8.5 (1965), p. 773. DOI: 10.1063/1.1761319.
- [135] S. K. Singh and S. Ansumali. "Fokker-Planck model of hydrodynamics". In: *Physical Review E* 91.3 (2015), p. 033303. DOI: 10.1103/PhysRevE.91.033303.
- [136] H. Struchtrup. *Macroscopic transport equations for rarefied gas flows*. Springer Berlin Heidelberg, 2005.
- [137] H. Struchtrup and M. Torrilhon. "Regularization of Grad's 13 moment equations: Derivation and linear analysis". In: *Physics of Fluids* 15.9 (2003), pp. 2668–2680. DOI: 10.1063/1.1597472.
- [138] M. Torrilhon and H. Struchtrup. "Regularized 13-moment equations: Shock structure calculations and comparison to Burnett models". In: *Journal of Fluid Mechanics* 513 (2004), pp. 171–198. DOI: 10.1017/S0022112004009917.
- [139] M. W. Tysanner and A. L. Garcia. "Measurement bias of fluid velocity in molecular simulations". In: *Journal of Computational Physics* 196.1 (2004), pp. 173–183. ISSN: 0021-9991. DOI: 10.1016/j.jcp.2003.10.021.
- [140] M. W. Tysanner and A. L. Garcia. "Non-equilibrium behaviour of equilibrium reservoirs in molecular simulations". In: *International Journal for Numerical Methods in Fluids* 48.12 (2005), pp. 1337–1349. DOI: 10.1002/flid.983.
- [141] W. G. Vincenti and C. H. Kruger. *Introduction to physical gas dynamics*. Krieger Pub Co, 1975. ISBN: 0-88275-309-6.
- [142] D. Wadsworth and D. Erwi. "Two-dimensional hybrid continuum / particle approach for rarefied flows". In: *23rd Plasmadynamics and Lasers Conference*. American Institute of Aeronautics and Astronautics, 1992. DOI: 10.2514/6.1992-2975.

- [143] W. Wagner. "A convergence proof for Bird's direct simulation Monte-Carlo method for the Boltzmann equation". In: *Journal of Statistical Physics* 66.3-4 (1992), pp. 1011–1044. DOI: 10.1007/bf01055714.
- [144] P. Wang, M. Tuan Ho, L. Wu, Z. Guo, and Y. Zhang. "A comparative study of discrete velocity methods for low-speed rarefied gas flows". In: *Computers & Fluids* 161 (2018), pp. 33–46. DOI: 10.1016/j.compfluid.2017.11.006.
- [145] J. Wu, K. Tseng, and F. Wu. "Parallel three-dimensional DSMC method using mesh refinement and variable time-step scheme". In: *Computer Physics Communications* 162 (2004), pp. 167–187. ISSN: 0010-4655. DOI: 10.1016/j.cpc.2004.07.004.
- [146] L. Wu, C. White, T. J. Scanlon, J. M. Reese, and Y. Zhang. "Deterministic numerical solution of the Boltzmann equation using the fast spectral method". In: *Journal of Computational Physics* 250 (2013), pp. 27–52. DOI: 10.1016/j.jcp.2013.05.003.
- [147] C. Zhang and Thomas E. Schwartzentruber. "Inelastic collision selection procedures for direct simulation Monte-Carlo calculations of gas mixtures". In: *Physics of Fluids* 25.10 (2013), p. 106105. DOI: 10.1063/1.4825340.
- [148] L. Zhou, C. J. Tucker, R. K. Kaufmann, D. Slayback, N. V. Shabanov, and R. B. Myneni. "Variations in northern vegetation activity inferred from satellite data of vegetation index during 1981 to 1999". In: *Journal of Geophysical Research: Atmospheres* 106.D17 (2001), pp. 20069–20083. DOI: 10.1029/2000JD000115.
- [149] T. Önskog and J. Zhang. "An accurate treatment of diffuse reflection boundary conditions for a stochastic particle Fokker–Planck algorithm with large time steps". In: *Physica A: Statistical Mechanics and its Applications* 440 (2015), pp. 139–146. ISSN: 0378-4371. DOI: 10.1016/j.physa.2015.07.003.